Monitoring Deformations of Embankments in Arctic Regions using Unmanned Aerial Vehicle Photogrammetry and Terrestrial Laser Scanning

by

Dylan Michael James Stafford

A Thesis submitted to the Faculty of Graduate Studies of

The University of Manitoba

in partial fulfillment of the requirements for the degree of

MASTER OF SCIENCE

Department of Civil Engineering

University of Manitoba

Winnipeg

Copyright © 2020 by Dylan Michael James Stafford

ABSTRACT

Embankments in Arctic regions are typically constructed during winter with no cuts in the ground to preserve the permafrost foundation. These embankments are susceptible to deformations in the summer immediately following construction as ice within the embankment fill melts and in subsequent years as permafrost at the embankment toe thaws. Unmanned aerial vehicle (UAV) photogrammetry and terrestrial laser scanning (TLS) were used to monitor deformations of four high-fill embankment sections along the newly constructed Inuvik-Tuktoyaktuk Highway (ITH). Two UAVs (senseFly albris and DJI Phantom 4 Pro) and one laser scanner (FARO Focus^{3D} X 330) were used. One of the high-fill sections was reinforced with wicking woven geotextiles to improve slope stability and instrumented to displacements within the embankment. UAV photogrammetry and TLS are both relatively new technologies being used to monitor deformations of structures. Significant effort was dedicated to learning about the technologies, developing best operating practices, calibrating the technologies to quantify their accuracies, and designing the on-site surveys.

UAV and TLS surveys were conducted during summer in three consecutive years (2017–2019). UAV imagery and TLS data were processed using specialized software to generate point clouds of the high-fill sections. An RTK system was used to measure positions of checkerboard ground control points (GCP) for georeferencing point clouds. The accuracy of UAV and TLS point clouds was quantified based on GCP errors. Alignment of point clouds was required because of poor quality GCP measurements. Point clouds from each year were compared using multiscale model-to-model cloud comparison (M3C2) to determine deformations. A cross-section analysis was also performed for each high-fill section.

High-fill sections along ITH showed deformations including toe subsidence and lateral spreading. Some of the high-fill sections showed positive change (e.g. heave, deposition) at the upper-slope and negative change (e.g. erosion, settlement) at the lower-slope, while other sections showed the opposite behaviour. The behaviours and magnitudes of UAV and TLS deformations were highly

sensitive to the point cloud alignment methods. UAV measured deformations underestimated the instrumentation displacement data at KM-82 by approximately 30 mm, while TLS measured deformations were reasonably close to the instrumentation data after point cloud alignment.

Due to the novelty of research methods and technologies used, a few mistakes were made during data acquisition. These mistakes were discovered while analyzing the field data. The data acquisition methods and accuracy of reconstructed point clouds were improved year-to-year; however, embankment deformations were too small to be detected by the UAV or TLS and the identification of deformation mechanisms was limited. Although the results were not as conclusive as originally intended, several lessons were learned that will be valuable for future researchers and practitioners. UAV photogrammetry is better suited for monitoring larger areas with greater deformation magnitudes and TLS is better suited for monitoring smaller areas with small-scale deformations. Generally, UAV photogrammetry is better suited for monitoring deformations of embankments. Results obtained by the albris were slightly more accurate than the Phantom, but the high cost of the albris is not justified by its overall performance compared to the Phantom.

ACKNOWLEDGEMENTS

These acknowledgements are dedicated to the many people that have each in their own way helped me to complete this thesis. I am forever grateful for their support over the past three years.

First and foremost, thank you to my advisor, Dr. Marolo Alfaro, for your guidance and support. Your patient, caring, and encouraging approach gave me a sense of confidence and enjoyment in my work and pushed me to be an independent, curious, and analytical researcher. Thanks as well to my advisory committee members, Dr. Lukas Arenson and Dr. Jitendra Paliwal, for your assistance and guidance on my research.

To my unofficial mentor over the past four years, Earl Marvin De Guzman, thank you for all the time you dedicated to my development and the numerous lessons you taught me. Samuel Kaluzny, your assistance collecting data on-site is greatly appreciated. Devon Adamson, your friendship and advice as we each strived to succeed in our similar but unique research projects was helpful and encouraging. And to the rest of my colleagues in E1-311, thanks for all the good times and beneficial discussions on life and research.

Special thanks to Kerry Lynch for your technical support and assistance with the UAV. And to Dave Tetreault of Dave's Aggregates, your permission to conduct UAV flights at your gravel pit was invaluable to my research. I'd also like to recognize the University of Manitoba, the Natural Sciences and Engineering Research Council of Canada, Transport Canada, and the Government of Northwest Territories Department of Infrastructure for their generous financial support.

To my family, your endless love and encouragement has given me the freedom and confidence to take on all of life's challenges. To my friends, thanks for always being there when I needed a laugh and for reminding me that there's more to life than school. To my lovely girlfriend, Monica, thank you for your unwavering support, patience, understanding, and strength—I couldn't have completed this thesis without you by my side. And last but not least, thank you to my best friend, Charlie, for your untiring enthusiasm and happiness each and every day, particularly on our walks.

TABLE OF CONTENTS

Abstract i

Acknowledgements iii

Table of Contents iv

List of Tables vii

List of Figures viii

List of Copyrighted Material with Permissions xiii

List of Appendices xiv

List of Acronyms and Symbols xv

Chapter 1: Introduction 1

1.1 Background 1

1.2 Motivation 5

1.3 Objectives 5

1.4 Hypothesis 6

1.5 Thesis Organization 6

Chapter 2: Literature Review 8

2.1 Monitoring Embankments in Arctic Regions 8

2.2 Unmanned Aerial Vehicle (UAV) Photogrammetry 12

2.2.1 Structure-from-Motion (SfM) Processing 14

2.2.2 UAV-SfM Survey Design and Accuracy 16

2.2.3 UAV-SfM Strengths, Limitations, and Applications 22

2.3 Terrestrial Laser Scanning (TLS) 25

2.3.1 TLS Survey Design and Accuracy 26

2.3.2 TLS Strengths and Limitations 28

2.4 Deformation Detection 29

2.5 Summary of Literature Review 33
Chapter 3: Technology Operating Procedures and Calibration Tests 35
3.1 UAV Photogrammetry 35
3.1.1 UAV Operation Certifications 35
3.1.2 UAV Models and Specifications, Operating Procedures, and Image Processing 36
3.1.3 UAV Calibration I—Target Displacement 43
3.1.4 UAV Calibration II—Image and Ground Control Parameters 48
3.2 TLS 68
3.2.1 TLS Model and Specifications, Operating Procedures, and Data Processing 68
3.2.2 TLS Calibration I—Sphere Target Displacement Accuracy 72
3.2.3 TLS Calibration II—Checkerboard Target Identification 76
3.2.4 TLS Calibration III—Site-Scale Setup, Target Identification, and Scan Registration . 79
3.3 RTK Survey System 81
3.3.1 RTK Model, Operating System, and Data Processing 81
3.3.2 RTK Calibration Tests 83
3.4 Summary of Technology Operating Procedures and Calibration Tests 86
Chapter 4: Data Acquisition and Processing 87
4.1 Site Selection 87
4.2 Site Visits and Data Acquisition 88
4.2.1 UAV Data Acquisition 88
4.2.2 TLS Data Acquisition 94
4.3 Data Processing 96
4.3.1 RTK GCP Processing 96
4.3.2 UAV Processing 98
4.3.3 TLS Processing 103

4.4 Deformation Analysis 106
4.4.1 Point Cloud Registration 106
4.4.2 M3C2 Point Cloud Comparison and Parameter Selection 109
4.4.3 Cross-Section Analysis 112
4.5 Summary of Data Acquisition and Processing 114
Chapter 5: Results and Discussion 117
5.1 UAV and TLS Deformations at KM-82 117
5.1.1 KM-82 UAV and TLS Deformations using M3C2 117
5.1.2 KM-82 Point Cloud Accuracy: UAV vs. TLS 136
5.1.3 Cross-Section Analysis Results and Instrumentation Comparison 140
5.1.4 Comparison of UAV Photogrammetry and TLS for Deformation Monitoring 145
5.2 UAV Deformations at High-Fill Sections 148
5.2.1 KM-48 151
5.2.2 KM-49 156
5.2.3 KM-117 163
5.2.4 Deformation Behaviours of High-Fill Sections 169
5.3 Summary of Results and Discussion 172
Chapter 6: Conclusion 174
6.1 Summary 174
6.2 Conclusions 176
6.3 Recommendations 179
6.4 Guideline for using UAV Photogrammetry to Monitor Deformations 182
References 183

LIST OF TABLES

Table 3.1 UAV specifications. 39

Table 3.2 Pix4D standard processing parameters. 42

Table 3.3 UAV Calibration I—target displacement distances and error measurements. 47

Table 3.4 UAV Calibration II—processing group parameters. 52

Table 3.5 UAV Calibration II—number and configurations of GCPs for each processing group. 53

Table 3.6 UAV Calibration II—RTK survey uncertainty statistical measures. 56

Table 3.7 FARO Focus^{3D} X 330 Laser Scanner specifications. 69

Table 3.8 FARO Focus^{3D} X 330 Laser Scanner settings. 71

Table 3.9 TLS Calibration I—target displacement errors between hand and scanner measurements. 75

Table 4.1 High-fill section locations, geometries, and characteristics. 88

Table 4.2 UAV data acquisition summary. 90

Table 4.3 TLS data acquisition summary. 95

Table 4.4 Horizontal, vertical, and 3D uncertainties for the RTK surveys of GCPs on-site. 97

Table 4.5 SfM-processed horizontal, vertical, and 3D errors at checkpoints for UAV surveys on-site. 101

Table 4.6 TLS point cloud registration errors 105

Table 4.7 M3C2 parameters 111

Table 4.8 Registration errors (*reg* values) for M3C2 comparisons. 112

Table 5.1 KM-82 2018–2019 point cloud vertical comparison results and selected 2019 point cloud vertical shifts 121

Table 5.2 2018–2019 point cloud vertical comparison results and selected 2019 point cloud vertical shifts. 151

LIST OF FIGURES

Figure 1.1 Inuvik-Tuktoyaktuk Highway map (Stewart, CBC News, 2017). 3

Figure 1.2 Embankment deformations along the Inuvik-Tuktoyaktuk Highway: a) longitudinal cracking at shoulder (photo by L. Arenson, 2015); b) slope failure (photo by J. Festa, 2015); c) slope movement with longitudinal cracking (photo by L. Arenson, 2015). 4

Figure 2.1 Vertical doming error represented by 3D wireframes and colour-shaded heat maps in idealized simulations of: a) a single stereo pair; b) a 10-image strip; and c) a four-strip image block (James & Robson, 2014). 19

Figure 3.1 senseFly albris UAV. 37

Figure 3.2 DJI Phantom 4 Pro UAV (DJI, 2018). 38

Figure 3.3 Checkerboard target. 43

Figure 3.4 UAV Calibration I—reconstructed point cloud with marked targets and GCPs. 44

Figure 3.5 UAV Calibration I—representation of UAV images acquired with green spheres identifying images' calibrated positions: a) grid images; b) POI images. 45

Figure 3.6 UAV Calibration II—plan view of the survey area with GCPs. 50

Figure 3.7 UAV Calibration II—example GCP configurations: a) 14 GCPs; b) 12 GCPs; c) 10 GCPs; d) 8 GCPs; e) 6 GCPs; f) 4 GCPs. 54

Figure 3.8 UAV Calibration II—box plot of the horizontal, vertical, and 3D RTK measurement uncertainties at GCPs for 20, 60, and 180 second RTK observation times. 56

Figure 3.9 UAV Calibration II—RMS of the processed 3D errors at checkpoints for all processing groups and numbers of GCPs. 58

Figure 3.10 UAV Calibration II—box plot of the processed errors at checkpoints when 12 GCPs were used to georeference for each processing group. 59

Figure 3.11 UAV Calibration II—RMS of the processed 3D, vertical, and horizontal errors at checkpoints for BASE, GSD8, and GSD6. 60

Figure 3.12 UAV Calibration II—RMS of the processed 3D, vertical, and horizontal errors at checkpoints for BASE, RTK1, and RTK3. 61

Figure 3.13 UAV Calibration II—RMS of the processed errors for BASE, OBL45, OBL60, and OBL75: a) vertical direction; b) horizontal plane. 62

Figure 3.14 UAV Calibration II—RMS of the processed 3D errors for MID and its corresponding individual parameter groups, plus vertical and horizontal errors for MID. 63

Figure 3.15 UAV Calibration II—RMS of the processed 3D errors for MAX and its corresponding individual parameter groups, plus vertical and horizontal errors for MAX. 64

Figure 3.16 UAV Calibration II—LoD for deformation measurements of point clouds from all processing groups and numbers of GCPs. 65

Figure 3.17 FARO Focus^{3D} X 330 Laser Scanner. 69

Figure 3.18 Sphere target for TLS. 73

Figure 3.19 TLS Calibration I—reconstructed point cloud with marked sphere targets. 74

Figure 3.20 TLS Calibration II: a) test setup; b) standing angle checkerboards. 77

Figure 3.21 Checkerboard stands with and without a checkerboard. 79

Figure 3.22 TLS Calibration III—photo of test site showing embankment and targets. 80

Figure 3.23 TLS Calibration III—plan view survey setup showing scanner locations (squares) and sphere and checkerboard targets: a) 20 m section; b) 40 m section. 81

Figure 4.1 Aerial images captured by the Phantom at KM-82 in 2018; shown in Pix4D with green spheres identifying the images' calibrated positions. 92

Figure 4.2 Examples of planned checkerboard GCP layouts for UAV surveys: a) KM-49; b) KM-82. 92

Figure 4.3 Aerial images captured by the Phantom at KM-82 in 2019; shown in Pix4D with green spheres identifying the images' calibrated positions. 93

Figure 4.4 TLS survey plans at KM-82 showing scanner locations (squares) and sphere and checkerboard targets: a) 2018; b) 2019. Dark blue targets in 2019 remained for scans of both slopes. 95

Figure 4.5 Box plot of the RTK survey 3D uncertainties at GCPs. 98

Figure 4.6 Box plot of the SfM-processed 3D errors at checkpoints for UAV surveys on-site. 100

Figure 4.7 Fine registration segment areas for UAV point clouds: a) KM-82; b) KM-117. 108

Figure 5.1 KM-82 albris UAV 2018–2019 initial M3C2 deformation (scale: ±400 mm). 118

Figure 5.2 KM-82 Phantom UAV 2018–2019 initial M3C2 deformation (scale: ±400 mm).....118

Figure 5.3 KM-82 TLS 2018–2019 initial M3C2 deformation (scale: ±400 mm). 119

Figure 5.4 Fine registration segment area for KM-82 TLS point clouds. 121

Figure 5.5 KM-82 albris UAV 2018–2019 M3C2 deformation after vertical shift (scale: ±100 mm). 122

Figure 5.6 KM-82 Phantom UAV 2018–2019 M3C2 deformation after vertical shift (scale: ±100 mm). 123

Figure 5.7 KM-82 TLS 2018–2019 M3C2 deformation after vertical shift (scale: ±100 mm). 123

Figure 5.8 KM-82 albris UAV 2017–2018 M3C2 deformation (scale: ±300 mm). 125

Figure 5.9 KM-82 albris UAV 2018–2019 final M3C2 deformation after vertical translation and rotation registration (scale: ±100 mm).....126

Figure 5.10 KM-82 Phantom UAV 2018–2019 final M3C2 deformation after vertical translation and rotation registration (scale: ±100 mm). 127

Figure 5.11 KM-82 TLS 2018–2019 final M3C2 deformation after vertical translation and rotation registration (scale: ±100 mm).....128

Figure 5.12 KM-82 albris UAV 2018–2019 M3C2 LoD estimates (scale: 36–45 mm). 131

Figure 5.13 KM-82 Phantom UAV 2018–2019 M3C2 LoD estimates (scale: 56–68 mm). 132

Figure 5.14 KM-82 TLS 2018–2019 M3C2 LoD estimates (scale: 33–45 mm).....132

Figure 5.15 KM-82 albris UAV 2018–2019 M3C2 significant change estimates. 133

Figure 5.16 KM-82 Phantom UAV 2018–2019 M3C2 significant change estimates. 134

Figure 5.17 KM-82 TLS 2018–2019 M3C2 significant change estimates. 134

Figure 5.18 KM-82 2018 point cloud comparisons (scale: ±50 mm): a) TLS-east vs. albris; b) TLS-west vs. albris; c) TLS-east vs. Phantom; d) TLS-west vs. Phantom; e) albris vs. Phantom. 137

Figure 5.19 KM-82 2019 point cloud comparisons (scale: ±50 mm): a) TLS vs. albris; b) TLS vs. Phantom; c) albris vs. Phantom. 139

Figure 5.20 KM-82 2018–2019 original cross-sections: a) reinforced zone; b) control zone. 142

Figure 5.21 KM-82 2018–2019 cross-sections with 10x vertical exaggeration: a) reinforced zone; b) control zone. 143

Figure 5.22 KM-82 2018–2019 final cross-sections with 10x vertical exaggeration and smoothing: a) reinforced zone; b) control zone. 144

Figure 5.23 KM-82 2017–2018 cross-sections—original and 10x vertical exaggeration with smoothing: a) reinforced zone; b) control zone. 145

Figure 5.24 Fine registration segment areas for UAV point clouds: a) KM-48; b) KM-49. 150

Figure 5.25 KM-48 UAV M3C2 deformation after vertical shift (scale: ±100 mm): a) albris; b) Phantom. 153

Figure 5.26 KM-48 UAV M3C2 deformation after vertical translation and rotation registration (scale: ±100 mm): a) albris; b) Phantom. 154

Figure 5.27 KM-48 UAV M3C2 LoD estimates: a) albris (scale: 46–56 mm); b) Phantom (scale: 67–80 mm). 155

Figure 5.28 KM-48 UAV M3C2 significant change estimates for the vertical shift comparison: a) albris; b) Phantom. 156

Figure 5.29 KM-48 cross-sections with 10x vertical exaggeration and smoothing. 156

Figure 5.30 KM-49 UAV M3C2 deformation after vertical shift (scale: ±100 mm): a) albris; b) Phantom. 159

Figure 5.31 KM-49 UAV M3C2 deformation after vertical translation and rotation registration (scale: ±100 mm): a) albris; b) Phantom. 160

Figure 5.32 KM-49 UAV M3C2 LoD estimates: a) albris (scale: 34–42 mm); b) Phantom (scale: 63–75 mm). 161

Figure 5.33 KM-49 UAV M3C2 significant change estimates for the vertical shift comparison: a) albris; b) Phantom. 162

Figure 5.34 KM-49 cross-sections with 10x vertical exaggeration and smoothing. 162

Figure 5.35 KM-117 albris UAV 2017–2018 M3C2 deformation after registration (scale: ±200 mm). 165

Figure 5.36 KM-117 albris UAV 2018–2019 M3C2 deformation (scale: ±100 mm): a) vertical shift; b) vertical translation and rotation registration 166

Figure 5.37 KM-117 point cloud segments showing vegetation: a) 2018 pre-clearing; b) 2019 post-clearing 166

Figure 5.38 KM-117 albris UAV M3C2 LoD estimates: a) 2017–2018 (scale: 89–100 mm); b) 2018–2019 (scale: 58–70 mm). 167

Figure 5.39 KM-117 albris UAV M3C2 significant change estimates: a) 2017–2018; b) 2018–2019 vertical shifted 168

Figure 5.40 KM-117 cross-sections with 10x vertical exaggeration and smoothing: a) 2017–2018; b) 2018–2019. 169

LIST OF COPYRIGHTED MATERIAL WITH PERMISSIONS

Figure 2.1 Vertical doming error represented by 3D wireframes and colour-shaded heat maps in idealized simulations of: a) a single stereo pair; b) a 10-image strip; and c) a four-strip image block (James & Robson, 2014).

LIST OF APPENDICES

Appendix A Ground Control Point (GCP) Uncertainty and Error Data

Appendix B Guideline for using UAV Photogrammetry to Monitor Deformations

LIST OF ACRONYMS AND SYMBOLS

σ_D	M3C2 standard deviation of points from the normal surface
σ_{dn}	M3C2 standard deviation of points intercepting the projection cylinder from the reference point cloud (σ_{d1}) and compared point cloud (σ_{d2})
2D	two-dimensional
2.5D	two-dimensional horizontal grid with a vertical coordinate value
3D	three-dimensional
AAT	automatic aerial triangulations
BA	bundle adjustment
C2C	cloud-to-cloud
C2M	cloud-to-mesh
CARs	Canadian Aviation Regulations
CMVS	clustering views for multi-view stereo
CSRS	Canadian Spatial Reference System
d	M3C2 projection scale diameter
D	M3C2 normal scale diameter
DEM	digital elevation model
DoD	digital surface models of difference
DSM	digital surface model
DTM	digital terrain model
GCP	ground control point
GCS	ground control station
GNSS	Global Navigation Satellite System
GNWT-DOI	Government of Northwest Territories Department of Infrastructure
GSD	ground sampling distance

i_n	M3C2 points in the reference point cloud (i1) or compared point cloud (i2) used for distance measurement
ICP	iterative closest point
IMU	inertial measurement unit
ITH	Inuvik-Tuktoyaktuk Highway
laser	light amplified by stimulated emission of radiation
LiDAR	light distance and ranging
LoD	level of detection
M3C2	multiscale model-to-model cloud comparison
mAh	milliamp hour
Mp	megapixel
Mpts	megapoints
mrad	milliradians
MVS	multi-view stereo
n_n	M3C2 number of points intercepting the projection cylinder from the reference point cloud (n_1) and compared point cloud (n_2)
NAD83	North American 1983 datum
navcam	navigation camera
No.	number
NRCan	Natural Resources Canada
PMVS2	patch-based multi-view stereo
POI	point-of-interest
PPP	precise point positioning
RANSAC	Random Sample Consensus
reg	M3C2 registration error

RGB	red-green-blue
RMS	root mean squared
RMSE	root mean squared error
RPAS	remotely piloted aircraft systems
RSS	root sum squared
RTK	real-time kinematic
s	M3C2 core point spacing
SAA	ShapeArray
SfM	Structure-from-Motion
SFOC	special flight operations certificate
SIFT	scale invariant feature transform
SLS	serviceability limit state
TB	target-based
TLS	terrestrial laser scanning
U of M	University of Manitoba
UAV	unmanned aerial vehicle
UTM	Universal Transverse Mercator
VLOS	visual line-of-sight

CHAPTER 1: INTRODUCTION

1.1 Background

Embankments in Arctic regions are usually constructed during winter to improve mobility of construction equipment on the frozen ground and minimize disturbance of permafrost by reducing heat input to the ground. Permafrost is defined as ground that remains at or below 0°C for a minimum period of 2 years (Williams, 1986). Construction processes impact the thermal regime of the area and if not properly managed can cause permafrost degradation beneath the embankment, which would have lasting detrimental effects on the embankment's stability. The passive design approach is commonly taken, where the embankment is designed thick enough for the fill material to provide enough insulation to the ground for the permafrost to aggrade into the embankment (Argue et al., 1981). The fill material is often locally available, frozen soil that can contain high ice contents. Melting of this ice during warming reduces the shear strength of the embankment fill (De Guzman et al., 2018) and causes instability, which is exhibited through slope movements. This is particularly observable during the first spring following construction.

Another common cause of embankment instability and deformation is thawing of the foundation soil at the toes. Soil at the toe thaws during summer due to lack of fill material and insufficient insulation. Snow drifts that build up at the toe during winter insulate the thawed ground and can prevent it from freezing (Fortier et al., 2011). Then during summer, the foundation soil continues thawing and the thawed zone can extend further beneath the embankment (Esch, 1983). As this cyclic process continues, large thaw zones can develop at the toes causing subsidence and an outward movement of the slope (McGregor et al., 2010). This can lead to longitudinal cracking along the embankment road surface and in extreme cases, slope failures. Deformations and slope movements are more extreme and critical to detect on high-fill embankments compared to low-fill design embankment sections. Low-fill embankments are more susceptible to excessive thaw settlement of

the entire section associated with permafrost degradation beneath the embankment. This occurs when the insulating effect of the fill material is less than that of the active layer.

The Inuvik-Tuktoyaktuk Highway (ITH) is a newly constructed highway in Northwest Territories, Canada that was opened to the public on November 15, 2017. The highway is located above the Arctic Circle in a continuous permafrost zone that is characterized by glacial deposits. Terrain in the ITH region is rolling with a complex network of thermokarst lakes and interconnected channels. A peat layer of varying thickness at ground surface covers most of the region with soil in the permafrost beneath containing excess ice in the form of ice veins, lenses, wedges, and massive ice (Rampton, 1988). Work from Tarnocai et al. (2004) in the Inuvik-Tuktoyaktuk region indicates the active layer ranges from 30 cm to over 150 cm. The highway was passively designed and constructed during winter using locally available fill materials with no cuts into the ground in order to preserve the permafrost foundation. The complex terrain and difficult ground conditions forced the highway to have several high-fill sections, some up to 12 m high. One of the high-fill sections along the highway was reinforced with wicking woven geotextiles as part of a larger research project at the University of Manitoba (U of M). The geotextile has two functions that can improve slope stability: 1) it provides a direct path to transport water out of the embankment fill, especially during the first spring thaw; and 2) it structurally reinforces the embankment and provides tensile strength. Instrumentation was installed in the reinforced test zone and a non-reinforced control zone to measure horizontal and vertical displacements and temperatures within the embankment. Data from the embankment instrumentation and an on-site weather station has been collected since 2016.

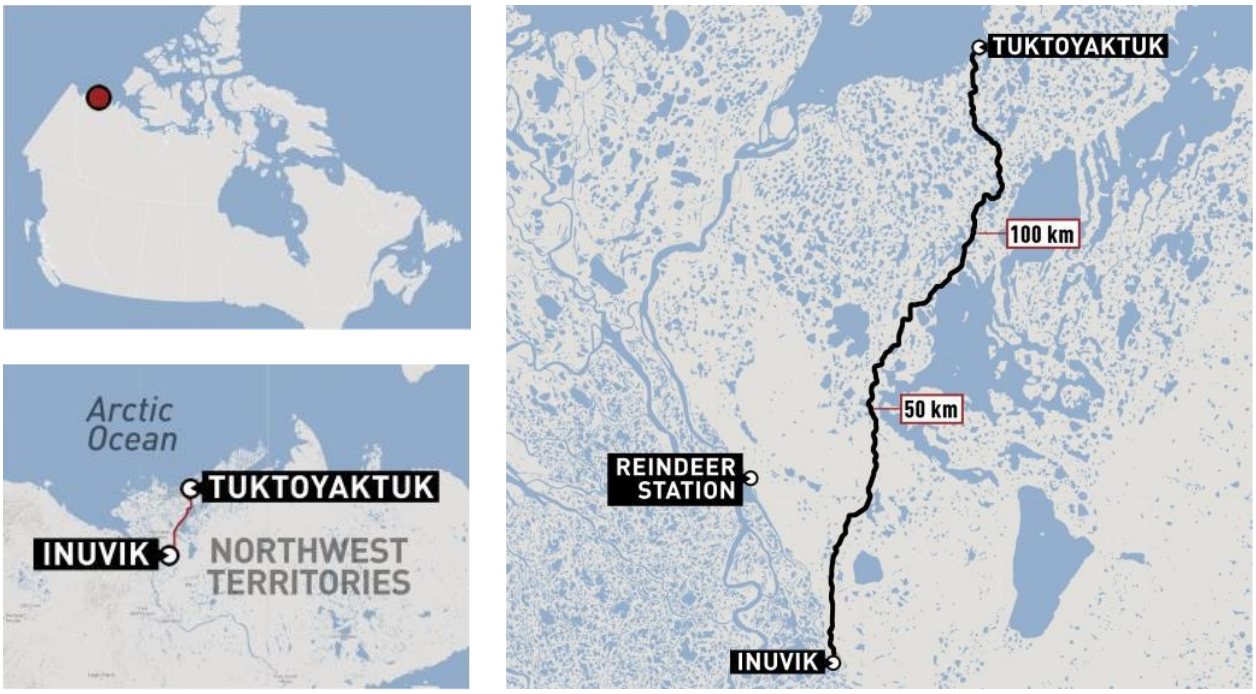

Figure 1.1 Inuvik-Tuktoyaktuk Highway map (Stewart, CBC News, 2017).

High-fill sections of ITH are susceptible to deformations that can jeopardize the structural stability of the embankment and the safety of its users. Monitoring the embankment and assessing its performance is crucial to provide confidence that sideslopes are stable and user safety is not of concern. Two imaging technologies were used to monitor the embankment and determine surficial deformations of high-fill sections along the highway: unmanned aerial vehicle (UAV) photogrammetry and terrestrial laser scanning (TLS). These technologies were selected for their ability to capture large amounts of accurate topographical data with high spatial resolution over a relatively short period of time (Fan et al., 2014). UAV photogrammetry involves the processing of aerial images using feature-matching algorithms to produce three-dimensional (3D) digital geometries of terrain and objects (Fonstad et al., 2013). This technology can cover large areas and has the advantage of being applicable in remote areas with limited access (Eltner et al., 2016). TLS captures 3D geometry by projecting a laser beam outward and measuring distances to objects based on the reflected laser (FARO Technologies Inc., 2015). TLS is better suited for small-scale sites with

steep slope angles (Westoby et al., 2012). The research section at KM-82 and three other high-fill sections along ITH were monitored. TLS was only conducted at KM-82 and UAV monitoring was performed at all high-fill sections.

Figure 1.2 Embankment deformations along the Inuvik-Tuktoyaktuk Highway: a) longitudinal cracking at shoulder (photo by L. Arenson, 2015); b) slope failure (photo by J. Festa, 2015); c) slope movement with longitudinal cracking (photo by L. Arenson, 2015).

Monitoring surficial deformations of high-fill sections along ITH using these technologies provided a method to assess the condition of the sections for safety reasons. Furthermore, monitoring provides researchers the opportunity to study the performance of high-fill embankment sections and better understand the mechanisms controlling deformations of embankments constructed during winter and subjected to seasonal freezing and thawing. Understanding these

mechanisms and the factors contributing to deformation is important for predicting how embankments in Arctic regions will perform in the future. Climate change is having a significant impact on the Arctic environment and a proactive approach considering environmental changes must be taken to design and maintain infrastructure in the Arctic.

1.2 Motivation

There is a limited understanding of how embankments constructed during winter using frozen material will perform both short-term following construction and long-term after years of seasonal freezing and thawing. The warming climate and degrading permafrost conditions exacerbate these embankment's susceptibility to slope movements and emphasizes the need to better understand their behaviour and predict how they will perform in the future. Monitoring these embankments can give insights to their deformation behaviour and overall performance; however, traditional methods for monitoring embankments using ordinary survey equipment are time-consuming, costly, and do not provide a satisfactory amount of data to fully understand embankment deformations. Methods for monitoring embankments in the Arctic that utilize advanced imaging technologies such as TLS and UAV photogrammetry need to be established in order to predict slope instabilities and improve safety, as well as to provide knowledge of the deformation mechanisms. These efforts could help to improve the design and construction of embankments built on permafrost.

1.3 Objectives

The main objectives for this research are as follows:

1. Determine the surficial deformations of high-fill sections along ITH using two imaging technologies: UAV photogrammetry and TLS.
2. Compare the UAV and TLS deformations to instrument displacement data at the KM-82 research site.
3. Determine the causes and contributing factors to deformations of the high-fill sections.

4. Assess the functionality of the imaging technologies and develop best practices for using UAV photogrammetry and TLS to measure deformations of embankments. This includes understanding the factors that control the accuracy of each technology, as well as developing methods to quantify and reduce errors during data acquisition and processing.
5. Compare surficial deformations of the reinforced and non-reinforced zones at KM-82 to determine if the benefits of reinforcing an embankment in the Arctic with wicking geotextiles are still detectable a few years after construction.

1.4 Hypothesis

UAV photogrammetry and TLS are two imaging technologies that can be used to produce high-resolution 3D point clouds of embankments. Surficial deformations determined by comparing UAV photogrammetry and TLS derived point clouds in successive years will be detectable and measurable. UAV and TLS measured deformations will agree with instrumentation displacement data at the KM-82 research site. Comparing the functionality and performance of the UAV and TLS systems will allow for a recommendation of which technology is better suited for monitoring embankment stability in Arctic regions. Overall, this research will provide a technical framework for monitoring the deformation and stability of high-fill embankments in permafrost regions using advanced imaging technologies.

1.5 Thesis Organization

Chapter 1 provides background information and motivation of the research and states the objectives and hypothesis. Chapter 2 is a review of literature pertinent to the research. The literature review is organized into four sections: monitoring embankment in Arctic regions, UAV photogrammetry, TLS, and deformation detection. Chapter 3 outlines the operating procedures and calibration tests for each technology. The calibration tests were performed to assess their accuracies and expected errors, determine optimal survey parameters, and design the on-site surveys that would be suitable for the

conditions on-site. Chapter 4 details the methods used to determine the high-fill sections for monitoring; design the on-site surveys for the UAV, TLS, and RTK; acquire and process data for each technology; and determine deformations at the high-fill sections. Chapter 5 presents and discusses the results of the deformation analysis. The results and discussion are separated into two sections: UAV and TLS results at KM-82, and UAV results at all high-fill sections. Chapter 6 summarizes the research methodology and results, states the conclusions, and provides recommendations and guidelines for monitoring deformations using UAV photogrammetry and TLS. A list of acronyms and symbols used throughout the thesis are provided on page xv to assist the reader.

CHAPTER 2: LITERATURE REVIEW

2.1 Monitoring Embankments in Arctic Regions

Embankments in Arctic regions are often more susceptible to long-term deformation than southern embankments because of the permafrost foundations they are built on. Construction of embankments can allow heat to infiltrate the ground if good practices are not followed. Vegetation and peat layers at the ground surface should not be stripped away. Water stored in the peat layer turns to ice during winter and provides more insulation than other soils due to additional latent heat required to melt the ice (De Guzman & Alfaro, 2018). Thus, underlying permafrost is better protected, and thawing does not penetrate as deep (Yi et al., 2007). Construction equipment should not cut into the ground when placing embankment fill material, as this removes the protective active layer and allows heat from sunlight to infiltrate the ground. Embankment construction should only use fill sections to preserve the permafrost foundation. After construction, embankments act as a snow fence that accumulates snow at the toe, insulating the ground and preventing it from refreezing (Fortier et al., 2011). Because frozen soil is stronger and less compressible than unfrozen soil, degrading permafrost beneath embankments or at the toes leads to deformations such as embankment settlement, toe subsidence, lateral spreading, or longitudinal cracking along the road surface (McGregor et al., 2010).

A large portion of infrastructure in Northern Canada has been constructed on continuous and discontinuous permafrost in problematic alluvial soils such as soft clays and peat deposits. Northern infrastructure was originally designed to rely on the properties of frozen materials for stability; however, due to climate change, the design assumption of stiff, frozen soil is no longer valid in many areas. From 1950 to 2010, the average annual temperature in Canada has increased by close to 1.5°C, which is approximately double the global average (Warren & Lemmen, 2014). Permafrost is thawing throughout the Northern Hemisphere and completely disappearing from discontinuous regions (Hinzman et al., 2005). Large areas of permafrost will continue to warm and thaw due to rising mean

air temperatures (Bush & Lemmen, 2019), increasing the risk of severe infrastructure instabilities. This ever-increasing risk of embankment deformations and instabilities is increasing the demand for new technologies and methods to monitor the performance of embankments in Arctic regions.

Traditional methods for monitoring embankments can be separated into two classifications: instrumentation and surveying. Instrumentation covers all instruments installed within, beneath, or surrounding an embankment to monitor a certain condition or behaviour. Most instrumentation for embankments is targeted at measuring the behaviour of either water, temperature, stress, or deformation. Groundwater influences the effective stresses present in the ground, and therefore plays an important role in the stability and settlement of embankments. The most common instrument used to measure groundwater is the piezometer. A variety of types and models of piezometers exist including standpipes, vibrating wires, and pneumatics (Durham Geo-Enterprises Inc., 2020). For embankment construction, piezometers can be used to determine initial site conditions, ensure safe fill placement, and estimate consolidation progress. In permafrost regions, piezometers can help asses the condition of permafrost as it thaws. This is particularly useful in discontinuous permafrost zones such as Northern Manitoba where piezometers can detect water moving towards the ground surface from melted ground ice lenses (Batenipour et al., 2010).

Temperature monitoring of embankments is extremely important in Arctic regions. Thermistors are the standard instrument used to measure ground temperatures. Thermistors can come as a single node to measure discrete points or as strings of nodes for a series of temperature readings. Temperature readings allow engineers to interpret the condition of permafrost, which is critical for analyzing and predicting the performance of an embankment. Not only is the temperature of the foundation of interest but also the temperature within the embankment itself. In Arctic regions, embankment fill material insulates the ground and permafrost will aggrade upwards into the embankment. Thermistors can be installed within embankment fill material during construction to

monitor the growth of permafrost post-construction and its degradation over time due to climate warming (De Guzman et al., 2019, submitted).

Stress is an important condition to monitor during embankment construction because the deformation of soil depends on the soil's stress state and applied stresses. The two main instruments used for measuring stresses in soils are pressure cells and stress transducers. They can be installed in foundation soil or on structures to measure vertical and lateral stresses. Pressure cells are commonly used in embankment construction to measure stress changes as fill material is placed for stability and settlement analyses. In Arctic regions, stress instrumentation can be installed at different levels in embankment backfill materials to measure frost heave pressures.

Deformation is ultimately the behaviour that determines the performance of many geotechnical structures. The serviceability limit state (SLS) will typically govern the design of embankments in Arctic regions. Therefore, instability of these embankments most often refers to an SLS failure such as excessive settlement. There are several types of instruments that can be used to monitor the deformation behaviours of Arctic embankments discussed previously. These instruments include, but are not limited to, slope inclinometers, settlement systems, and ShapeArrays (SAA). Slope inclinometers monitor subsurface movement. Common practice is to install them vertically at the shoulder, mid-slope, or toe of an embankment to measure deformation of the slope. This application allows for the depth and rate of slope movement to be measured, providing early signs of impending instabilities. Slope inclinometers can also be installed horizontally along the base of an embankment to monitor settlement profiles. Settlement systems are used to monitor settlement of embankments. Many types of settlement systems exist including settlement plates, vibrating wire liquid settlement systems, and magnetic settlement systems. In Arctic regions, settlement systems can also be used to monitor heave in embankments. ShapeArrays are a newer instrument that are becoming more popular in geotechnical engineering. A ShapeArray is an array of rigid segments separated by joints that measure the displacement of each joint (Measurand, 2019). Similar to slope inclinometers,

ShapeArrays can be installed vertically or horizontally to measure deformations of an embankment. Their advantage is that they can monitor the development of deformation along its length to a high degree of accuracy (e.g. 1.5 mm), as well as measure temperature at each joint (Measurand, 2019). Instrumentation is invaluable for monitoring embankments; however, it can be expensive and only offers measurements at discrete points. Interpreting instrumentation data also requires extensive analysis to understand deformation behaviour.

Surveying equipment is regularly used to monitor construction and deformation of embankments. Fundamentally, surveying is the technique or science of measuring the 3D coordinates of points on earth's surface. During construction of an embankment, surveying techniques are used to stake out reference points, identify fill heights, and mark progress. Surveying can also be used post-construction to monitor the displacement of key features or survey rods. The most common surveying equipment are levels (digital or automatic) and rods, total stations, and real-time kinematic (RTK) global navigation satellite systems (GNSS). Level and rod is the most rudimentary technique and requires two operators. Total stations are electronic, optical instruments that measure both vertical and horizontal angles and slope distance from the instrument to a reflector prism. Standard total stations require two operators: one for the instrument and one to hold the prism. New robotic total stations allow the instrument to be controlled remotely or automatically, eliminating the need for a second operator to hold the prism. RTK systems use two GNSS antennas—a static reference antenna and a mobile measuring antenna—to quickly measure the point coordinates. RTK systems have the advantage of not needing to maintain visual line of sight with the reference instrument to measure a point's coordinates.

Surveying techniques are highly accurate and can measure point coordinates to near millimetre accuracy. Construction monitoring applications have traditionally been performed by trained personnel operating survey equipment, but these activities can be time consuming, hazardous, and costly (Miller et al., 2008). Furthermore, surveying equipment has a glaring limitation for

deformation monitoring: it only measures discrete points. This restricts the analysis of embankment deformation and can limit understanding of deformation behaviour. New imaging and sensing technologies such as UAV photogrammetry and TLS are revolutionizing the science of deformation monitoring and providing engineers with new methods of assessing structural performance. These technologies have been used around the world for a wide variety of earth science and engineering applications; however, until now, there has been limited applications of UAV photogrammetry and TLS for monitoring embankments in Arctic regions.

2.2 Unmanned Aerial Vehicle (UAV) Photogrammetry

Photogrammetry is the science of making measurements and creating 3D surface models from images. It is particularly useful for processing aerial imagery, providing a wide range of mapping, inspection, and monitoring applications. In traditional photogrammetry, images are processed in pairs using a stereo restitution instrument that allows the images to be precisely oriented relative to each other and a stereoscopic image to appear. The human operator would then mechanically manipulate the restitution instrument to change the stereo image and investigate 3D coordinates of features for mapping (Vermeer & Ayehu, 2018). The traditional approach requires calibrated cameras and the 3D location and orientation of the cameras, or the 3D location of a series of control points, to be known (Westoby et al., 2012). This general approach was adapted into computer programs, yet the process remained relatively slow and had limitations.

Some of the earliest work in aerial photogrammetry were Aimé Laussedat's experiments using kites and balloons to obtain aerial imagery for topographic mapping (Laussedat, 1899). Manned airborne photographs were the primary source for aerial photogrammetry until the late 1970s when the development of modern UAVs began. Przybilla and Wester-Ebbinghaus (1979) performed a test with a radio-controlled, fixed-wing UAV with a length of 3 m and equipped with an optical camera. The next year, the same team used a model helicopter equipped with a Rolleiflex camera to aerially

document an old streel structure (Wester-Ebbinghaus, 1980). The model helicopter was the first successful use of a rotary-wing UAV for photogrammetry. Since then, and particularly over the last two decades, UAV photogrammetry has rapidly developed into an effective technology to obtain high-quality 3D surface models for monitoring earth surface processes and civil infrastructure. This rapid development has been driven by advances in the size and quality of sensors and improved battery technologies.

All modern UAVs require three main components to fly: the UAV, a ground control station (GCS), and a data communication link. The three components together make up the unmanned aerial system (UAS). The GCS is a stationary or transportable hardware plus software device used to monitor and command the UAV. Most UAVs now can be connected to a laptop, tablet, or smartphone GCS for ease of transport, setup, and operation. The data communication link connects the UAV to the GCS and must be maintained throughout the entire flight. Most UAVs are programmed to land immediately when the communication link is lost for a given time period to prevent fly-offs or crashes. Within the UAV, there are several other components critical for flying such as the inertial measurement unit (IMU), navigation sensor, imaging sensors. These will be discussed in detail in Section 3.1.

There are two main classifications of UAVs: fixed-wing and rotary. Fixed-wing UAVs cruise at higher speeds and can therefore cover larger areas. They also have longer flight times due to their aerodynamic design, making them suitable for large mapping, agricultural, and environmental projects (Wade, 2015). Rotary UAVs cruise at lower speeds, have shorter flight times, and have lower capacities to resist wind forces (Wade, 2015). For these reasons, they are more suited for monitoring smaller areas and obtaining more accurate measurements for surveying and photogrammetry. Most modern rotary UAVs have four propellers (i.e. quadcopters); however, some are designed with eight propellers (i.e. octocopters).

2.2.1 Structure-from-Motion (SfM) Processing

Aerial photogrammetry has been revolutionized in the past two decades due to advances in computing capacities and computer vision (Eltner et al., 2016). This rapid development in computing capabilities has led to a new class of photogrammetric processing: structure from motion (SfM). SfM operates under the same basic principles as traditional stereoscopic photogrammetry, allowing a 3D scene to be reconstructed from a set of overlapping images. The fundamental difference between them is that SfM is fully automated, with the scene geometry and camera positions and orientations all solved automatically without the need to specify any targets a priori. The approach is best suited for sets of images with a high degree of overlap that capture the entire 3D structure of the scene viewed from a wide array of positions (Westoby et al., 2012). This is most commonly accomplished with a moving camera, hence the name—structure from motion.

The SfM workflow is a series of feature-matching and positioning algorithms. Various programs and software have slightly different methods and algorithms for processing, but the basic concepts and process are commonly used by all. The first step is to identify 2D features in all input images using the scale invariant feature transform (SIFT) algorithm (Lowe, 1999; Lowe, 2004). The algorithm identifies features based on multiscale image brightness and colour gradients, invariant to image scaling. Using gradients, instead of absolute pixel values like the kernel approaches of traditional digital photogrammetry, means that an object seen from multiple viewpoints can be identified as a common feature due to the colour gradient between the object and its background, despite changes in scale or lighting (Fonstad et al., 2013). The kernel-based image correlation approaches of traditional photogrammetry were very sensitive to change in scale between images, thus more difficult to obtain matches (Fonstad et al., 2013). Once features are identified (i.e. keypoints), they are assigned a descriptor that can be matched with the same feature in other images.

Following keypoint identification is the bundle adjustment (BA), which estimates the 3D positions of keypoints and cameras, as well as the orientation of cameras. Keypoints in multiple

images are matched using specialized algorithms and the scene is reconstructed through iterative triangulation of keypoint positions and transformations of camera positions and orientations (i.e. camera external parameters) (Westoby et al., 2012). The BA performs a least squares minimization to minimize the overall residual error between keypoints. The camera internal parameters (focal length and two lens distortion parameters per image) are also included in the BA (i.e. camera self-calibration). The output of the BA is a sparse 3D point cloud made up of matched keypoints.

Another major difference between SfM and traditional digital photogrammetry is the point in the workflow at which the reconstruction is georeferenced to a real-world coordinate system. The traditional approach requires coordinates of either the cameras or ground control points (GCPs) prior to determining the positions of any features within the scene. A GCP is an easily identifiable point with known coordinates that can be marked in images. Artificial GCPs such as checkerboard targets are most commonly used for aerial photogrammetry applications. Natural, explicitly identifiable features over stables areas are an alternative to artificial GCPs in areas where artificial GCP placement would be difficult or on projects where relative deformation is preferred and absolute coordinates are not necessary (Eltner et al., 2016). SfM photogrammetry does not require any coordinate input to reconstruct the scene; the reconstructed point cloud can exist in an arbitrary coordinate system if real-world coordinates are not necessary. To georeference when using SfM, coordinates of GCPs within the scene are inputted and a 3D Helmert transformation with seven parameters (three translations, three rotations, and one scale) transforms the point cloud from an arbitrary coordinate system to a real-world coordinate system (Harwin & Lucieer, 2012). This was originally done after the BA and was called a 2-stage BA. Development in SfM programming demonstrated that when GCP coordinates are included in the BA calculation (i.e. 1-stage), systematic positional errors of the keypoints are minimized (Eltner et al., 2016). Similarly, identifying GCP locations should be done on the images themselves rather than in the reconstructed point cloud to reduce error and improve overall accuracy (Eltner et al., 2016).

The sparse point cloud produced by the BA typically has only a few tens of thousands of points, representing the 3D coordinates of the most prominent features with a set of images (James & Robson, 2012). Once the BA has established correspondence among multiple cameras, a set of multi-view stereo (MVS) image-matching algorithms is executed to greatly increase the number of points and generate a dense surface model. The clustering views for multi-view stereo (CMVS; Furukawa et al., 2010) algorithm is first implemented to decompose overlapping input images into clusters of manageable size (Westoby et al., 2012). CMVS uses the camera orientations and surface points to automatically select and group images, based on scene visibility, into optimized clusters for sequential processing (James & Robson, 2012). The patch-based multi-view stereo (PMVS2; Furukawa & Ponce, 2007) algorithm is then implemented to independently reconstruct 3D data from these individual clusters. PMVS2 generates large numbers of points by working over a grid of pixels in an image, finding the best matches for each grid cell (James and Robson, 2012). The MVS process uses redundant information to weaken the influence of occlusion and noise (Shao et al., 2016). Noisy data is efficiently filtered out of the point cloud and the number of reconstructed points typically increased by two to three orders of magnitude (James & Robson, 2012). The reconstructed dense point cloud is the product of the SfM process. Further processing and analysis of the 3D data can be performed for a variety of monitoring applications (e.g. deformation detection), which will be discussed in Section 2.4.

2.2.2 UAV-SfM Survey Design and Accuracy

The quality of the reconstruction is highly dependent on several factors including image resolution and scale, image network geometry, surface texture, lighting conditions, and control point characteristics (Westoby et al., 2012; Eltner et al., 2016). Higher quality images will logically lead to more accurate point clouds with a higher number of points. Image network geometry refers to the number of images, image overlap, camera-to-surface distance, and image orientation (e.g. incidence angle, convergence). The number of photos varies with the size and complexity of the project, but any

specific region that will be reconstructed must be visible in a minimum of three photos (James & Robson, 2012). A higher number of images in a given area will increase the number of keypoints matched; however, increasing the number of images does not linearly the accuracy of the reconstructed point cloud (Eltner et al., 2016). Increasing the number of images also increases computation time, so the number of images needs to be chosen appropriately for the project. Higher image overlap is recommended to improve keypoint matching and increase the density of the reconstructed point cloud (Stumpf et al., 2015; Westoby et al., 2012). Image overlap should be consistent across the study area to ensure uniform coverage of the feature of interest (Westoby et al., 2012). James and Robson (2012) recommend a minimum image overlap of 60%, while Pix4D (2019) recommends a front overlap (with respect to flight direction) of at least 75% and a side overlap (between flying tracks) of at least 60%.

Decreasing the camera-to-surface distance increases the images' resolution, enhancing the density of keypoints and resolution of the point cloud (Westoby et al., 2012). Setting the camera-to-surface distance too small however reduces the coverage and/or overlap of the image set. Stumpf et al. (2015) demonstrated that cm-accurate measurements can be made with distances less than 200 m. SfM processing is tolerant to different scales and for large study areas, imagery at more than one distance is recommended to help reduce systematic distortions over large distances (Fonstad et al., 2013). On the contrary, too extreme of a difference in scale between images due to different camera-to-surface distances can cause changes in texture at the surface, making it difficult to identify keypoints and ultimately for images to be rejected as useless (James & Robson, 2012). The ground sampling distance (GSD) is the distance between pixel centres measured on the ground. It is an important measurement that represents the combined effect of the camera quality and camera-to-surface distance, and strongly influences the quality of the reconstructed point cloud. When designing UAV surveys, GSD is often the design parameter and camera-to-surface distance is a function of the GSD.

UAV imagery is most often acquired following a parallel-axes image scheme, where the UAV flies in a horizontal grid pattern capturing nadir images at uniform spacing. This scheme has proven to be effective for aerial photogrammetric reconstruction because of its efficient use of UAV battery and uniform coverage (James & Robson, 2014; Westoby, et al., 2012). One drawback of a horizontal grid parallel-axes scheme is a systematic doming error in the vertical direction that develops because the radial lens distortion cannot be derived accurately during the self-calibration of camera parameters during the BA (Fonstad et al., 2013; James & Robson, 2014; Eltner et al., 2016). Reconstructions can achieve cm-scale accuracy and still contain large systematic doming of the surface (James & Robson, 2014). Figure 2.1 provides a visualization of the vertical doming error and the strong influence it can have on UAV image-reconstructed point clouds. In a reconstruction 100 m x 100 m, the vertical doming error can have a magnitude of approximately +0.75 m in the middle and -1.25 m at the extents. Although this is a simulation without real imagery, it demonstrates the significant negative impact of the vertical doming error.

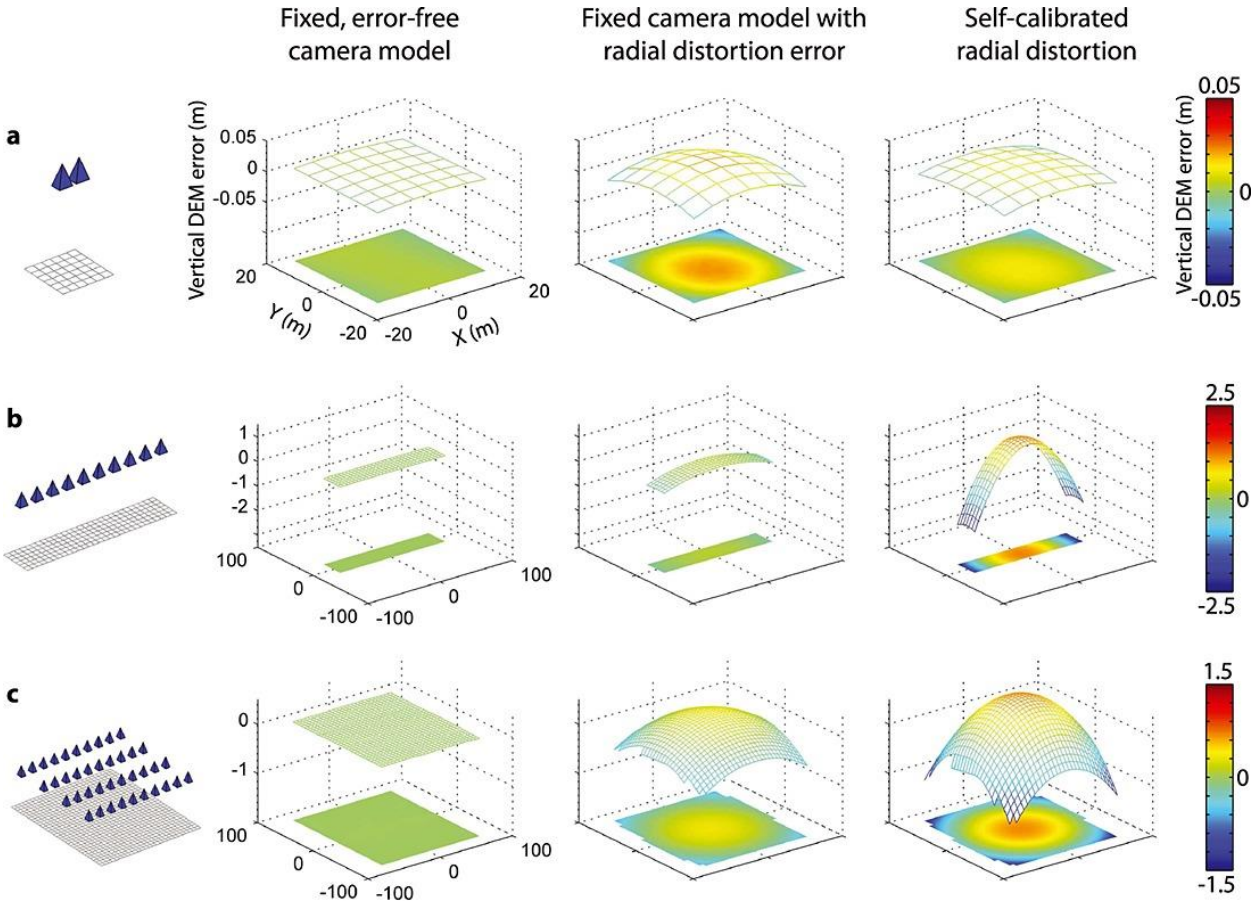

Figure 2.1 Vertical doming error represented by 3D wireframes and colour-shaded heat maps in idealized simulations of: a) a single stereo pair; b) a 10-image strip; and c) a four-strip image block (James & Robson, 2014).

There are two main methods to reduce this doming error. The first method, which will be discussed in further detail below, is to include GCPs strategically placed throughout the scene. The second method is to include oblique images in the UAV survey. James and Robson (2014) demonstrated that collecting only a small number of oblique images (approximately four to ten), in addition to nadir images, can reduce doming errors by up to two orders of magnitude (James & Robson, 2014). Oblique imagery should not be captured at incidence angles less than 30° to the surface because more extreme obliqueness decreases data quality and makes feature matching more difficult (Stumpf et al., 2015). When designing any UAV survey, one must consider all factors of the

image network geometry (e.g. image overlap, GSD, incidence angle) while being conscious of the flight time and UAV battery life.

Surface texture and illumination play a key role in identifying features and matching keypoints. High-textured surfaces with many distinct features will produce larger amounts of keypoints, while low-textured surfaces with few distinct features will cause difficulties obtaining matches (Fonstad et al., 2013). Examples of low-textured surfaces that can present difficulties in SfM are snow and water. Water can also absorb and scatter light, further reducing textural detail and yielding low point densities (Fonstad et al., 2013). Areas of highly variable texture such as vegetation cause difficulties obtaining matches because vegetation features appear different depending on the camera's perspective (Fonstad et al., 2013). Vegetation also can move in the wind and appear different from different perspectives over time. There must be adequate lighting conditions during image acquisition. Images will not capture enough detail if it is too dark, but if it is too bright there may be glared surfaces (James & Robson, 2012). James and Robson (2012) report that overcast but bright days are most suitable for imaging to avoid strong shadows or glares. Eltner et al. (2016) recommend that surveys should last no longer than 30 minutes to avoid large changes in lighting.

Another important aspect of UAV photogrammetry is GCPs for georeferencing and scaling of the reconstruction. Because SfM processing reconstructs the scene in an arbitrary coordinate system, georeferencing shifts the reconstruction to a specified coordinate system, which allows for direct measurement of deformation when point clouds are compared temporally. GCP coordinates are surveyed with a high-quality GNSS system and inputted during processing. A minimum of three GCPs are required to account for model rotation, translation, and scale; but increasing the number of GCPs provides a more robust solution that is less sensitive to error at any one point and generally reduces georeferencing errors (James & Robson, 2012). There is however a law of diminishing returns and continuously increasing the number of GCPs does not correlate to a constant decrease in errors. In addition to georeferencing, GCP implementation also helps to reduce the doming error that results

in SfM reconstructions from parallel-axis image configurations (Eltner et al., 2016). This is only the case in a 1-stage BA where GCPs are included in the adjustment calculation and positional errors at the GCPs are minimized (Eltner et al., 2016); 2-stage BAs do not reduce doming errors. Javernick et al. (2014) found that the vertical error at check points (i.e. GCPs not included in the BA) was 7x the error at control points, demonstrating that some residual systematic vertical error remains even when suitable GCPs are included in the BA. This strengthens the case to collect additional oblique imagery, which is relatively quick and easy when using rotary UAVs with camera gimbals.

Harwin and Lucieer (2012) state that the optimal distance between GCPs for UAV applications is 1/5 to 1/10 the distance of the object of interest. Tahar (2013) found 8 GCPs to be the most accurate for surveying a road construction site. Pix4D (2019), one of the leading SfM photogrammetry software companies, recommends using between 8 and 12 GCPs. The GCP network should be widely distributed, located at the edge or outside of the study area so that coordinate transformations are not being extrapolated outside the volume encompassed by the control points (James & Robson, 2012). Eltner et al. (2016) also recommend for more GCPs to be placed in areas of high relief. If well-distributed GCPs is not achievable, relative comparisons between successive point clouds can be carried out by aligning the point clouds based on mutual areas known not to have changed (James & Robson, 2012). When processing, GCP contribution should be weighted according to their precision and outliers should be eliminated to avoid adverse effects to the point cloud accuracy (James et al., 2017). Another method to georeference UAV image-derived point clouds is to use direct georeferencing, where the location and position of the UAV camera are measured in real-time using a GNSS and inertial measurement unit (IMU). The GNSS accuracy of current UAVs is not high enough to neglect the use of GCPs for most applications, but georeferenced images are still desired because it majorly increases the efficiency of processing. New models of UAVs now include on-board RTK-GNSS units that nearly render GCPs negligible.

Error in a reconstructed 3D point cloud can be assessed with respect to accuracy and precision. Accuracy is the closeness of a measurement to a reference. The accuracy of a point cloud can be estimated by analyzing control point coordinates in the reconstruction compared to their reference coordinates. Precision is the repeatability of a measurement; for example, it indicates how rough a planar surface is represented. The most common measurements of error in point clouds are the mean error, standard deviation, and root mean squared (RMS) error. Positive and negative deviations can compensate for each other when calculating the mean error, which can impede the recognition of systematic errors such as symmetric tilting (Eltner et al., 2016). Standard deviation can also hide systematic errors in the reconstruction because it only gives confidence intervals around the mean error (Pix4D, 2019). If the differences among the measurements is minimal but the mean error of those measurements is not close to the reference value, the standard deviation will not accurately represent that error. RMS error is the most representative measurement of error in a reconstruction because it accounts for both the mean error and the variance (Pix4D, 2019). RMS error is a recognized and relatively easily understood proxy for determining error when the reference dataset is a set of distributed points rather than a continuous surface (Harwin & Lucieer, 2012). James et al. (2017) acknowledge the important of RMS error measurements on control and check points, and recommend for the measurements to be augmented by visualisation of spatial error distribution to protect against hidden systematic errors.

2.2.3 UAV-SfM Strengths, Limitations, and Applications

The use of UAVs for monitoring and inspection has exploded in the industrial, commercial, and academic sectors because of their high-quality sensors, ease of use, and relatively low cost. UAVs can be used in all kinds of environments but are especially useful in remote areas with limited site access (Eltner et al., 2016). Their ability to capture high quality images from aerial perspectives provides great opportunities for both qualitative and quantitative analyses. The simple and automated workflow of SfM has made UAV photogrammetry more attractive for nontechnical users and has

promoted its widespread use. An advantage of SfM is that images from several cameras (both metric and non-metric) can be processed together because camera parameters are calibrated during the BA. A key aspect of image-derived point clouds is that they include colour information, whereas scanned point clouds often do not. Colour provides valuable information and improves qualitative analysis of the scene. It also significantly enhances visualization of point clouds and helps to communicate features and processes identified in the scene with non-technical personnel. As technology and software continue to develop, images can also be re-processed with newer methods to improve point cloud density and quality (Shao et al., 2016).

Arguably the most useful application of UAV photogrammetry is monitoring deformation. Deformation monitoring with a UAV can be done for projects over a wide range of scales and environments, for both man-made structures and natural processes. For projects with scales up to approximately 100 m, UAV photogrammetry provides a convenient technique to acquire high-resolution 3D datasets, which can be used to visualize and quantify volumetric and cross-sectional changes (James & Robson, 2012). UAVs have been used extensively for monitoring soil erosion processes such as coastal morphology (Harwin & Lucieer, 2012) and fluvial morphology (Javernick et al., 2014; Eltner et al., 2015). In fact, many of the deformation detection methods used today were developed for fluvial morphology such as sediment displacement estimates (Wheaton et al., 2010). Another common natural process monitored by UAVs are mass movements such as landslides and rockfalls. Rothmund et al. (2017) generated 3D point clouds, DSMs, and orthomosaics by UAV photogrammetry to identify and analyze landslide kinematics and morphologic features such as ridges, bulges, and fissures of the Super-Sauze landslide in Southeastern France. Meeks et al. (2017) used a UAV and SfM processing in combination with other remote sensing technology to build a detailed 3D geometry model of a complex rock instability in British Columbia, Canada. Gómez-Gutiérrez et al. (2014) and Immerzeel et al. (2014) demonstrated the usefulness of UAVs to monitor glacial deformation in mountainous regions with limited access.

UAV photogrammetry is a valuable tool commonly used to monitor deformation of infrastructure because of its ability to cover large areas and detect small-scale surficial changes. Cigna et al. (2017) used a UAV to monitor small-scale deformation of embankments and earth-retaining structures in Northern Ireland. Siebert and Teizer (2014) evaluated the performance of an autonomous UAV system for monitoring large-scale excavations and earthworks, concluding that UAV photogrammetry can make efficient and accurate measurements with the main limitation being UAV battery life. Ridolfi et al. (2017) used UAV photogrammetry to develop 3D models of dams, investigating the influence of GCP georeferencing on the accuracy of the models. Buffi et al. (2017) also used UAV photogrammetry to inspect dams, validating the image-derived model through comparison with other survey technologies (laser scanner, GNSS, and total station). UAV photogrammetry can also aid in developing risk management and decision-making systems for monitoring the condition of infrastructure (Kovacevic et al., 2016).

UAV photogrammetry clearly has a wide and growing range of applications in civil engineering. The technology does have some drawbacks though that limit its use. Areas of similar texture and/or high reflectivity (e.g. snow, sand, water, etc.) are difficult to match keypoints (Fonstad et al., 2013). Conversely, areas of highly variable texture such as vegetation are also difficult to obtain matches because it can appear different from various perspectives (Fonstad et al., 2013). The systematic doming errors caused by parallel-axis imagery and self-calibrating camera parameters is a major limitation. Minimization of doming errors by good GCP distribution and including oblique images was discussed in detail above. James and Robson (2012) outline the three main factors that limit the accuracy of SfM reconstructions. The first is that the SIFT algorithm can produce poor positional precision of features, which leads to errors in the BA and final point clouds. The second is that the camera calibration model used is not as refined as those in traditional photogrammetry, which can cause issues near image edges where distortion effects are greatest. Thirdly, SfM can add errors because different camera models and parameters are calculated for each image, even though images

are typically acquired using one camera with a fixed lens. These limitations of SfM will be reduced and the accuracy of reconstructions will improve as algorithms are refined with advancements in the field of computer vision.

2.3 Terrestrial Laser Scanning (TLS)

TLS is an advanced surveying technique that utilizes electromagnetic radiation to acquire information of the surrounding physical environment (Abellan et al., 2014). Electromagnetic radiation is emitted from an energy source as a low-divergence *light amplified by stimulated emission of radiation*, ubiquitously referred to as a *laser* (Heritage and Large, 2009). Another commonly used name for laser scanning is *LiDAR*, an acronym for *light distance and ranging*. Terrestrial means that the laser scanning is ground-based, and most-often comprises of a laser scanner set up on a tripod. Laser light is emitted in a single direction with a well-defined wavelength and amplitude. When a laser strikes a surface, light is either transmitted through, absorbed by, or reflected off the surface. The reflected light can be directed away from the surface at an angle equal to the incidence angle (i.e. specular reflection) or scattered in all directions (i.e. diffuse reflection). Most natural surfaces exhibit a combination of both types of reflection; more specular deflection for smooth surfaces and more diffuse reflection for rough surfaces. The distance of objects from the scanner can be measured based on the time it takes for the laser to return to the source (Heritage and Large, 2009). Most modern laser scanners emit infrared lasers and can detect extremely small energy reflections from distant surfaces. For example, the FARO Focus^{3D} X 330 scanner can detect objects up to 330 m away (FARO Technologies Inc., 2015). Laser scanning technologies have revolutionized the modelling and characterization of surfaces at resolutions and scales that were previously unattainable.

Classification of terrestrial laser scanners can be split in two broad classifications based on the technique used to measure the reflected laser: pulse ranging (or time-of-flight) measurement or phase change measurement. The time-of-flight method allows much longer distances to be measured

but at a reduced rate and lower accuracy than the phase change method (Petrie and Toth, 2009). The limited range of phase change scanners restricts its use for many applications. Time-of-flight scanners still provide relatively good accuracy with greater range and are therefore used more in TLS applications for earth surface monitoring (Abellan et al., 2014). Whichever classification a laser scanner belongs, it consists of four main components: laser emitting unit, reflector mechanism, receiver unit, and data encoder. The laser emitter, reflector, and receiver allow for the scan distance data to be measured, and the encoder records the positional data measured. Most modern scanners will also include other components such as a GNSS sensor for supplemental position information. Cameras are another commonly integrated component of scanners, which allow for full-colour photorealistic 3D scans when the images are processed with the scan data.

2.3.1 TLS Survey Design and Accuracy

The main parameters that differentiate TLS systems and affect the quality of scan datasets are range accuracy, resolution, maximum range, and survey design (Abellan et al., 2014). Range accuracy refers to the closeness of a range measurement to the actual distance. It typically spans from mm to cm values and depends on the object's distance from the scanner—a longer distance typically corresponds with slightly lower accuracy. Properties of the objects and terrain being scanned also influence the accuracy of TLS measurements; specifically, the reflectivity and roughness of the scanned surface. Rough surfaces scatter the laser and low-reflectivity surfaces reduce the intensity of the reflected beam, both reducing the ability of the scanner to accurately measure the object's distance.

Spatial resolution determines the level of detail that can be observed in the scan-reconstructed point cloud (Pesci et al., 2011). Resolution is a function of the point spacing and spot dimension (Abellan et al., 2011). Point spacing can be manually defined by the user. Spot dimension is a measure of the laser beam diameter and increased with distance due to beam divergence. The spot dimension may even be greater than the point spacing at long distances. The maximum resolution for most TLS

systems if not ideal for most earth surface observation applications because it results in unnecessary data redundancy (Lichti & Jamtsho, 2006). High resolution scans also produce massive datasets that require more computer processing power and time. The maximum range of a laser scanner is controlled by the instrument type (e.g. pulse ranging or phase change), laser wavelength, survey conditions, and reflectivity of the scanned surface. Advances in TLS technologies have been steadily improving the range, resolution, and accuracy of scanners.

Survey design is a critical stage of the TLS workflow, where the TLS practitioner can have the largest influence. Thorough planning of TLS surveys prior to site visits is strongly recommended to optimize scan data quality (Lim et al., 2009). Any errors that are incurred while acquiring scan data will propagate through the data processing, compounding to have an exaggerated affect on the final analysis application. Several factors must be considered while designing a TLS survey such as distances and incidence angles to surfaces and targets, number and locations of scans, scan resolution and overlap, and number and locations of targets for registration and georeferencing. These considerations should be made with the final application (e.g. deformation measurement) in mind to ensure an appropriate point density and overall point cloud accuracy. Since accuracy decreases with increasing range and incidence angle, these parameters should be reduced to an appropriate level while maintaining sufficient coverage and overlap. Abellan et al. (2014) recommends a minimum overlap of 30% between scans. Decreasing the scanner-to-surface incidence angle is also helpful for reducing the occurrence and size of occlusions. Weather and lighting conditions can also affect scan data quality. Rain, fog, and dust all negatively impact scan data and TLS surveys should be planned around these conditions if possible. Atmospheric transmission of laser light is best under clear, cool, dry conditions and may be severely affected by elevated water vapour levels (Heritage and Large, 2009).

Accuracy of TLS datasets is not only influenced by measurement errors in the raw scan data; registration errors also contribute significantly (Abellan et al., 2014). Registration uncertainty is one

of the main sources of uncertainty in TLS point cloud comparison for change detection (Lague et al., 2013). Georeferencing a TLS point cloud to a reference coordinate system is typically performed during registration. Accurate georeferencing is essential for reducing uncertainty of deformation measurements between TLS point clouds. There are two main approaches to georeferencing in TLS: direct and indirect. Direct georeferencing uses the known coordinates of the scanner to transform every point in the scan, and indirect georeferencing uses GNSS measurements of targets visible in the scan. Indirect georeferencing has been proven to be more accurate; however, it requires more time in the field to set up the target network and measure coordinates (Mukupa et al., 2017). Natural or artificial targets can be used as GCPs, but artificial targets are more commonly used because they can be set up in optimal locations and have a precise point for GNSS measurements and marking in the scan point cloud. During field work, operators must ensure high-quality scan data collection of GCPs by minimizing the scanner-to-target distance and incidence angle to a reasonable operational level. Increasing the number of targets is also a solution to improve the reliability of georeferencing (Mukupa et al., 2017). Similarly to UAV photogrammetry, accuracy and precision are measured by evaluating the location of scan data points to their known coordinates and by quantifying point-to-point noise of a planar surface, respectively (Lato et al., 2015).

2.3.2 TLS Strengths and Limitations

TLS has revolutionized the earth surveying and monitoring fields due to the technology's accuracy, resolution, and convenience. The combination of millimetre level accuracy and high spatial resolution has allowed for detailed monitoring and a rapid increase in understanding natural systems and structures. Traditional high-accuracy surveying techniques such as tachometric surveying or GPS acquire data at an extremely low density and much longer times compared to TLS (Abellan et al., 2014). TLS allows for the collection of mass point cloud data from a remote perspective in a relatively short period of time (Miller et al., 2008). TLS instruments are also fast and simple to set up. Static

instrument locations provide potentially more accurate measurements compared to dynamic instruments like airborne laser scanning (Abellan et al., 2014).

TLS has a few limitations that must be considered. One operational limitation is the issue of viewing angles and occlusions. Because the accuracy and resolution of TLS measurements decrease with increasing scanner-to-surface incidence angles, TLS is not suited for flat terrains or mapping applications. TLS is better suited for monitoring vertical surfaces like cliffs or structures (e.g. buildings, walls). Multiple scans from different locations are often required to eliminate occlusions in the scan dataset. Another technological limitation of a TLS system is that the GNSS sensors within are typically not accurate enough to render indirect georeferencing applicable. This means that most TLS systems rely on GCPs for georeferencing and require additional equipment such as an RTK system or total station to measure GCP positions. This limitation will likely be overcome as the accuracy of GNSS sensors increases. A high-level issue of TLS is the willingness of operators to accept TLS data as accurate without proper scrutiny. The visually impressive and apparently complete appearance of TLS data often leads to unwarranted acceptance of data and distracts operators from errors due to automated collection and processing. This tendency to overlook errors is a major issue, and assessment of data quality should be performed throughout the TLS workflow; after scanning, processing, and registration. The problem of data quality is especially critical when a single (or small amount of) viewpoint(s) is employed, as is often the case with TLS (Abellan et al., 2014).

2.4 Deformation Detection

Compared to the sensing instruments available for reconstructing 3D point clouds, solutions for comparing point clouds are scarce (Lague et al., 2013). The four most common methods are: 1) digital surface model of difference, 2) cloud-to-cloud, 3) cloud-to-mesh, and 4) multiscale model-to-model cloud comparison. The purpose, operating algorithms, applications, and limitations of these four

methods is discussed. Sources of uncertainty in point cloud comparisons and methods to account for uncertainty are described below as well.

A digital surface model (DSM) is the result of gridding a point cloud to produce a raster surface dataset. A DSM includes 3D data in a 2.5D format—the Z (vertical) coordinate is a value attributed to the XY location in the grid. The Z value is determined by interpolation of the local data points. DSM is also referred to as a digital elevation model (DEM) or digital surface model (DTM). A DSM of difference (DoD) is the comparison of DSMs by differentiating elevations on a pixel-by-pixel basis. The result is a grid of vertical differences representing deformation. DoD is the most common method of point cloud comparison in earth sciences for planar scene geometries (Lague et al., 2013). The accuracy of DoD comparisons depends on the quality of the DSMs, which are affected by several factors. Topographic data is reduced when point cloud data is converted from 3D to a 2.5D DSM (Mukupa et al., 2017). The quality of a DSM is an unknown function of the raw point cloud quality, sampling strategy, surface composition, topographic complexity, and interpolation methods (Wheaton et al., 2010). Data interpolation between points decreases accuracy for rough surfaces, limiting the resolution of small-scale details and the ability to detect deformations (Lague et al., 2013; Eltner et al., 2016; Mukupa et al., 2017).

The most common approach to quantifying uncertainty in DoD comparisons is to specify a minimum level of detection (LoD). The LoD defines the minimum statistically significant change that can be detected. Deformations less than the LoD are considered error or noise and those greater than are considered actual change. LoD values are typically calculated for a 95% confidence interval, or put another way, set to 2x the standard deviation for a normal distribution (James et al., 2017; Meeks et al., 2017). Standard error assessments of GCPs, such as RMS error, can be used to estimate the LoD. Most estimates of DoD uncertainties are relatively simplistic and assume uncertainties are spatially uniform. In areas with lower errors (e.g. flat surfaces with strong feature identification), the single LoD may be larger than the LoD for that specific area and real deformations may be unnecessarily

discarded. Alternatively, in areas with higher errors (e.g. steep slopes), the single LoD may not be high enough to account for the errors in that area, and errors may be misinterpreted as deformation (Wheaton et al., 2010). Another important limitation of DoDs is that they only provide 1D elevation differences. This is problematic for 3D models where surficial deformations are unrestricted to the vertical direction (Mukupa et al., 2017). In these situations, DoD deformation results can overestimate the actual change, particularly in steep terrain where small lateral offsets can produce large vertical differences (Abellan et al., 2014; Cook, 2017).

Cloud-to-cloud (C2C) comparisons are performed directly on the point clouds and do not require interpolating or gridding. The technique was developed for rapid change detection on very dense clouds rather than accurate distance measurement (Girardeau-Montaut et al., 2005). It is the fastest method for 3D point cloud comparisons because it does not require meshing, gridding, or calculation of surface normals (Lague et al., 2013). Its simplest version measures the distance between a point in the compared cloud to the closest point in the reference cloud. Improvements in C2C distance accuracy can be made by performing a least squares fit of the closest point neighbours in the reference cloud (Girardeau-Montaut et al., 2005). C2C measurements are highly sensitive to point cloud roughness, outliers, and differing point densities (Lague et al., 2013). This can cause deformations to be over or underestimated. C2C algorithms also do not return signed displacements (i.e. positive or negative), so the measurements are absolute values (Mukupa et al., 2017).

Cloud-to-mesh (C2M) comparisons involve creating a detailed 3D meshed surface of the reference point cloud and calculating the cloud-to-mesh distance along the mesh surface normal (Monserrat & Crosetto, 2008). This method generally provides accurate distance measurements, but issues arise in areas where the two point clouds do not overlap or where the point cloud contains very few points (Lague et al., 2013). All non-overlapping areas must be manually removed in order to obtain accurate distance measurements, which is time-consuming and introduces a source of human error to the measurements (Stumpf et al., 2015). Issues of interpolation that affect DSM generation are present

with C2M as well. Although meshed surfaces are truly 3D and more complex than DSMs, mesh construction smooths out small-scale details that may be important for assessing local roughness (Lague et al., 2013). Interpolation introduces an additional source of error to the point cloud and interpolation artifacts may bias deformation measurements (Stumpf et al., 2015).

A newer and more advanced method for measuring distances between clouds is multiscale model-to-model cloud comparison (M3C2; Lague et al., 2013). The method was developed for TLS point clouds that capture detailed surface roughness. It is based on three key characteristics: 1) operates directly on point clouds without meshing or gridding; 2) computes the local distance along the normal surface direction; and 3) estimates a level of detection (LoD) for each distance measurement based on local point cloud roughness and registration error. A full explanation of M3C2 is available in Lague et al. (2013). Barnhart & Crosby (2013) reported that M3C2 provides a better accounting of uncertainty than C2M because it considers surface roughness and registration errors. Stumpf et al. (2015) and Gómez-Gutiérrez et al. (2014) both found lower error measurements with M3C2 compared to C2C and C2M. Comparisons of M3C2 to C2C and C2M also demonstrated that M3C2 was superior in measuring small-scale deformations over time (Lague et al., 2013; Barnhart & Crosby, 2013).

A few other techniques exist for monitoring deformation that are not exactly point cloud comparisons. One of those is feature tracking, which is simply identifying key features in the point cloud and tracking their displacement over time. Lato et al. (2017) used this technique on a TLS dataset to monitor a landslide in British Columbia. Although feature tracking has smaller errors than C2C for example (Abellan et al., 2014), identifying reliable features to track can be challenging. This is especially relevant on projects such as ITH where embankment fill material is visually uniform. Another technique to quantify deformation is estimating the volume change between two point clouds. Accomplishing this requires both point clouds to be interpolated to meshed surfaces. Volume change between the surfaces is then calculated by gridding the compared dataset into domains,

measuring the difference vector between the compared surface and the reference surface, and integrating each domain across the entire failure surface (Lato et al., 2015). Volume change estimates are typically done on large-scale projects such as landslides (Lato et al., 2015; Hsieh et al., 2016), and may not be the more appropriate measure for small-scale embankment deformation. One last technique is to compare cross-sections (i.e. profiles, slices) of the point cloud. It is a common method to analyze terrain evolution and is particularly useful for linear structures such as embankments. Cross-sections can be taken at distinct locations to focus on a particular feature or on sets or parallel equally spaced tangents to analyze the spatial development of deformation (Hsieh et al., 2016).

2.5 Summary of Literature Review

Embankments built on permafrost during winter are susceptible to deformations in the summer immediately following construction as ice within the embankment melts and in subsequent years as permafrost at the embankment toe thaws. As the climate changes and temperatures in the Arctic rise, permafrost will continue to thaw and infrastructure will suffer deformations and instabilities. New imaging technologies such as UAV photogrammetry and TLS are needed to more accurately monitor linear infrastructure in the Arctic. It will help in understanding deformation behaviour and in assessing stability for safety reasons.

UAV photogrammetry uses a series of feature-matching and positioning algorithms called SfM to process aerial imagery captured by UAVs and produce point clouds of the scene. GCPs with positions measured by survey equipment, most often an RTK system, are used to georeference the image-reconstructed point clouds to a coordinate system. The quality of the image set and GCPs strongly impacts the accuracy of the point clouds.

TLS uses a laser scanner mounted on a tripod to measure distances of objects in the surrounding environment and reconstruct a 3D point cloud of the scene. Multiple scans from various scanner locations are registered together using targets such as spheres and checkerboards. TLS point clouds

are also georeferenced using target positions. Scanner parameters and survey design are both critical for producing high-quality TLS point clouds. TLS can generally produce more accurate point clouds and measure finer deformations than UAV image-reconstructed point clouds.

There are several methods that can be used to compare point clouds and determine deformations, each with its own set of drawbacks and limitations. M3C2 is a newer point cloud comparison method that addresses much of the limitations of past methods and can provide more accurate deformation measurements with spatially variable LoD estimates.

CHAPTER 3: TECHNOLOGY OPERATING PROCEDURES AND CALIBRATION TESTS

This section outlines the operating procedures and calibration tests for each technology. The calibration tests were performed on each technology to assess their accuracies and expected errors, determine optimal survey parameters, and design the on-site surveys that would be suitable for the conditions along ITH.

3.1 UAV Photogrammetry

3.1.1 UAV Operation Certifications

Transport Canada is the federal organization responsible for ensuring UAVs in Canada are flown legally and safely. UAV pilots must follow the rules in the Canadian Aviation Regulations (CARs) Part IX—Remotely Piloted Aircraft Systems (RPAS). RPAS, UAV, and drone are used synonymously. To legally fly a UAV in Canada before June 1, 2019, the pilot needed to complete a licensed UAV Ground School training program. The author completed their UAV Ground School training in June 2017 with M3 Aerial Productions. The training involved an online learning and testing program, as well as an in-class portion. The Ground School covered a wide range of topics including UAV operation, safety, rules and regulations, flight planning in Canadian airspace with NAV CANADA, meteorology, insurance and liability, and UAV mission planning. Under the old regulations (i.e. before June 1, 2019), a person needed to be granted a Special Flight Operations Certificate (SFOC) in order to fly a UAV. The only time an SFOC was not required was if the UAV flight met the 'exemptions' criteria. These criteria however were limiting, and most UAV operations did not meet the strict criteria. For the research team's situation on ITH, the UAV operation did not meet exemptions and an SFOC was required to legally fly the UAV along the highway.

The SFOC application was lengthy and comprehensive. It required details on the personnel involved in the operation (e.g. pilot in command, visual observer) and their respective certifications,

information on the UAVs to be used during operations, liability insurance certificates, and highly detailed explanations of the UAV operation including a site survey, pre-flight and post-flight checklists, security plan, and emergency plan. In 2017, Earl De Guzman was the pilot-in-command and the author was the visual observer. In 2018, Earl De Guzman was the pilot-in-command and Samuel Kaluzny was the visual observer. The SFOC applications submitted in 2017 and 2018 were both granted.

UAVs exploded in popularity in recent years and Transport Canada was overwhelmed with the processing of SFOC applications. This prompted them to release new rules and regulations related to UAV operations, which came into affect on June 1, 2019. Transport Canada took a more relaxed and streamlined approach with the new regulations, eliminating the need for UAV operators to obtain SFOCs. Under the new regulations, UAV operations are categorized into Basic or Advanced operations. Basic operations are those that: 1) fly in uncontrolled airspace; 2) fly more than 30 m horizontally from bystanders; and 3) never fly over bystanders. UAV operations on ITH fall under the Basic operations category. In order to conduct Basic or Advanced RPAS operations, a person must pass an online test provided by Transport Canada. The author completed the Basic operations online test and was awarded their Small RPAS Pilot certificate on May 28, 2019. The certificate allowed the author to conduct UAV flights in Canada as long as the three Basic operations criteria (listed above) were met. Additionally, the UAVs were required to be registered with Transport Canada and remain in visual line-of-sight (VLOS) with the UAV during all operations.

3.1.2 UAV Models and Specifications, Operating Procedures, and Image Processing

Two quadcopter UAVs were used in this research to acquire aerial imagery of the high-fill sections along ITH: a senseFly albris and a DJI Phantom 4 Pro. The albris (Figure 3.1) is a top-of-the-line inspection UAV. Its 38 Mp main camera is one of the best in its class and allows it to capture high-quality imagery, which improves feature matching during SfM processing. The albris also has an advanced set of sensors that allows it to navigate and stabilize while in its different flight modes.

These sensors include inertial measurement units (IMUs) to measure acceleration and orientation, a GNSS receiver to determine its global position, barometers to measure its altitude, ultrasonic sensors to measure distances to surrounding objects, and navigational cameras (navcams) to help determine its speed relative to surfaces (senseFly, 2016). The albris is capable of flying in three flight modes: 1) autonomously on user-designed missions following a specified flight path and capturing images at specified locations; 2) interactive where the pilot controls movements and sensors are used to automatically stabilize and compensate for wind; or 3) manually where the pilot controls movements and it does not stabilize itself or compensate for wind. Sophisticated UAV systems like the albris that can fly autonomously on missions allow for more efficient and consistent flights that provide more reliable results in the form of higher-quality reconstructed point clouds. For its ground control station (GCS), the albris uses a laptop with eMotion 3 (senseFly, 2019). eMotion 3 allows the pilot to control and monitor the albris during flight, as well as design missions for the albris to complete autonomously. The albris uses a set of antennas that is plugged into the GCS laptop as a communication link between the UAV and GCS. Table 3.1 outlines some technical specifications of the albris and its sensors.

Figure 3.1 senseFly albris UAV.

The Phantom 4 Pro (Figure 3.2) is a high-end consumer level UAV. The Phantom is a smart-flying photography UAV with a sensor to capture 20 Mp images. It has vision and infrared obstacle sensors that make it able to avoid obstacles during flight, as well as a barometer, IMU, and GNSS receiver for positioning and navigation. The Phantom has three flight modes: positioning, sport, and attitude. In positioning mode, the UAV utilizes GNSS and the vision and infrared sensors to stabilize, compensate for wind, and avoid objects during flight. In sport mode, obstacle sensing systems are disabled and the UAV's maximum flight speed and handling are increased to enhance maneuverability. Sport mode is not intended to be used to photogrammetry applications. In attitude mode, the UAV does not use its GNSS or sensor systems and only uses its barometer for altitude control. The Phantom does not have an autonomous flight mode to follow user-designed missions; therefore, it was flown manually to acquire imagery during site visits. For its GCS, the Phantom uses DJI GO 4 (an app) on a tablet-like monitor connected to a handheld remote controller. The controller also has integrated antennas for a communication link between the GCS and UAV. Table 3.1 outlines some technical specifications of the Phantom 4 Pro and its sensors.

Figure 3.2 DJI Phantom 4 Pro UAV (DJI, 2018).

Table 3.1 UAV specifications.

Parameter	senseFly albris	DJI Phantom 4 Pro
Camera resolution	38 Mp	20 Mp
Camera field of view	60°	84°
Weight (with battery and propellers)	1.77 kg	1.388 kg
Battery	8500 mAh	5870 mAh
Max flight time (approximate)	22 minutes	30 minutes
Max airspeed (manual flight)	43 km/h	72 km/h
Max airspeed (autonomous flight)	29 km/h	N/A
Max wind speed (manual flight)	10 m/s	10 m/s
Max wind speed (autonomous flight)	8 m/s	N/A
Operating temperature	-10 to 40 °C	0 to 40 °C

Pix4Dmapper (Pix4D, 2019) was the software used in this research to process UAV imagery. Pix4D processes imagery by executing a series of SfM and MVS feature matching algorithms to generate 3D point clouds of the scene captured by the images. The general workflow in Pix4D was as follows. First, initial processing of the imported imagery is performed, which included identification of keypoints, keypoint matching between images, and orientation of the keypoints to create a sparse point cloud. Pix4D uses the SIFT algorithm (Lowe, 1999; Lowe, 2004) to identify features, followed by the approximate nearest neighbour and Random Sample Consensus (RANSAC) algorithms to create tracks that link specific keypoints in multiple images and remove transient features (e.g. moving objects) from the dataset. During initial processing, images can be down-sampled (i.e. reduced in size) to increase processing speed. Down-sampling results in fewer keypoints (Harwin & Lucieer, 2012) and was therefore avoided throughout this research. Pix4D performs iterative automatic aerial

triangulations (AAT), bundle block adjustments (BBA), and calibrations of the camera parameters until an optimal reconstruction geometry is achieved.

Once the spare point cloud is generated, GCP coordinate data is imported to Pix4D and GCPs are marked in the images. Marking GCPs in the images themselves reduces errors and improves overall accuracy compared to marking GCPs in the point cloud (Eltner et al., 2016). The sparse point cloud is then reprocessed to include the marked GCP positions in the BA. Including GCPs in the BA is referred to as a 1-stage BA and has been shown to reduce systematic doming errors compared to a 2-stage BA where the GCP georeferencing only shifts the point cloud and does not affect the point cloud's structure (Eltner et al., 2016).

After georeferencing with the GCPs, the next step is densification of the point cloud. Pix4D utilizes iterations of the clustering view for multi-view stereo (CMVS) and patch-based multi-view stereo (PMVS2) algorithms to organize the point cloud into manageable clusters of data and then generate additional points using the data within the clusters. The dense point cloud is the product of the SfM-MVS process. Pix4D has a point cloud editor that allows the user to manually remove points that are unwanted or erroneous such as remnants of a moving object. The final point cloud can then be exported to other software for deformation measurements or other analysis techniques. Pix4D can further process the dense point cloud to generate products such as a meshed surface composed of triangles or a digital surface model (DSM). Meshed surfaces and DSMs can be valuable for deformation detection, depending on the application. For the purposes of this research, all deformation measurements were performed using the dense point clouds and the meshed surfaces and DSMs were not generated.

Pix4D has several parameters that can be modified during each stage of processing. It was important early on to establish standard processing parameters that would be applied consistently to image sets throughout the research. The processing parameters would be selected to optimize the quality of the reconstruction with respect to density of the point cloud. The Pix4D manual (Pix4D,

2019) provided guidance and recommendations on certain parameters according to the type of imagery and application. For the remaining parameters, a parametric analysis was performed on the 2017 albris images from KM-82. The images were processed using the different settings and parameters available in Pix4D. The processing time and density of the resulting point clouds were compared to determine which settings and parameters produced a point cloud with the highest density in minimal time. Point cloud density was considered more important than processing time; however, if two settings produced equivalent densities, the setting that resulted in lower processing times was selected. Table 3.2 outlines the standard Pix4D processing parameters that were used throughout this research. There were two processing parameters options: image sets with only nadir images or image sets with nadir and oblique images.

Table 3.2 Pix4D standard processing parameters.

STEP 1: INITIAL PROCESSING		
General	Keypoints Image Scale	Full
	Quality Report	☐ Generate Orthomosaic Preview in Quality Report
Matching	Matching Image Pairs	Aerial Grid Flight: Aerial Grid or Corridor Oblique Flight: Free Flight or Terrestrial
	Matching Strategy	☑ Use Geometrically Verified Matching
Calibration	Targeted Number of Keypoints	Automatic
	Calibration Method	Standard
	Internal Parameters Optimization	All
	External Parameters Optimization	All
	Rematch	Custom — ☑ Rematch
	Export	☑ Camera Internal and Externals, AAT, BBA ☐ Undistorted Images
STEP 2: POINT COUD AND MESH		
Point Cloud	Image Scale	1 (Original image size) ☑ Multiscale
	Point Density	Optimal
	Minimum Number of Matches	3
	Point Cloud Classification	☐ Classify Point Cloud
	Export	None. Can be manually exported later.
3D Textured Mesh	Generation	☑ Generate 3D Textured Mesh
	Settings	High Resolution ☐ Use Color Balancing for Texture
	Export	None. Can be manually exported later.
Advanced	Matching Window Size	9x9
	Image Groups	☑ All
	Point Cloud Filters	☑ Use Processing Area ☑ Use Annotations ☑ Limit Camera Depth Automatically
	Sample Density Divider	1

3.1.3 UAV Calibration I—Target Displacement

On July 23, 2018 at Dave's Aggregates gravel pit east of Winnipeg (49.77634° N, -96.600864° E), a calibration test was performed using the albris UAV and the RTK system to determine their ability to measure displacement of checkerboard targets (Figure 3.3). Checkerboard targets were prepared by cutting hardwood sheaths into 60 cm x 60 cm pieces and spray painting them black and bright pink or orange. No RTK base station was set up because the RTK rover could connect to the Lewis base station network. The survey was set up on and around a sand dune with a total of 14 checkerboard targets (Figure 3.4). The material and geometry of the sand dune is similar to the embankment fill material and geometry of the high-fill sections along ITH, allowing for comparable feature matching and georeferencing between the calibration test and site conditions.

Figure 3.3 Checkerboard target.

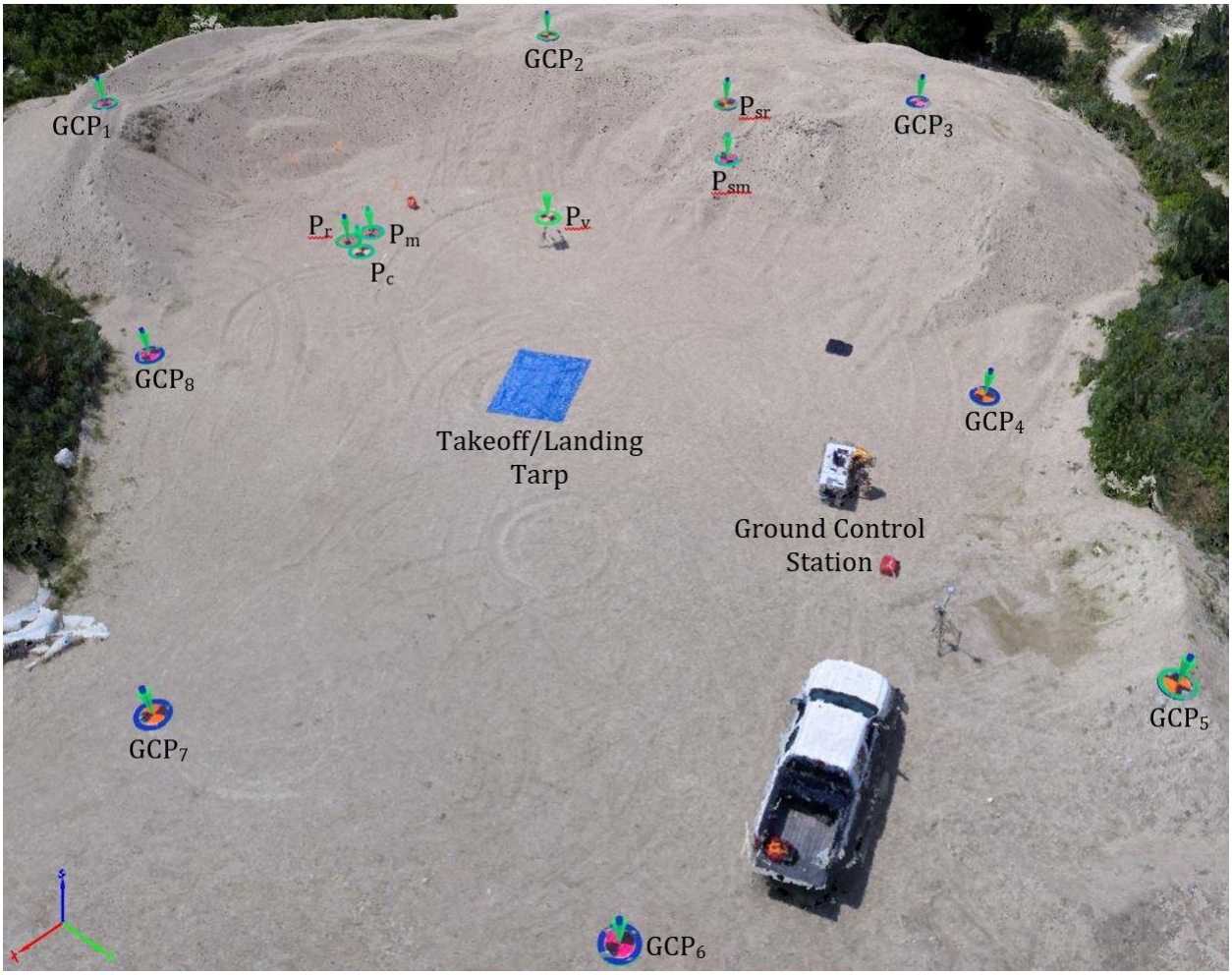

Figure 3.4 UAV Calibration I—reconstructed point cloud with marked targets and GCPs.

Two UAV surveys were conducted for the calibration test. Ten of the checkerboard targets were not moved between surveys and were used as GCPs for georeferencing; the other four checkerboards were used to measure displacements. Two checkerboard targets assessed horizontal displacement accuracy, one assessed vertical displacement accuracy, and one assessed the displacement accuracy of a target moved down the sand dune slope. The horizontal displacement targets (P_{hc} and P_{hm}) were laid on the ground and their positions were measured by two methods—the RTK system and a tape measure distance to a reference GCP. The vertical displacement target (P_v) was set up on a tripod. Its position was not measured using the RTK system because the top of the tripod was inaccessible with the RTK. The displacement of P_v was therefore only measured by hand with a tape measure. It is

understood that hand measurements with the tape measure have minor errors associated with them; however, care was taken to measure distances correctly to the millimeter and the hand measurements were taken as truth for the horizontal and vertical displacements in this calibration test. The slope displacement target (P_{sm}) position was only measured using the RTK system due to difficulties accurately measuring the target's distance from a reference GCP with a tape measure.

UAV flights for the calibration test were designed using eMotion 3 (senseFly, 2019) and the flight parameters were the same as those used on-site. This allowed the determined accuracies in the calibration test to be representative of expected displacement accuracies on-site. Both UAV surveys included two flight schemes: a grid scheme and a point-of-interest (POI) scheme (Figure 3.5). Each grid scheme captured 46 nadir images that had a GSD of 1 cm and an overlap of 75% in both directions. The POI schemes captured 12 images at 30° radial spacing and a 60° viewing angle to the ground surface.

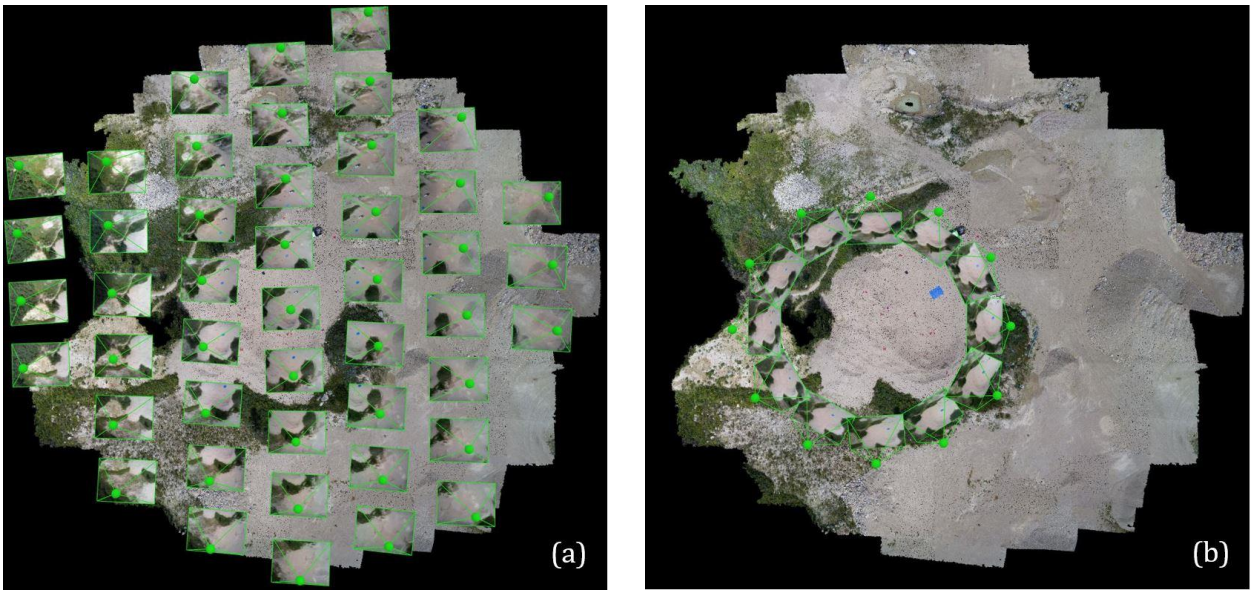

Figure 3.5 UAV Calibration I—representation of UAV images acquired with green spheres identifying images' calibrated positions: a) grid images; b) POI images.

The displacement measurements and associated errors for this calibration test are provided in Table 3.3. Accuracy of the RTK system was quantified by comparing the computed distances between target RTK points and the hand-measured distances for the targets moved horizontally (P_{hc} and P_{hm}). The RMS error between the RTK and hand-measured distances was 4.5 mm. This result demonstrates the RTK system can measure checkerboard target positions to a reasonably acceptable accuracy.

Accuracy of the UAV photogrammetry processing was quantified by two methods. The first method compared distances between targets in the Pix4D point cloud to the hand-measured and RTK distances. Comparing the hand-measured and Pix4D distances, the RMS errors for P_c, P_m, and P_v were 6.2 mm horizontally and 3.0 mm vertically. The vertical errors should theoretically be larger because RTK and UAV photogrammetry both typically have larger errors in the vertical direction; however, the 3.0 mm vertical RMS error was only based on one measurement. It is expected that if more vertical target distances were measured, the vertical RMS error would be larger than the horizontal. Comparing the RTK and Pix4D distances for P_c, P_m, and P_{sm} determined the RMS errors were 9.4 mm horizontally and 17.2 mm along the slope. These were larger than the Hand vs. RTK and Hand vs. Pix4D errors because these errors accounted for errors in the RTK measurements and SfM processing. However, the RTK vs. Pix4D distance errors only ranged between 0.3% and 1.1% of the distance measurement.

The second method to quantify the UAV photogrammetry accuracy assigned certain targets as checkpoints (P_c, P_m, and P_{sm}) and compared the targets' measured RTK positions to their positions computed by SfM processing in Pix4D. This analysis determined checkpoint RMS error values to be 26.5 mm and 19.9 mm for the first and second UAV surveys, respectively.

Table 3.3 UAV Calibration I—target displacement distances and error measurements.

Technology comparison	Direction	Reference target	Compared target	Hand dist. (mm)	RTK dist. (mm)	Pix4D dist. (mm)	Error (mm)	Error RMS (mm)
Hand vs. RTK	Horizontal	P_r	P_c	1000	998		-2	
		P_r	P_{m1}	1000	994		-6	4.5
		P_r	P_{m2}	2000	2005		+5	
Hand vs. Pix4D	Horizontal	P_r	P_c	1000		1008	+8	
		P_r	P_{m1}	1000		996	-4	6.2
		P_r	P_{m2}	2000		1993	-7	
	Vertical	P_{v1}	P_{v2}	300		303	+3	3.0
RTK vs. Pix4D	Horizontal	P_r	P_c		998	1008	+11	
		P_r	P_{m1}		994	996	+2	9.4
		P_r	P_{m2}		2005	1993	-12	
	Along Slope	P_{sr}	P_{sm1}		2690	2708	+18	17.2
		P_{sr}	P_{sm2}		5744	5761	+17	

This calibration test showed that fine displacements of artificial targets can be measured using UAV photogrammetry. One of the main reasons this test was able to detect such fine displacements is because the same GCPs were used for both UAV surveys. When the same GCPs are used, the point cloud is georeferenced based on the same coordinate inputs and the errors associated with those GCP position measurements are irrelevant. However, when different GCPs are used for two UAV surveys, the GCP position errors negatively impact georeferencing and cause differences between the two reconstructed point clouds. Therefore, uncertainties of deformation measurements increase when comparing point clouds reconstructed from UAV surveys that used different GCPs.

At the time of this calibration test and analysis, the displacement errors determined by UAV photogrammetry using the selected flight parameters seemed acceptable for measuring deformations of high-fill embankments because the errors were significantly smaller than the expected deformations of the high-fill sections. It was not until later, while researching the various methods of change detection, that a method was developed to use GCP positional errors in a reconstructed point cloud to estimate the accuracy of that point cloud and the reliability of deformation measurements between point clouds. This newfound understanding, which will be explained in the following section, prompted the development of an experiment with the UAV to study the effect of various image and ground control parameters on the accuracy of reconstructed point clouds.

3.1.4 UAV Calibration II—Image and Ground Control Parameters

The accuracy of UAV image-reconstructed point clouds can be estimated by determining errors at checkpoints. Positional errors at checkpoints can be measured by comparing control point coordinates in the reconstruction to their known reference coordinates. The errors at checkpoints can be analyzed and used as an estimate of the errors associated with other points in the point cloud. Using UAVs to monitor deformation will have a tolerance for the uncertainty of measurements; zero uncertainty is unachievable. The accuracy of deformation measurements between point clouds is directly proportional to the accuracy of the point clouds themselves (Lague et al., 2013), where lower accuracy point clouds results in less confident deformation estimates. The level of detection (LoD) is a common approach to quantifying uncertainty for deformation measurements between point clouds. LoD is the minimum statistically significant change that can be detected. A 95% confidence interval is most often used to define the LoD, where deformation measurements less than the LoD are considered error or noise (Lague et al., 2013; Wheaton et al., 2010). Deformation must be greater than the error at the 95% confidence interval boundary to be deemed as actual change. The LoD is highly dependent on the scale of images used to reconstruct the point cloud and can range from 1 cm

to 30 cm (Brasington et al., 2003; Cook, 2017; Eltner et al., 2015; Lane et al., 2003). The targeted LoD for a project will depend on the scale of the structure, the mechanism causing deformation, and the importance of the structure. Understanding the critical factors that influence accuracy of UAV image-reconstructed point clouds allows for more effective design of UAV surveys to obtain a targeted LoD.

This experiment investigated the impact that image blocks and ground control parameters have on the accuracy of UAV image-reconstructed point clouds by analyzing GCP positional errors in a set of point clouds. The four parameters that were investigated were: (1) GSD of the images, (2) number of GCPs, (3) RTK observation time at GCPs, and (4) oblique image incidence angle. Point cloud errors were used to quantify an LoD for each point cloud to show the impact the four parameters can have on deformation monitoring applications. The purpose of this experiment was to improve the image and data acquisition methods that would be implemented on-site.

3.1.4.1 Experiment Methods

UAV imagery and ground control data were acquired at Dave's Aggregates gravel pit on June 2, 2019. Only the albris was used for this experiment because of its flight planning capabilities. The survey area was approximately 80 m x 50 m with a sand surface and two large rock piles approximately 8 m high (Figure 3.6). This area was selected for the terrain relief of the rock piles and their geometric similarity to the high-fill sections along ITH. The RTK system was used to measure precise coordinates of checkerboard GCPs. No RTK base station was set up because the RTK rover could connect to the Lewis baste station network. Sixteen (16) GCPs were distributed throughout the survey area (Figure 3.6). The position of each GCP was measured thrice, each for a different length of observation time: 20 seconds, 1 minute, and 3 minutes.

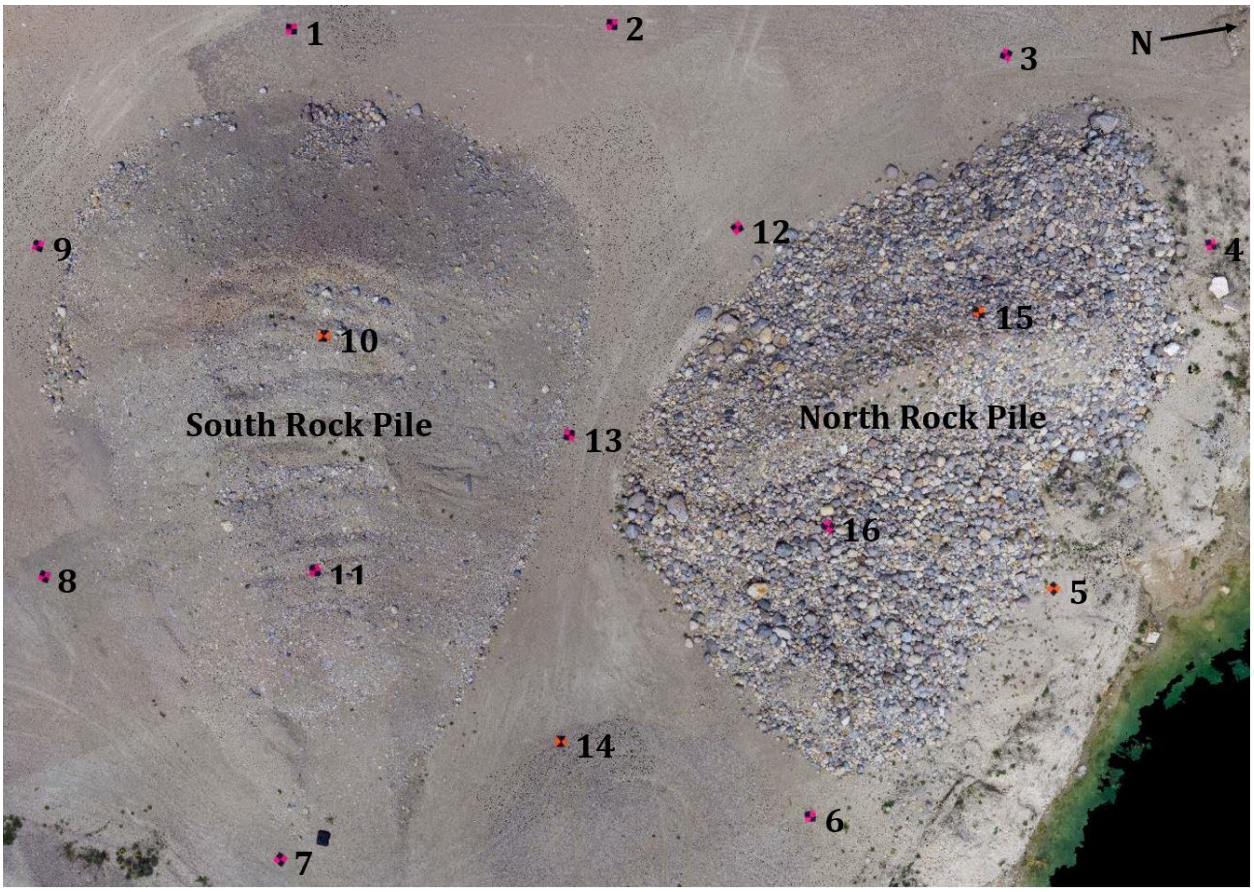

Figure 3.6 UAV Calibration II—plan view of the survey area with GCPs.

Several UAV flights were conducted to acquire images with various parameters for the chosen image blocks. The flights consisted of two image schemes: grid schemes and POI schemes. Grid schemes followed a horizontal grid flight path above the entire survey area and captured nadir images with 75% overlap (both longitudinal and lateral to the UAVs flight path). Three grid flights were conducted at varying GSDs: 10 mm, 8 mm, and 6 mm. These corresponded to UAV flight heights of 57 m, 46 m, and 35 m, respectively. POI schemes followed a circular flight path and collected oblique imagery oriented towards the centre of the survey area between the rock piles. POI schemes were effective because they captured the full survey area from a wide array of perspectives on a relatively short flight path. POI flights were conducted from three viewing angles: 45°, 60°, and 75°

to the ground surface. Each POI scheme included 12 images, equally spaced at 30° intervals surrounding the POI.

Ground control survey data was processed using Leica Infinity (Leica, 2019) to a format accepted by Pix4D. Each RTK measurement at a GCP included the 3D coordinates of the point, along with the horizontal, vertical, and 3D uncertainty of the measurement. These uncertainties were analyzed to quantify the direct effect of the RTK observation time.

Pix4D processing followed the standard workflow with the optimal parameters described in Section 3.1.2. GCP coordinate data was imported to Pix4D and each GCP was marked in the images. Jaud et al. (2016) estimated the accuracy of manually marking images to be 0.3 pixels. This would correspond to 3, 2.4, and 1.8 mm for images with GSDs of 10, 8, and 6 mm, respectively. Each GCP was marked in a minimum of 8 images to provide a reasonable estimate of the GCP centre, with additional markings on images where required. The point cloud was georeferenced by reprocessing the Pix4D project to include the marked GCP coordinates in the BA. checkpoint errors in the georeferenced sparse point clouds were used to quantify the accuracy of the point clouds.

In the SfM workflow, georeferencing optimizes the point cloud geometry by reducing the overall error between the computed GCP positions and their input coordinates. Errors at points between GCPs are most-often higher than errors at the GCPs. This experiment used checkpoints to measure errors and quantify the accuracy of the point clouds. A checkpoint provides an unbiased accuracy estimation of a point cloud.

The analysis was organized into ten processing groups that each had a unique combination of three parameters: 1) image GSD, 2) RTK observation time, and 3) viewing angle of oblique imagery (Table 3.4). The baseline group (i.e. Group 1) had a GSD of 10 mm, an RTK observation time of 20 seconds, and no oblique imagery. Groups 2–8 varied one of the three parameters and left the other two parameters as they were in Group 1. This allowed the effect of each individual parameter to be analyzed. Groups 9 and 10 varied multiple parameters to quantify their combined effect. Within each

processing group, the point cloud was reprocessed several times, each with a unique number and configuration of GCPs. The number of GCPs included in georeferencing varied from 4–14; GCPs not included in georeferencing were classified as checkpoints and used to measure errors. The numbers of GCPs investigated were 4, 6, 8, 10, 12, and 14.

Table 3.4 UAV Calibration II—processing group parameters.

Group	ID	GSD (mm)	RTK observation time (sec)	Oblique viewing angle (°)	No. of GCPs investigated
1	BASE	10	20	No oblique images.	4, 6, 8, 10, 12, 14
2	GSD8	8	20	No oblique images.	4, 6, 8, 10, 12, 14
3	GSD6	6	20	No oblique images.	4, 6, 8, 10, 12, 14
4	RTK1	10	60	No oblique images.	4, 6, 8, 10, 12, 14
5	RTK3	10	180	No oblique images.	4, 6, 8, 10, 12, 14
6	OBL45	10	20	45	4, 6, 8, 10, 12, 14
7	OBL60	10	20	60	4, 6, 8, 10, 12, 14
8	OBL75	10	20	75	4, 6, 8, 10, 12, 14
9	MID	8	60	45	4, 6, 8, 10, 12, 14
10	MAX	6	180	45	4, 6, 8, 10, 12, 14

Different configurations of GCPs were processed to determine error estimates at checkpoints. Within each processing group, each GCP was classified as a checkpoint six times, resulting in 96 data points to analyze for a certain number of GCPs. The number of configurations required to reach 96 checkpoints was highest when 14 GCPs were processed (48 configurations) because only 2 checkpoints were used each time. When 4 GCPs were processed, only 8 configurations were required to reach 96 checkpoints. For 6 GCPs, four of the GCPs were classified as checkpoints seven times instead of six. A summary of the GCP configurations is provided in Table 3.5. The GCP configurations

were designed to satisfy three criteria. Firstly, all GCPs were classified as checkpoints the same number of times to ensure the results were not weighted higher/lower to a GCP that was selected more/less. This criterion was satisfied for all numbers of GCPs except for 6 GCPs because the 96 GCP data points was not divisible by 6 (the number of checkpoints per configuration). Secondly, the configurations needed to cover as much of the survey area as possible. This was done because typical GCP networks are distributed widely across the study area (James & Robson, 2012) and a consistent GCP coverage area provided comparable results between different numbers of GCPs. Thirdly, repetitive use of checkpoint combinations was minimized to reduce the likelihood that certain repeated checkpoint combinations influenced the results. A random generator was not used to determine GCP configurations because it resulted in GCP grouping that did not cover the entire survey area. Figure 3.7 shows examples of configurations for 4, 6, 8, 10, 12, and 14 GCPs.

Table 3.5 UAV Calibration II—number and configurations of GCPs for each processing group.

No. of GCPs	No. times each GCP classified as checkpoint	Checkpoints per configuration	No. of checkpoint data points	No. of configurations
14	6	2	96	48
12	6	4	96	24
10	6	6	96	16
8	6	8	96	12
6	6.25	10	100	10
4	6	12	96	8

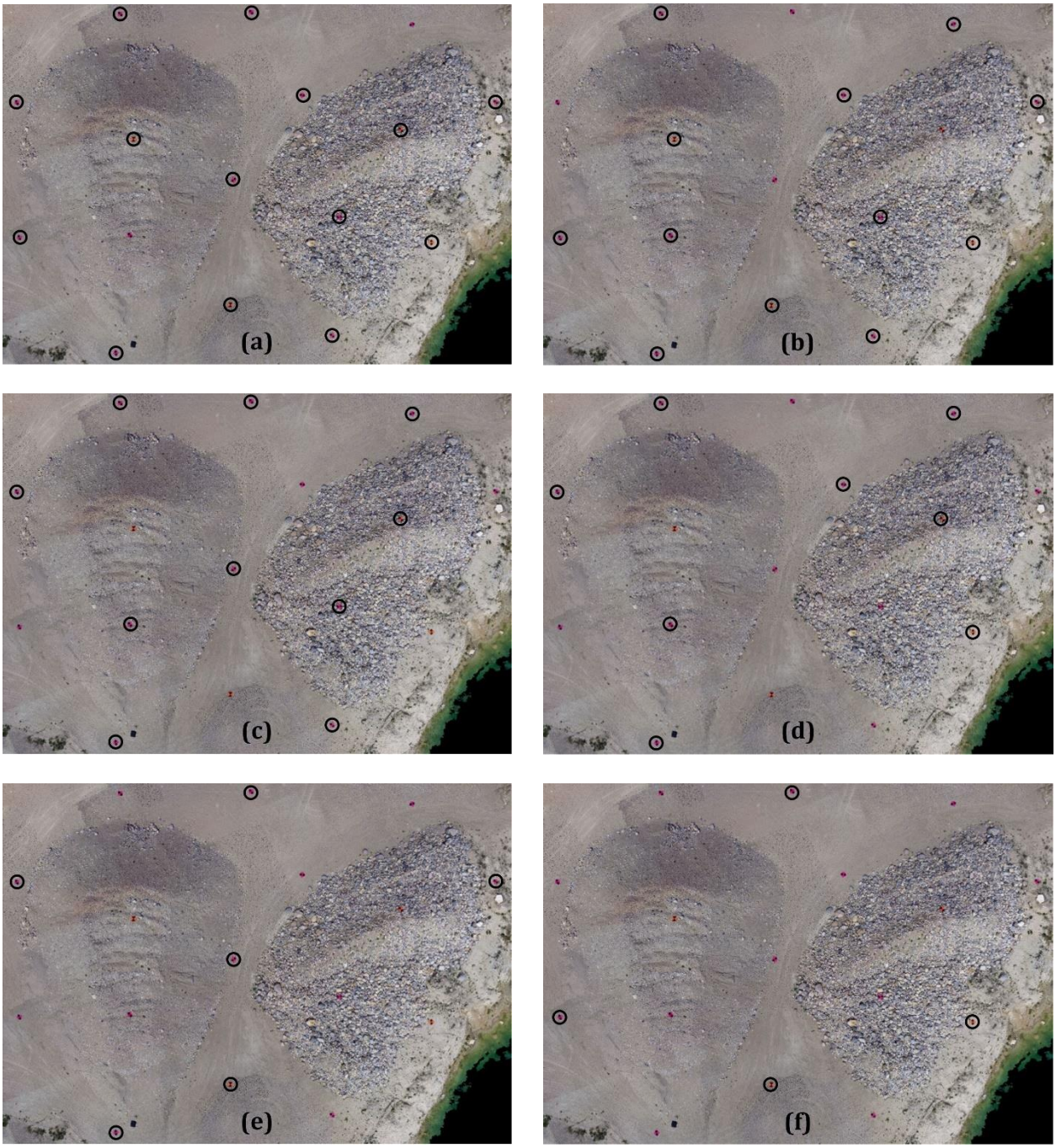

Figure 3.7 UAV Calibration II—example GCP configurations: a) 14 GCPs; b) 12 GCPs; c) 10 GCPs; d) 8 GCPs; e) 6 GCPs; f) 4 GCPs.

For every configuration in a processing group, a new Pix4D file was created based on the original file for that processing group. This ensured that every configuration had identical initial datasets and

eliminated the gradual reduction of GCP errors that can occur in files that are continuously reprocessed with different GCP networks (Pix4D, 2019). Once a file was reprocessed, errors in the X, Y, and Z directions for all checkpoints in the configuration were recorded. This procedure was repeated for all configurations and processing groups. The resulting dataset consisting of X, Y, and Z errors at checkpoints was analyzed to determine the accuracy of point clouds in the different processing groups and quantify the impact of the image block and ground control parameters.

The LoD for deformation measurements between two point clouds can be calculated as:

$$LoD_{95\%} = \pm 1.96 \times \sqrt{{RMSE_{3D(1)}}^2 + {RMSE_{3D(2)}}^2} \quad (3.1)$$

where $RMSE_{3D(1)}$ and $RMSE_{3D(2)}$ are the 3D RMS errors of the two clouds being compared and ±1.96 is the normal distribution Z value for the 95% confidence interval. This equation is a simplified estimate of LoD based on Wheaton et al. (2010) and Lague et al. (2013). In this study, all UAV flights were conducted on the same day; therefore, no point clouds were compared to determine deformation. LoD was calculated for each group assuming that a second point cloud with the same image block and ground control parameters would have identical errors as those determined in this study (i.e. $RMSE_{3D(1)} = RMSE_{3D(2)}$). Therefore, LoD in this study was calculated as:

$$\text{LoD} = 1.96 \times \sqrt{2 \times \left({RMSE_{3D}}^2\right)} \quad (3.2)$$

3.1.4.2 Experiment Results

The measured RTK survey uncertainties at GCPs showed that horizontal, vertical, and 3D uncertainties decreased as the RTK observation time increased (Table 3.6). The mean uncertainty consistently decreased as observation time increased; however, standard deviation only decreased at 180 seconds and there was no significant change from 20 to 60 seconds. For all three collection times, the mean and standard deviations for vertical uncertainty were higher than horizontal uncertainty, as is typical of RTK surveys (Saghravani et al., 2009). The box plot of the RTK measurement uncertainty (Figure 3.8) illustrates the benefits of longer observation times. Significant

decreases in the mean and variance of RTK uncertainties can be obtained when observation time increases. These results can help plan RTK surveys when a specific uncertainty level is targeted.

Table 3.6 UAV Calibration II—RTK survey uncertainty statistical measures.

Parameter	Horizontal uncertainty			Vertical uncertainty			3D uncertainty		
Observation time (sec)	**20**	**60**	**180**	**20**	**60**	**180**	**20**	**60**	**180**
Maximum (mm)	15	16	10	21	17	12	26	23	16
Minimum (mm)	9	8	5	12	10	7	15	13	9
Mean (mm)	12.3	10.5	7.6	16	13.6	9.8	20.2	17.3	12.3
Standard deviation (mm)	1.9	2.3	1.4	2.5	2.4	1.5	3	3.3	1.9
Root mean squared (mm)	12.4	10.7	7.7	16.2	13.8	9.9	20.4	17.5	12.4

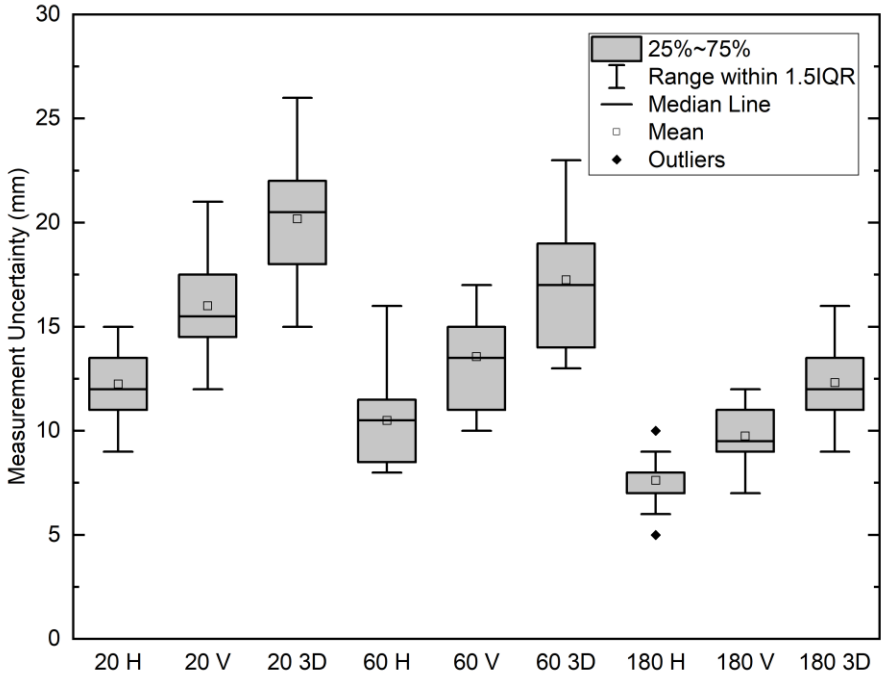

Figure 3.8 UAV Calibration II—box plot of the horizontal, vertical, and 3D RTK measurement uncertainties at GCPs for 20, 60, and 180 second RTK observation times.

Processed errors at checkpoints were analyzed for each processing group and number of GCPs. Results of the statistical analysis are presented primarily using RMS error because it accounts for the mean and variance of errors and is the most representative measurement of error point clouds (Pix4D, 2019). Figure 3.9 shows the RMS of the processed 3D errors for all processing groups and numbers of GCPs. Generally, RMS errors decreased with more GCPs. This result agrees with the literature (Harwin & Lucieer, 2012; James & Robson, 2012; Tonkin & Midgley, 2016). There was however inconsistent evidence that accuracy continued to improve past 12 GCPs; RMS error decreased in some groups and increased in others. For 12 and 14 GCPs, the distance from a checkpoint to the closest GCP is approximately equal in most configurations. Larger distances from GCPs to checkpoints cause larger errors (Tonkin and Midgley, 2016), but since the GCP to checkpoint distances for 12 and 14 GCPs are approximately equal, errors are primarily due to the different configurations and combinations of GCPs used in the georeferencing. Accuracy increased or decreased in each processing group depending on the GCP coordinates because the GCP coordinates changed slightly based on the RTK observation time.

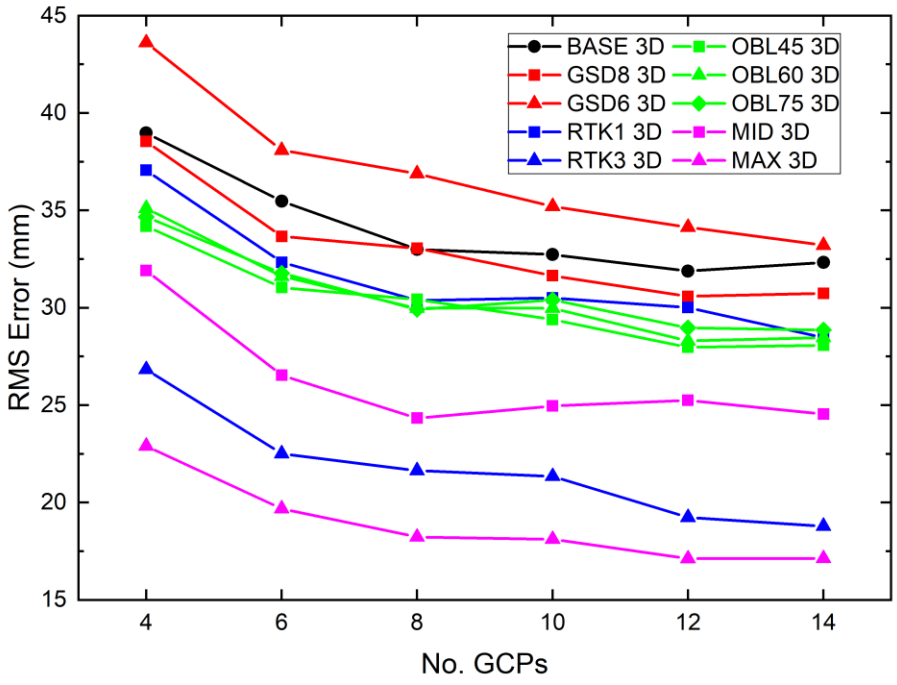

Figure 3.9 UAV Calibration II—RMS of the processed 3D errors at checkpoints for all processing groups and numbers of GCPs.

Although RMS error is a representative measure, it only gives an overview of the point cloud accuracy and more can be learned by examining box plots of errors. The box plot of the processed errors at checkpoints for 12 GCPs (Figure 3.10) showed that RTK observation time at GCPs had the largest impact on the mean and variance of errors. RTK observation time had the strongest impact on reducing the variance of errors, shown in RTK1, RTK3, MID, and MAX. Additionally, groups that used a combination of parameters produced lower means and variances than the individual parameters alone (e.g. MID vs. GSD8 or RTK1; MAX vs. GSD6 or RTK3).

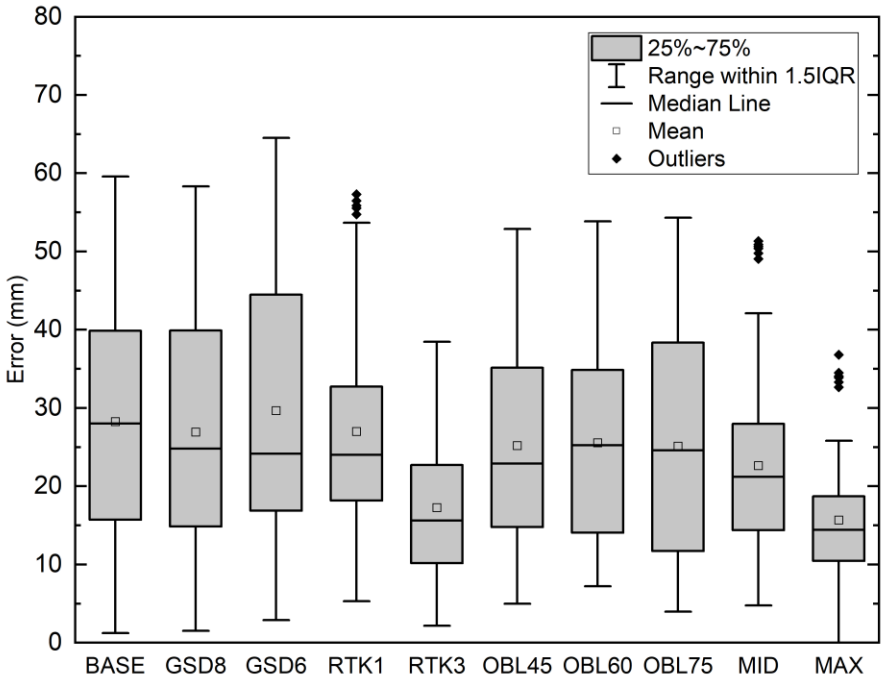

Figure 3.10 UAV Calibration II—box plot of the processed errors at checkpoints when 12 GCPs were used to georeference for each processing group.

A large discrepancy was observed in Figure 3.9 where GSD6 resulted in larger errors than BASE and GSD8. GSD6 images were taken at shorter camera-to-surface distances, which should have resulted in a more accurate point cloud and smaller errors. GSD8 showed improvements compared to BASE, as expected with closer-range images. Comparing the 3D, vertical, and horizontal RMS errors for BASE, GSD8, and GSD6 (Figure 3.11) showed that horizontal errors were similar for all groups. Vertical errors for GSD6 were higher than those for BASE and GSD8. If the cause of increased GSD6 errors was inaccurate marking of GCPs in the images, horizontal errors would have been affected because all images were nadir. Since horizontal errors were unaffected (Figure 3.11), it can be concluded that the larger vertical errors in GSD6 were due to image processing. It is unclear as to what part of processing caused the GSD6 vertical errors. The author's theory is that because the images were closer to the surface and viewed less surface area, there could have been a minor doming effect occurring at areas in the point cloud where GCPs were not viewed in images. This could have

caused vertical errors such as those observed. Regardless of what caused the larger vertical errors, results showed that 20 second RTK observation times are insufficient for close-range (e.g. 6 mm GSD) UAV images. Higher quality GCP measurements are required if close-range UAV images are collected, as that combination (e.g. MAX group) resulted in reducing point cloud errors (Figure 3.9).

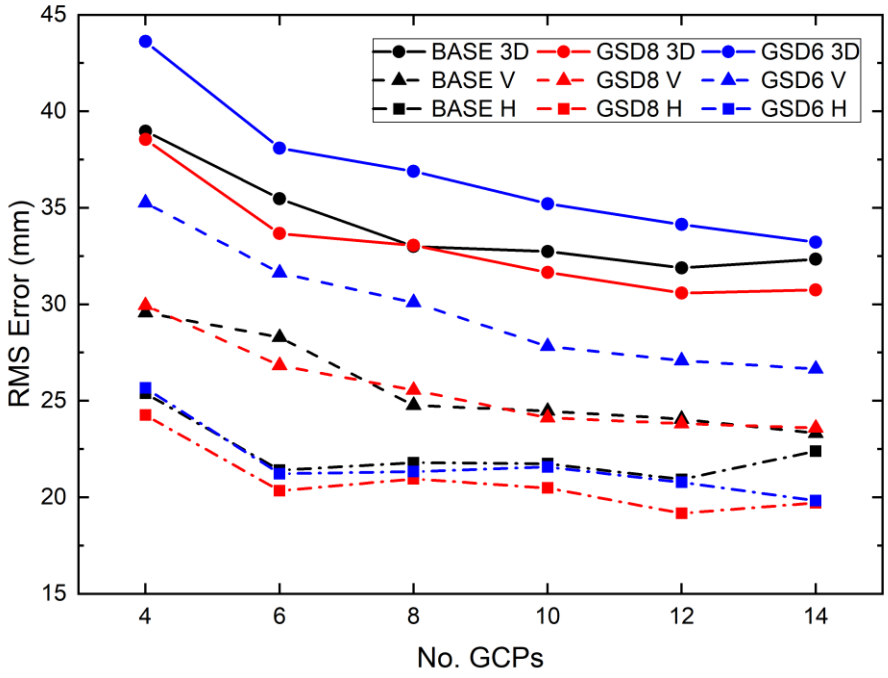

Figure 3.11 UAV Calibration II—RMS of the processed 3D, vertical, and horizontal errors at checkpoints for BASE, GSD8, and GSD6.

RTK observation time proved to be the most effective parameter to reduce errors at checkpoints (Figure 3.9). Plotting the 3D, vertical, and horizontal RMS errors for BASE, RTK1, and RTK3 (Figure 3.12) demonstrated that increasing RTK observation time worked by reducing both vertical and horizontal errors. This contributed to a significant error decrease in 3D errors, particularly from RTK1 to RTK3.

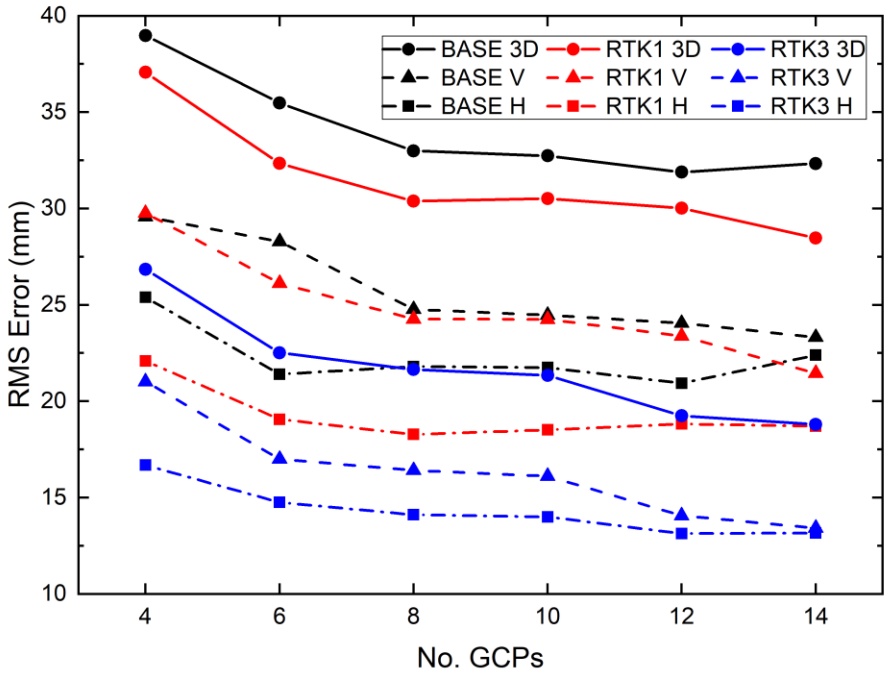

Figure 3.12 UAV Calibration II—RMS of the processed 3D, vertical, and horizontal errors at checkpoints for BASE, RTK1, and RTK3.

Including oblique images in processing reduced vertical errors in the point cloud by approximately 15% compared to the same image set without oblique images (Figure 3.13). This result agreed with the literature, although the error reduction was not as drastic as others reported (James and Robson, 2014). Including oblique images also reduced horizontal errors (Figure 3.13), though significantly less than vertical errors. Oblique images at 45° provided the greatest improvement in vertical accuracy, likely because more of the scene and GCPs was captured in the images at shallower viewing angles. Including 12 oblique images in the image block substantially improved the accuracy. Oblique images at 60° contributed to slightly lower point clouds errors than 75°. Stumpf et al. (2015) showed that oblique imagery should not be captured at incidence angles less than 30° to the surface because more extreme obliqueness decreases data quality and makes feature matching difficult. Based on this observation and the results presented here, it seems that the optimal oblique viewing angle to reduce errors in point clouds is near 45°.

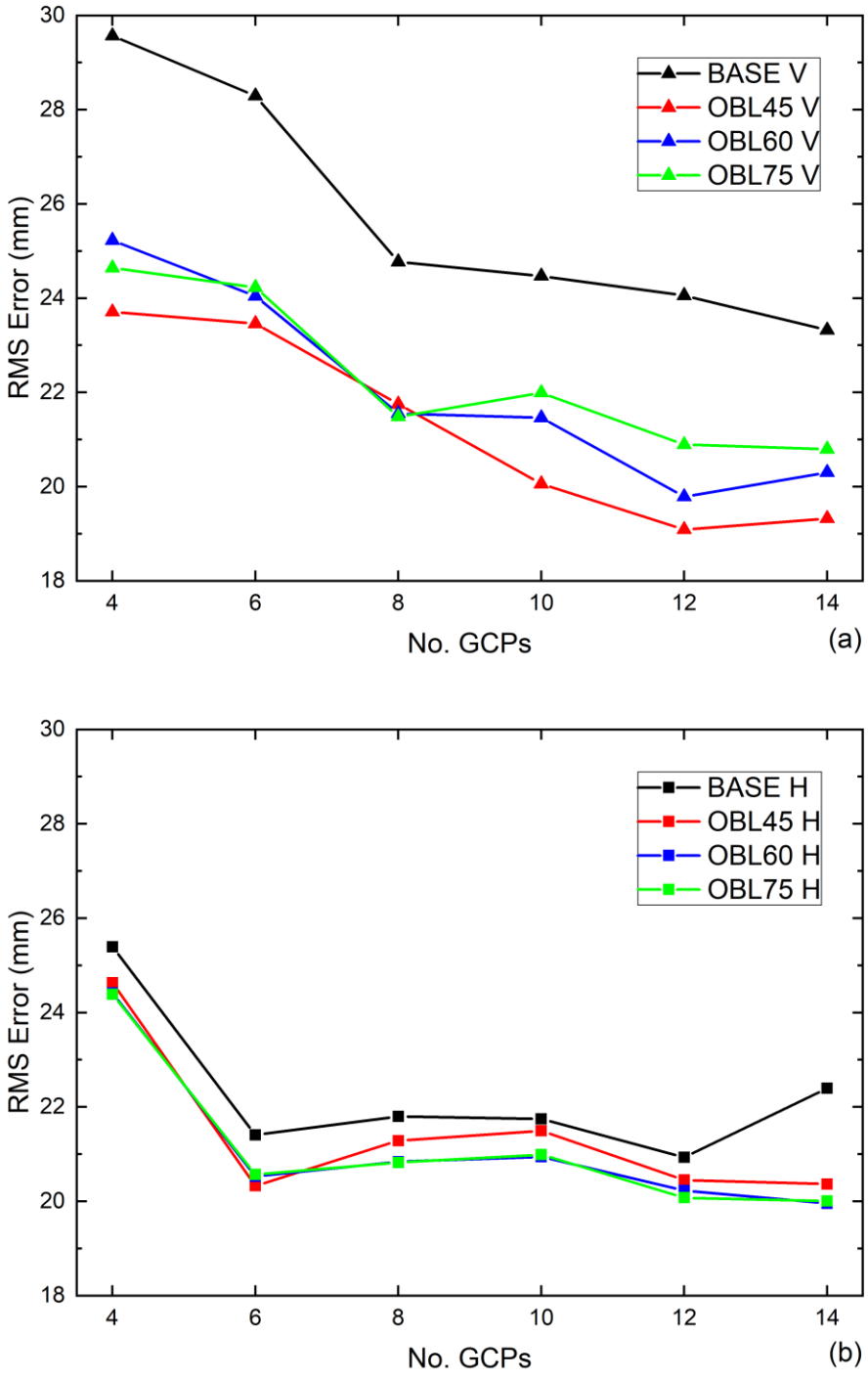

Figure 3.13 UAV Calibration II—RMS of the processed errors for BASE, OBL45, OBL60, and OBL75: a) vertical direction; b) horizontal plane.

To exhibit the accuracy improvements that occurred when parameters were combined, RMS errors were plotted for MID against BASE, GSD8, and RTK1 and for MAX against BASE, GSD6, and RTK3 (the group of combined parameters against the groups of its individual parameters; Figure 3.14 and Figure 3.15, respectively). Combining parameters was effective at further reducing errors in point clouds. Interestingly, error reductions for MID and MAX were approximately equal to the cumulative effect of their corresponding individual parameter groups, excluding GSD6 because of the vertical processing errors. MID and MAX were also the only two groups where the vertical RMS errors were less than the horizontal RMS errors. Error reductions in the vertical (Z) direction were substantial; however, the vertical axis still resulted in the largest errors because horizontal errors represent the planar errors composed of the X and Y errors.

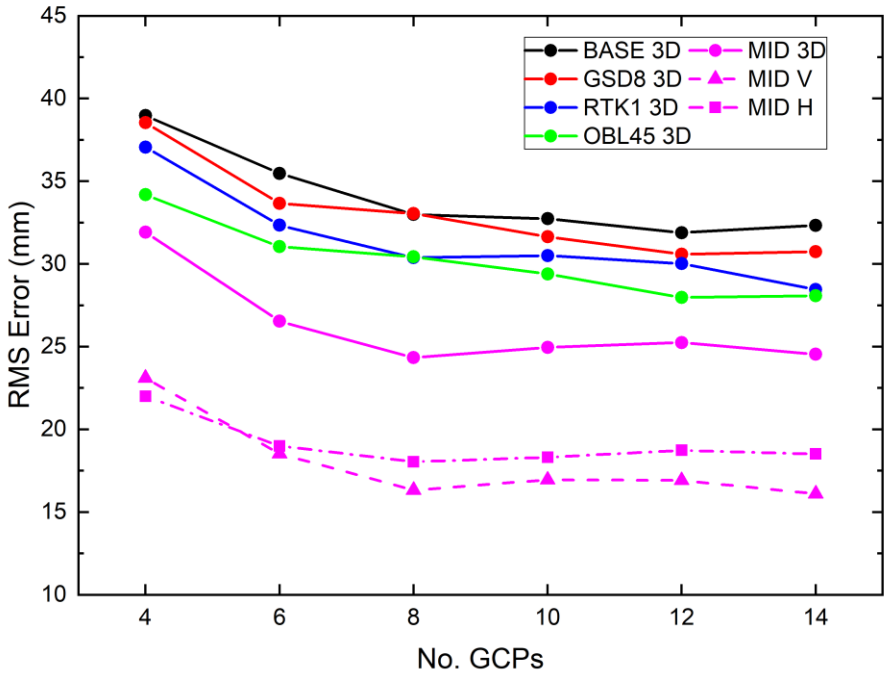

Figure 3.14 UAV Calibration II—RMS of the processed 3D errors for MID and its corresponding individual parameter groups, plus vertical and horizontal errors for MID.

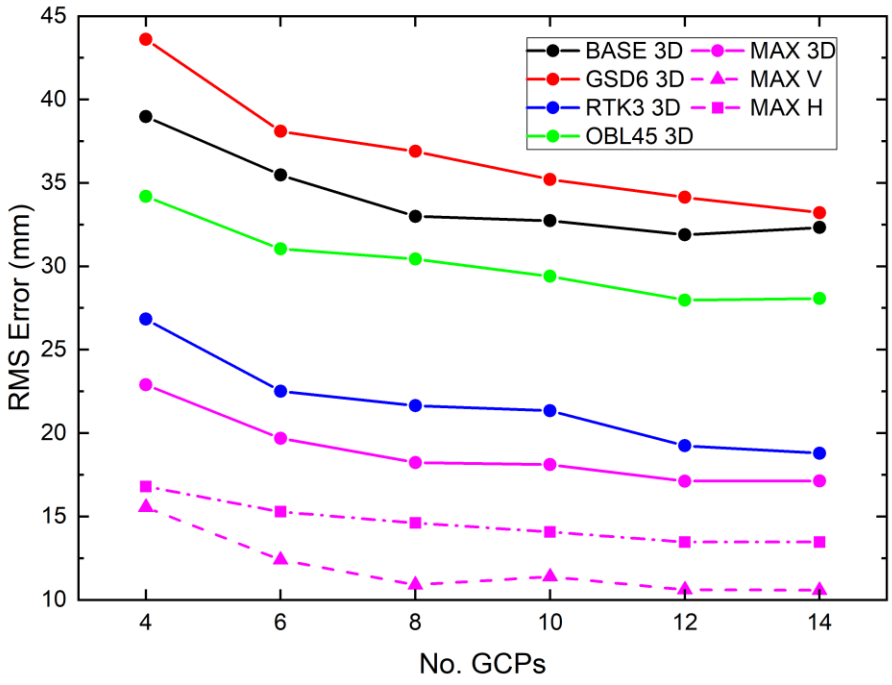

Figure 3.15 UAV Calibration II—RMS of the processed 3D errors for MAX and its corresponding individual parameter groups, plus vertical and horizontal errors for MAX.

The LoD analysis on the point cloud errors was included to demonstrate an application where accuracy of reconstructed point clouds is important. Comparing the RMS errors (Figure 3.9) and the LoDs (Figure 3.16) shows how important point cloud accuracy can be for deformation monitoring applications. Comparing 12 GCPs for BASE and MAX, 3D RMS errors were 32 mm and 17 mm, respectively, and LoDs were 90 mm and 47 mm, respectively. A 15 mm RMS error reduction in the point cloud GCPs may not seem significant, but it translates to a 42 mm reduction in LoD, which is significant if attempting to measure small-scale deformations of highway embankment.

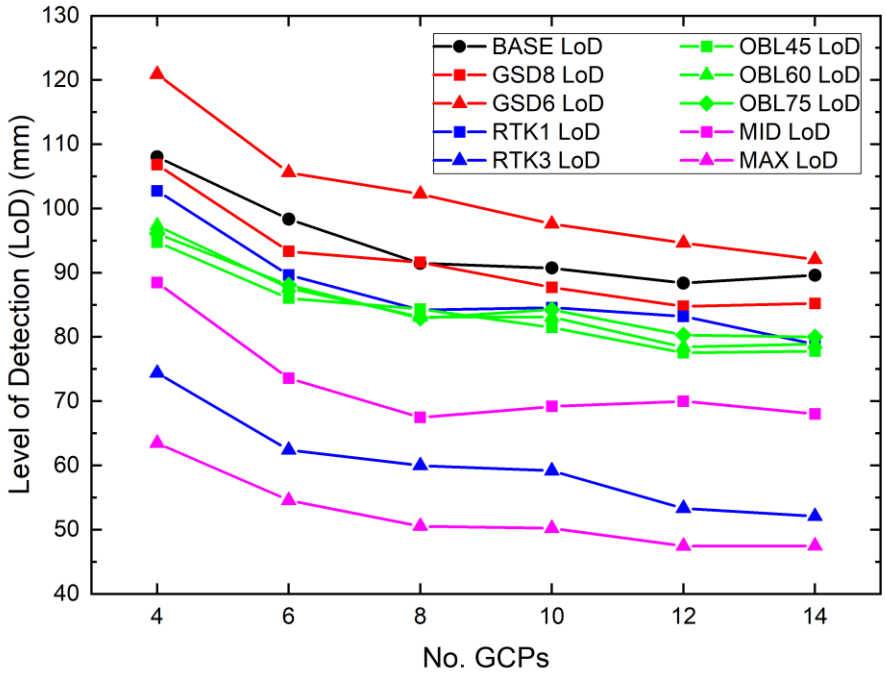

Figure 3.16 UAV Calibration II—LoD for deformation measurements of point clouds from all processing groups and numbers of GCPs.

3.1.4.3 Experiment Discussion and Conclusion

UAVs are becoming increasingly popular for deformation monitoring applications; however, the accuracy (or inaccuracy) of results is often overlooked (James et al., 2017). Using checkpoints to evaluate errors in the point cloud and analyze output statistics should be an essential part of any UAV SfM survey (James & Robson, 2014). This experiment showed that an important parameter to consider when conducting UAV surveys with an RTK system is the RTK observation time at GCPs. Increasing RTK observation time reduced point cloud errors more than the other investigated parameters and worked in combination with the other parameters to further reduce errors. Small changes in the accuracy and measured coordinates of GCPs are carried through the entire SfM workflow and can result in significant errors in the reconstructed point cloud. Point cloud errors then contribute to uncertainty of deformation detection when point clouds are compared, so it is understandable how more accurate GCP coordinate inputs can have such a powerful effect. The large

effect of RTK observation time at GCPs does not make designing the image block less significant though. Increasing RTK observation time provided major accuracy improvements in this experiment because the baseline image block was appropriately designed to reconstruct the survey area. If the image block was insufficiently designed (i.e. low image overlap, large GSD, less coverage, etc.), the SfM reconstructed point cloud would be less accurate and have a lower density. In that case, high RTK observation times would not provide as significant benefits. Defining what qualifies as a sufficient design for a UAV survey is project dependent. The results of this study demonstrated that with an image block appropriate for the scale of a project, increasing RTK observation times can significantly reduce errors in the reconstructed point cloud.

The downside of increasing RTK observation times is the additional time required to survey GCPs. In the field, time is often a critical factor in conducting UAV surveys because adverse weather conditions can ground flights. Nevertheless, increasing RTK observation times evidently improves point cloud accuracy and this study showed that the quality of GCP coordinates is more important than the quantity of GCPs. For example, a UAV survey using RTK1 parameters with 14 GCPs would require 14 minutes of total GCP observation time and a survey using RTK3 parameters with 6 GCPs would require 18 minutes of total GCP observation time. When the time required to set up the GCP network is considered, these two surveys require approximately the same time to survey GCPs. RTK3 with 6 GCPs produces an LoD of only 55 mm, whereas RTK1 with 14 GCPs produces an LoD of 80 mm (Figure 3.16). For projects of similar scale using comparable equipment, selecting a lower number of GCPs with higher accuracy is the better for the overall accuracy of the point clouds.

Including a small number of oblique images in the image block was effective for reducing vertical errors in the point cloud (Figure 3.13a). It is especially effective when considering the small amount of time required to collect the images compared to the time for a full grid survey. The benefits of decreasing GSD were not significant in this study (Figure 3.11). The primary purpose of decreasing GSD sub-centimeter is to provide a more detailed and dense reconstruction of the small-scale surface

variations. By only assessing accuracy based on checkpoint errors, the benefits of detailed point clouds reconstructed by images with lower GSDs was not realized. The benefits of lowering GSD would become more apparent when the denser reconstructed point clouds are compared to determine deformation (Monserrat & Crosetto, 2008).

The results of this experiment can help researchers and engineers to design UAV surveys for monitoring deformations of structures or natural environments. Small-scale projects where small deformations are expected would require a lower LoD to confidently measure deformations, and vice-versa. The importance of a structure also is a factor in determining the targeted LoD. If an engineered structure such as an embankment would have severe consequences if its slope failed, monitoring the embankment would require a highly precise LoD to provide accurate deformation measurements and time for evacuation if signs of impending failure were detected. A targeted LoD can be determined early in the monitoring schedule and can be used to design UAV surveys. This study provided recommendations on the critical parameters to consider during the UAV survey design. This experiment and analysis led to the following conclusions:

- Positional errors in reconstructed point clouds decrease with increasing numbers of GCPs. However, there appears to be an optimal GCP density after which accuracy does not consistently improve with more GCPs.
- RTK observation time was the most effective parameter to reduce vertical and horizontal errors in point clouds. Increasing RTK observation time also worked in combination with other parameters to further reduce errors.
- Image GSD alone did not have a significant effect on point cloud accuracy. Higher-quality images captured at a smaller GSD require more accurate GCP input coordinates to achieve accuracy improvements.
- Including additional oblique imagery in the image block reduced vertical errors by approximately 15%. Horizontal errors were also slightly reduced. An oblique viewing angle

of 45° contributed to lower errors than 60°and 75° because more of the scene and GCPs can be seen in the images at shallower viewing angles.

3.2 TLS

3.2.1 TLS Model and Specifications, Operating Procedures, and Data Processing

The FARO Focus^{3D} X 330 Laser Scanner (Figure 3.17) was the TLS model used in this research. The Focus^{3D} is a tripod-mounted high-speed laser scanner that can produce detailed 3D models of complex environments in minutes. It emits an infrared laser beam that is reflected off a rotating mirror towards the area being scanned and calculates distances and orientations of objects to the scanner by measuring the phase shift of the infrared beam reflected off the objects (FARO Technologies Inc., 2015). The Focus^{3D} has a range of 330 m and can capture data in a 360° horizontal range and 300° vertical range, only missing data directly beneath the scanner's tripod. The scanner has a high-quality camera to capture red-green-blue (RGB) imagery of the scene, allowing for full-colour 3D point clouds to be generated. The Focus^{3D} also has several sensors that provide additional information to improve post-processing. This includes a GNSS receiver to correlate individual scans together, an electronic compass to associate directional data, and an altimeter for altitude measurement. Table 3.7 outlines some technical specifications of the Focus^{3D} and its sensors.

Figure 3.17 FARO Focus^{3D} X 330 Laser Scanner.

Table 3.7 FARO Focus^{3D} X 330 Laser Scanner specifications.

Parameter	FARO Focus^{3D} X 330
Unit weight	5.2 kg
Laser classification	Class 1
Wavelength	1550 nm
Beam diameter at exit	2.25 mm
Beam divergence	0.19 mrad / 0.011°
Scan range	0.6 to 330 m
Measurement error (one sigma @ 25 m)	±2 mm
Scan speed	122,000 to 976,000 pts/sec
Horizontal field-of-view	360°
Vertical field-of-view	300°
Camera colour resolution	70 Mp
Max battery life	4.5 hours
Operating temperature	5 to 40 °C

The Focus^{3D} has a variety of scan profiles with predefined settings for certain applications. For example, the profiles differentiate between indoor or outdoor, close- or long-range, and low- or high-quality scans. The settings in each profile can also be modified manually. *Outdoor 20m…* is a pre-set settings profile in the Focus^{3D} scanner that was used throughout this research (Table 3.8). A resolution of ¼ results in a total of 44 Mpts in the point cloud and a point-to-point distance of 6.1 mm at 10 m from the scanner. The scanner would be set up less than 10 m from the embankment on-site; therefore, this resolution is acceptable for the application. The quality setting affects the amount of noise in the scan and quality of the data points. Increasing quality from the *Outdoor 20m…* default of 4x to 2x resulted in an increase in scan time from 11 minutes to 33 minutes. Because multiple scans would be required on each sideslope of a high-fill section, that time increase was deemed infeasible. Further discussions with Dr. Matt Lato, Senior Geotechnical Engineer at BGC Engineering and expert in remote sensing technologies (personal communication, May 14, 2018), regarding the resolution and quality parameters reinforced the selected parameters. He expressed that increasing the resolution past ¼ would result in a very high-density point cloud with redundant points that would only marginally improve results and cause unnecessary increases in processing time. The full vertical and horizontal scan ranges were used to ensure all data surrounding the scanner was measured and because modifying the ranges did not affect the scan time due to how the scanner collects data with the rotating mirror. Exposure metering mode sets how the integrated colour camera determines the exposure for taking photos. Horizon weighted metering is best for scenarios when measuring objects at the horizon with bright light coming from above. This suits the conditions on-site where scans would be performed during the day with the Arctic summer sunlight almost directly above. The other settings specify to use all the scanner's integrated sensors and to apply the clear contour and clear sky filters to remove erroneous scan points at edges of objects and in the sky, respectively.

Table 3.8 FARO Focus^{3D} X 330 Laser Scanner settings.

Setting	FARO Focus^{3D} X 330
Profile name	Outdoor 20m…
Resolution	¼
Quality	4x
Number of points	44 Mpts
Point-to-point distance @ 10 m	6.1 mm
Vertical range	-60° to 90°
Horizontal range	0° to 360°
Exposure metering mode	Horizon weighted
Inclinometer	On
Compass	On
Altimeter	On
GNSS	On
Clear contour filter	On
Clear sky filter	On
Distance range	Normal

Data acquired with the Focus^{3D} is processed and managed using FARO's processing software SCENE (FARO Technologies Inc., 2019a). SCENE processes raw scan data to generate scan point clouds that can be registered together to form large project point clouds composed of several individual scans. The general workflow in SCENE is as follows. Raw scan data is first imported to the SCENE project and preprocessing of the raw scans is performed. During preprocessing, SCENE can automatically detect and identify objects such as checkerboards and spheres, which are both often used to improve registration of scans and for georeferencing. Scans are roughly aligned during preprocessing by using the available sensor data (e.g. GNSS, altimeter, etc.). Following preprocessing

is the registration of multiple scans together. Most projects require several scans from a variety of positions in order to provide good structure and details of the environment (FARO Technologies Inc., 2019b). Registration is technically the transformation of scans to be closely aligned into one overall project coordinate system. SCENE offers several methods of registration; however, the two most popular and relevant to this research are target-based registration and cloud-to-cloud registration. Target-based registration uses the positions of targets such as checkerboards and spheres to align scans together. Cloud-to-cloud registration uses the actual scan point data to align the scans. The approaches to how these two registration methods were applied in this research are discussed in Section 4.3.3.

The next step of processing is to georeference the project point cloud. Similar to UAV data processing, georeferencing for TLS is done using GCPs with known coordinates. SCENE requires GCP coordinate data to be imported as .csv filetype. The project can then be re-registered, this time including the GCP coordinate data, to transform the point cloud into the GCP real-world coordinate system. Once all scans are properly registered and georeferenced, the project point cloud can be exported from SCENE to be used in other software for deformation measurement.

3.2.2 TLS Calibration I—Sphere Target Displacement Accuracy

On June 7, 2018 at the quad field on the U of M campus, a calibration test with the Focus^{3D} scanner was performed to determine its accuracy measuring the displacement of sphere targets (Figure 3.18). The spheres, which were included with the purchase of the Focus^{3D} scanner, are designed to be mounted on tripods and set up throughout the survey area to improve registration of scans. Spheres are a particularly useful type of artificial target for TLS because they appear identical from any orientation. This allows SCENE to analyze the scan points on the sphere's surface and identify the centroid of the sphere, which is used as a common point between scans during registration.

Figure 3.18 Sphere target for TLS.

For the calibration test, six spheres were set up in pairs at distances of approximately 15 m, 20 m, and 30 m from the first scanner location. A total of four scans were performed: two with the initial sphere setup and two more after the spheres had been displaced. For the two spheres located 15 m from the first scanner location, one was displaced horizontally (sphere H_{15}) and the other was displaced vertically (sphere V_{15}). Similarly, for the spheres at 30 m, one was displaced horizontally (sphere H_{30}) and the other was displaced vertically (sphere V_{30}). For the spheres at 20 m, one remained in the same position for all scans to act as a reference point and the other sphere was displaced horizontally a large distance. The displacements of each sphere were measured by hand using a tape measure. Figure 3.19 shows the calibration test setup.

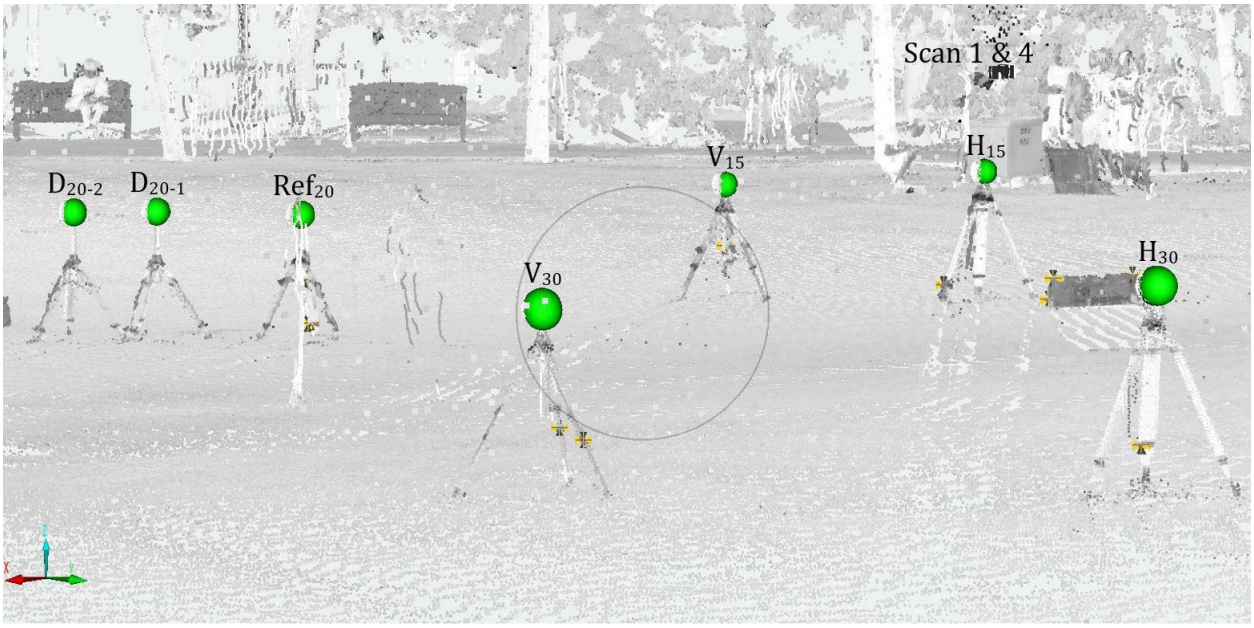

Figure 3.19 TLS Calibration I—reconstructed point cloud with marked sphere targets.

Scans were performed using the *Outdoor 20m…* profile. Scan data was imported to SCENE for post-processing and analysis. The individual scans were registered using target-based registration. Initially, only the spheres were used as targets for registration. Once the scans were aligned using the spheres, precise points (e.g. box corners) were marked throughout the scans to provide more common points and improve registration. Displacements for each of the spheres were measured directly in SCENE and compared to the hand-measured displacements. The differences between the hand-measured distances and distances between targets in SCENE were considered errors. The horizontal and vertical errors for each sphere target were analyzed (Table 3.9) to determine the accuracy of the Focus^{3D} scanner to measure deformation.

Table 3.9 TLS Calibration I—target displacement errors between hand and scanner measurements.

Target	Horizontal error (mm)	Vertical error (mm)	3D error (mm)
H_{15}	7.3	-2.4	7.7
H_{30}	2.3	-1.8	2.9
V_{15}	-1.5	-1.6	2.2
V_{30}	-3.8	2.6	4.6
$D_{20\text{-}1}$	1.0	-	1.0
$D_{20\text{-}2}$	-2.0	-	2.0
RMS	3.7	2.1	4.1

The 3D RMS error for the target displacements was less than 5 mm. The largest error occurred at sphere H_{15}, where the horizontal error was 7.3 mm. The hand-measured and scanner-measured errors were 29 mm and 21.7 mm, respectively. It seems that the horizontal displacement hand-measurement was overestimated because the H_{15} horizontal error was significantly larger than the other error measurements. If H_{15} is ignored, the resulting 3D RMS error for the target displacements was only 2.8 mm. This error estimate was also accounting for human error in measuring the displacements with the tape measure. The true error of the TLS would likely be less than the determined errors if a more precise measurement of the true displacement was available. Hand measurements do have appropriately small errors though and the determined error values were thought to be acceptable for measuring deformation of embankments that were estimated to be at least one order of magnitude larger.

3.2.3 TLS Calibration II—Checkerboard Target Identification

Registering several TLS scans together requires a network of targets and control points appropriately spaced and viewable from the scanner locations. The Focus^{3D} scanner package came with six sphere targets, which are ideal for registering scans; however, six targets were insufficient for scanning the high-fill embankment sections. Additionally, the site conditions (e.g. embankment fill material, terrain, and vegetation) do not present objects with distinct features that can be easily used as targets. Therefore, additional artificial targets were required to register scans on-site.

Checkerboards were the best option for artificial targets because they are simple to construct at a desired size, have precise centres that can be measured using survey equipment, and can be marked automatically in SCENE during post-processing of scan data. Checkerboard targets were constructed out of plywood sheathing cut into 60 cm x 60 cm pieces. The checkerboards were spray painted pink/orange and black and coated with a chalkboard clearcoat to protect the wood and paint from water damage.

The viewing angle between the scanner and checkerboard target influences the number of scan points on the target and therefore the accuracy of the marked checkerboard centrepoint. For reference, a 0° viewing angle means the checkerboard face is oriented directly towards the scanner. On June 29, 2018, a test was set up at the U of M quad to test: 1) the effect of the checkerboard's standing angle (i.e. angle of the checkerboard to the ground surface) on the scanner's ability to accurately mark the checkerboard centre; and 2) the effect of the viewing angle between the scanner and checkerboard on the scanner's ability to accurately mark the checkerboard centre. The test set up (Figure 3.20) included: scans from two scanner locations spaced 15 m apart; three vertical checkerboards centred between the scans (7.5 m in the X direction) at distances of 5 m, 7.5 m, and 10 m from the scans in the Y direction; and five checkerboards with a range of standing angles placed between the scans at 25 m in the Y direction. The six sphere targets were setup surrounding the checkerboard targets to register the two scans together and ensure all measurements were done

within the area enclosed by the spheres. The test setup was designed based on the dimensions of the high-fill embankment sections and estimated distances between scanners and targets on-site.

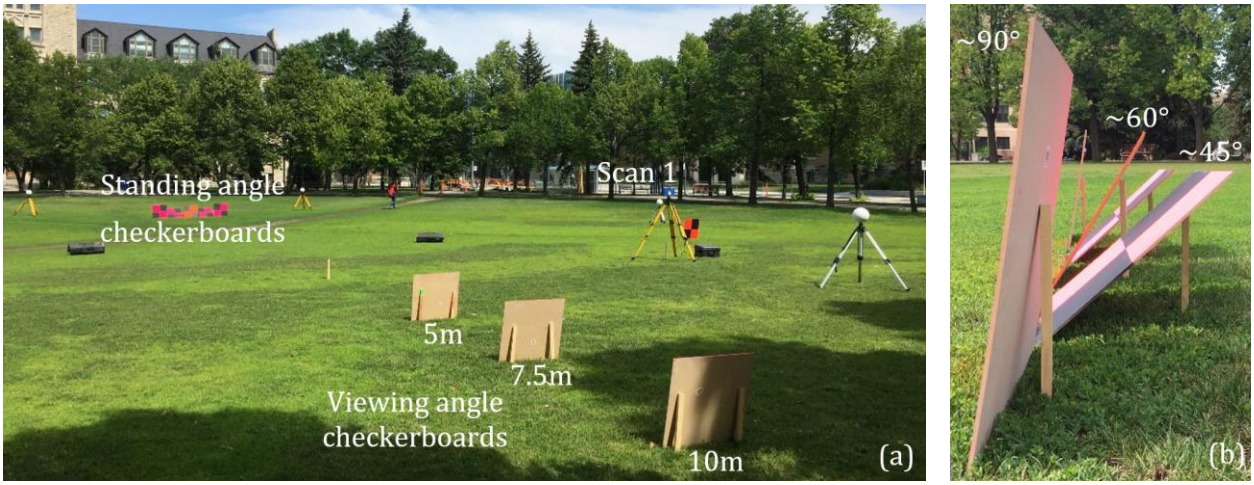

Figure 3.20 TLS Calibration II: a) test setup; b) standing angle checkerboards.

The results of TLS Calibration II confirmed that the distances and orientations between scanners and targets would be sufficient for identifying and marking the checkerboard targets. The target centres were not measured with any survey equipment and therefore the accuracy of the target markings was not determined. Based on visual observation of the markings, most were positioned at or near the centre of the targets.

The three viewing angle checkerboards at Y distances of 5 m, 7.5 m, and 10 m from the scanner correspond to viewing angles of 56.3°, 45°, and 36.9°, respectively. The target at 10 m produced the highest density of scan points on the target. There was a moderate difference in scan point density between targets at 10 m and 7.5 m, and there was a more significant reduction in scan point density for the target at 5 m. This observation reinforces the general guideline to limit the scanner-to-target viewing angle to 45° as a method to reduce inaccuracies of marking the target (Lato, personal communication, May 14, 2018).

As expected for the standing angle checkerboards, the near-vertical targets had the most scan points on their surface. This occurred because they have the largest surface area with respect to the

orientation of the scanner. The difference in the number of scan points on the checkerboard surfaces was larger between the 60° and 45° targets than it was between the 90° and 60° targets. Although the change in standing angle is less for 60° to 45°, there is a larger reduction in the target's viewable surface area. A higher scan point density on a checkerboard target surface should theoretically correspond to a more accurate identification of the target centre. However, there is some variation in the quality of the paint job on the checkerboards (e.g. imperfect lines, paint overlap, paint smudging at centre, etc.), which may reduce the accuracy of marking centrepoints when processing scan data. For surveying the high-fill sections, checkerboard targets were required on the ground surface along the toe and on the embankment shoulders. The ideal standing angle of the checkerboard targets along the toe was determined to be approximately 75°. At this standing angle, the targets would optimize the viewable surface area for scans completed along the toe and on the embankment shoulder. The ideal standing angle of the checkerboard targets on the shoulder was vertical. Vertical targets on the shoulder provide an optimal orientation towards scans completed on the shoulder and is the best option to maximize target surface area towards scans completed along the toe. Checkerboards oriented downwards from the shoulder (i.e. standing angles > 90°) would be impractical to set up and were not pursued.

In order to set up the checkerboards at these standing angles on-site, the targets required some sort of stand. Checkerboards leaning against stakes hammered into the ground, like that used in TLS Calibration II, would not have worked because wind on-site would blow the targets over. The checkerboards required something sturdier. The checkerboard stands needed to be sturdy enough to be unaffected by wind, as well as collapsible, easy to assemble, and lightweight for practicality on-site and while transporting. The most economical option was to build the stands. An easel-like design built out of wood was chosen. The stands had an A-frame (three pieces) that the checkerboard would rest on and a back leg to adjust the standing angle (Figure 3.21).

Figure 3.21 Checkerboard stands with and without a checkerboard.

I used 2" x 2" lumber cut into 2 ft pieces and held together by bolts and wingnuts for the frame. Wingnuts were selected because they could be tightened and loosened by hand. To attach the checkerboards to the stands, long screws were fastened through the checkerboards into the A-frame. Mini shelf brackets were placed in pre-drilled holes at the checkerboard centres. This allowed the RTK rover to sit directly at the checkerboard centre and measure the position so the checkerboard could be used as a GCP for georeferencing. Lastly, 1 ft nails were hammered through the back leg into the ground to act as an anchor point and stabilize the stand against wind. A total of 12 stands were built for the TLS surveys on-site.

3.2.4 TLS Calibration III—Site-Scale Setup, Target Identification, and Scan Registration

The third TLS calibration was designed to test the performance of the Focus^{3D} scanner to identify targets and register scans for a survey setup similar to one that would be conducted at the ITH KM-82 research section. The calibration test was conducted on July 24, 2018 at Castle Park, a park on the U of M campus located next to a 5 m high dike road embankment (Figure 3.22). Castle Park was an

ideal location for the calibration test because it was easily accessible and provided an embankment with dimensions like KM-82 and space along the toe to set up the TLS surveys.

Figure 3.22 TLS Calibration III—photo of test site showing embankment and targets.

Two TLS surveys of the embankment were conducted: one for a 20 m section and another for a 40 m section. Both surveys were designed to have the full embankment section covered by the scans within a 45° viewing angle from the scanner locations. Sphere and checkerboard targets were used. Checkerboard targets were set up on the checkerboard stands at maximum viewing angles of 45° to the scans. The checkerboard centres were surveyed with the RTK system to be used as GCPs. The 20 m and 40 m section surveys scanned the embankment from three and five locations, respectively. For each survey, the scanner was set up at 15 m spacing parallel to the road and either directly at the shoulder or 5 m from the toe. The full survey setup is shown in Figure 3.23. Furthermore, the entire calibration test including set up, RTK surveying, scanning, and take down was timed to give an estimate for site visits.

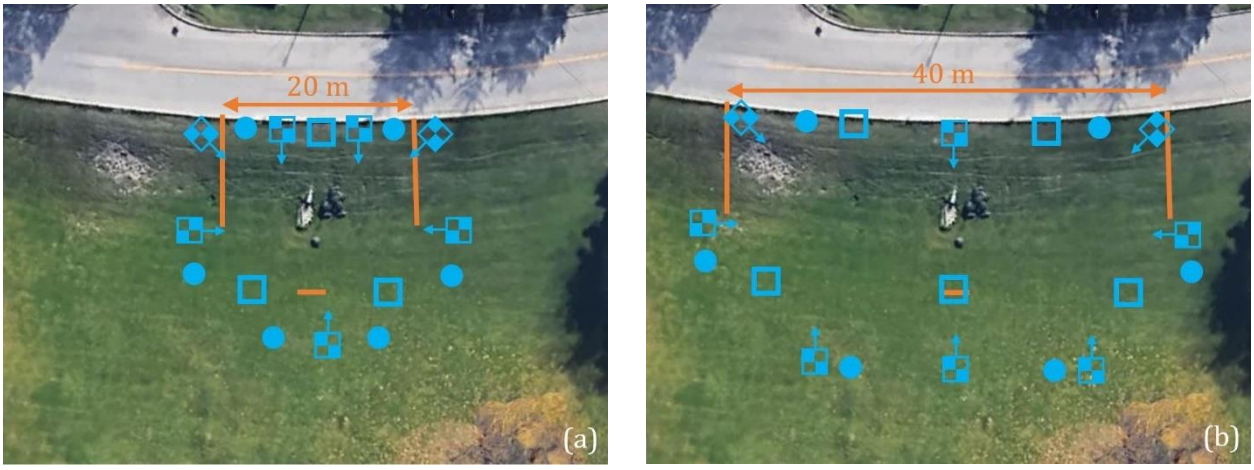

Figure 3.23 TLS Calibration III—plan view survey setup showing scanner locations (squares) and sphere and checkerboard targets: a) 20 m section; b) 40 m section.

TLS Calibration III proved to be a successful test. All targets were identified and marked in every scan for the 20 m survey. However, not all targets were marked in every scan for the 40 m survey because some of the scanner-to-target distances were too far. Although this was not ideal, it was acceptable because there were enough targets near each scan to accurately register the scans together. Overall, both TLS surveys provided dense 3D point clouds of the embankment with manageable registration errors. The 40 m section survey design would be used on-site because it would cover the full research section at KM-82, including the 20 m reinforced zone and 20 m control zone. Additionally, the full test set up took approximately 6 hours. Therefore, a full day was budgeted for scanning KM-82 on-site visits because both embankment sideslopes needed to be scanned.

3.3 RTK Survey System

3.3.1 RTK Model, Operating System, and Data Processing

Real-time kinematic (RTK) survey systems use GNSS technology to accurately measure the 3D positions of points in the field. RTK systems are more secure and fast than standard GNSS survey systems and have the advantages of shorter measurement time, higher positioning accuracy, and direct result of exact point coordinates in the field (Xu, 2012). They are considered to be the most

time-efficient means of surveying GCPs for UAV photogrammetry applications (Harwin & Lucieer, 2012). The RTK system used in this research included a pair of Leica GS14 antennas and a Leica CS20 controller. One GS14 antenna is set up on a tripod and referred to as the base station. The other GS14 is set up on top of a long rod and carried by the operator to measure the positions of points; it is referred to as the rover. The CS20 is a remote controller that allows for data communication with the GS14 antennas. It is typically attached to the rover and carried around site with the operator. The CS20 provides the operator with full control of the RTK system, allowing them to input the base station and rover setup parameters, select the data link format for communication between antennas, define satellite tracking settings, record point measurements, and more.

During RTK operations, the base station is set up on a static point with fixed coordinates and transmits its raw observations of satellite coordinates to the rover through the data link. The rover uses the base station's and its own real-time satellite observations to compute its position relative to the base station as a vector (Donahue et al., 2013). When surveying a point with the rover, the point's position is measured for a specified measurement time. The positional data over the measurement time is analyzed to determine the position of that point. All points will be referenced to the position of the base station at the time of the measurement. With every point position measurement, the RTK system also provides horizontal, vertical, and 3D uncertainty estimates. The uncertainties are the standard deviation of the positional data over the measurement time.

All measured points must be referenced to a certain coordinate system. The Leica RTK system can reference to any coordinate system uploaded. This research used the North American 1983 datum (NAD83) Canadian Spatial Reference System (CSRS) coordinate system with the Universal Transverse Mercator (UTM) Zone 14N and Zone 8N projections for surveys in Manitoba and Northwest Territories, respectively. The accuracy of point measurements with an RTK system can vary significantly depending on many factors such as quality of the RTK sensors, number of visible satellites, the elevation mask, environmental and atmospheric conditions, operating range between

the rover and base antennas, and observation time at the point (Trimble, 2019; Leica Geosystems, 2016). Leica Geosystems (2016) states the accuracy of the GS14 base station is 3 mm horizontally and 3.5 mm vertically after post-processing the observation data. The accuracy of points measured by the GS14 rover are stated to be 8 mm horizontally and 15 mm vertically (Leica Geosystems, 2016). These accuracies assume normal to favourable conditions. The Leica GS14 antennas are capable of tracking satellite signals from all the major satellite networks including GPS, Glonass, BeiDou, and Galileo (Leica Geosystems, 2016).

RTK survey data was processed using Leica's proprietary processing software Leica Infinity (Leica Geosystems, 2019a). The software has a variety of powerful analysis functions, yet its use in this research was limited. The primary purpose for using Leica Infinity was to reformat the survey data from its raw format recorded by the RTK system to a format accepted by the UAV photogrammetry and TLS software. Its second purpose was to shift RTK survey data to using the post-processed precise base station coordinates. This process will be elaborated on in Section 4.3.1.

3.3.2 RTK Calibration Tests

There were no calibration tests specifically for the RTK system. However, during UAV and TLS calibration tests, certain processes and parameters for the RTK surveys were investigated to help develop on-site RTK survey procedures. The two most notable tests that helped develop the RTK survey procedures were TLS Calibration III and UAV Calibration II.

3.3.2.1 RTK Survey Methods during TLS Calibration III

TLS Calibration III was a site-scale test of the TLS and RTK procedures to confirm they provided correct results. RTK procedures included setting up the base station, determining precise coordinates of the base station, communicating between the base station and rover, completing the RTK survey, and processing the data. Accurate GCP data is critical for conducting deformation monitoring with UAV or TLS because the 3D models from those technologies use the GCP data for georeferencing and models from different epochs must be georeferenced to the same coordinate system for proper

comparison. The first and most important step to complete an RTK survey is setting up the base station.

There are three options for setting up the base station: 1) set up over an unknown point; 2) set up over a known point; and 3) set up over an arbitrary "known" point. Option 1 is used to establish the reference control point for a site. The base station is set up over a unique and easily identifiable point (e.g. steel rebar hammered into the ground) as an unknown point and left alone to observe satellite signals. The observation data is post-processed to determine the precise coordinates of the unknown point. That point then becomes the reference point for that site and all future RTK surveys are set up over that point. This is only done once for each site. An RTK rover survey should not be performed during this process. Option 2 is used after the site's reference point has already been established. The base station is set up over the reference point and the precise coordinates of the reference point are inputted to the base station. An RTK rover survey can be performed and all measured points will be relative to the same reference point.

Option 3 is used if a reference control point has not been established for the site but an RTK survey needs to be done immediately. This could occur on-site if an RTK reference point has not been established and weather conditions are ideal for a UAV flight. The concept behind this method is to set up the base station over an unknown point that will become the reference point but define it as a known point. Although the point's coordinates are initially unknown, arbitrary coordinates can be inputted to the base station and the RTK survey is conducted with all points referenced to the arbitrary coordinates. The base station observes satellite tracking data during the RTK survey and after the survey is completed, the precise point of the base station can be determined using the satellite observation data. Using Leica Infinity, the RTK survey data can then be updated to reference the precise base station coordinates instead of the arbitrary coordinates inputted at the start. The coordinates of all the rover measurements undergo the same transformation and will be referenced to the precise base station position. Using Options 1 and 2 in combination is a straight-forward

method to conduct RTK surveys. Option 3 is slightly more complicated. It was tested during TLS Calibration III to ensure it worked and provided correct results.

As discussed in Section 3.2.4, TLS Calibration III was successful. The methods used to set up the base station, perform the RTK survey, and post-process the data (i.e. Option 3) worked as expected. The test provided confidence in the methods that would be used to acquire data on-site.

3.3.2.2 GCP Network Parameters during UAV Calibration II

UAV Calibration II tested the effects of image and GCP parameters on the accuracy UAV image-reconstructed point clouds. The two GCP parameters investigated were the number of GCPs and the observation time at GCPs. The details of the calibration test are discussed thoroughly in Section 3.1.4. The test clearly demonstrated that longer RTK observation times at GCPs contributed to significantly lower uncertainties in the GCP position measurements and subsequently lower errors in the point clouds (Figure 3.8 and Figure 3.9). Although this result was expected, the magnitude of the error reduction was larger than anticipated. Unfortunately, longer observation times comes at a cost. Weather conditions dictate when UAV and TLS operations can be performed on-site, and time is often a critical constraint. The observation times at GCPs during site visits would be maximized to reduce errors, while considering the weather and time constraints presented at the time.

With respect to the number of GCPs, accuracy of the point clouds consistently improved as the number of GCPs was increased to 12. However, increasing from 12 to 14 GCPs did not provide consistent accuracy improvements. Therefore, it was determined that the optimal number of GCPs to use on-site was 12. The survey area for the calibration test was based on the UAV survey area required at KM-82. For the larger high-fill sections like KM-117, more GCPs may be required to provide the level of accuracy measured in UAV Calibration II.

3.4 Summary of Technology Operating Procedures and Calibration Tests

This research used the senseFly albris and DJI Phantom 4 Pro UAVs to acquire aerial imagery and Pix4D for image processing. The FARO Focus^{3D} X 330 laser scanner and FARO SCENE software were used to acquire and process scan data. Several tests were performed with each technology to determine best operating procedures and design surveys for site.

First for the UAVs, a parametric analysis of Pix4D processing options was performed to determine optimal processing parameters that were used throughout the research. Second, a calibration test was performed using the albris UAV and RTK survey system to determine their accuracy of measuring displacement of checkerboards targets. The calibration showed that fine displacements can be measured with the albris when the same GCPs are used in two surveys. Third, another calibration test with the albris was performed to investigate the effects of certain image network and GCP parameters on the accuracy of image-reconstructed point clouds. The calibration test led to a few conclusions that would be used to design on-site UAV surveys: 1) RTK observation time at GCPs was the most effective parameter to reduce errors in point clouds; 2) image GSD alone did not significantly affect point cloud accuracy—low GSD images require longer RTK observation times to achieve accuracy improvements; and 3) the optimal oblique viewing angle for images was 45°.

Once the optimal scanner settings were determined, three TLS calibration tests were performed. The first measured the displacement of six sphere targets. Compared to hand-measurements, the TLS measured displacements with 3D RMS errors less than 3 mm. The second calibration test investigated the standing and viewing angles of checkerboard targets to help design on-site TLS surveys. The third calibration test simulated the on-site survey design to confirm that the scanner could identify targets, register scans together, and produce accurate point clouds.

The Leica GS14 antennas and CS20 controller were the RTK survey system used to measure GCP positions for georeferencing point clouds. During the UAV and TLS calibration tests discussed above, the RTK system calibrations were performed and on-site procedures were determined.

CHAPTER 4: DATA ACQUISITION AND PROCESSING

This section details the methods used to determine the high-fill sections for monitoring; design the on-site surveys for the UAV, TLS, and RTK; acquire and process data for each technology; and determine deformations at the high-fill sections.

4.1 Site Selection

High-fill sections along ITH were selected for monitoring using the plan, elevation, and cross-section construction drawings for the highway (Government of Northwest Territories, 2013). Twelve high-fill sections were originally selected based solely on embankment height, with sections only greater than 6 m selected. The twelve sections were then analyzed considering other factors like length, alignment, symmetry, proximity to bodies of water, and presence of culverts and/or toe berms. Monitoring was restricted to four high-fill sections due to the limited time during site visits (Table 4.1). The research site at KM 82 was guaranteed to be one of the four high-fill sections because the instrumentation displacement data at the site would allow for validation of the UAV and TLS deformations by comparison. KM-82 is a 6 m high, 120 m long, straight section with a toe berm on the east slope to improve stability of the sideslope. The reinforced zone (KM 82+380 to 82+400) and non-reinforced control zone (82+400 to 82+420) are located approximately 10 m north of the culvert.

A high-fill section at KM 117 was selected because it is the thickest section on ITH, standing 12 m high. KM-117 is a 200 m long symmetrical section with a toe berm on both sideslopes, oriented north with a slight curve to the northwest. A large diameter culvert was constructed in the middle of the section to transmit water between two lakes on either side of the highway. The remaining two high-fill sections were selected to be geometrically similar with KM-82 to allow for a more direct comparison of the deformations. These two sections were located at KM 48 and KM 49. These sections were also selected because their proximity to each other allowed for only one RTK base

station to be set up and used at both sections, saving valuable time on-site. KM-48 is an 8 m high, 120 m long section with a toe berm on the west slope, oriented northwest with a slight curve to the north. KM-49 is an 8 m high, 160 m long, straight section with a toe berm on the west slope.

Table 4.1 High-fill section locations, geometries, and characteristics.

Section	Latitude (°)	Longitude (°)	Height (m)	Length (m)	Alignment	Toe Berm Slope
KM-48	68.8047	133.5395	8	120	Curved	West
KM-49	68.8121	133.5516	8	160	Straight	West
KM-82	69.018	133.2684	6	120	Straight	East
KM-117	69.2506	132.9001	12	200	Curved	Both

4.2 Site Visits and Data Acquisition

This research included three site visits to acquire data for deformation monitoring of the ITH high-fill sections. The site visits were completed in August 2017, August 2018, and June 2019. All site visits were during summer because the entire embankment was visible without snow and the UAV, TLS, and RTK systems do not function in sub-zero temperatures.

This section summarizes the data acquired during these site visits. The survey designs for the TLS scans at KM-82 and UAV flights at all four high-fill sections are discussed. Survey parameters for each technology are stated and justifications for the survey designs are provided, with reference to the technology calibration tests when applicable.

4.2.1 UAV Data Acquisition

In 2017, the research team only had the albris UAV on-site. The Phantom had not been purchased yet. During a flight with the albris in 2017, one of the propellers broke and the UAV crashed. Fortunately, the albris crash was covered by insurance and the UAV was replaced before the next site

visit. The crash made the research team aware of the risks of flying UAVs. The Phantom UAV was purchased in response to provide two UAVs on-site in case of another crash. In 2018 and 2019, both the albris and Phantom UAVs were used to acquire imagery of the high-fill sections for deformation monitoring. A newly formed objective in the research was to compare the deformations results from the two UAVs and investigate any differences between using an expensive inspection UAV like the albris and a consumer-level UAV like the Phantom.

UAV missions for the albris and Phantom had certain aspects that were consistent between both, such as the number of GCPs at a high-fill section. However, there were major differences between their flight designs since the albris could fly autonomously on pre-designed missions and the Phantom could not. The albris flights were carefully designed using quantifiable parameters including GSD and image overlap. The Phantom flights were manually controlled and images were captured to cover approximately the same area with similar image overlap as the albris missions.

Table 4.2 summarizes the UAV data that was acquired during the three site visits, including the UAV model, types of flights (e.g. grid, POI, or manual), numbers of GCPs, and other important flight parameters. The following sections will detail the flights from each site visit and provide background information for how and why the data was collected. At larger high-fill sections such as KM-117, multiple UAV flights were required to complete missions due to battery life of the UAVs.

Table 4.2 UAV data acquisition summary.

Year	Section	UAV	Type of flight	No. images	GSD (mm)	No. GCPs	RTK observation time at GCPs (seconds)
2017	KM-82	albris	Grid	90	10	-	-
	KM-117	albris	Grid	140	10	10	30
2018	KM-48	albris	Grid	81	10	10	30
		Phantom	Manual	64	-		
	KM-49	albris	Grid POI	97 18	10	10	30
		Phantom	Manual	209	-		
	KM-82	albris	Grid POI	109 18	10	10	30
		Phantom	Manual	52	-		
	KM-117	albris	Grid	87	10	10	30
2019	KM-48	albris	Grid POI	124 24	8	13	60
		Phantom	Manual	149	-		
	KM-49	albris	Grid POI	148 24	8	13	60
		Phantom	Manual	170	-		
	KM-82	albris	Grid POI	119 24	8	13	60
		Phantom	Manual	220	-		
	KM-117	albris	Grid POI	145 24	8	14	60

4.2.1.1 2017 UAV Data Acquisition

The albris was used to acquire aerial imagery of KM-82 and KM-117 in 2017. The albris crashed during a flight at KM-117, preventing imagery from KM-48 and KM-49 from being acquired. Only grid flights were conducted in 2017 because the benefits of including oblique imagery (e.g. through POI flights) for reducing reconstruction errors had not been discovered or investigated yet. The albris missions were designed to have an image overlap of 75% in both directions—longitudinal and lateral with the UAVs flight path. This satisfied the minimum overlap criteria recommended by James and Robson (2012) and Pix4D (2019). The GSD for the flights was 10 mm, corresponding to a flight height of approximately 57 m. Other UAV deformation studies (Tonkin & Midgley, 2016; James et al., 2017; van der Sluijs et al., 2018) reported that the vertical LoD can be estimated as 3x GSD, based on the vertical RMS error of GCPs. Using this approach, the LoD using a GSD of 10 mm was estimated to be 30 mm. This LoD seemed appropriate for the predicted deformation of the high-fill sections.

Due to late delivery of the shipment containing checkerboards, the flight at KM-82 was performed without GCPs. This lack of GCPs would cause errors in the reconstructed point clouds and challenges during deformation measurement between point clouds. Ten checkerboards GCPs were used at KM-117; however, incorrect set up of the RTK base station caused inaccurate GCP measurements. This also led to challenges when comparing the 2017 point clouds.

4.2.1.2 2018 UAV Data Acquisition

In 2018, both the albris and Phantom were used to acquire aerial imagery of KM-48, KM-49, and KM-82. Only the albris was used at KM-117 due to time constraints the day that section was visited. Using the albris, grid missions were conducted at all high-sections and POI missions were only conducted at KM-49 and KM-82 due to time constraints. Grid missions acquired imagery with an image overlap of 75% (both directions) and a GSD of 10 mm. POI missions acquired 18 oblique images oriented to the centre of the high-fill section, equally spaced at 20° intervals and at 45° viewing angles to the ground surface. 45° was the optimal oblique viewing angle determined in UAV Calibration II. The

Phantom was flown manually and aerial imagery was captured at manual locations (Figure 4.1). The pilot attempted to capture aerial imagery in tracks parallel to the embankment. 10 checkerboard GCPs were used at each high-fill section. Examples of the planned layouts of GCPs are provided in Figure 4.2.

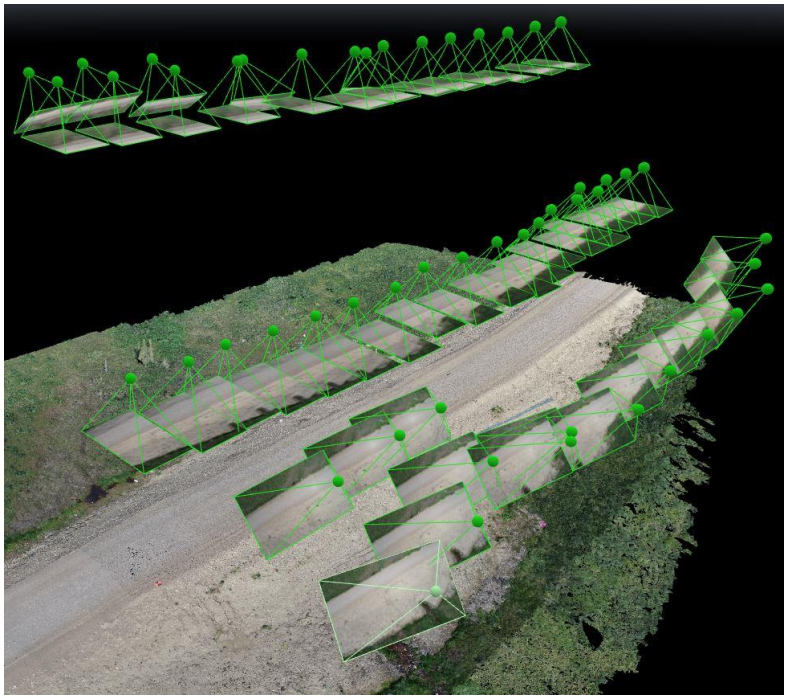

Figure 4.1 Aerial images captured by the Phantom at KM-82 in 2018; shown in Pix4D with green spheres identifying the images' calibrated positions.

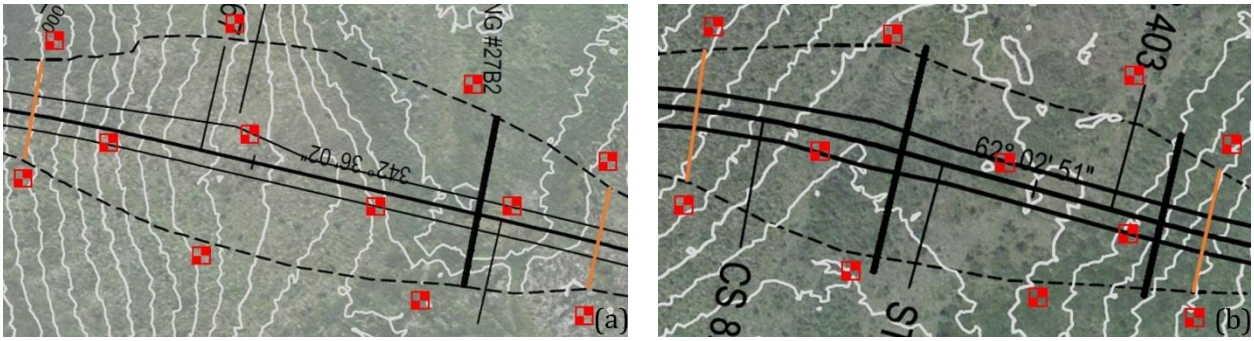

Figure 4.2 Examples of planned checkerboard GCP layouts for UAV surveys: a) KM-49; b) KM-82.

4.2.1.3 2019 UAV Data Acquisition

Again in 2019, both UAVs were used to acquire aerial imagery of KM-48, KM-49, and KM-82. Only the albris was used at KM-117 because the Phantom was not used at that section the previous year. Grid and POI missions were completed at all high-fill sections. Grid missions acquired imagery with an image overlap of 75% (both directions) and a GSD of 8 mm. POI missions acquired 24 oblique images oriented to the centre of each high-fill section, equally spaced at 15° intervals and at 45° viewing angles to the ground surface. The Phantom was flown manually and aerial imagery was captured at manual locations in tracks parallel to the embankment (Figure 4.3). The pilot attempted to capture approximately the same number of images with the Phantom as the albris for each high-fill section. More images were taken in 2019 than 2018 to improve accuracy of the reconstructed point cloud (Figure 4.1 and Figure 4.3). Either 13 or 14 checkerboard GCPs were used at each high-fill section (Table 4.2).

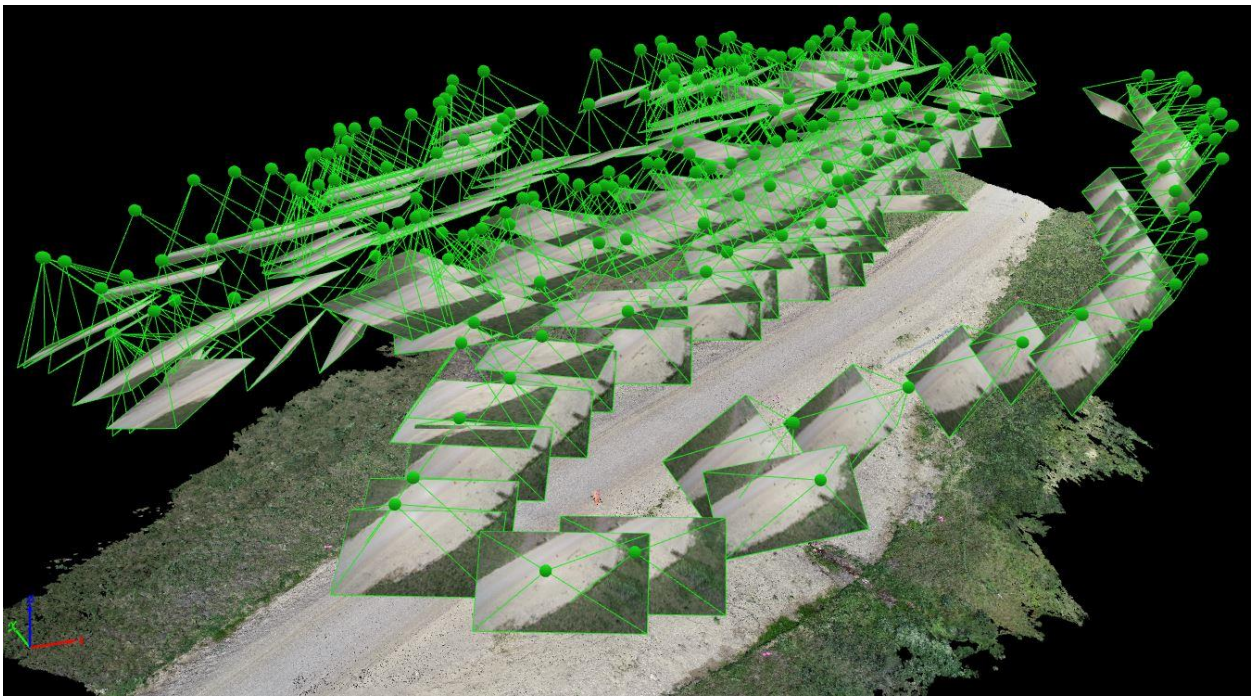

Figure 4.3 Aerial images captured by the Phantom at KM-82 in 2019; shown in Pix4D with green spheres identifying the images' calibrated positions.

4.2.2 TLS Data Acquisition

The Focus^{3D} scanner was used to scan the embankment at KM-82 in 2018 and 2019. Only KM-82 was scanned due to limited time on-site and the time-intensive nature of TLS surveys. KM-82 allowed for comparison of the deformations measured by TLS, UAV photogrammetry, and embankment internal instrumentation. TLS surveys were designed according to two basic principles. Firstly, the maximum viewing angle from a scanner to a checkerboard target was 45°. This ensured proper identification and marking of targets during post-processing. Secondly, the scanner was set up to cover 100% of the embankment section within a 45° viewing angle of five scans—three along the toe and two at the shoulder. This ensured a densely reconstructed point cloud across the entire high-fill section. Specific distances and angles of the scanner and targets were tested and validated in the TLS calibration tests (Section 3.2).

The TLS surveys conducted at KM-82 are summarized in Table 4.3 and the survey designs are shown in Figure 4.4. Five scans were used to survey each sideslope in 2018 and 2019. The approximate locations of the scanner were consistent in both years. All checkerboard targets were set up on the checkerboard stands (Section 3.2.3) to facilitate RTK measurement. The 2018 scans used three sphere targets and nine checkerboards for each slope, with RTK observation times of 30 seconds at checkerboard centres. None of the targets remained in the same position for scans of both sideslopes. Therefore, the two slopes could not be registered together. To correct this in 2019, six targets (two spheres and four checkerboards) were set up along the road surface and scanned for both sideslopes as shown in the photo taken from the UAV (Figure 4.4). All six spheres were brought to site and used for surveys of each sideslope in 2019, in addition to 10 checkerboards. The RTK observation time was also increased to 60 seconds at each GCP to reduce positional measurement errors. The *Outdoor 20m…* profile (Table 3.8) on the Focus^{3D} scanner was used for all scans in both years.

Table 4.3 TLS data acquisition summary.

Year	Slope	No. scans	No. targets		RTK observation time at GCPs (seconds)
			Spheres	Checkerboards	
2018	East	5	3	9	30
	West	5	3	9	30
2019	East	5	6	10	60
	West	5	6	10	60

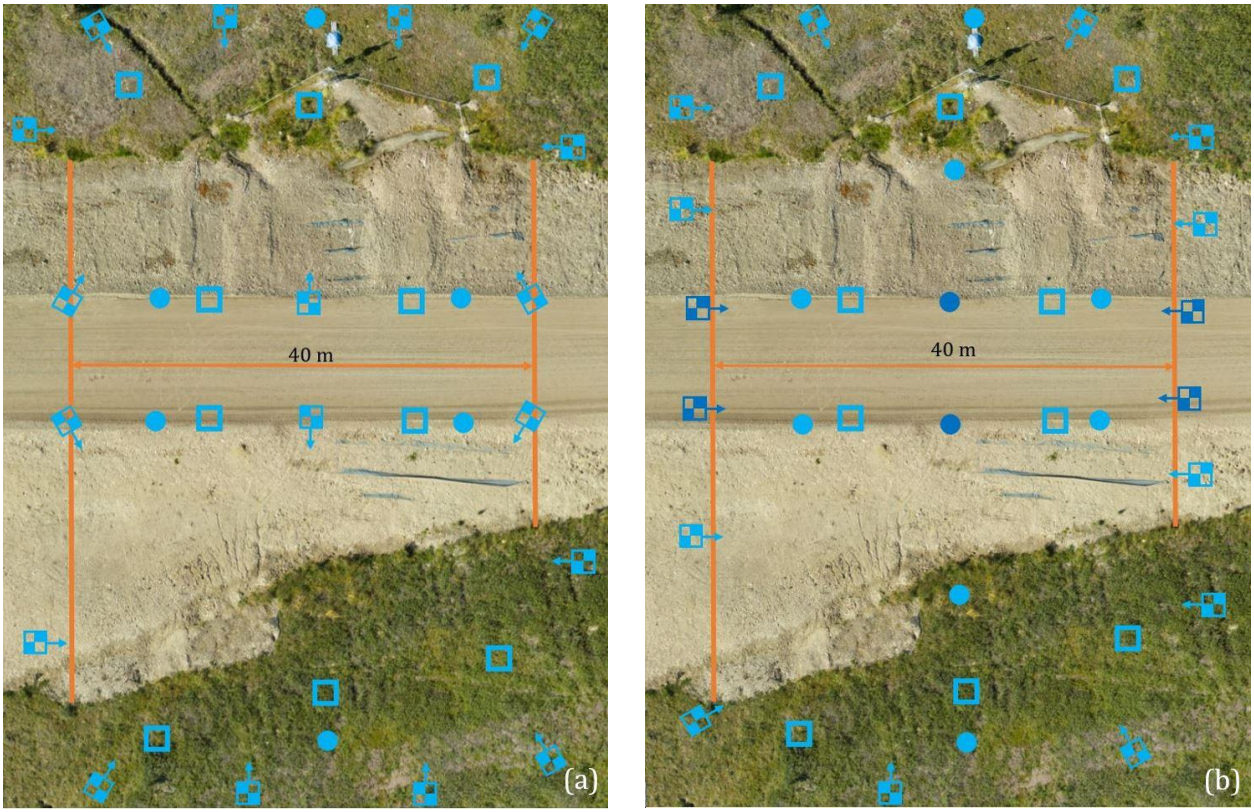

Figure 4.4 TLS survey plans at KM-82 showing scanner locations (squares) and sphere and checkerboard targets: a) 2018; b) 2019. Dark blue targets in 2019 remained for scans of both slopes.

4.3 Data Processing

This section describes the methods used to process the data acquired with the RTK, UAV, and TLS. The analysis of the data quality and associated errors is presented.

4.3.1 RTK GCP Processing

A 1 m steel rod was hammered deep into the permafrost at each high-fill section in 2018. The steel rods were the benchmark locations for all RTK surveys at that section. The RTK base station was set up directly above the steel rod and left alone to geolocate its position for 5–8 hours (Option 1 in Section 3.3.2.1). The raw satellite observation data from each base station were converted from the M00 file to a RINEX file using Leica Infinity. The RINEX file, which contained all base station observation data, was uploaded to Natural Resources Canada (NRCan) Canadian Spatial Reference System Precise Point Positioning (CSRS-PPP). CSRS-PPP is an online application for GNSS data post-processing that allows users to compute higher-accuracy positions from raw satellite observation data (Natural Resources Canada, 2019). The website requires RTK observation data to be in the RINEX format. CSRS-PPP outputs a report that includes the precise coordinates of the base station setup. This process was done for the benchmark at each high-fill section. For all future RTK surveys, the base station was set up directly above the section's benchmark and the CSRS-PPP coordinates were inputted as the reference coordinates.

UAV Calibration II demonstrated the significant impact of RTK observation times at GCPs on the accuracy of UAV image-reconstructed point clouds. The positional uncertainties from GCP surveys on-site were analyzed (Table 4.4 and Figure 4.5) to understand the impact of the RTK survey accuracy on the total errors developed in the reconstructions. For sections where albris and Phantom flights were conducted, the same GCP network and corresponding RTK data was used.

The RTK uncertainties clearly indicate there was an issue with the 2017 survey at KM-117. Vertical uncertainties were approximately 2x horizontal uncertainties throughout all surveys (Table 4.4). The results also show there was a consistent decrease in RTK uncertainty from 2018 to 2019.

This was due to increasing the observation time at each GCP from 30 to 60 seconds. Increasing observation time at GCPs caused the mean and deviation of RTK uncertainties to decrease (Figure 4.5). The only outlier to this observation was the 2019 TLS survey. It is unclear what caused the higher uncertainties in that survey compared to other surveys in 2019; however, it could be partly caused by human error holding the RTK rover stable at the centre of the checkerboards. It is more difficult to stabilize the RTK rover on the checkerboards when they are set up on the stands for TLS surveys compared to when they are laying horizontally on the ground for UAV surveys.

Table 4.4 Horizontal, vertical, and 3D uncertainties for the RTK surveys of GCPs on-site.

Year	Survey	Horizontal RMS uncertainty (mm)	Vertical RMS uncertainty (mm)	3D RMS uncertainty (mm)
2017	KM-82 UAV	-	-	-
	KM-117 UAV	13.5	30.0	32.9
2018	KM-48 UAV	6.9	13.0	14.6
	KM-49 UAV	6.4	11.4	13.1
	KM-82 UAV	6.0	11.4	12.8
	KM-82 TLS	7.1	11.5	13.5
	KM-117 UAV	6.0	11.7	13.1
2019	KM-48 UAV	3.9	8.0	8.8
	KM-49 UAV	4.0	6.8	7.6
	KM-82 UAV	3.3	6.0	6.7
	KM-82 TLS	4.2	10.4	11.2
	KM-117 UAV	3.3	7.2	8.0

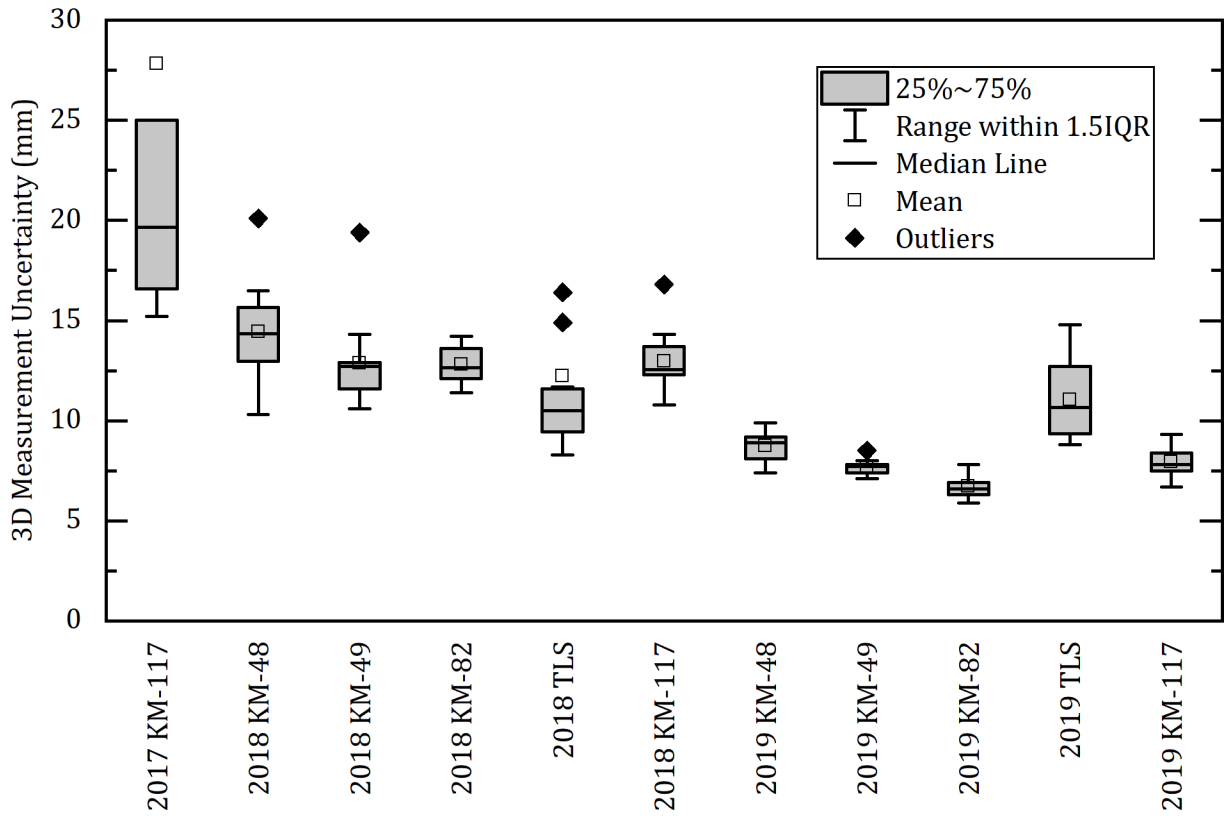

Figure 4.5 Box plot of the RTK survey 3D uncertainties at GCPs.

4.3.2 UAV Processing

UAV imagery and data were processed in Pix4D using the procedure and standard processing parameters (Table 3.2) outlined in Section 3.1.2. Prior to uploading image files to Pix4D, albris images were converted from their raw image format (DNG) to JPG image files using eMotion 3. Pix4D cannot process DNG files and requires images to be JPG files. DJI imagery is saved as JPG files and therefore does not need to be converted before uploading to Pix4D. After a Pix4D project is created and images uploaded, initial processing was performed to generate a sparse (non-georeferenced) point cloud. GCP data was uploaded to the Pix4D project as a CSV file. All GCP data from site was referenced to the NAD83 (CSRS) UTM Zone 8N coordinate system. GCPs were then marked in Pix4D a minimum of six times to ensure accurate marking of the checkerboard centre. For albris projects with nadir images (i.e. from grid missions) and oblique images (i.e. from POI missions), GCPs were carefully

marked in both kinds of imagery to ensure the reconstruction was georeferenced based on both orientations. Once images were marked, the project was reprocessed to produce a georeferenced sparse point cloud. The final processing step in Pix4D was densification of the sparse point cloud using the optimal processing parameters (Table 3.2). The final dense point cloud for each UAV survey was exported from Pix4D to other software for the deformation analysis.

4.3.2.1 UAV Image-Reconstructed Point Cloud Accuracy

For deformation monitoring between successive point clouds, it is important to understand the accuracy of each point cloud. The accuracy of the UAV image-reconstructed point clouds at high-fill sections was quantified by classifying GCPs as checkpoints and analyzing the checkpoint errors after reprocessing. The same process was used in UAV Calibration II to estimate the accuracies of point clouds in that test. In Pix4D, checkpoints are not included in the bundle adjustment and therefore the point cloud geometry is not influenced by checkpoint positions. For each high-fill section point cloud, one of the GCPs was classified as a checkpoint and the Pix4D project was reprocessed. Positional errors at the checkpoint were measured by comparing the computed checkpoint coordinates to its known reference coordinates. Checkpoint errors were recorded, and the process was repeated for all GCPs in that project. The checkpoint errors for each project were analyzed to estimate the overall errors in the entire point cloud.

This approach to estimate point cloud accuracy using checkpoints is performed on the sparse point cloud (i.e. before densification). Although the dense point cloud positional errors are not directly studied, analyzing checkpoint errors in the sparse point cloud is a valid approach to estimate the accuracy of a dense point cloud because the position of a GCP in the point cloud does not change as the dense reconstruction algorithms are performed. Therefore, the errors at checkpoints and estimated accuracy of the dense point cloud are equivalent to those of the sparse point cloud measured with this approach.

The accuracy of all UAV image-reconstructed point clouds at the high-fill sections was quantified using the checkpoint errors approach. The results of each point cloud were compared (Table 4.5 and Figure 4.6) to better understand the variance of errors and gain insights on the factors contributing to point cloud accuracy. The full datasets from the checkpoint error analyses are provided in Appendix A.

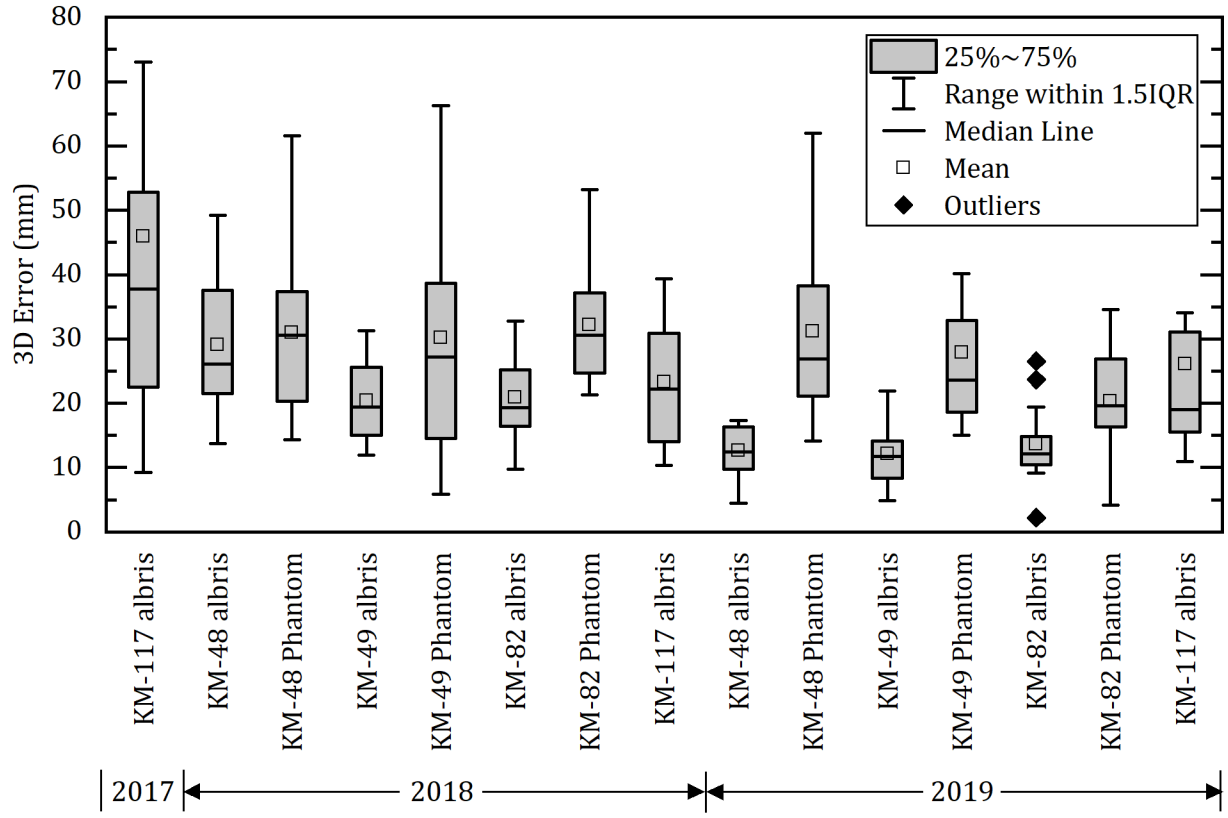

Figure 4.6 Box plot of the SfM-processed 3D errors at checkpoints for UAV surveys on-site.

Table 4.5 SfM-processed horizontal, vertical, and 3D errors at checkpoints for UAV surveys on-site.

Year	Section	UAV	Horizontal RMS error (mm)	Vertical RMS error (mm)	3D RMS error (mm)
2017	KM-82	albris	-	-	-
	KM-117	albris	18.6	55.1	58.1
2018	KM-48	albris	17.2	26.1	31.3
		Phantom	31.1	13.1	33.7
	KM-49	albris	16.1	14.0	21.3
		Phantom	32.9	12.3	35.1
	KM-82	albris	17.1	13.7	21.9
		Phantom	27.8	18.7	33.5
	KM-117	albris	12.6	22.0	25.3
2019	KM-48	albris	6.2	11.7	13.2
		Phantom	26.2	21.3	33.8
	KM-49	albris	6.6	11.4	13.1
		Phantom	25.7	15.6	30.1
	KM-82	albris	6.5	13.5	15.0
		Phantom	17.9	13.5	22.4
	KM-117	albris	11.7	28.4	30.7

Analyzing the horizontal and vertical RMS errors (Table 4.5) reveals an interesting observation: the vertical and horizontal errors are approximately equivalent in the full dataset of checkpoint errors. Vertical RMS errors were larger than the horizontal RMS errors in half of the point clouds, and vice-versa. This is unlike the RTK uncertainties where the vertical uncertainties were consistently

greater than the horizontal uncertainties. The large vertical RTK uncertainties were expected to cause the checkpoint errors to be larger vertically than horizontally, but this was not the case.

The 2017 point cloud errors at KM-117 were significantly larger than any other UAV survey due to the high-uncertainty RTK survey at that site. Low-accuracy GCP measurements cause hard adjustments in the SfM bundle adjustment to force the point cloud geometry to account for the GCP data. When a GCP is assigned as a checkpoint, the bundle adjustment is not forced to compensate for its position, leading to large checkpoint errors between its computed position and measured (inaccurate) RTK position. From 2018 to 2019, there was a remarkable decrease in errors for the albris point clouds (Figure 4.6). This improvement in point cloud accuracy was a combined effect of the reduced GSD from 10 mm to 8 mm and the increased RTK observation time from 30 seconds to 60 seconds. The decrease in errors for the Phantom point clouds was notable; however, much less significant than the albris point clouds.

Comparing albris and Phantom point cloud errors, particularly in 2019, showed a major difference in their errors. This is interesting because the albris and Phantom point clouds at each section used the same GCP data. The differences in processing that contributed to the error discrepancy were the quality of images (38 Mp albris vs. 20 Mp Phantom) and the image network (grid with POI albris vs. manual Phantom). It is unclear which factor contributed more to the error discrepancy. An interesting experiment would be to fly the albris and Phantom on identical missions and acquire images at the same positions, and then compare the errors in the reconstructed point clouds. This would eliminate the image network factor and allow the difference image quality to be studied directly. Unfortunately, a third-party flight-planning software was not used for the Phantom and this comparison could not be made.

Overall, the techniques implemented in 2019 to improve the accuracy of UAV image-reconstructed point clouds were successful. If more time was available on-site, more improvements

would have been implemented such as even longer RTK observation times at GCPs (e.g. 3 minutes) and a further reduced GSD (e.g. 5 mm).

4.3.3 TLS Processing

KM-82 was the only high-fill section where TLS was conducted. Separate point clouds were generated for the east and west slopes in 2018 because there were no consistent targets for scans of both slopes. Scans of both sideslopes were registered together in 2019 to produce one point cloud. TLS data was processed in SCENE using the general workflow as described in Section 3.2.1. After the scans were preprocessed, targets marked, and GCP data imported, the crucial stage of registration and georeferencing began. Unlike the beginning steps of the TLS processing, registration and georeferencing in SCENE was not straight-forward and required a few creative workarounds. A method was implemented that used cloud-to-cloud (C2C) and target-based (TB) registrations consecutively to register scans and produce an optimal point cloud with minimal errors.

In SCENE, the only method to georeference a point cloud with GCP data is by performing a TB registration (FARO Technologies Inc., 2016). During TB registration, point cloud geometry is determined by identifying matching targets in different scans and minimizing the overall error between matched targets. In SCENE, a target that is matched between two scans is called a correspondence. If GCP data is available during a TB registration, correspondences are created between GCP positions and marked checkerboard targets. The georeferencing error for a target correspondence can be determined as the difference between the imported GCP position and computed target position. There can be multiple georeferencing errors for a certain target if there are multiple correspondences between the imported GCP position and marked targets in various scans. The scan point errors, which are the differences in point cloud positions between scans, can also be outputted from a TB registration. To define the scan point errors, two metrics are used: mean error and percentage of points with errors less than 4 mm.

TB registration was initially used to register scans. This ensured GCP data was used to georeference the point cloud to a common coordinate system for deformation measurement. However, TB registration was producing point clouds with large errors; target mean errors ranged from 12 to 18 mm and scan point mean errors ranged from 10 to 12 mm. These were significantly larger than the reported millimetre-scale accuracy of many TLS systems (Abellan et al., 2014; FARO Technologies Inc., 2015). This led to the use of C2C registration.

C2C registrations were producing point clouds with scan point errors of approximately 5 mm—a major improvement from TB registration. Three parameters can be modified for a C2C registration in SCENE: subsampling point distance, maximum number of iterations, and maximum search distance. A simple parametric analysis was performed to study the affect of the three parameters on the scan point errors. Minimizing subsampling point distance to 0.01 m reduced errors but increased computation time. Increasing the maximum number of iterations also reduced errors and increased computation time; however, the error reduction plateaued around 100 iterations. Maximum search distance did not significantly affect the results, so the default value was used. Therefore, the optimal C2C registration parameters used were as follows: average subsampling point distance of 0.01 m; maximum number of iterations of 100; and maximum search distance of 10 m. The objective of the C2C registrations was to minimize scan point errors, and target errors were not considered. Table 4.6 provides summary error statistics of the final C2C registrations of each TLS survey.

The C2C registrations were not influenced by target positions, and the resulting target errors in those registrations were extremely large (e.g. > 40 mm). After the final C2C registration for a cluster of scans, the cluster was locked to prevent the point cloud geometry from changing. The locked cluster of scans was then registered again, this time using TB registration. The idea was to maintain the high scan point accuracy from C2C registration while allowing the point cloud to be georeferenced from TB registration. The approach worked and produced a georeferenced point cloud; however, target errors after georeferencing were significantly larger than scan point errors.

Target errors means and deviations ranged from 20 to 25 mm and 7 to 8 mm. An important conclusion can be taken from this observation: the relatively large errors in the TLS point clouds is caused by RTK uncertainties and inaccuracy of GCP measurements, not the TLS system or survey setup. This finding will be further discussed in Section 5.

To address the large target errors, target correspondences with the largest errors were deleted. The point cloud started with all correspondences from the TB registration and correspondences were methodically deleted one-by-one based on error. Each time a correspondence was deleted, the point cloud was re-registered and the target errors were recorded. The correspondences were also checked each time to ensure that every target had at least one correspondence. This ensured that errors did not develop in areas of the point cloud where GCPs were missing. If a target was found to have zero correspondences, the process was reversed to a re-registration with all targets corresponding and then proceeded forward following a different path of deleting correspondences. The individual correspondence errors for each re-registration were analyzed, and the optimal point cloud for each TLS survey was determined as the registration with the lowest target correspondence RMS error. The TB registration errors for the final point cloud of each TLS survey are provided in Table 4.6. These point clouds were then exported from SCENE for the deformation analysis.

Table 4.6 TLS point cloud registration errors.

Survey	Scan point errors		Target errors		
	Mean (mm)	**< 4 mm (%)**	**Mean (mm)**	**Std. dev. (mm)**	**RMS (mm)**
2018 East	4.1	50.0	15.7	6.0	16.7
2018 West	3.0	62.7	13.6	7.1	15.3
2019	5.2	41.6	16.6	6.5	17.8

4.4 Deformation Analysis

The deformation analysis covers the comparison of UAV and TLS point clouds over the three-year monitoring period. All point cloud comparisons and related analyses to determine deformations of the high-fill sections were completed in the open-source software CloudCompare (CloudCompare, 2019). CloudCompare is a 3D point cloud and mesh processing software that includes several deformation measurement algorithms. The software is commonly used by researchers in the change detection and deformation monitoring fields of science and engineering. The CloudCompare analysis is separated into three sections: point cloud registration, point cloud comparison, and cross-section analysis.

4.4.1 Point Cloud Registration

Registration of the 2017 and 2018 point clouds was required because the 2017 point clouds at both high-fill sections had georeferencing issues (see Section 4.2.1.1). At KM-82, the albris flights were performed without GCPs. At KM-117, the RTK base station was not properly set up and the rover survey of GCPs was inaccurate. For both sections, the 2017 point cloud was aligned to the 2018 point cloud because the 2018 point clouds were more accurate. In situations where there are stable areas of a point cloud that are not deforming and unstable areas that are (e.g. rockfall monitoring), unstable areas can be temporarily removed and the point clouds can be registered based on the stable areas (Gruen & Acka, 2005; Meeks et al., 2017). For the high-fill sections along ITH, no areas were certainly stable due to possible settlement and slope movements, which added a source of uncertainty to the registration process.

Point clouds were registered using iterative closest point (ICP) in CloudCompare. ICP is a least squares matching algorithm that adjusts the transformation (translation and rotation) of the aligned point cloud to the reference point cloud, minimizing the total distance between the point clouds in each iteration. A few parameters needed to be defined before executing ICP: target RMS difference, point cloud overlap, random sampling limit, translation directions, and rotation axes. The default

RMS difference is $1x10^{-5}$. An RMS difference of $1x10^{-9}$ was selected to ensure a fine registration. Point cloud overlap was set to 100% because the point clouds were aligned based on identical segments (discussed below). Random sampling limit is the number of points used to calculate the RMS difference, and the default value is 50,000 points. A random sampling limit of 5,000,000 points was selected, corresponding to approximately 20–50% of the aligned point cloud segments. Translation in all directions and rotation around all axes was allowed.

The following procedure was used for registration at the high-fill sections. First, was a rough manual registration of the point clouds because ICP requires both point clouds to be roughly aligned. Manual registration was performed by translating the 2017 point cloud (no rotation) and aligning the culverts. Culverts were selected for alignment because they were thought to be relatively stable structures, with distinct and unique features, and located near the middle of the point cloud. Following rough registration, the second step was to isolate matching segments of each point cloud for the fine registration. Segments were selected to be within the area encompassed by GCPs in the two point clouds being aligned. This ensured that doming errors, which developed outside the GCP coverage area, did not influence registration. For the KM-82 2017–2018 registration, the selected segments (Figure 4.7a) were based only on the 2018 GCP layout because there were no GCPs in 2017. At KM-117, GCPs in 2018 were clustered near the middle of the section. Therefore, the KM-117 segment for registration was based on the 2018 GCP survey (Figure 4.7b).

Figure 4.7 Fine registration segment areas for UAV point clouds: a) KM-82; b) KM-117.

The third step was fine registration of the point cloud segments using ICP. 2018 point cloud segments were used as the reference and 2017 point cloud segments were aligned. The fourth and final step was to copy the transformation of the 2017 point cloud segment and apply it to the full 2017 point cloud. This method allowed for the full point clouds to be aligned based on the most accurate sections of the point clouds (i.e. the areas within GCP coverage). However, one disadvantage of this method is that if there is poor GCP coverage such as at KM-117 in 2018, the point clouds are registered only using a small portion of the point cloud. If the 2018 GCPs were spread out and encompassed the entire high-fill section, the whole section could have been used for registration. Registration of the 2018 and 2019 point clouds was not required initially because base station benchmarks were established at each high-fill section and all point clouds (both UAV and TLS) were georeferenced using the benchmarks.

4.4.2 M3C2 Point Cloud Comparison and Parameter Selection

Reconstructed point clouds were compared using M3C2 (Lague et al., 2013). The method operates directly on point clouds without meshing or gridding, computes deformation along the normal surface direction, and estimates an LoD for each distance measurement based on local point cloud roughness and registration error. The main parameters required for M3C2 comparisons are core point spacing (*s*), normal scale diameter (*D*), projection scale diameter (*d*), and point cloud registration error (*reg*).

Core points are a sub-sampled version of the reference point cloud to speed up calculations. Using the entire reference point cloud for distance calculations would be cumbersome and inefficient. Core point spacing defines the distance between points of the sub-sampled reference point cloud. For each core point, a normal vector is determined by fitting a plane to the neighbouring points that are within a radius of *D/2* from the core point. The standard deviation of the distances between the neighbours and the best-fit normal plane is recorded and used as a measure of the point cloud roughness (σ_D). The normal plane can be estimated based on the reference cloud, compared cloud, or an average of both. The normal of the reference point cloud is generally used because deformation of the compared cloud depends on the baseline geometry of the reference cloud. The reference cloud was used for all normal vector calculations in this research.

For each core point, a cylinder with a radius of *d/2* and axis through the core point oriented along the surface normal is defined. Using the points from each point cloud that intercept the cylinder, the average position of each point cloud along the normal direction (i_1 and i_2) is determined. The local distance between the two clouds is calculated as the distance between i_1 and i_2. The standard deviation of the intercepting point positions provides an estimate of local point cloud roughness (σ_{d1} and σ_{d2}). An LoD is calculated for each core point using for following equation:

$$LoD = \pm 1.96\left(\sqrt{\frac{{\sigma_{d1}}^2}{n_1} + \frac{{\sigma_{d2}}^2}{n_2}} + reg\right) \tag{3.3}$$

n_1 and n_2 are the number of points from each point cloud intercepting the projection cylinder used to calculate the local roughness. *reg* is assumed isotropic and spatially uniform. ±1.96 is the normal distribution Z value for the 95% confidence interval, which is most commonly used in earth science change detection applications (Wheaton et al., 2010). The LoD equation indirectly accounts for reconstruction and georeferencing errors through *reg*. For example, if there was poor registration between scans for TLS or a low number of images for UAV photogrammetry, *reg* would increase and translate to a higher LoD.

Selecting appropriate parameters was a critical stage of the deformation analysis. Lague et al. (2013) provided some guidance on this process. Core point spacing does not impact the magnitude of computed distances, only the processing time and visualization of results. Lague et al. (2013) used an *s* of approximately 10x the reference point cloud spacing. A very fine spacing of 10 mm was attempted but it resulted in the program crashing. A spacing of 25 mm was selected. *D* is an important parameter to properly define because it affects the normal vector and all distance measurements. *D* should be selected large enough to not be affected by surface roughness because rough surfaces can dramatically vary the normal direction for small *D* values. M3C2 also allows for a range of *D* values to be defined and the *D* with the most planar surface is used to define the normal direction. A uniform *D* is faster but results in lower accuracy. As a rule of thumb, *D* should be at least 20x (25x ideally) larger than the roughness σ_D. *d* should be set so that the subset sizes, n_1 and n_2, are both greater than 4 and ideally greater than 30. There should also be a large degree of overlap between core point projection scales. Therefore, *s* and *d* must be coordinated.

Trial M3C2 comparison were performed as a parametric study to investigate the effects of changing *D* and *d*. σ_D values the high-fill embankments were recorded for varying *D* values. σ_D ranged from 0.015 to 0.025 m. Based on these values, *D* should be ideally set to at least 0.375–0.625 m. *D* was selected to range from 0.5 to 1.0 m at increments of 0.1 m (e.g. 0.5, 0.6, 0.7, 0.8, 0.9, 1.0 m). The numbers of neighbours surrounding each point were then measured for varying *d* values. To meet

the recommendation of having each point with more than 30 neighbours, the optimal *d* ranged from 0.1 to 0.2 m. A *d* value of 0.2 m to ensure the value was applicable to all high-fill sections. The same *D*, *d*, and *s* values were used for M3C2 comparisons at all high-fill sections for consistency. For comparison, Barnhart and Crosby (2013) used 0.3 m for *D* and 0.5 m for *d*. The parameters selected are within the same range.

Table 4.7 M3C2 parameters.

Normal scale diameter *D* (m)	**Projection scale diameter *d* (m)**	**Core point spacing *s* (m)**	**Point cloud registration error *reg* (m)**
Most planar of [0.5, 0.6, 0.7, 0.8, 0.9, 1.0]	0.2	0.025	Varies

reg was determined uniquely for each M3C2 comparison (Table 4.8) using the GCP errors of the point clouds being compared, UAV (Table 4.5 or Appendix A) or TLS (Table 4.6 or Appendix A). Three methods of determining *reg* were investigated. Method 1 determined the standard deviation of 3D GCP errors for each point cloud and calculated the root sum square (RSS) of the standard deviations. This method was used by Wheaton et al. (2010) for DoD comparisons. It lacks merit because it only considers deviation around the mean error and not the magnitude of the mean error itself. Method 2 built on the deficiencies of Method 1 and considered RMS errors instead of standard deviations. This method determined the RMS of 3D GCP errors for each point cloud and calculated the RSS of the RMS errors. Method 3 considered all GCP errors from both point clouds as one dataset and calculated the combined RMS of 3D GCP errors. Lague et al. (2013) used an approach similar to Method 3. Method 1 resulted in the lowest estimates of *reg*, followed by Method 2, then Method 3. For example, the M3C2 comparison of 2018 and 2019 TLS point clouds resulted in *reg* values of 9 mm, 17 mm, and 24 mm for Methods 1, 2, and 3, respectively. Method 2 was ultimately used for the M3C2 comparisons

in this research because it results in a lower *reg* and therefore lower LoD than Method 3. Method 2 also has validity because it was used by the developer of the M3C2 algorithm.

Table 4.8 Registration errors (*reg* values) for M3C2 comparisons.

Section	Technology	*reg* (mm)	
		2017-2018	2018-2019
KM-48	albris	-	23
	Phantom	-	34
KM-49	albris	-	17
	Phantom	-	32
KM-82	albris	22	18
	Phantom	-	28
	TLS	-	17
KM-117	albris	45	29

4.4.3 Cross-Section Analysis

A cross-section analysis was performed at each high-fill section to provide a clear visual of the deformation at embankment sections of interest. Volume change estimates were not performed because the volumes of material deforming at the high-fill sections were too small to accurately detect. There were also no clear zones of soil loss and gain; opposite to a landslide with clear zones of material loss and deposition, where volume change estimates are commonly used. Feature tracking was not used because the visually uniform fill material made it challenging to identify features. There was also construction work at the sections such as gravel resurfacing and human traffic during site visits, which may have displaced features of interest and influenced the feature tracking analysis.

Cross-sections were extracted only from the albris point clouds because TLS point clouds were only at KM-82 and Phantom point clouds were less accurate than the albris point clouds. One cross-section was analyzed at each high-fill section, except for KM-82 where two cross-sections were analyzed. All cross-sections were oriented perpendicular to the highway alignment. The two cross-sections at KM-82 were selected to align with the SAAs in the reinforced and control zones. This allowed the UAV and TLS deformations to be compared with the SAA deformation data. The cross-section at KM-48 was located approximately 7 m north of the culvert at the thickest part of the embankment. The cross-section at KM-49 was located approximately 65 m (roughly 1/3 of the total sections length) from the north extent of the high-fill section. This cross-section was selected instead of the high-fill section's midpoint because the 2018 GCPs were clustered in the north of the section and cross-sections outside the GCP coverage would be influenced by doming errors. The cross-section at KM-117 was located approximately 20 m south of the culvert where the embankment was approximately 10 m thick.

Cross-sections were cut from the point clouds using the Cross Section tool in CloudCompare. The tool works by defining a box with specified dimensions, location, and orientation, then extracting all points from a selected point cloud that are within the box. The box height was defined to cover the entire high-fill section. The box length was defined to be slightly outside the embankment toe to capture embankment deformations and toe subsidence if present. The box thickness was set to 10 mm. If there were multiple points within the 10 mm thickness at any point in the cross-section, all points were extracted. At each high-fill section, the same box dimensions were used for point clouds from all years. Point clouds were extracted as CSV files and further analysis was done in Microsoft Excel. A common starting point was selected for each high-fill section and the horizontal distance from the starting point was calculated for all points in each cross-section using the following equation:

$$Distance = \sqrt{(X_i - X_o)^2 + (Y_i - Y_o)^2} \tag{3.4}$$

where X_i and Y_i are the X and Y coordinates for any given point and X_0 and Y_0 are the X and Y coordinates for the starting point. Distance vs. elevation was then plotted for each cross-section.

Deformations were not visible on the original cross-section comparisons because of the extremely small-scale deformations relative to the embankments. For example, if a 6 m high embankment settled 60 mm vertically, the 1% deformation to height was not visible (Figure 5.20). To address this issue and allow deformations to be visualized, vertical differences between the compared cross-sections were exaggerated 10x. For all cross-section comparisons, the 2018 cross-section remained at its measured elevation and the 2017 or 2019 cross-sections were vertically exaggerated.

There was significant point-to-point elevation variability in the cross-sections (Figure 5.21). Three factors contributed to this: 1) roughness of the embankment fill material; 2) imprecise image reconstruction of the slope surface; and 3) the 10 mm thick cross-section box extracted multiple points at a certain distance with varying elevations. To reduce variability, a series of moving average calculations was performed on the elevation data for each cross-section. This resulted in smoother cross-section plots that were easier to interpret (Figure 5.22).

4.5 Summary of Data Acquisition and Processing

Four high-fill sections along ITH were monitored. KM-48 and KM-49 were surveyed by the albris and Phantom in 2018 and 2019. KM-82 was surveyed only by the albris in 2017, then by the albris, Phantom, and TLS in 2018 and 2019. KM-117 was only surveyed by the albris in all three years. GCP measurements were not accurate in 2017. In 2018, benchmarks were established at each section for RTK surveys. The average 3D RMS uncertainties of the RTK surveys decreased from 33 mm in 2017 to 13 mm in 2018 and 8 mm in 2019. The decrease in RTK measurement uncertainties year-to-year occurred primarily because the RTK observation time was increased from 30 seconds to 60 seconds.

10–14 checkerboard GCPs were used for UAV surveys. The albris and Phantom imagery was processed using Pix4D and the accuracy of the reconstructed point clouds was determined using

check point errors. The average 3D RMS errors in the UAV point clouds of 2017, 2018, and 2019 were 58 mm, 29 mm, and 22 mm, respectively. The decrease in UAV point cloud errors year-to-year was due to the combined effect of reducing the image GSD from 10 mm to 8 mm and increasing the RTK observation time. Additionally, the albris point clouds were notably more accurate than the Phantom points clouds, despite both UAVs using identical GCP data. Two factors contributed to this difference: image quality (38 Mp albris vs. 20 Mp Phantom) and image network (grid with POI albris vs. manual Phantom). Overall, the techniques implemented in 2019 to improve the accuracy of UAV image-reconstructed point clouds were successful.

12–14 targets (spheres and checkerboards) were used on each sideslope for TLS surveys at KM-82. Scans were registered in SCENE using a combination of cloud-to-cloud and target-based registrations, and point cloud accuracies were quantified based on checkerboard target errors. Mean scan point errors of the 2018 and 2019 TLS point clouds, which are measurements of the point cloud geometry accuracies, ranged from 3 mm to 5 mm. Target errors, which quantifies the georeferencing accuracy, ranged from 14 mm to 17 mm. These results demonstrate how the GCPs limit the accuracy of the georeferenced point clouds. Furthermore, targets set up along the road surface and scanned for both sideslopes in 2019 were successful in generating a single point cloud of the entire embankment. This was a major improvement to 2018, which produced separate point clouds for the east and west slopes.

Point clouds that were not properly georeferenced were aligned using the ICP registration algorithm in CloudCompare. Point clouds were aligned based on segments within GCP coverage to eliminate the influence of doming errors. However, registration accuracy was limited due to poor GCP coverage in 2018. A parametric analysis was performed to determine the optimal M3C2 parameters for comparing the high-fill section point clouds. M3C2 comparisons were performed after alignment using CloudCompare. Registration error values for M3C2 comparisons ranged 22–45 mm and 17–29 mm for the 2017–2018 and 2018–2019 comparisons, respectively. The enhanced

registration accuracy of the 2018-2019 comparisons was due to improvements in the data acquisition techniques, described above. A cross-section analysis was also performed at each high-fill section. Cross-sections data was exaggerated and smoothed to provide more visually appealing plots that were easier to interpret.

CHAPTER 5: RESULTS AND DISCUSSION

The results of the deformation analysis and corresponding discussion are separated into two main sections. The first compares the TLS and UAV results at KM 82, and the second covers the UAV results at all four high-fill sections.

5.1 UAV and TLS Deformations at KM-82

This section is separated into five sub-sections. First, UAV and TLS deformations determined by M3C2 comparison are presented. Issues that were discovered during the M3C2 comparisons and the subsequent solutions implemented are explained. Second, the albris, Phantom, and TLS reconstructed point clouds are compared for each year to investigate their accuracy and quality relative to each other. Third, the cross-section analysis results are presented, with a comparison to the instrumentation deformations. Fourth, performance of the geotextile-reinforced and non-reinforced zones are compared and discussed, with reference to the M3C2 and cross-section analyses. Lastly, UAV photogrammetry and TLS for monitoring embankment deformations are compared.

5.1.1 KM-82 UAV and TLS Deformations using M3C2

Initial 2018–2019 deformations are shown directly below (Figure 5.1 to Figure 5.3). An unexpected vertical difference between the 2018 and 2019 point clouds was evident in all three M3C2 results. The magnitude of the vertical difference at the high-fill sections varied from 0.11 m to 0.47 m.

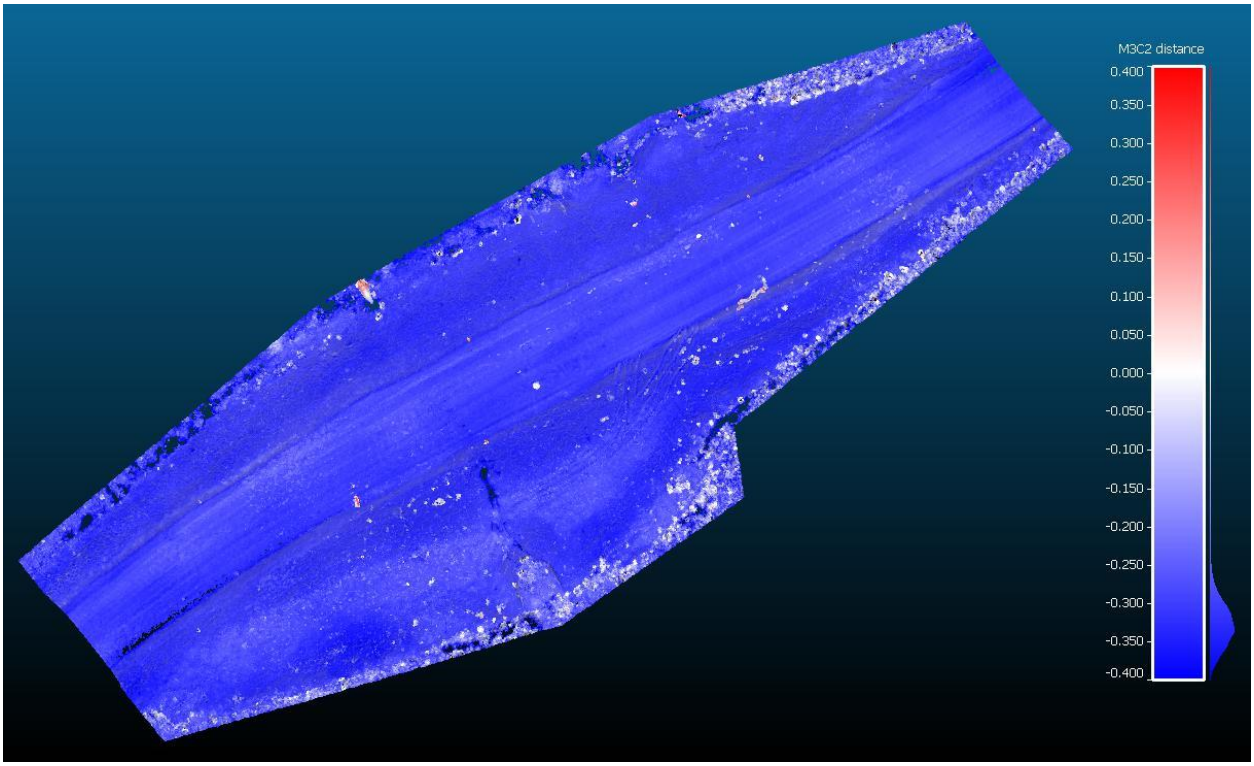

Figure 5.1 KM-82 albris UAV 2018–2019 initial M3C2 deformation (scale: ±400 mm).

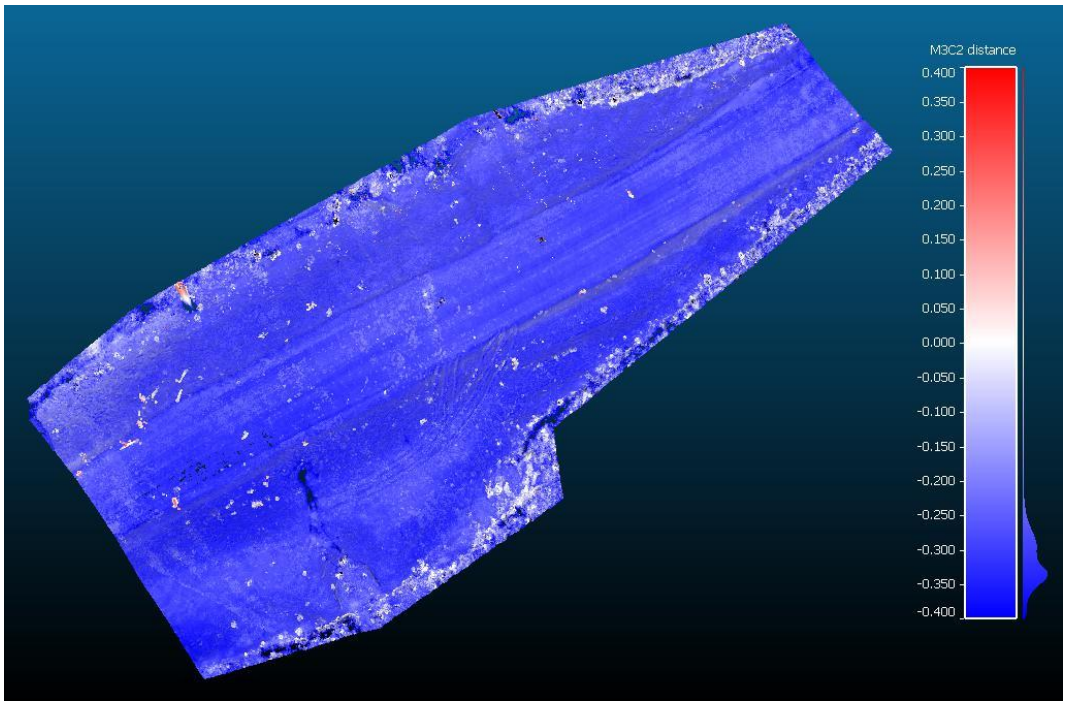

Figure 5.2 KM-82 Phantom UAV 2018–2019 initial M3C2 deformation (scale: ±400 mm).

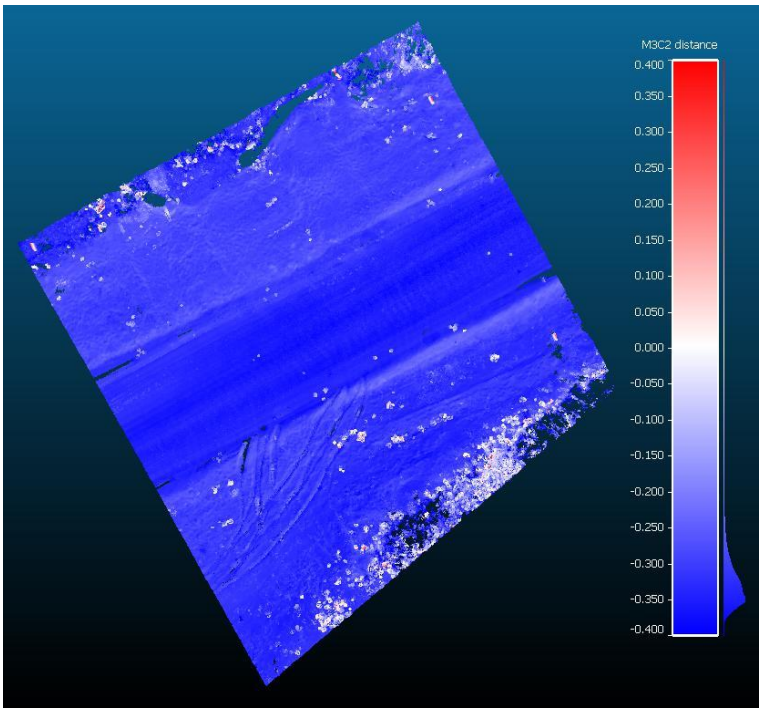

Figure 5.3 KM-82 TLS 2018–2019 initial M3C2 deformation (scale: ±400 mm).

Careful analysis of the data and discussion with the research team revealed the cause of the vertical difference between the 2018 and 2019 point clouds. The vertical difference was due to a mistake made while setting up the base station and measuring its height above the benchmark. In 2018, the base station height was measured from the base station to the ground surface beside the steel rod benchmark. But in 2019, the height was measured from the base station to the top of the steel rod. The CSRS-PPP benchmark coordinates that were used as reference points in 2018 and 2019 were determined based on a base station setup with its height measured to the ground surface. Inputting a shorter height in 2019 (i.e. only the base station to the steel rod) caused the base station to compute it was at a higher elevation than in 2018. Then when the 2019 RTK surveys were adjusted to reference the 2018 CSRS-PPP benchmark coordinates, it shifted the RTK-measured GCP elevations to decrease approximately the height of the steel rod. This shift in the RTK survey was transferred to the georeferenced point clouds and manifested as an apparent decrease in elevation when the 2018

and 2019 point clouds were compared. The magnitude of the vertical difference at a section depended on the height of the steel rod above ground surface.

The solution implemented was to shift the 2019 point cloud vertically to match the elevation of the 2018 point cloud at each section. However, it was impossible to know the correct difference to shift the point cloud, which presented a challenge. To determine the optimal shift distance, vertical M3C2 comparisons were performed on the 2018 and 2019 clouds at each section. The vertical comparisons also used segments of the point clouds within GCP coverage to ensure doming errors did not influence the results (Figure 4.7a and Figure 5.4). The vertical distances between the point clouds were analyzed to determine the optimal vertical shift distance for each section. Table 5.1 provides analysis results of the KM-82 vertical M3C2 comparisons, as well as the shift distances determined for the 2019 point clouds. The selected shift distances were based on the mean, median, and peak of the vertical distance distributions. It is interesting that although the albris and Phantom point clouds used the same GCPs in 2018 and 2019, the resulting vertical differences between the point clouds were different. Different distances were required for the TLS east and west slopes because those were separate point clouds in 2018 and the vertical distance distributions were notably different. Results from the other three sections are provided later in Table 5.2.

.

Figure 5.4 Fine registration segment area for KM-82 TLS point clouds.

Table 5.1 KM-82 2018–2019 point cloud vertical comparison results and selected 2019 point cloud vertical shifts.

Technology	2018–2019 measured vertical difference (m)			Selected 2019 point cloud shift (m)
	Mean	Median	Peak of distribution	
albris	-0.340	-0.341	-0.340	+0.340
Phantom	-0.332	-0.336	-0.340	+0.332
TLS-east	-0.340	-0.346	-0.353	+0.353
TLS-west	-0.322	-0.322	-0.316/-0.337*	+0.322

* vertical difference distribution resembled a bimodal distribution with two peaks.

After the vertical shift had been applied, M3C2 comparisons between the 2018 and shifted 2019 point clouds were performed again (Figure 5.5 to Figure 5.7). These comparisons were performed in the surface normal directions as M3C2 typically is. The comparisons identified that there was positive change (e.g. soil deposition, heave, etc.) on the west slope (facing northwest) and negative change (e.g. erosion, settlement, etc.) on the east slope (facing southeast). However, such extreme differences between the east and west slopes does not seem realistic. There is no reasonable explanation for the

entire west slope to be heaving while the entire east slope is settling. Embankment deformations were expected to be more uniform on both slopes than these comparisons detected. Additionally, the magnitude of deformations between the albris, Phantom, and TLS comparisons were highly variable.

Varying the vertical shift magnitude strongly influenced the types and magnitudes of deformations detected. This underscores the issue with the vertical shift approach. To fix the base station height mistake, raw point cloud data had to be modified in order to determine deformations. To put it another way, the data was modified to fit a preconceived understanding of embankment deformation behaviour. Nevertheless, the non-uniform (positive and negative) slope deformations was measurable regardless of the vertical shift magnitude.

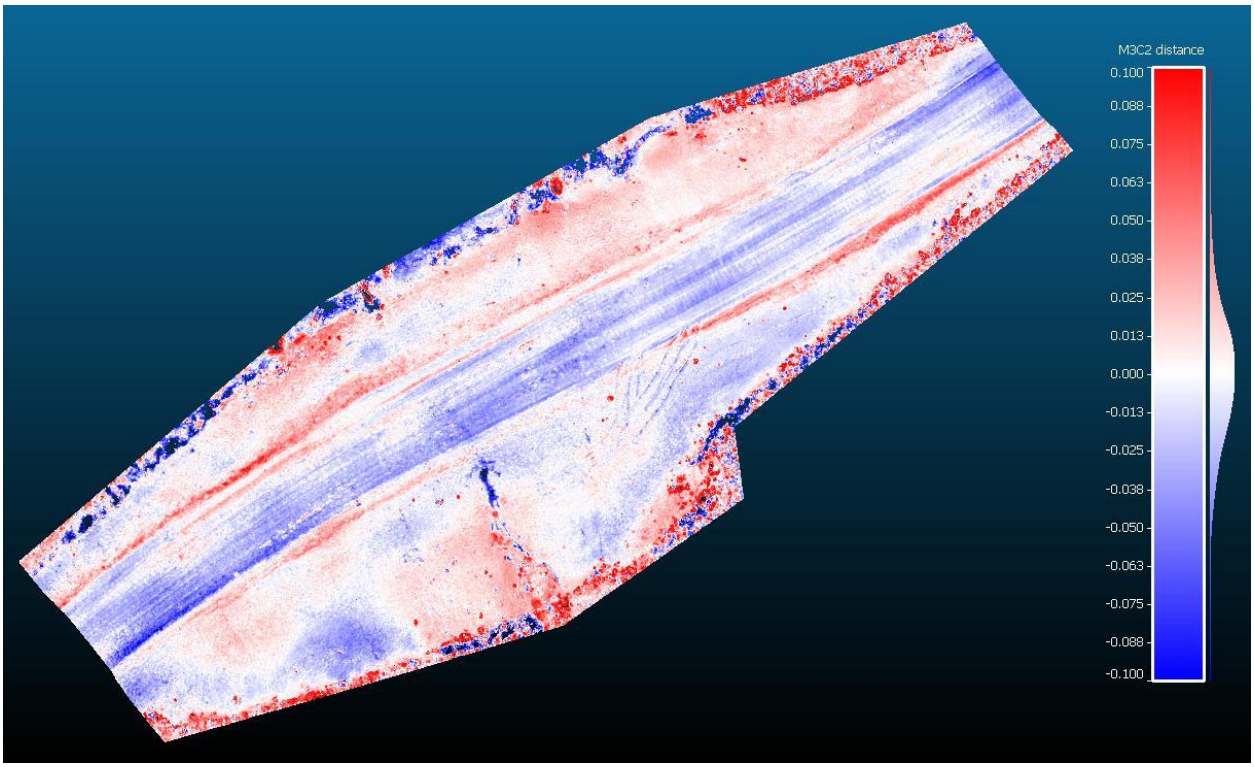

Figure 5.5 KM-82 albris UAV 2018–2019 M3C2 deformation after vertical shift (scale: ±100 mm).

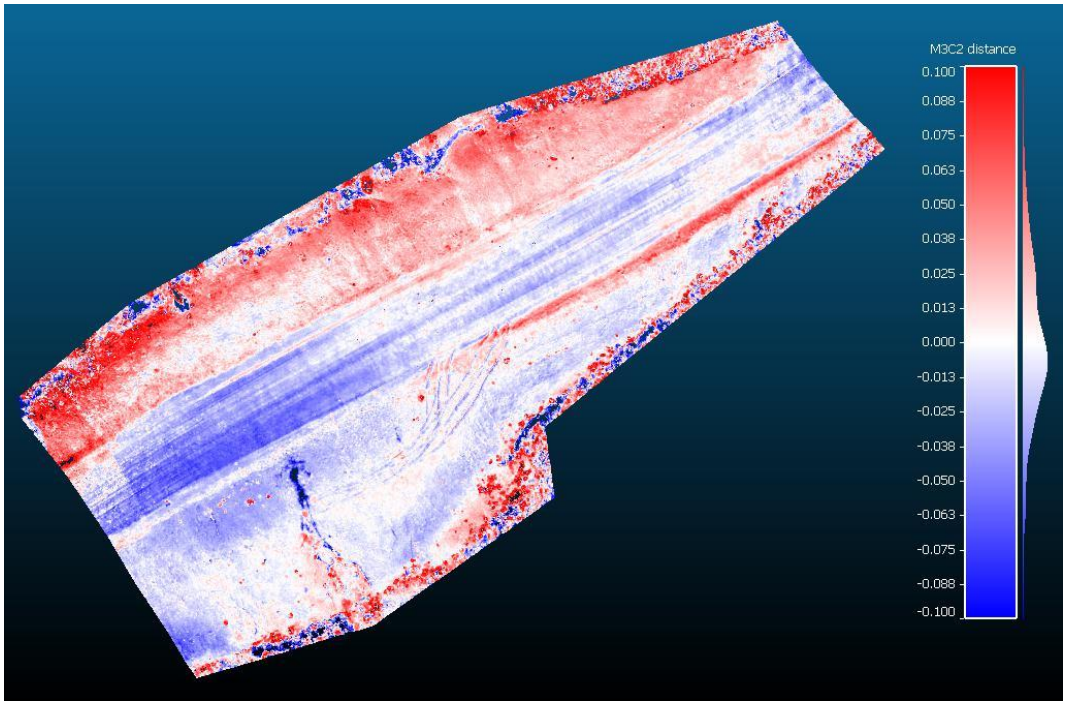

Figure 5.6 KM-82 Phantom UAV 2018–2019 M3C2 deformation after vertical shift (scale: ±100 mm).

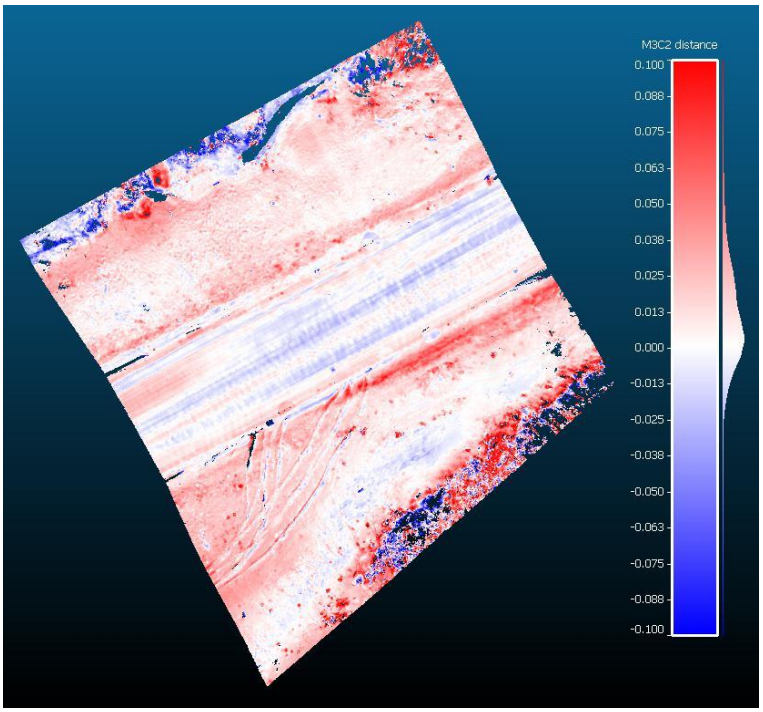

Figure 5.7 KM-82 TLS 2018–2019 M3C2 deformation after vertical shift (scale: ±100 mm).

A more likely cause of the non-uniform deformations would be an issue with georeferencing the point clouds. The author's hypothesis is that during one or some of the RTK surveys of GCPs, the base station was not levelled correctly. The base station assumes it was set up level. If it was not, vector measurements between the base station and rover would be incorrectly oriented and the resulting GCP network would be tilted in the opposite direction of the base station tilt. This tilting of the GCP network would then be transferred to the georeferenced point clouds and manifest as non-uniform, positive and negative slope deformations.

The M3C2 deformations after the vertical shift provided evidence that there was tilting of some point clouds. In order to fix this and allow for better deformation estimates, the 2019 point cloud was registered to the 2018 point cloud. The process was similar to that of registering the 2017 and 2018 point clouds together (Section 4.4.1). Point cloud segments within GCP coverage (Figure 4.7a and Figure 5.4) were used to ensure the registration was not influenced by doming errors. Fine registration of the 2018 and 2019 point clouds was performed on the original point clouds (before vertical shifting). Registration was limited to translation only in the Z direction to correct the vertical difference and allowed to rotate on all three axes because the orientation of the point cloud tilt was unknown. Final M3C2 comparisons were performed between the 2018 and registered 2019 point clouds (Figure 5.9 to Figure 5.11). No vertical shifting was attempted for the 2017–2018 comparisons because no GCPs were used at KM-82 in 2017. Instead, only the registered 2017 and 2018 albris point clouds were compared (Figure 5.8).

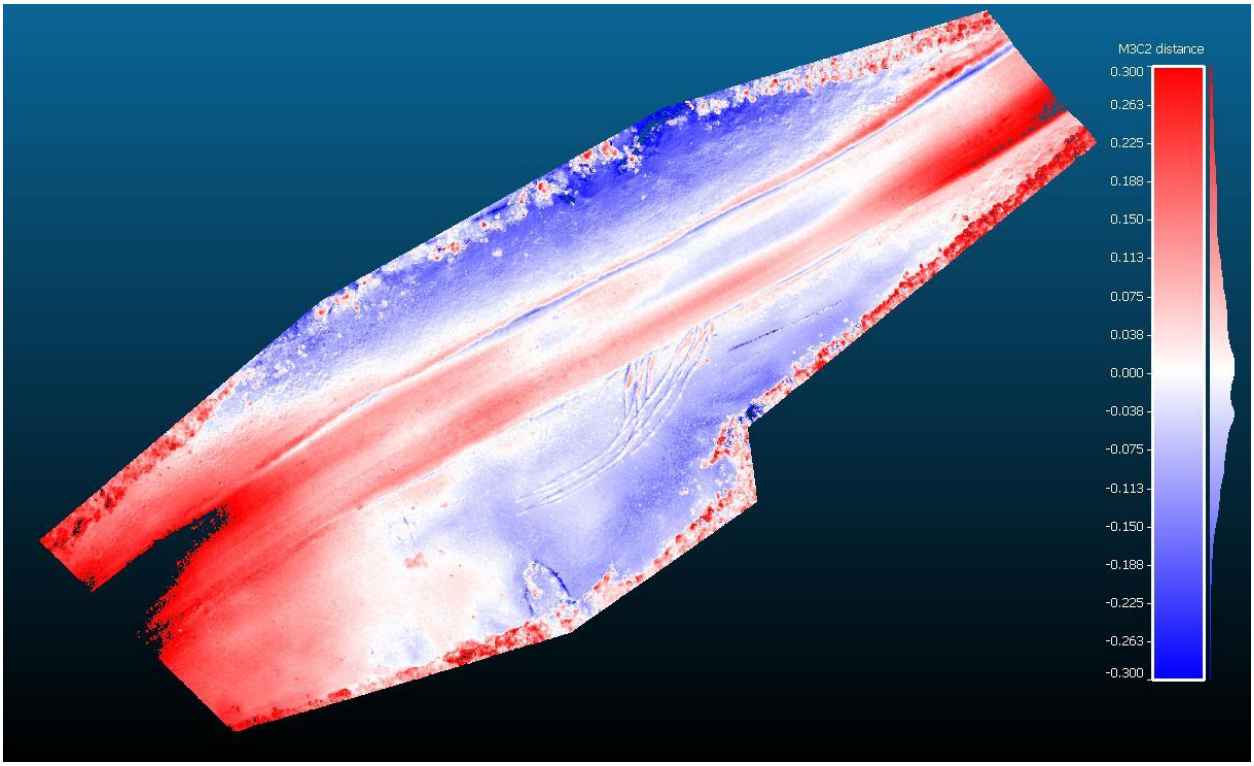

Figure 5.8 KM-82 albris UAV 2017–2018 M3C2 deformation (scale: ±300 mm).

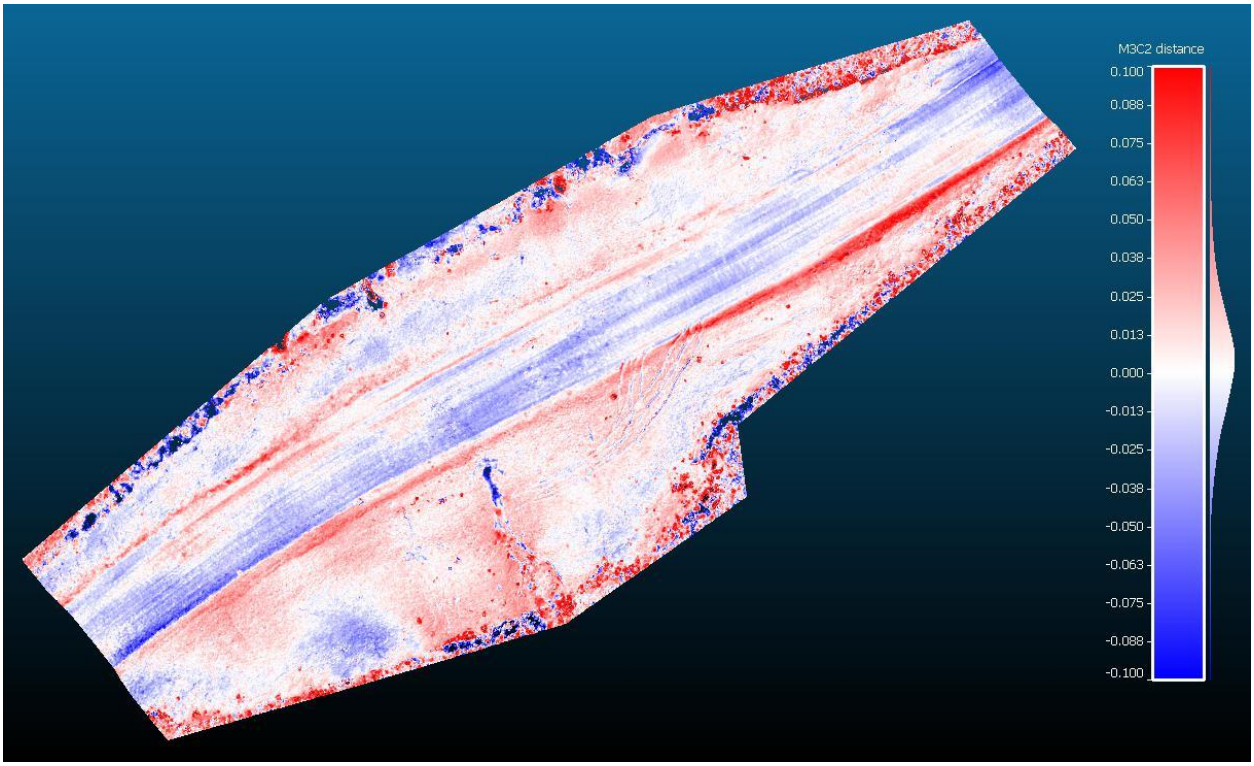

Figure 5.9 KM-82 albris UAV 2018–2019 final M3C2 deformation after vertical translation and rotation registration (scale: ±100 mm).

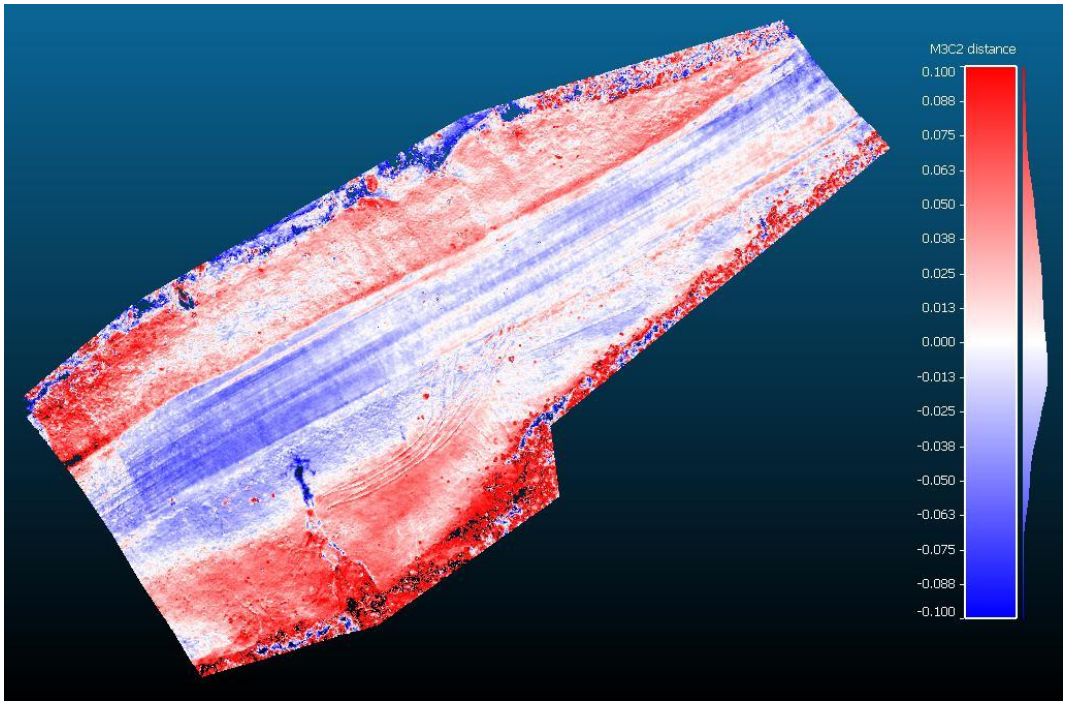

Figure 5.10 KM-82 Phantom UAV 2018–2019 final M3C2 deformation after vertical translation and rotation registration (scale: ±100 mm).

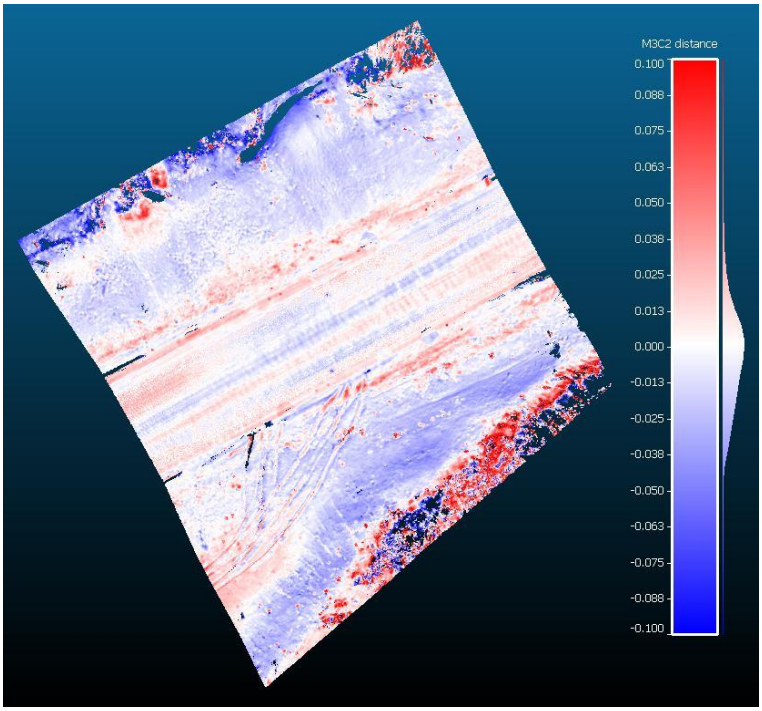

Figure 5.11 KM-82 TLS 2018–2019 final M3C2 deformation after vertical translation and rotation registration (scale: ±100 mm).

2017–2018 M3C2 comparisons (Figure 5.8) showed extreme positive change at the edges of the reconstruction (> 300 mm). This was not actual deformation of the embankment; rather, it was the manifestation of a systematic doming error that occurred in the 2017 point cloud because there were no GCPs. The doming error caused the extents of the 2017 point cloud to be computed at a lower elevation than reality. When the 2018 point cloud with no doming errors is compared, M3C2 erroneously computes it as positive change. Figure 5.8 also showed subsidence of approximately 100 mm at the mid-slope and toe. It is unlikely however that this is true deformation because the SAAs within the high-fill section measured significantly less than 100 mm of settlement (close to 0 mm). The observed subsidence behaviour is likely only appearing because of the vertical doming error and registration process implemented. The area displaying subsidence is near the middle of the reconstruction, which was computed at a higher elevation than reality (opposite to the reconstruction extents). This caused the appearance of negative change when compared to the 2018

point cloud. There is also an inherent methodological issue with the registration process. Registering one point cloud to another point cloud that has major vertical doming errors will inevitably be skewed to the doming errors and cause errors in the deformation measurements. In order to compare the point clouds, there was no way around this issue; however, it is a notable limitation of the method. If there was subsidence of the embankment, it would have been substantially less than estimated here and it was undetectable with the data quality available. The fact that there were no GCPs in the 2017 UAV survey, which made registration mandatory and caused vertical doming errors, makes it difficult to draw any meaningful conclusions from the 2017–2018 deformations at KM-82.

Comparing the 2018–2019 deformations, the albris and TLS results show agreement (Figure 5.9 and Figure 5.11). The Phantom results, however, were markedly different (Figure 5.10). Phantom results showed positive change of approximately 50 mm along the west slope at the instrumented zones. The west half of the Phantom M3C2 comparison showed an area of depression at the road surface and major positive change on both slopes. This type of behaviour could have occurred, but the measured magnitudes are too large. After driving the highway in 2019, the author can confirm that a significant depression of the road surface was not present at that location. It is likely that the erroneous Phantom deformations are due to inaccuracies in the 2018 point cloud. Only 52 images were used to reconstruct the 2018 Phantom point cloud, compared to 127 images for the 2018 albris point cloud (Table 4.2 and Figure 4.1). Furthermore, the albris image quality was higher and the grid+POI image network of the albris provided more uniform coverage of the high-fill section. Based on these factors, it can be concluded that the albris deformations are more reliable than the Phantom deformations for the 2018–2019 KM-82 comparison.

Both the albris and TLS deformations showed negative change along the road surface, which was likely caused by road traffic. They also both showed positive change along the shoulders of the embankment. It is likely that this was caused by spreading of the resurfacing gravel that was laid in 2017. It is natural for built-up gravel surfacing to deform laterally, especially with traffic loading, and

this behaviour was captured by the albris and TLS. Positive change at the upper-slope transitions to negative change near the mid-slope and lower-slope. This negative change could be the detection of settlement or subsidence of the slope; however, it is difficult to conclude the embankment slopes are settling because of modifications to the point cloud data (e.g. vertical shift and rotation due to base station setup mistakes).

It is important to consider the deformation uncertainty estimates (i.e. LoD) and significant change outputs of the M3C2 comparisons. LoD estimates for the 2018–2019 albris, Phantom, and TLS M3C2 comparisons (Figure 5.12 and Figure 5.14) range mostly between 33 mm and 40 mm on the embankment. LoD estimates are higher along the toes due to vegetation. TLS produced generally lower LoDs than the albris UAV. Interestingly, lower LoD estimates for the albris corresponded to the areas where POI images were centered. Oblique imagery improved the precision of the reconstruction and translated to lower LoD estimates. LoD estimates for the Phantom (Figure 5.13) were approximately 20 mm higher than the albris and TLS because of the Phantom's poor 2018 reconstruction quality.

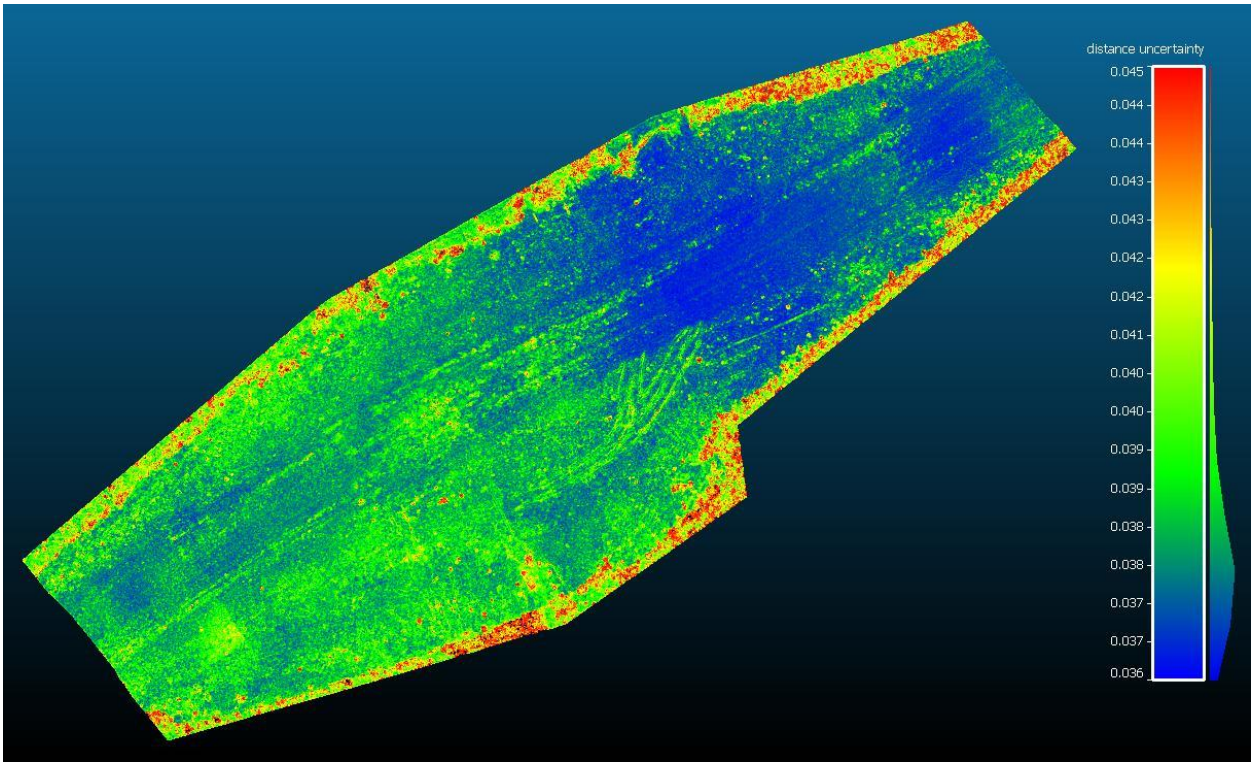

Figure 5.12 KM-82 albris UAV 2018–2019 M3C2 LoD estimates (scale: 36–45 mm).

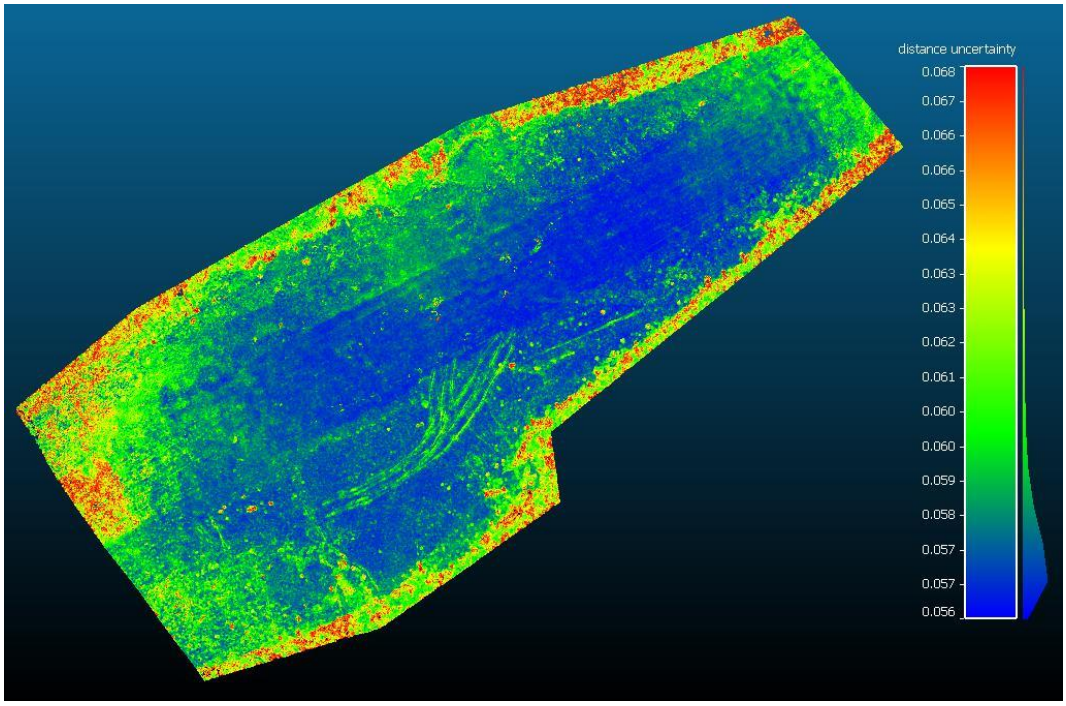

Figure 5.13 KM-82 Phantom UAV 2018–2019 M3C2 LoD estimates (scale: 56–68 mm).

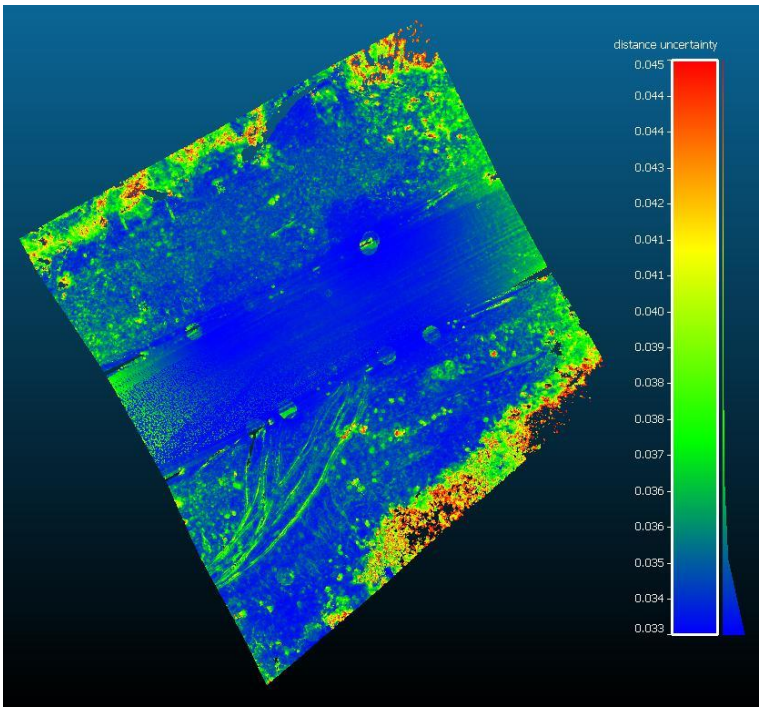

Figure 5.14 KM-82 TLS 2018–2019 M3C2 LoD estimates (scale: 33–45 mm).

The significant change estimates for the 2018–2019 albris, Phantom, and TLS M3C2 comparisons (Figure 5.15 to Figure 5.17) show that almost the entire high-fill section can not be considered actual change. Red areas represent significant change where deformation is greater than the LoD. The M3C2 measured deformations (Figure 5.9 to Figure 5.11) are less than the corresponding spatially variable LoD estimates (Figure 5.12 to Figure 5.14). If surface roughness was ignored and only registration error (*reg*) was considered for calculating LoD (Equation 3.3), the LoD for the 2018–2019 albris, Phantom, and TLS comparisons would be 35 mm, 55 mm, and 33 mm, respectively. Comparing these values to the computed LoDs demonstrates the large influence of *reg*. Surface roughness of the embankment only contributed a maximum of 5 mm to the LoD. *reg* values were large because of high GCP position uncertainties from the RTK surveys.

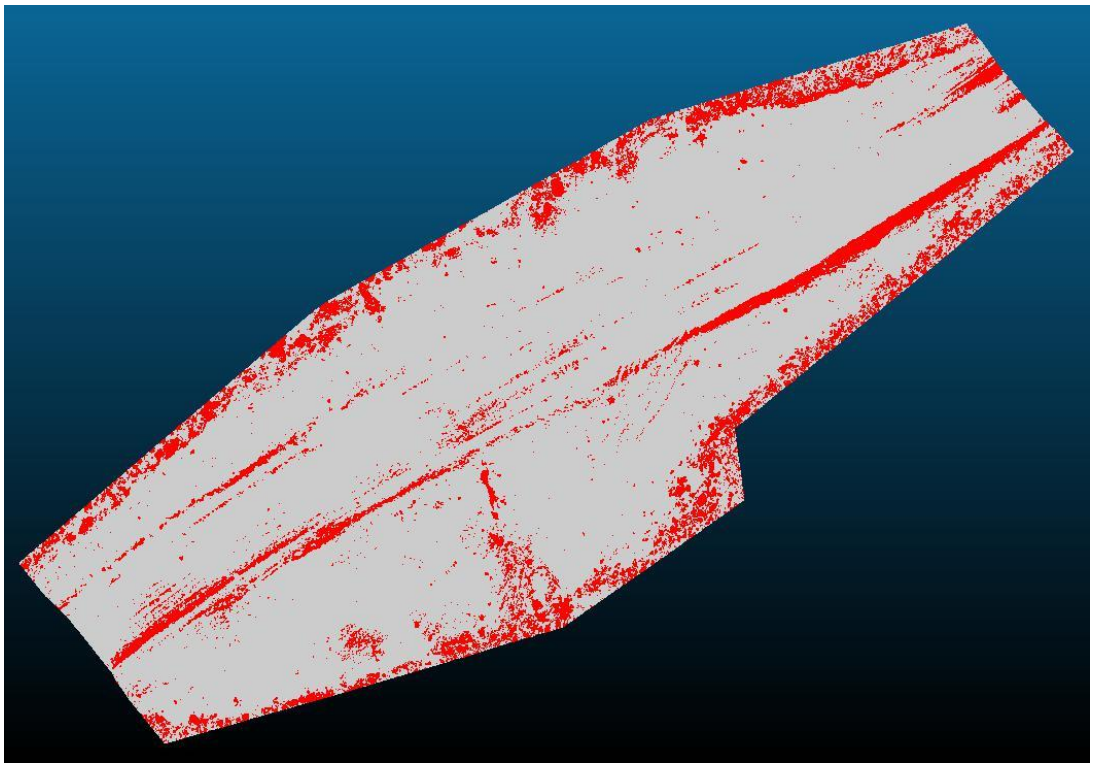

Figure 5.15 KM-82 albris UAV 2018–2019 M3C2 significant change estimates.

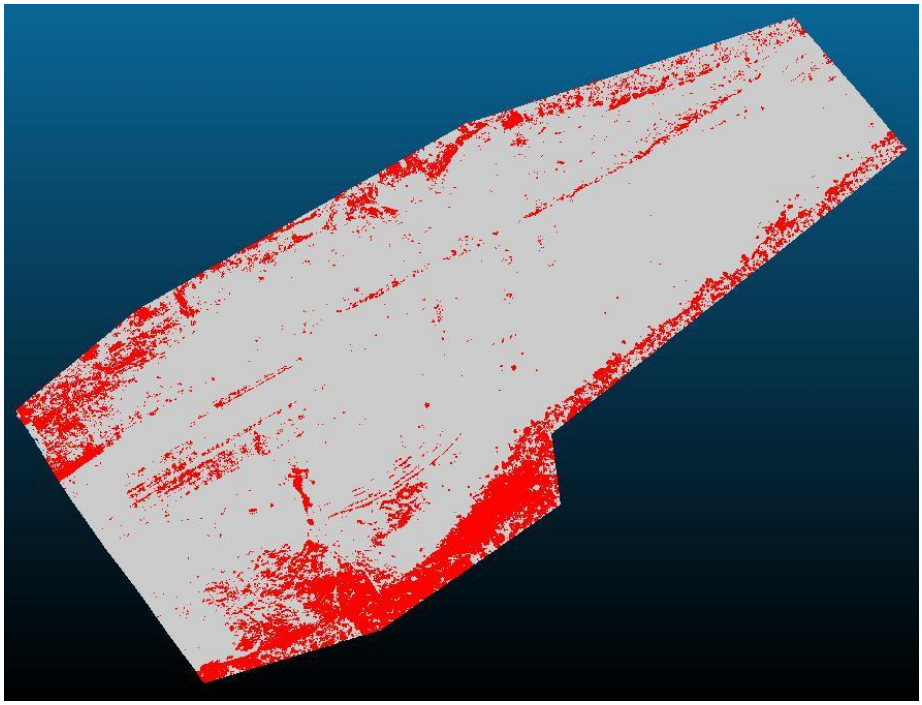

Figure 5.16 KM-82 Phantom UAV 2018–2019 M3C2 significant change estimates.

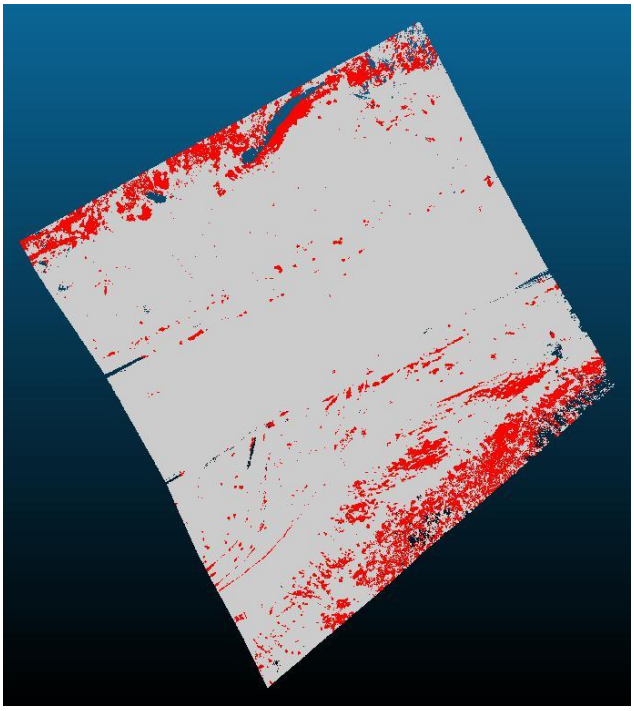

Figure 5.17 KM-82 TLS 2018–2019 M3C2 significant change estimates.

One last observation from the KM-82 results that is worth mentioning is the negative change 'channel' that was detected in the 2018–2019 comparison on the east upper-slope parallel to the culvert. The channel was detected by the albris and Phantom, and is one of the only deformations on the embankment that was considered significant change. The deformation comparisons measured the channel to be approximately 100 mm deep, which is significant considering the rest of the embankment was deforming less than 30 mm. Although it is unclear what exactly caused the deformation, it seems unlikely that it is merely coincidence that the deformation occurred in line with the culvert. Heat flowing through the culvert in summer could be influencing the thermal conditions within the embankment and manifesting as deformations at the embankment surface. It could also be that deformations parallel to the culvert are occurring across the entire embankment and the detected channel was only detected because it was the greatest deformation. This can not be confirmed from the existing data, though. More accurate UAV monitoring in future years could confirm if the channel deformation is growing and provide better insights to its cause.

The quality of data acquired on-site led to several challenges during processing and ultimately, low confidence in the final deformation results. Imagery and data directly from the UAV and TLS were good. It was the GCP data acquired with the RTK system that caused the issues and inaccuracies. Modifications of the point cloud data and high LoDs, both of which were due to low RTK accuracy, restrict meaningful conclusions being drawn from the deformation results. General deformation behaviour of the embankment can still be derived, but precise magnitudes and confidence in the results are unattainable. If RTK surveys are to be used to acquire GCP positions for UAV or TLS deformation monitoring, RTK observation times need to be sufficiently high (3–5 minutes minimum) in order to reduce measurement uncertainty. Otherwise, another surveying technique should be used to acquire GCP positions, such as a total station. A total station was not used in this research because the limitations of measuring GCPs with an RTK system were not realized early in the research.

5.1.2 KM-82 Point Cloud Accuracy: UAV vs. TLS

KM-82 point clouds of the same year from each technology were compared to assess their accuracy relative to each other. M3C2 was used to perform the comparisons with the same parameters as the deformation comparisons (Table 4.7). TLS data was acquired one day prior to UAV flights in both years. Therefore, there was no actual deformation between any of the reconstructed point clouds. Any deformation detected is a result of the data processing, georeferencing, and registration methods used. The 2018 and 2019 comparisons are shown in Figure 5.18 and Figure 5.19, respectively. The 2018 TLS east and west point clouds were compared to UAV point clouds separately in order to visualize both distance distributions next to the M3C2 scales. All comparisons were performed on the original georeferenced point clouds without any registering, shifting, or rotating.

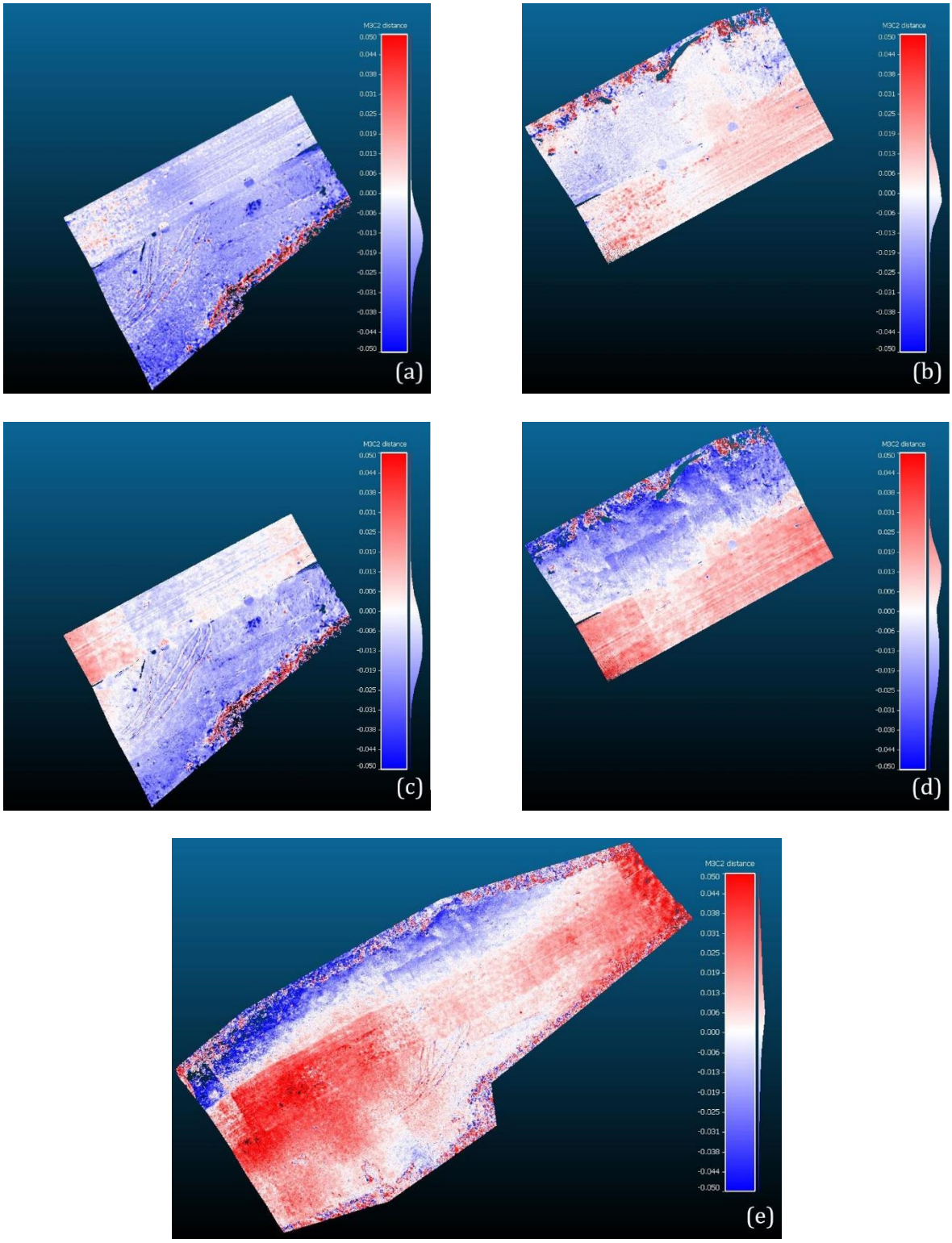

Figure 5.18 KM-82 2018 point cloud comparisons (scale: ±50 mm): a) TLS-east vs. albris; b) TLS-west vs. albris; c) TLS-east vs. Phantom; d) TLS-west vs. Phantom; e) albris vs. Phantom.

The 2018 albris vs. Phantom comparison (Figure 5.18e) showed minor distances (< 10 mm) throughout most of the point clouds except in three areas with relatively larger distances (25–50 mm). Two of the areas, located along the west lower-slope and on the road surface in the west half, correspond to areas with large deformation in the Phantom comparisons (Figure 5.10). As discussed in Section 5.1.1, the large distances at these two areas are associated with poor reconstruction quality of the 2018 Phantom point cloud due to a low number of images. The area at the east extent with large distances is likely due to poor image coverage in both the albris and Phantom reconstructions.

For the TLS vs. UAV comparisons, it is important to consider the high accuracy of the TLS point cloud geometry with scan point mean errors ≤ 5 mm in 2018 and 2019. Georeferencing the TLS point clouds using GCPs with high positional uncertainty was the largest factor contributing to point cloud inaccuracies and may have caused tilting of the point clouds. In both TLS-east vs. UAV comparisons (Figure 5.18a and c), the deviation of point cloud distances was relatively small; however, the distance distribution was shifted approximately -15 mm. It appears that there was some sort of georeferencing issue that caused the TLS-east point cloud to be at a lower elevation. The TLS-west vs. albris comparison (Figure 5.18b) resulted in small distances between the point clouds with a mean of approximately zero and most distances within ±10 mm. The TLS-west vs. Phantom comparison (Figure 5.18d) produced relatively large point cloud distances at the lower-slope and along the road surface. Both of these areas are consistent with areas of large errors in the albris vs. Phantom comparison (Figure 5.18e); therefore, it is likely that the errors in the TLS-west vs. Phantom comparison are due to inaccuracies in the 2018 Phantom point cloud.

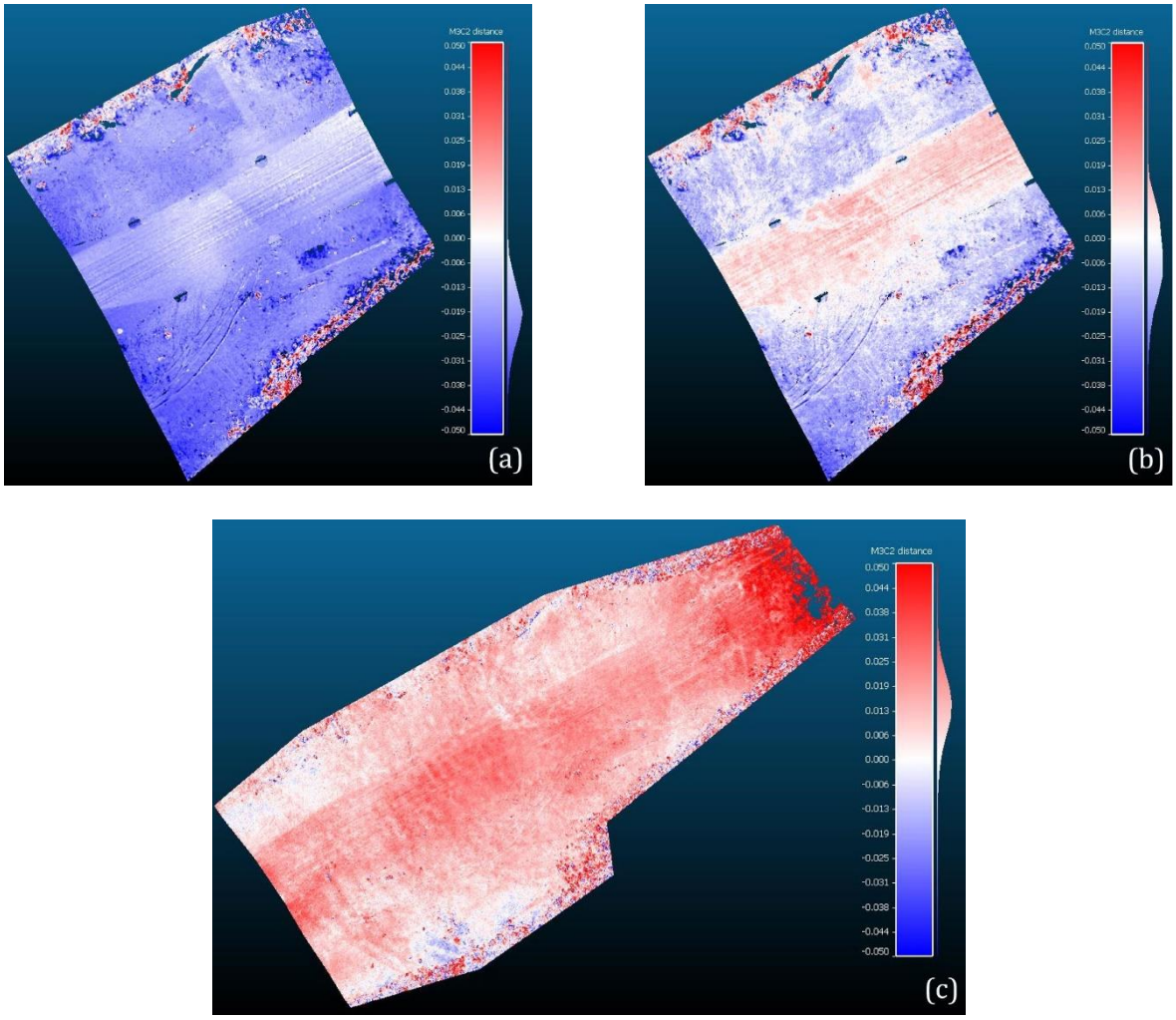

Figure 5.19 KM-82 2019 point cloud comparisons (scale: ±50 mm): a) TLS vs. albris; b) TLS vs. Phantom; c) albris vs. Phantom.

There was no evidence of tilting in the 2019 point clouds, demonstrated by the relatively uniform distances on both sideslopes in each of the three point cloud comparisons. This is starkly different than the 2018 point clouds. The most remarkable difference between the three 2019 point clouds was the elevation of the albris point cloud. Figure 5.19a showed negative change from the TLS point cloud to the albris point cloud and Figure 5.19c showed positive change from the albris point to the Phantom point cloud; both of which had magnitudes of ±15–20 mm. A vertical comparison of the point clouds was performed, and it confirmed that the computed distances were due to the albris

point cloud being at a lower elevation than the Phantom and TLS point clouds. Interestingly, the same GCPs were used to georeference the albris and Phantom point clouds. The exact cause of the elevation difference is unclear. The elevation difference must have occurred during the SfM processing and been caused by the different image networks of the albris and Phantom. Other than the elevation differences, distances in the albris comparisons were minor. The only area with large errors were the east extent where there was poor image coverage in both UAV reconstructions.

It was apparent that elevations of the 2019 TLS and Phantom point clouds aligned because the mean of the distance distribution is near zero (Figure 5.19b). The comparison identified differences of positive change on the road surface and negative change on the slopes. These differences are likely caused by SfM reconstruction errors of the UAV point cloud because the TLS point cloud had extremely low scan point errors. Nonetheless, distances of the 2019 TLS vs. Phantom comparison were relatively small with respect to the other comparisons.

5.1.3 Cross-Section Analysis Results and Instrumentation Comparison

Original cross-section comparisons for the reinforced and control (i.e. non-reinforced) zones at KM-82 (Figure 5.20) were not useful because the deformations were extremely small relative to the embankment height. To allow deformations to be visualized, elevation data of the 2017 and 2019 cross-sections was exaggerated 10x (Figure 5.21). The exaggerated deformations showed significant point-to-point elevation variability in the cross-sections. To reduce variability, elevation data was smoothed using a moving average calculation (Figure 5.22). Cross-sections of the vertical shifted 2019 point cloud were included along with the registered 2019 point cloud cross-sections (Figure 5.22) to examine the effects of rotation registration. Tilting was evident in the 2018 TLS point clouds (Figure 5.18), but it difficult to know for certain if tilting occurred in the original albris point clouds. Tilting in the albris point cloud was certainly not as extreme as the TLS point clouds. It is impossible to know which 2019 albris point cloud (rotation registered or vertical shifted) is truly more accurate.

The detected settlement behaviour on the east slope is a realistic and possible behaviour for an embankment on permafrost. The settlement could be caused by permafrost thawing and subsequent subsidence at the embankment toe. The positive change detected on the west slope would not be caused by heave or deposition of soil. The most logical explanation for the positive change on the west slope is lateral spreading of the embankment. This behaviour can also be caused by permafrost thawing at the toe if the shear strength of thawed soil is too low to resist deforming under the lateral stresses beneath the embankment. Large deformations detected at the toe are due to vegetation growth, which is highly variable year-to-year.

Cross-sections of the embankment surface in the reinforced and control zones were extracted from above the vertical and horizontal SAAs. This allowed for comparison to instrumentation data. SAAs measured less than 15 mm of vertical and lateral deformations in 2018–2019. Vertical displacements from the horizontal SAAs are expected to be less than surface settlements because the SAAs are buried under fill material at mid-height of the embankment. The Phantom detected positive change on the slope, which is opposite to the SAA measurements. The albris underestimated the SAA data by approximately 30 mm, detecting slightly positive but near-zero deformations. The TLS measured deformations were reasonably close to the instrumentation data after point cloud alignment.

The settlement and lateral spreading behaviours discussed above mechanistically make sense; however, the deformation magnitudes do not agree with instrumentation data. Instrumentation is more reliable than the UAV and TLS deformations in this case because of the modifications that were made to the point cloud data. The embankment could in reality be undergoing small deformations (< 15 mm), and the UAV and TLS detected deformations could simply be caused by point cloud inaccuracies and modifications. Furthermore, M3C2 comparisons concluded that most of the embankment deformation was insignificant (i.e. less than the LoD; Figure 5.15 to Figure 5.17). Much

of the deformations identified in the cross-section comparisons could merely be the product of inaccurate reconstructions.

2017–2018 cross-section comparisons (Figure 5.23) were included to demonstrate the significant impact of the doming error in 2017. Without exaggeration, 2017–2018 deformations are comparable to 2018–2019 deformations that were exaggerated 10x. The exaggerated cross-sections clearly show the major doming error in the 2017 albris point cloud that occurred because there were no GCPs.

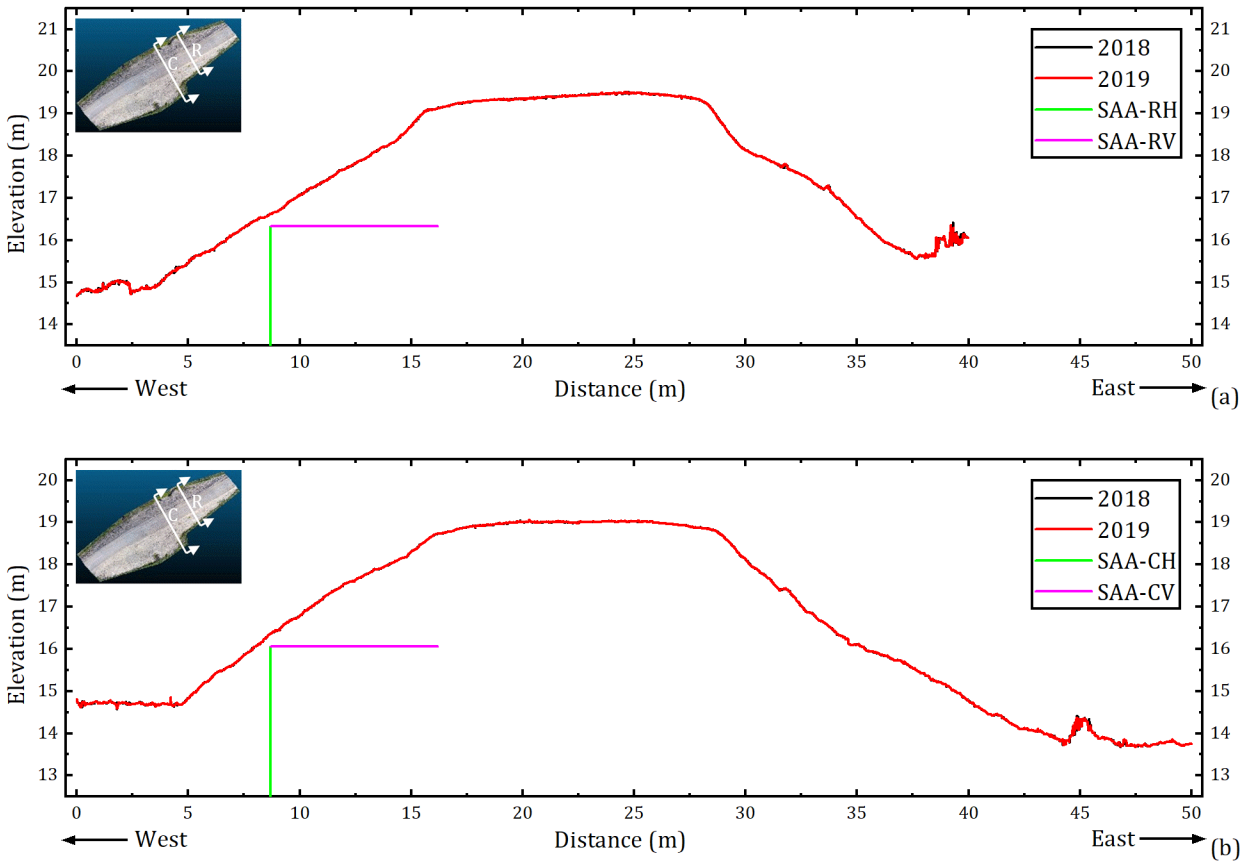

Figure 5.20 KM-82 2018–2019 original cross-sections: a) reinforced zone; b) control zone.

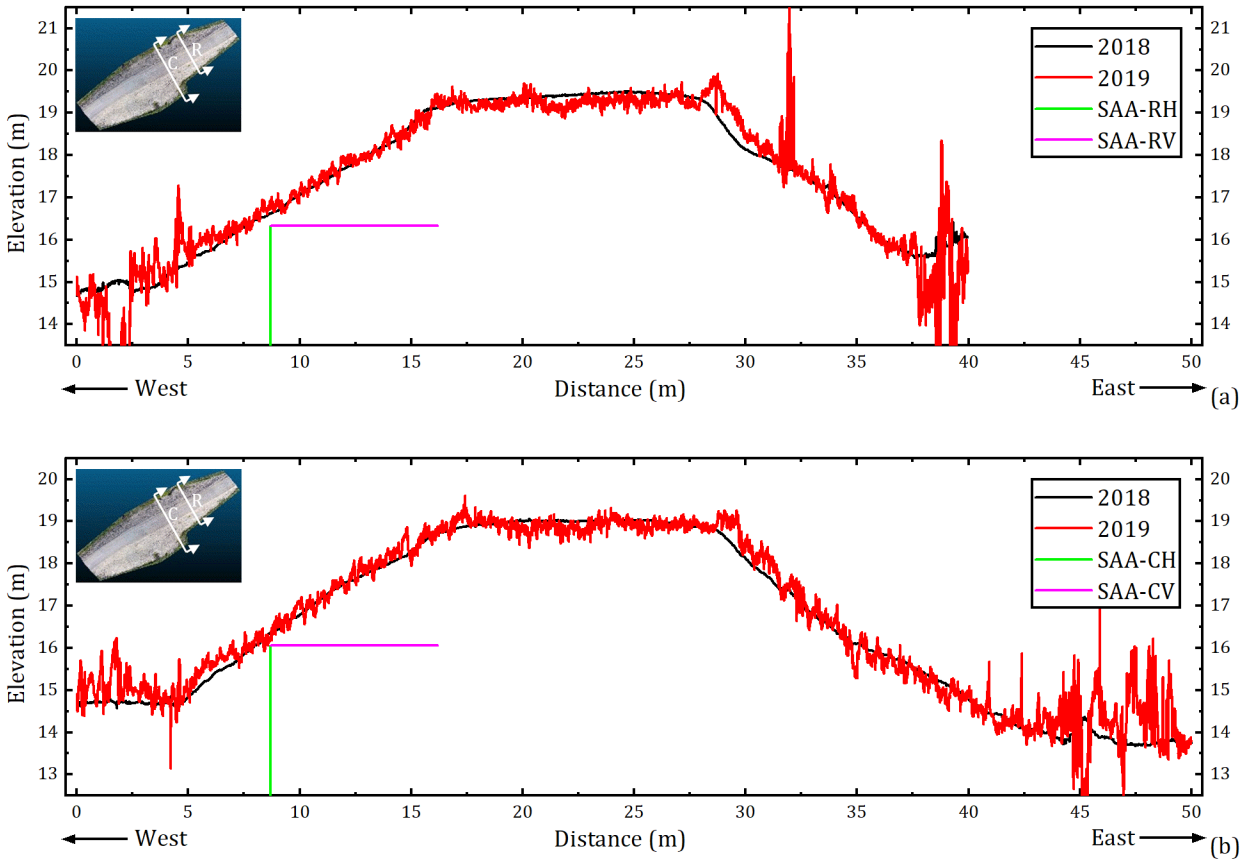

Figure 5.21 KM-82 2018–2019 cross-sections with 10x vertical exaggeration: a) reinforced zone; b) control zone.

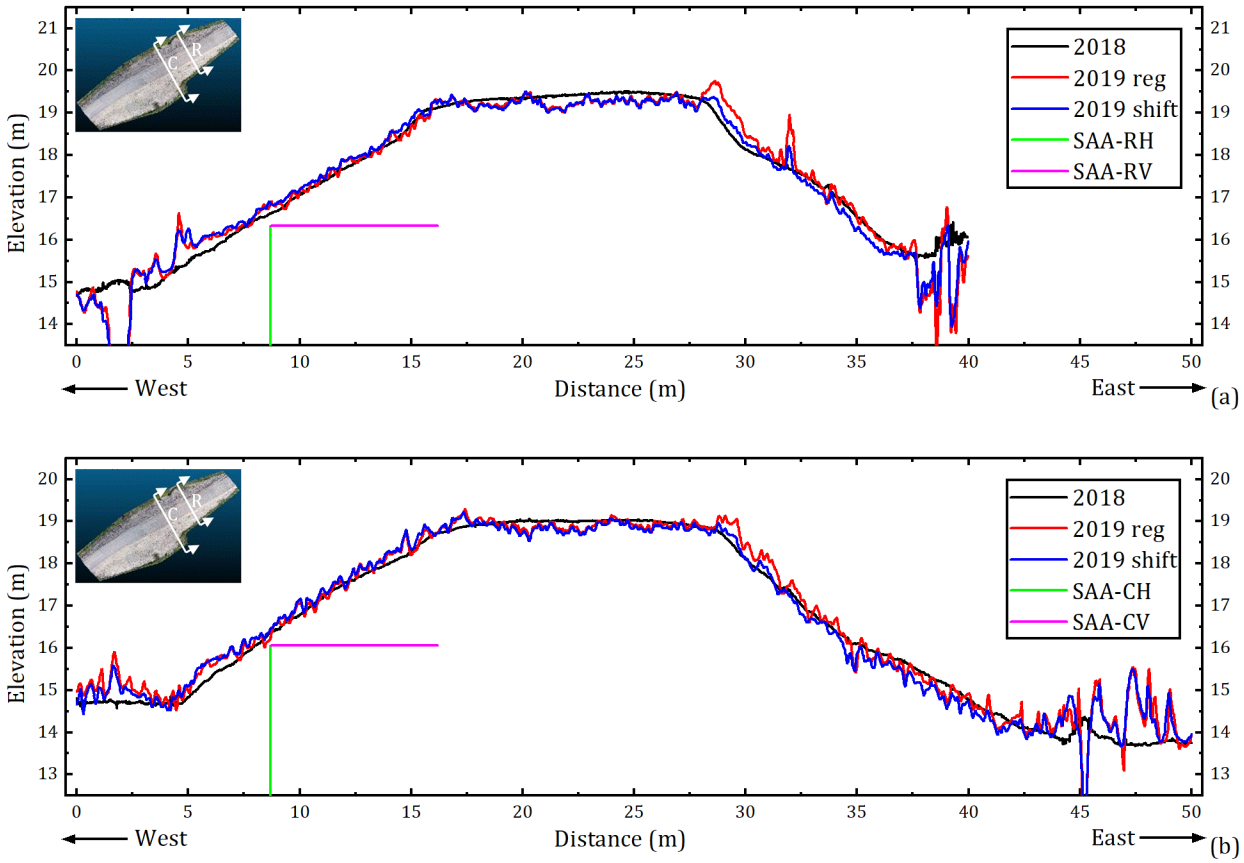

Figure 5.22 KM-82 2018–2019 final cross-sections with 10x vertical exaggeration and smoothing: a) reinforced zone; b) control zone.

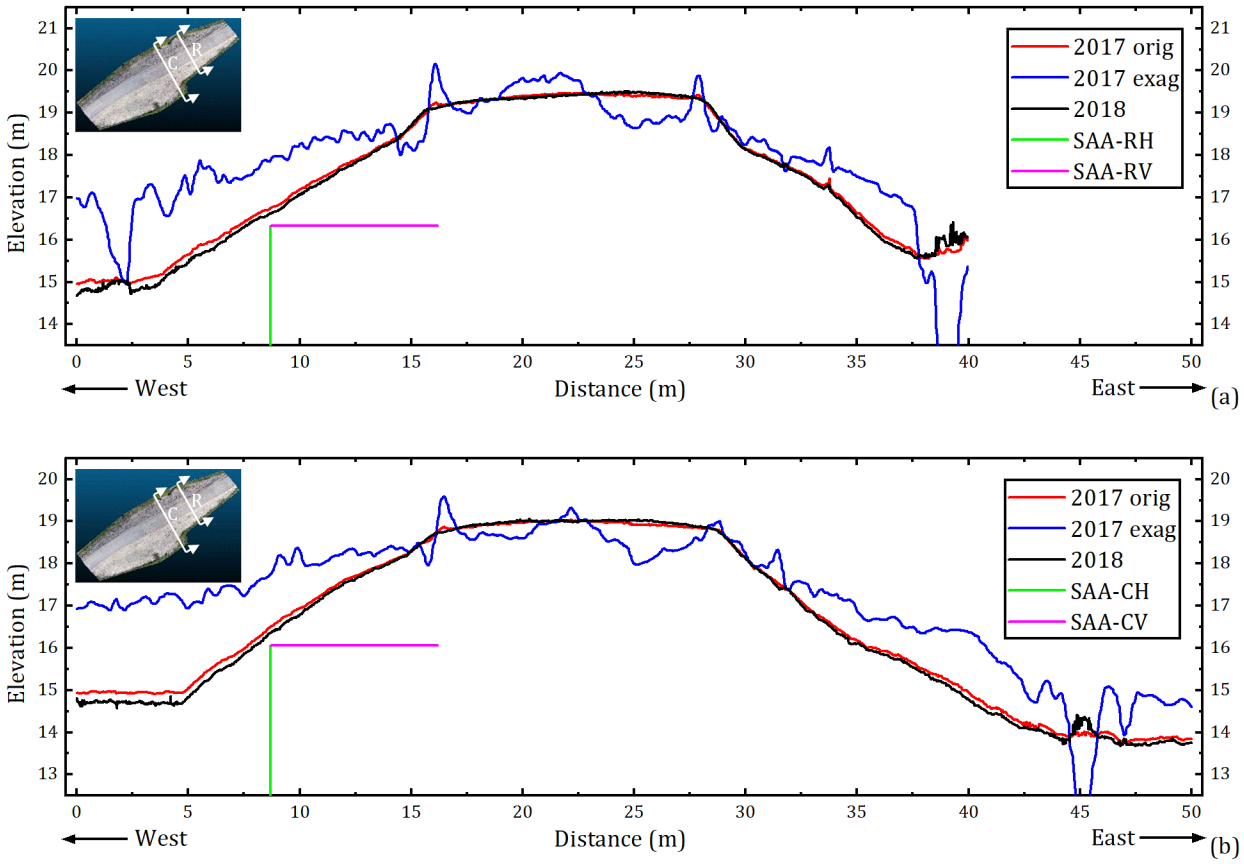

Figure 5.23 KM-82 2017–2018 cross-sections—original and 10x vertical exaggeration with smoothing: a) reinforced zone; b) control zone.

5.1.4 Comparison of UAV Photogrammetry and TLS for Deformation Monitoring

UAV photogrammetry and TLS are two of the most promising and rapidly growing technologies in the fields of remote sensing and structural monitoring. Both have a wide-ranging profile of applications, with many overlapping; yet, there are strengths and weaknesses of each technology that make them more suitable for certain applications. This section discusses the attributes of UAV photogrammetry and TLS and how they affect monitoring deformation, in this case of embankments. The discussion includes both quantitative (e.g. accuracy, errors) and qualitative (e.g. ease of operations) attributes that were discovered through this research.

Accuracy of the UAV or TLS reconstructed point clouds is an important factor to consider for deformation monitoring applications. Accuracy and errors are antonymous to a limited degree; low

point cloud errors are equivalent to high accuracy. In this research, TLS produced errors that were on the same scale but marginally better than the UAV (Table 4.8). The method and parameters used to measure GCP positions with the RTK system caused large point clouds errors and was a limitation for both UAV and TLS. TLS point cloud geometry was highly accurate, demonstrated by low scan point errors (< 5 mm) between the individual scans in a TLS survey (Table 4.6). However, georeferencing TLS point clouds with GCPs increased the target errors, and therefore point cloud errors, to be nearly equivalent (~20 mm) to UAV point cloud errors (Table 4.5). The scan point errors provide a reasonable estimate of the upper limit accuracy of the TLS point clouds. Alternatively, there is no equivalent upper limit estimate for UAV image-reconstructed point clouds. That is because of how SfM processing includes GCPs in the bundle adjustment. TLS is capable of producing high-accuracy point clouds without GCPs, whereas UAV photogrammetry requires GCPs to correct the reconstruction geometry (i.e. minimize vertical doming errors) and produce accurate point clouds. There are newer UAVs with on-board RTK sensors that reduce the need for GCPs; however, they are much more expensive and not popular in the drone industry yet. It is also unclear that RTK-UAVs will eliminate the need of GCPs. At least for the foreseeable future, GCPs will remain a crucial aspect of UAV photogrammetry.

RTK accuracy limiting the detection of deformation in this research does not mean that RTK systems are not an appropriate technique or tool for measuring GCPs for UAV or TLS monitoring applications. A more precise conclusion is that RTK systems require longer observation times at GCPs to provide high accuracy measurements for georeferencing point clouds and detecting small-scale deformations (e.g. < 30 mm). GCP accuracy required for georeferencing a point cloud will be dependent on the scale of deformation being measured. Small-scale projects where small deformations are expected would require a lower LoD, and therefore higher GCP accuracy, to confidently measure deformations, and vice-versa. It would have been valuable in this research to investigate the errors in UAV and TLS point clouds if GCP positions were measured with different

surveying equipment such as a total station. Total stations can measure GCP positions to the sub-millimetre accuracy (Leica Geosystems, 2019b) and it would have been interesting to study the affect this would have on point cloud accuracy. Comparing the accuracy of point clouds with GCPs measured by RTK and total station could provide valuable insights for engineers conducting UAV or TLS monitoring of structures.

In this research, TLS surveys took approximately 2x more time than UAV surveys. The main reason for this was the excessive amount of time it took to set up the TLS target network. Artificial targets (e.g. checkerboards, spheres) were required because the remote environment did not provide any natural features that could be used to help register scans. The checkerboards and their stands required a substantial amount of time to set up and lay out around the high-fill section. Setting up the targets on-site also required careful planning and close attention to ensure target distances and viewing angles were appropriate and scan-to-target sightlines were clear. Specific to embankments, separate target setups and scans are required on the east and west slopes, thereby essentially doubling the effort and time required to conduct TLS. In other environments with more unique, static features, such as a building or mountainous area, natural features in the environment can be used as targets. This can allow for less artificial targets (e.g. spheres, checkerboards) and improve scan registration accuracy. The calibration tests performed on the U of M campus in this research were a crucial aspect of the TLS survey design process. Overall, TLS required more preparation and planning with respect to survey setup than UAV. UAV photogrammetry simply requires a certain number of CGPs to be laid surrounding and throughout the survey area. Less time and effort are required to determine the optimal GCP layout for a UAV survey than required to design a TLS survey.

It should be noted that TLS surveys that took 2x as much time as UAV surveys only covered a 40 m long section at KM-82. This demonstrates one of the UAV's main advantages: it can quickly and efficiently survey large areas. If TLS was used to survey a full high-fill section such as KM-117, it would have required significantly more time to set up and conduct the scans. Not only can UAVs cover

much larger areas, they can access unique aerial perspectives and capture data from a wide array of viewing angles. One area that TLS outperforms UAV is the conditions under which its operable. UAVs are more sensitive to weather conditions, particularly wind. In this research, flights were often restricted because of wind or rain during site visits. TLS can not be used in rain or freezing temperatures (neither can UAVs), but wind is generally not an issue. Although it may seem trivial, weather conditions on-site at the time of monitoring is an important factor that must be considered when conducting UAV or TLS monitoring, or when deciding which technology to use.

To conclude, UAV and TLS can both produce detailed reconstructions but rely heavily on accurate GCPs for georeferencing point clouds, which is critical for measuring deformation between point clouds. Unfortunately, the RTK system and GCP accuracies of the on-site surveys limited the detection of deformations and prevented the technologies being used to their full potential. Given the strong influence of GCP measurements on point cloud accuracies, care must be taken to properly lay out the GCP network and set up the RTK system. Based on the inconclusive results of this research, TLS is better suited for monitoring smaller areas and measuring small-scale deformations. UAV photogrammetry is better suited for monitoring larger areas with deformation magnitudes greater than TLS. UAV photogrammetry is especially useful for remote areas with poor access, where TLS would be challenging. Additionally, weather and strong winds are important considerations that can severely slow progress and cause site visit extensions if UAV flights can not be performed. TLS is less affected by wind.

5.2 UAV Deformations at High-Fill Sections

This section includes an analysis of the UAV deformations at KM-48, KM-49, and KM-117. Examination of the KM-82 deformations was provided in the last section. The general deformation behaviours identified at the four high-fill sections are discussed, as well as a comparison of the albris and Phantom UAVs for monitoring deformation of embankments.

The vertical difference between 2018 and 2019 point clouds was evident at all high-fill sections. This vertical difference was caused by inconsistent measurement of the RTK base station height above the benchmark in 2018 and 2019. The magnitude of the vertical difference varied between sections and was dependent on the steel rod benchmark's height above ground surface. Vertical distances between the 2018 and 2019 point clouds at each high-fill section were analyzed to determine the distance to vertically shift the 2019 point clouds (Table 5.2). The deformation results after the vertical shift and subsequent M3C2 comparisons showed that point cloud tilting was evident, again caused by georeferencing issues with the RTK data. Therefore, registration (vertical translation and rotation) of the 2018 and 2019 point clouds was executed to align them. Point clouds were registered based on segments of the point clouds that were within the area encompassed by GCPs (Figure 4.7 and Figure 5.24) to negate doming error influence. However, these segments were only minor portions of the full point clouds because of the poor GCP coverage in 2018. The negative impact this had on the deformation results is discussed below.

Results for KM-48, KM-49, and KM-117 include M3C2 comparisons of the point clouds that were aligned by: a) vertical shifting, and b) vertical translation and rotation registration. Both comparisons are included because the results of the two were notably different than each other. Comparing the vertical shift and registration point cloud comparisons allows for a more thorough discussion of the detected deformations and gives insights to the limitations of each alignment method. Cross-sections were extracted from the point clouds after vertical shifting or registration for comparison. The cross-sections selected at each site were within the GCP coverage area to eliminate the influence of doming errors. Cross-section comparisons were exaggerated 10x and cleaned for better visualization and interpretation of deformations.

Figure 5.24 Fine registration segment areas for UAV point clouds: a) KM-48; b) KM-49.

Table 5.2 2018–2019 point cloud vertical comparison results and selected 2019 point cloud vertical shifts.

Section	Technology	2018–2019 measured vertical difference (m)			Selected 2019 point cloud shift (m)
		Mean	Median	Peak of distribution	
KM-48	albris	-0.113	-0.113	-0.113	+0.113
	Phantom	-0.139	-0.135	-0.133	+0.133
KM-49	albris	-0.151	-0.148	-0.145	+0.145
	Phantom	-0.138	-0.136	-0.133	+0.133
KM-82	albris	-0.340	-0.341	-0.340	+0.340
	Phantom	-0.332	-0.336	-0.340	+0.332
	TLS-east	-0.340	-0.346	-0.353	+0.353
	TLS-west	-0.322	-0.322	-0.316/-0.337*	+0.322
KM-117	albris	-0.474	-0.472	-0.484	+0.472

* vertical difference distribution resembled a bimodal distribution with two peaks.

5.2.1 KM-48

All M3C2 comparisons (albris and Phantom, shifted and registered) showed similar deformation behaviours at KM-48. On the east slope, negative change was consistently detected, which was likely settlement of the slope caused by weakening and movement at the toe. The west slope exhibited positive change at the upper-slope and negative change at the lower-slope. The negative change at the lower-slope could be settlement, similar to the east slope behaviour. The positive change at the west upper-slope could be a lateral spreading or slumping behaviour of the upper-slope under traffic loading as the toe berm restricts movement of the mid-slope.

Although the deformation behaviours were consistent between comparisons, the magnitudes of deformation varied. The albris generally detected larger deformations than the Phantom. It is unclear

what caused this. It could be that the higher quality albris images produced a more accurate point cloud with more surface details, which causes larger deformations to be detected. There were also differences between the comparisons of the registered and vertical shifted point clouds. It appears that the vertical shifted point clouds were better aligned than their registered counterparts. This is based on the deformations detected at the embankment toes. Deformation at the east and west toes should be relatively uniform. The vertical shifted point cloud comparisons showed this, but the registered point cloud comparisons did not. The latter showed positive change along the east toe (50–100 mm) and negative change (-50–0 mm) along the west toe. This non-uniformity occurred during the registration process likely because the registration segment (Figure 5.24) covered a larger portion of the east slope. The registration algorithm was influenced more by the east slope, thereby overcompensating for the east slope points and causing the registered point cloud to be tilted.

The LoD estimates (Figure 5.27) suggest that the albris point cloud is more accurate than the Phantom point cloud. This was primarily due to larger registration errors at GCPs in the Phantom reconstruction (Table 4.8). The M3C2 significant change estimates (Figure 5.28) were shown for the vertical shifted point cloud comparisons because it was deemed they were more accurate than the registered point cloud comparisons. Significant change estimates showed that the majority of detected deformations are less than the LoD. The only deformations computed as significant are changes at the road surface and vegetation growth near the extents. The entire sideslopes, which are the focus of this research, were deemed insignificant change by the M3C2 comparison. The cross-section comparison (Figure 5.29) showed minor differences between the shifted and registered 2019 point clouds. The LoD limitation and influence of the registration method (e.g. vertical shift or rotation registration), as well as other factors that affected interpretation of the results, will be further discussed in Section 5.2.4.

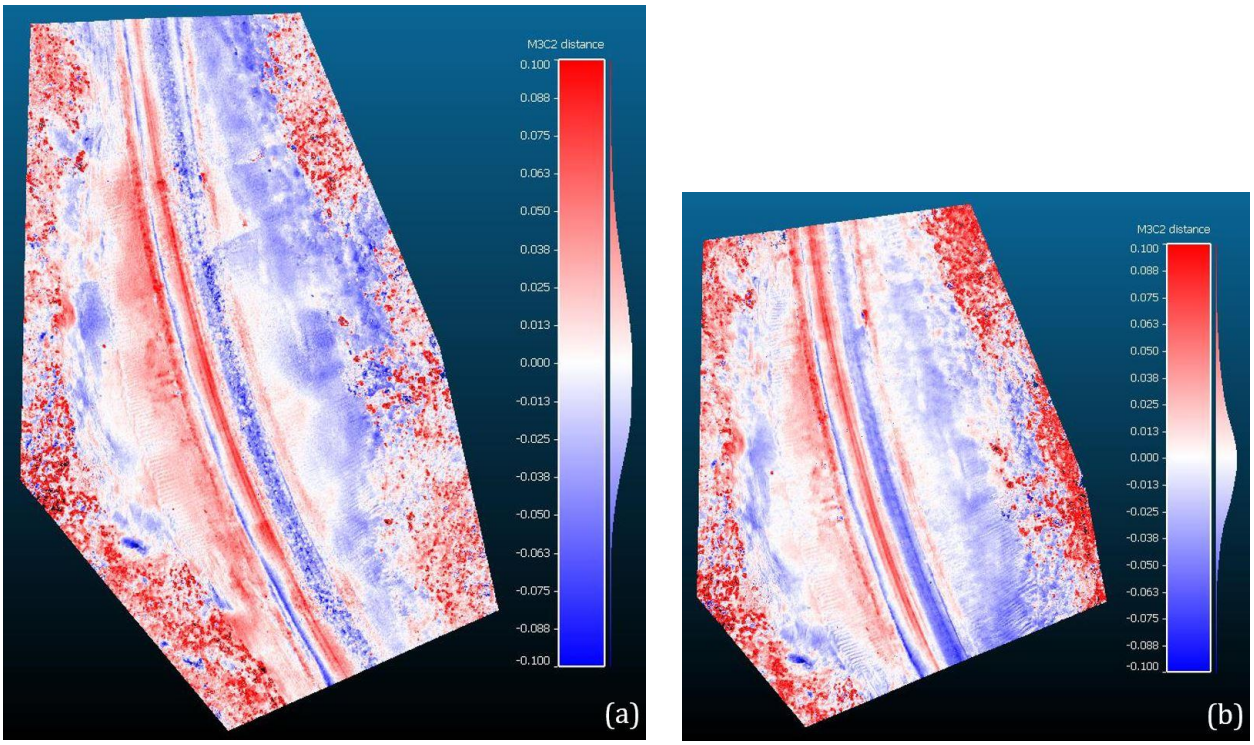

Figure 5.25 KM-48 UAV M3C2 deformation after vertical shift (scale: ±100 mm): a) albris; b) Phantom.

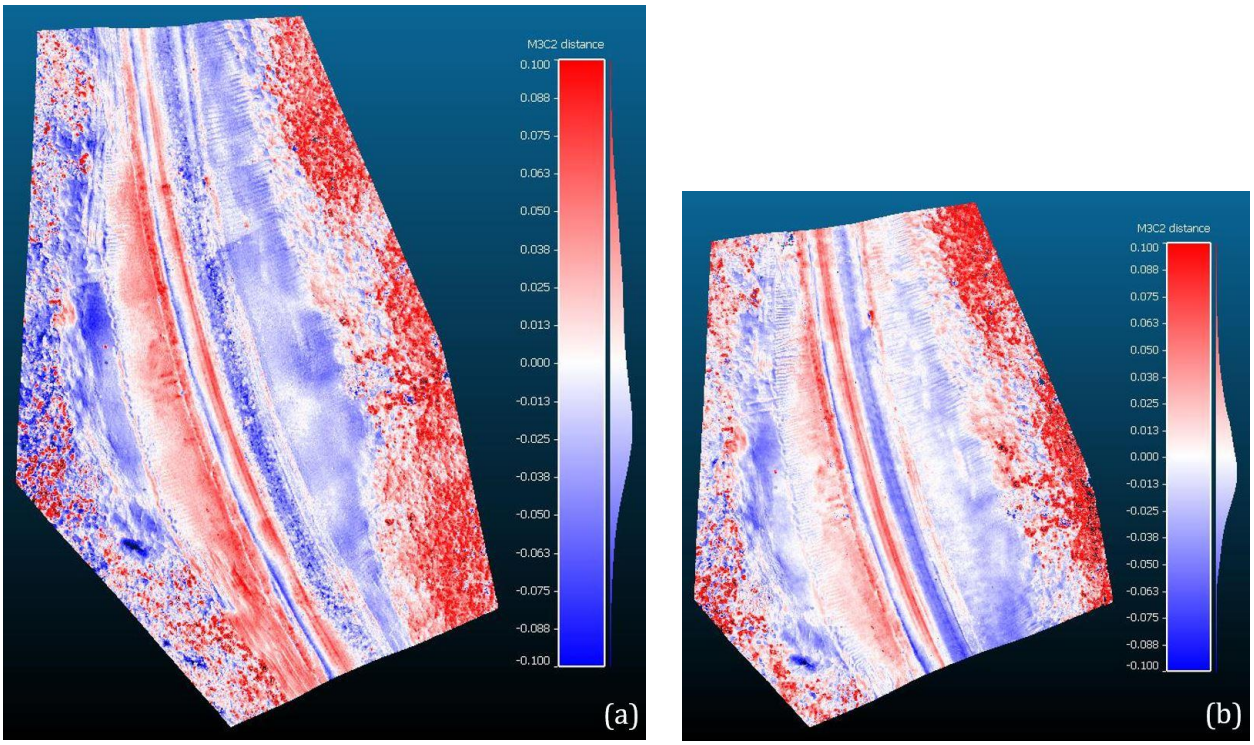

Figure 5.26 KM-48 UAV M3C2 deformation after vertical translation and rotation registration (scale: ±100 mm): a) albris; b) Phantom.

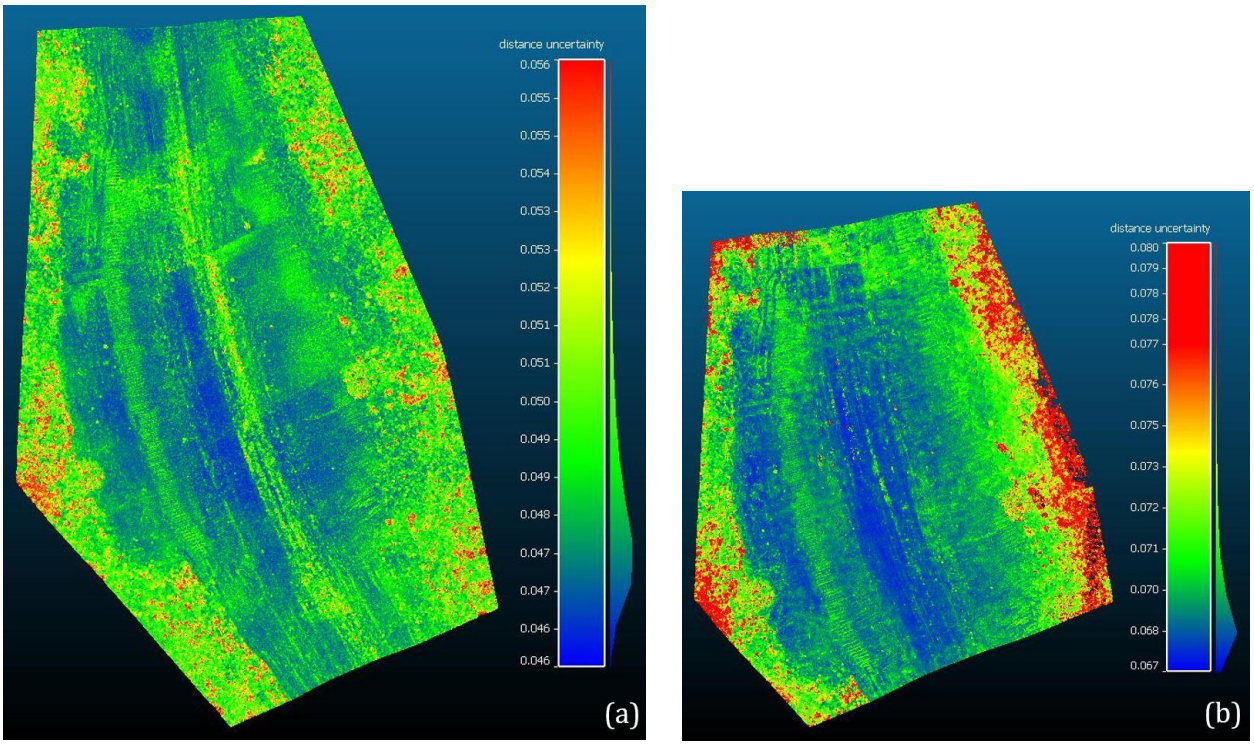

Figure 5.27 KM-48 UAV M3C2 LoD estimates: a) albris (scale: 46–56 mm); b) Phantom (scale: 67–80 mm).

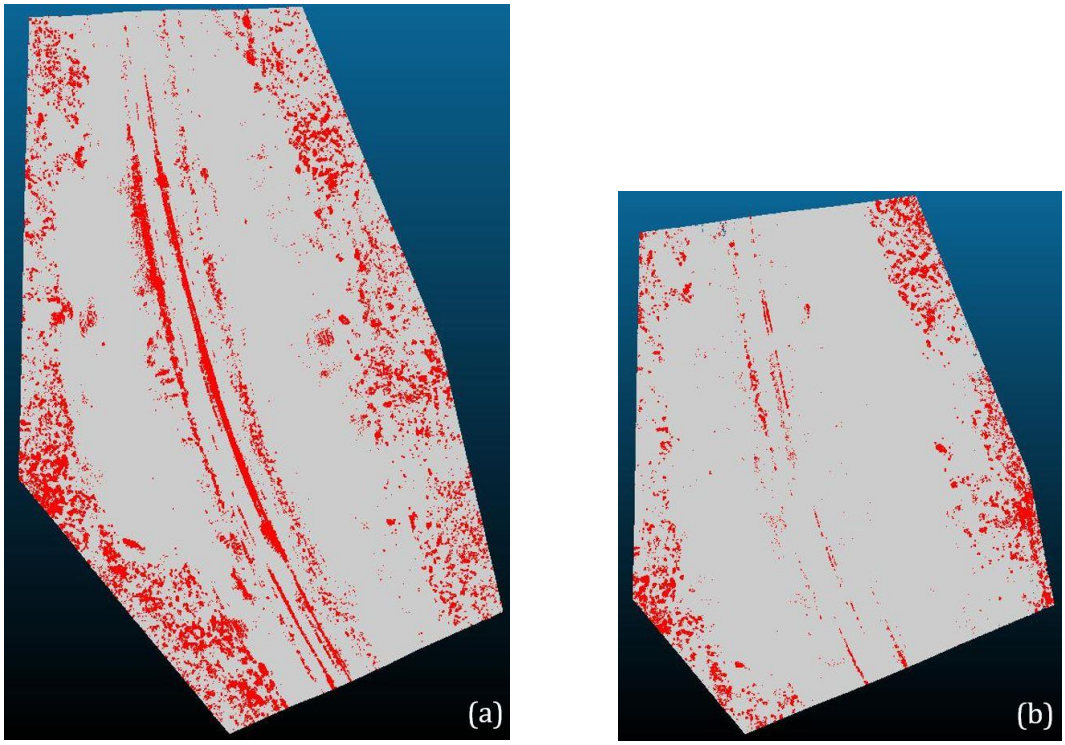

Figure 5.28 KM-48 UAV M3C2 significant change estimates for the vertical shift comparison: a) albris; b) Phantom.

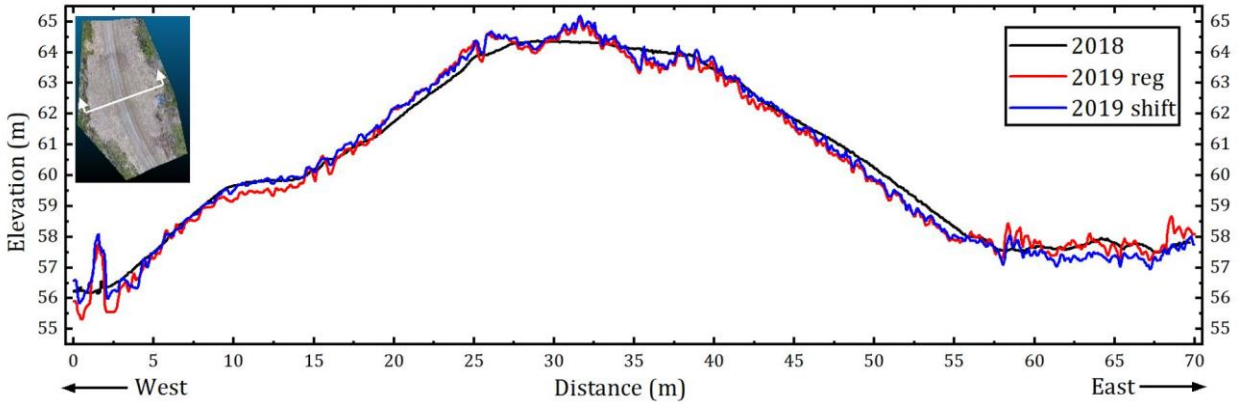

Figure 5.29 KM-48 cross-sections with 10x vertical exaggeration and smoothing.

5.2.2 KM-49

The albris and Phantom point cloud comparisons at KM-49 produced notably similar results; despite the fact the point clouds were shifted vertically by different distances. Conversely, the vertical shifted

and registered point cloud comparisons produced dramatically different deformation results. With exception of the northwest area along the road surface and west slope, none of the deformations detected were consistent between the vertical shifted and registered point cloud comparisons. The vertical shifted point cloud comparison detected negative change ranging from 50 to 100 mm near the middle of the reconstruction along the road surface and down the east slope. This deformation is quite different than the rest of the comparison and is most likely inaccurate, at least to the extreme magnitude detected. The registered point cloud comparison showed approximately zero deformation in the middle of the reconstruction along the road surface and extreme positive change (< 80 mm) along the slopes and toes in the entire south half. This extreme difference between the vertical shifted and registered comparisons highlights the major influence that the registration process can have on the deformation results. The two registration methods produced deformation results that were not only drastically different in magnitudes but opposite directions of change.

My interpretation of the deformation results is that the negative change in the middle of the vertical shifted comparisons (Figure 5.30) was caused by a vertical doming error in the 2018 point cloud. Doming errors can cause the middle of reconstructions to be generated at higher elevations than reality if GCPs are not properly located. In the 2018 UAV surveys, GCPs were clustered in the north half away from the detected negative change (Figure 5.24). When the 2019 point cloud was compared to the domed 2018 point cloud, it appeared as negative change in the middle. The extreme positive change at the south extents of the registered point cloud comparisons were caused by inaccurate alignment of the 2019 point cloud during registration. Due to GCP coverage in 2018, the point clouds were registered using only a small portion of the point clouds (Figure 5.24). Any rotation of the point cloud segment is extrapolated outwards and the rotation effects are stronger further away from the segment. Rotation must have occurred during registration and since the registration segment was located in the north half of the point clouds, the south extents experienced major

elevation increases. When the registered point clouds were compared, the rotation resulted in the detection of erroneous positive change greater than 100 mm (Figure 5.31).

The north segment of the comparisons within the 2018 GCP coverage is the only semi-reliable deformations at KM-49. *semi* is emphasized because even though there was no doming influence, the measured deformations are still subject to the alignment process of vertical shifting or rotation registration. The cross-sections extracted from the north segment (Figure 5.34) show negative change at the road surface, which was likely displacement of the gravel surfacing due to traffic. At this cross-section, the east slope deformed minorly and the west slope appears to be spreading laterally outwards. Although this is a possible deformation behaviour of an embankment on permafrost, the detected lateral spreading is likely not accurate because of the point cloud alignment and accuracy issues discussed above.

LoD estimates for KM-48 (Figure 5.32) replicated the results from KM-49, showing that LoD estimates of the albris comparisons were approximately half the magnitude of the Phantom comparisons. This would typically translate to a much higher level of confidence in the deformation measurements; however, because of poor point cloud errors and alignment, the albris does not produce results any more meaningful than the Phantom. Significant change estimates of the vertical shift comparisons at KM-49 (Figure 5.33) confirm this finding. Similar to KM-48, most of the embankment slopes deformations were less than the computed LoD. The only areas of the point cloud comparisons that were deemed significant change were located: a) in the middle of the reconstructions where doming errors occurred in 2018; and b) surrounding the embankment at the toes where vegetation growth occurred.

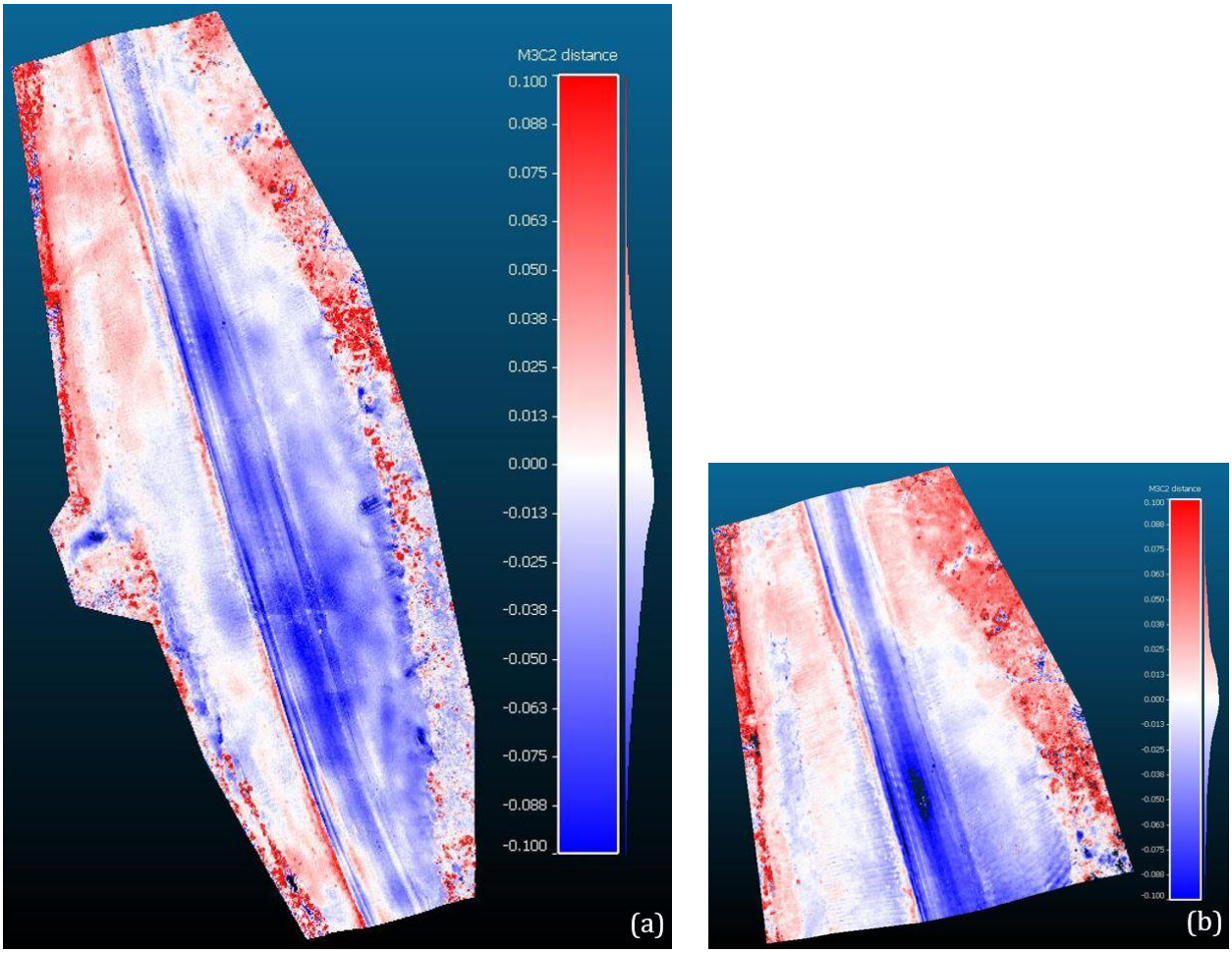

Figure 5.30 KM-49 UAV M3C2 deformation after vertical shift (scale: ±100 mm): a) albris; b) Phantom.

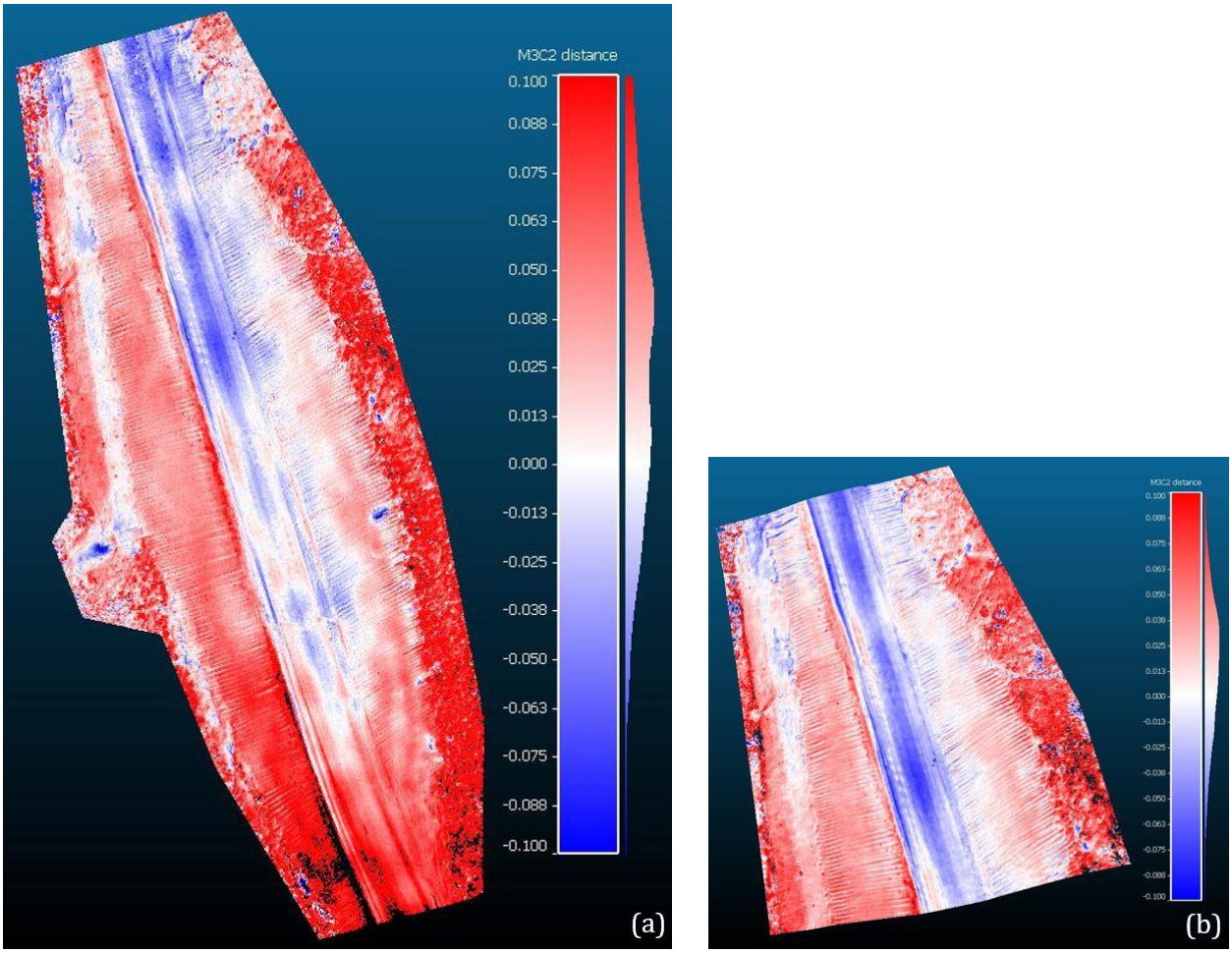

Figure 5.31 KM-49 UAV M3C2 deformation after vertical translation and rotation registration (scale: ±100 mm): a) albris; b) Phantom.

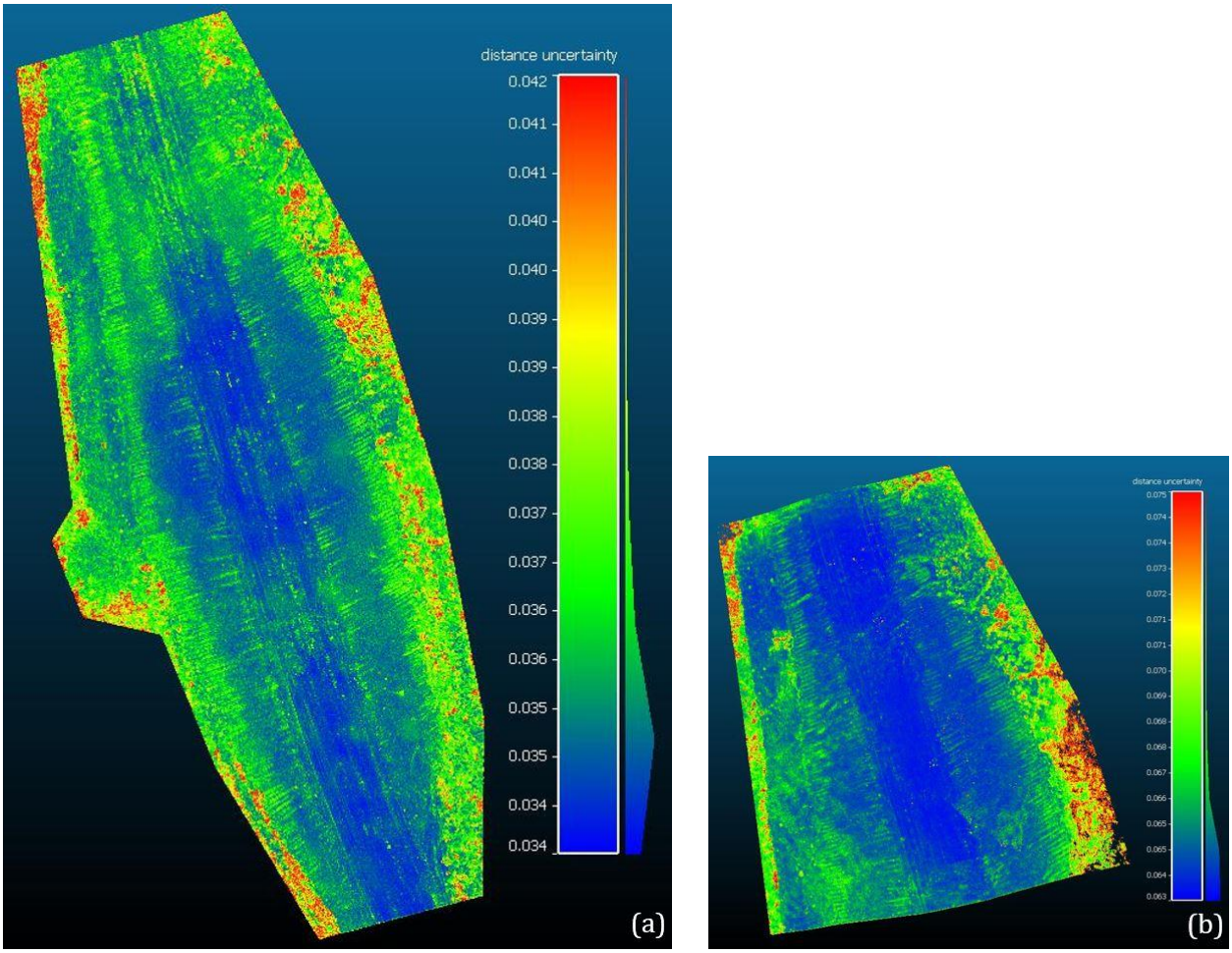

Figure 5.32 KM-49 UAV M3C2 LoD estimates: a) albris (scale: 34–42 mm); b) Phantom (scale: 63–75 mm).

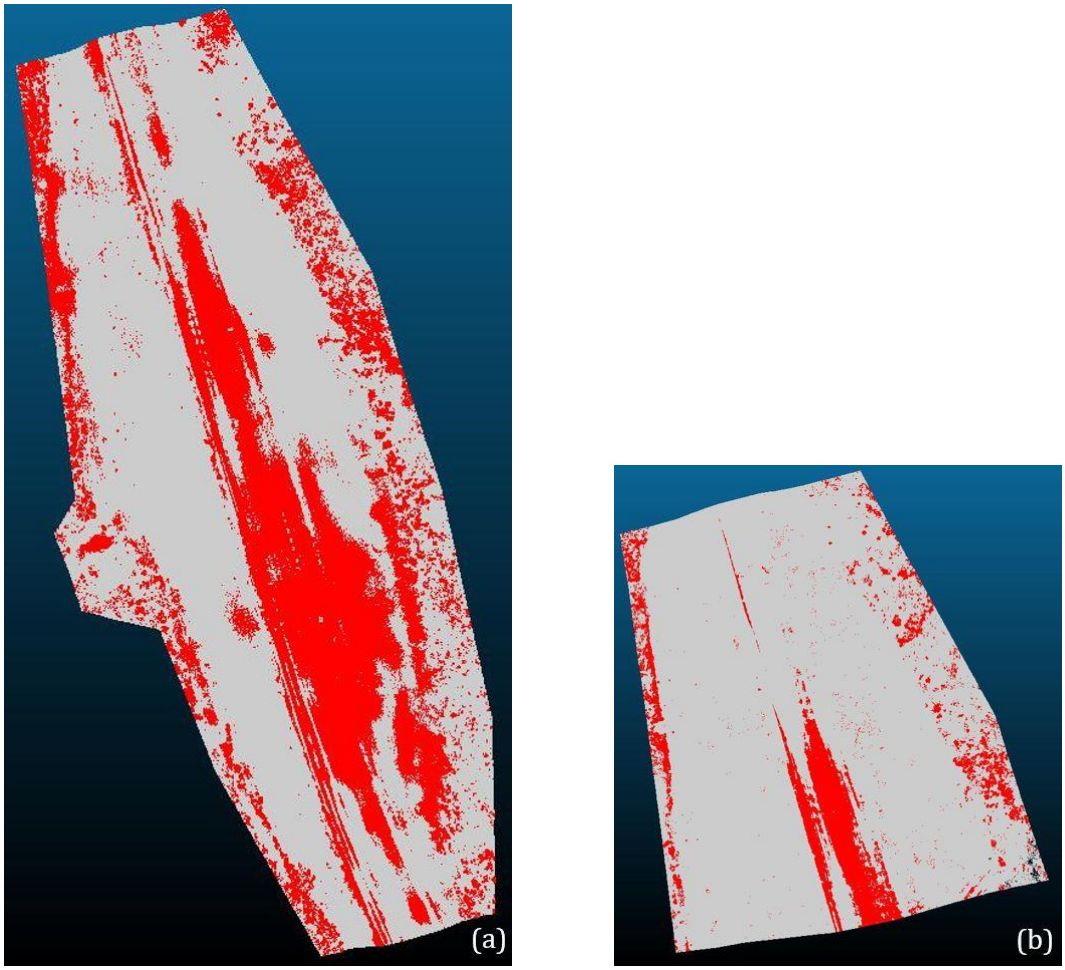

Figure 5.33 KM-49 UAV M3C2 significant change estimates for the vertical shift comparison: a) albris; b) Phantom.

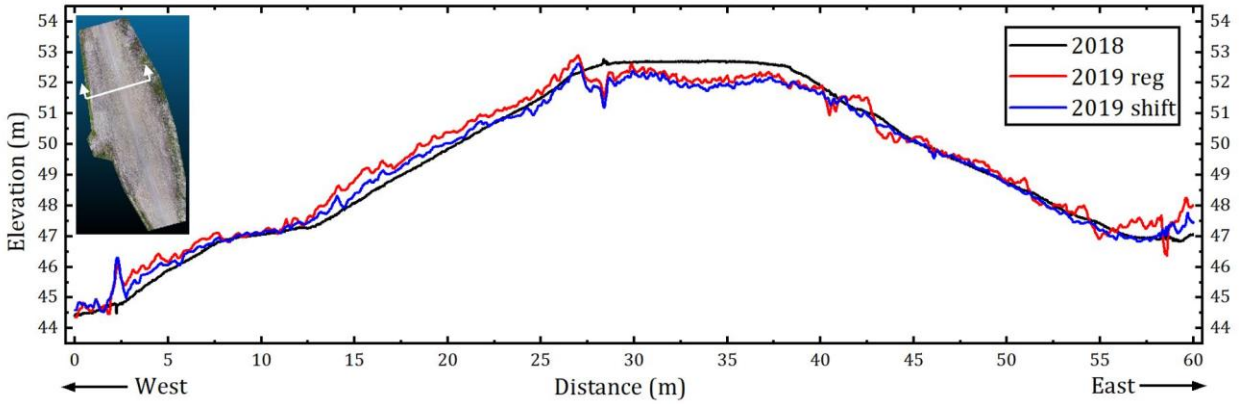

Figure 5.34 KM-49 cross-sections with 10x vertical exaggeration and smoothing.

5.2.3 KM-117

2017–2018 deformations at KM-117 (Figure 5.35) were larger than 2018–2019 deformations (Figure 5.36). Note the deformation scale of ±200 mm in 2017–2018 compared to ±100 mm in 2018–2019. The large deformations in 2017–2018 were most likely not actual deformation, but instead a product of poor reconstruction quality of the 2018 point cloud Two factors contributed to the poor quality: 1) poor GCP measurement quality and therefore large registration error (Table 4.8); and 2) no oblique images in the image set. The 2017–2018 cross-section comparison (Figure 5.40a) emphasized the deformation behaviours detected by M3C2. Positive change along the road surface was due to gravel resurfacing that occurred after the UAV flights in summer 2017. Other spots of extreme positive change throughout the comparison, particularly on the east slope, was due to vegetation growth (Figure 5.37a).

Generally in 2017–2018, there appears to be negative change occurring at the upper-slopes that is reduced to near-zero deformation at the toe berms (Figure 5.35 and Figure 5.40a). However, this behaviour is opposite to that detected at the other high-fill sections. KM-48, KM-49, and KM-82 all detected positive change at the upper-slope. The deformation behaviour at KM-117 could be different because of its large scale (12 m high). Although, if the negative change at the upper-slope was actual deformation, the movement of fill material would have to manifest as positive change at the lower-slope because: a) the embankment fill material is not consolidating; and b) the permafrost foundation beneath the embankment is not settling. Because positive change at the lower-slope was not detected, the negative change is likely only an erroneous artefact of the registration process. For this comparison, the 2017 point cloud was registered towards the 2018 point cloud because the 2018 point cloud was thought to be more accurate. The gravel resurfacing occurred after the 2017 UAV flights; therefore, it was only in the 2018 point cloud. The resurfacing influenced the registration algorithm and caused the 2017 point cloud to be shifted slightly upwards for the road surfaces to align. Then when the point clouds were compared, negative change was detected at the upper-slope

due to the upwards shift. 2017–2018 LoD estimates (Figure 5.38a) were larger than the 2018–2019 LoD estimates (Figure 5.38b) due to high uncertainties in the RTK survey of GCPs in 2017. The only areas that were deemed significant change in the 2017–2018 comparison were the resurfaced road and spots of vegetation growth (Figure 5.39a).

2018–2019 deformation measurements at KM-117 were very similar for the vertical shifted and registered point cloud comparisons (Figure 5.36). The positive change of up to 100 mm at the north and south extents was not actual deformation, but instead it was the manifestation of a doming error that occurred outside the 2018 GCP coverage. The extreme negative change (> 100 mm) at the east upper-slope adjacent to the shoulder is evidence of the vegetation clearing that occurred (Figure 5.37b). Near-zero deformation was detected throughout most of the area encompassed by GCPs. Perhaps the most interesting deformation detected was the negative change 'channels' running parallel to the culvert on both slopes. The same channel deformation behaviour occurred at KM-82. It is unclear what caused these 100 mm deep channels to form. One possibility is that warm air passing through the culverts in summer is influencing the thermal conditions within the embankment. Temperature variations could change the thermal conditions and causing fill material around the culvert to expand or contract with temperature changes. These movements within the embankment could manifest as deformations at the embankment slope surfaces such as the channels. This concept is currently being researched using numerical modelling within the author's research group. More accurate and precise UAV monitoring is required to confirm the channel behaviour and obtain better estimates of the deformation magnitude.

Significant change estimates of the 2018–2019 vertical shifted point cloud comparison (Figure 5.39b) showed that only a few areas on the embankment had deformations large enough to be considered significant: 1) the negative change channels; 2) the vegetation clearing area; 3) along the embankment shoulders where regrading occurred; and 4) a rock and gravel deposit on the west

upper-slope, which was likely dumped during shoulder regrading. Generally, the embankment slope deformations were determined to be insignificant by M3C2.

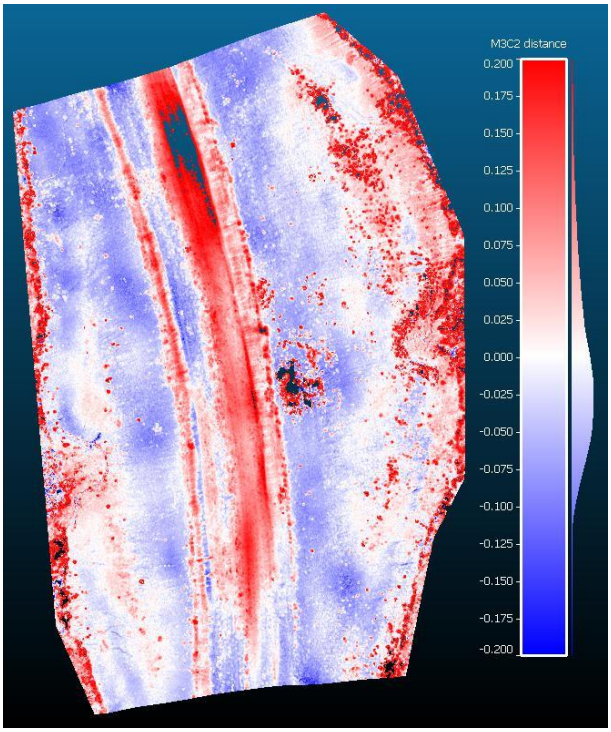

Figure 5.35 KM-117 albris UAV 2017–2018 M3C2 deformation after registration (scale: ±200 mm).

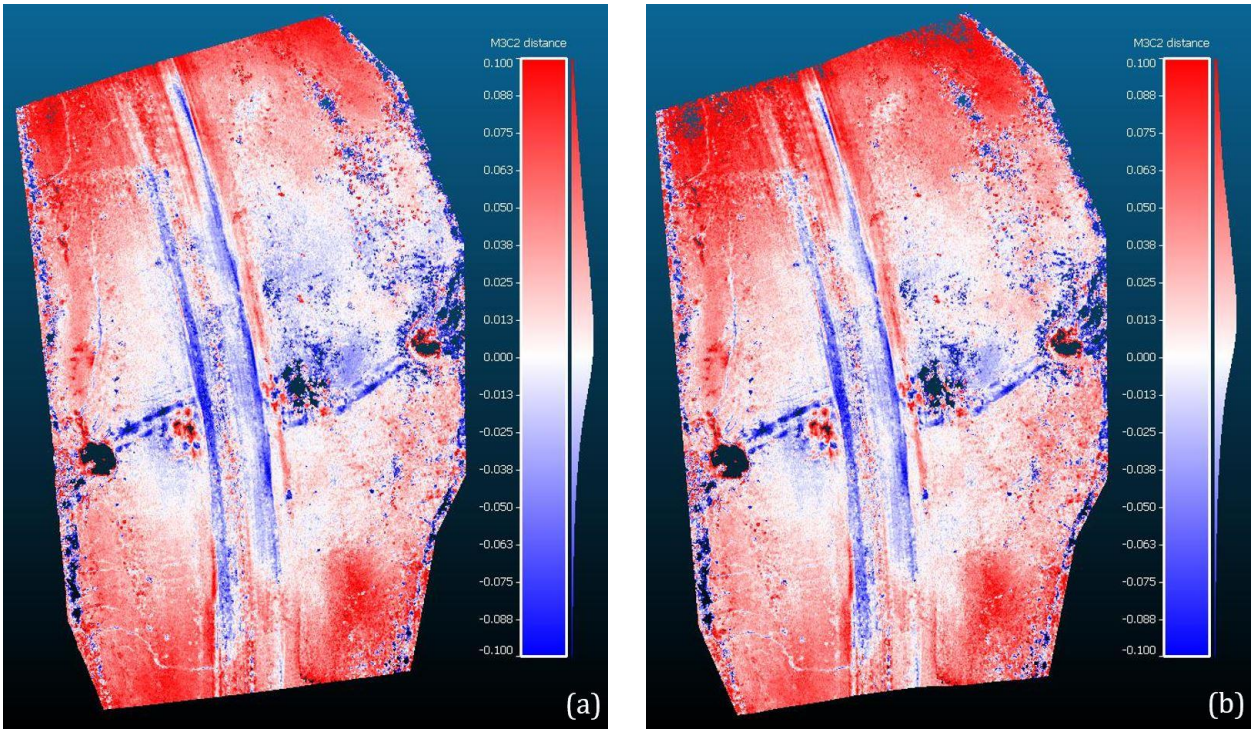

Figure 5.36 KM-117 albris UAV 2018–2019 M3C2 deformation (scale: ±100 mm): a) vertical shift; b) vertical translation and rotation registration.

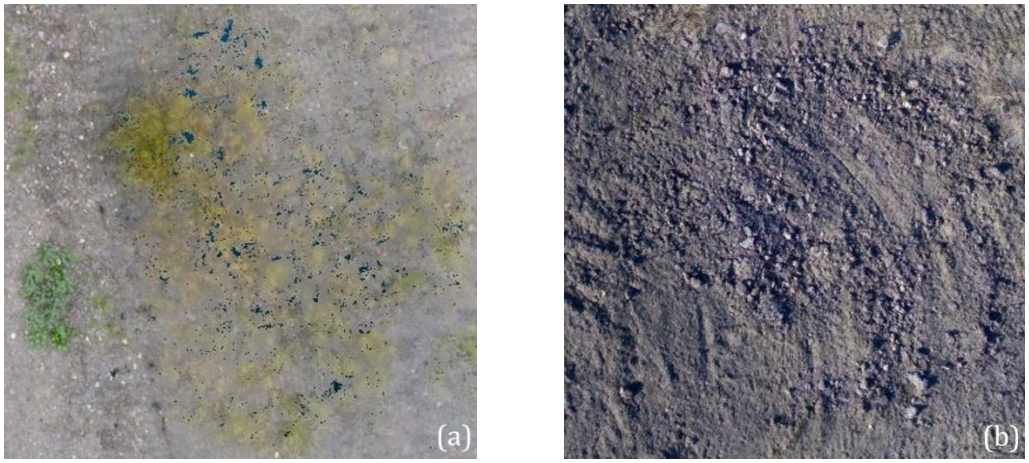

Figure 5.37 KM-117 point cloud segments showing vegetation: a) 2018 pre-clearing; b) 2019 post-clearing.

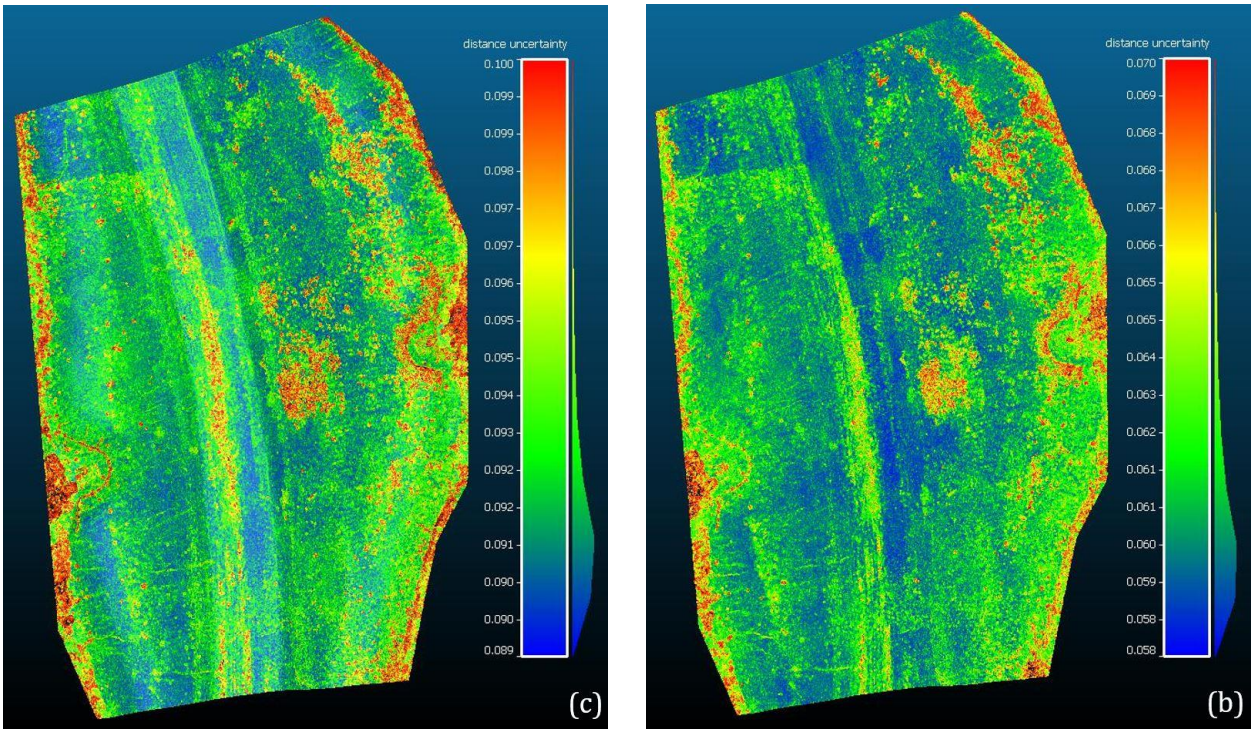

Figure 5.38 KM-117 albris UAV M3C2 LoD estimates: a) 2017–2018 (scale: 89–100 mm); b) 2018–2019 (scale: 58–70 mm).

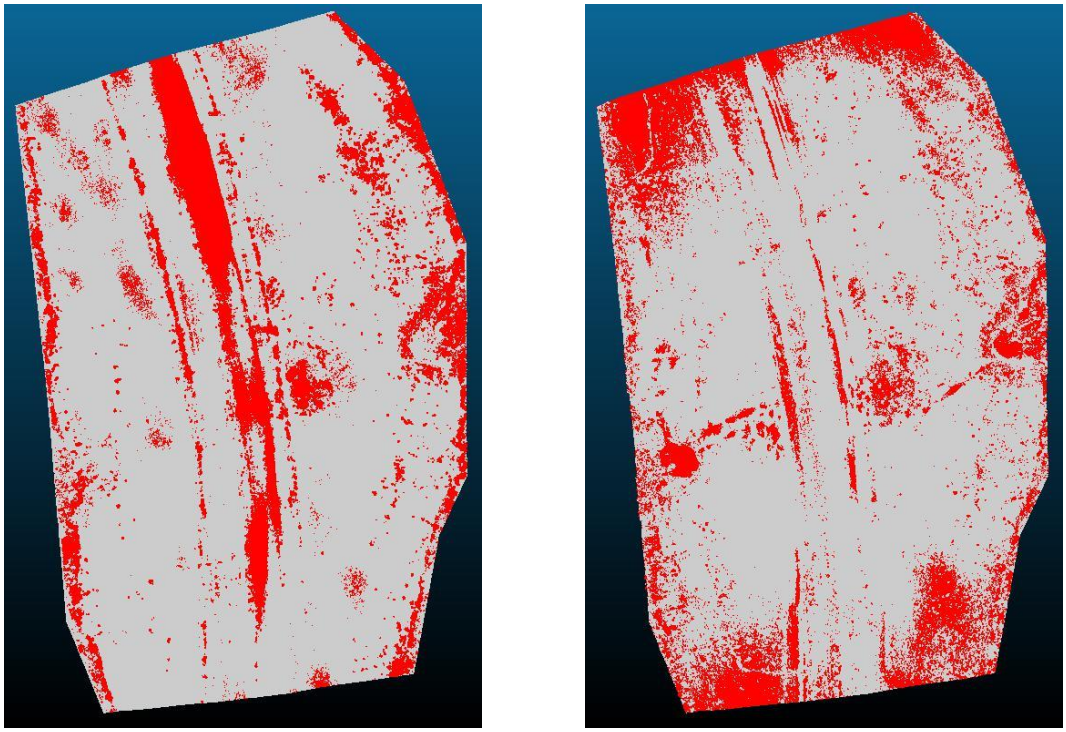

Figure 5.39 KM-117 albris UAV M3C2 significant change estimates: a) 2017–2018; b) 2018–2019 vertical shifted.

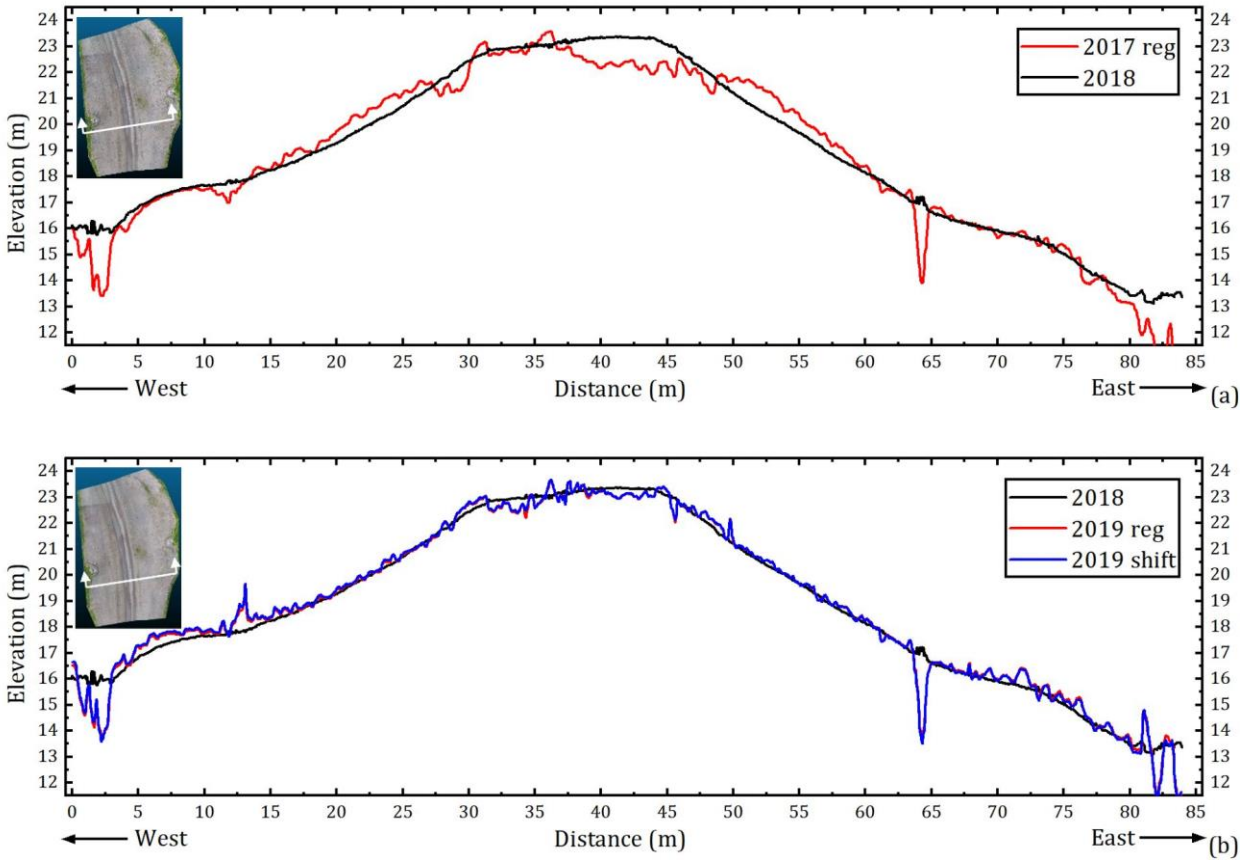

Figure 5.40 KM-117 cross-sections with 10x vertical exaggeration and smoothing: a) 2017–2018; b) 2018–2019.

5.2.4 Deformation Behaviours of High-Fill Sections

Deformations detected at the four high-fill sections were inconsistent in their general behaviours. For examples, deformations at KM-117 were markedly different in the two monitoring years. Or at KM-48, positive change was detected on the west slope and negative change on the east slope. Likewise, KM-49 had major differences between deformations on its east and west slopes. Deformation magnitudes were relatively consistent in the 2018–2019 comparisons at the four high-fill sections; however, differences in the deformation behaviours between sections heavily outweigh the similarities.

There were also differences in the results of the albris and Phantom UAVs. KM-82 Phantom results showed larger deformation magnitudes and distinct inaccuracies throughout the reconstructions.

The inaccuracies occurred in the Phantom comparisons because there were fewer and lower quality images processed. albris and Phantom results were remarkably similar at both KM-48 and KM-49. The only difference was that the albris deformations were slightly larger than the Phantom deformations; opposite to the results at KM-82. LoD estimates of the albris comparisons ranged from 20 to 30 mm lower than the Phantom comparisons. This was mainly because of the higher quality albris camera capturing more detailed imagery. In this case though, the lower LoD of the albris comparisons did not provide any benefits because: a) inaccurate point cloud alignment methods prevented actual deformations from being measured; and b) the actual deformations of the embankment (measured by instrumentation) were still less than the lower LoD. The true benefits of using a high-quality senseFly albris instead of a consumer-level DJI Phantom 4 Pro could therefore not be properly assessed.

Four mistakes during data acquisition caused errors in the image-reconstructed point clouds and ultimately led to the inconsistent deformation behaviours. The first mistake was inconsistently measuring the RTK base station height above the steel rod benchmarks (discussed in detail in Section 5.1.1). This caused a vertical difference between the 2018 and 2019 point clouds, which required modification of point cloud data in order to align the point clouds for comparison. It was impossible to know the exact distance the point cloud should have been shifted. It was therefore a matter of approximating the vertical shift distance, which is an imperfect method and was likely not done to a high degree of accuracy. Furthermore, the fact that the albris and Phantom point clouds required different vertical shift distances questions the method's accuracy.

The second mistake was improperly setting up the RTK base station on a tilt (i.e. not level; discussed in detail in Section 5.1.1). The tilt in the base station was transferred to the reconstructed point clouds when they were georeferenced using the RTK-measured GCPs and caused non-uniform deformations on the embankment slopes. This non-uniform deformation was most-prevalent in the TLS comparisons at KM-82, yet the possibility of tilting in the UAV point clouds introduced an entirely

new source of error. Rotation registration of the point clouds was used to correct the tilting. However, the registration method had inherent limitations, and it was difficult to asses which point cloud was more accurate (e.g. pre- or post-registration).

The third mistake was poor layout of GCPs in 2018. The GCP network should ideally be equally spaced surrounding the entire high-fill section; as was the case in 2019. Regrettably in 2018, the GCPs were clustered near the centre of the high-fill section. This caused doming errors to develop in the 2018 point clouds and prevented accurate deformation measurements in areas outside the GCP coverage. Of the 2018 GCP networks, KM-82 was definitely the most widely distributed around the embankment. This resulted in the KM-82 2018–2019 comparisons having similar deformation behaviours on both slopes and no areas with extreme deformations caused by doming errors. This demonstrates the importance of having a widely distributed GCP network. Additionally, better GCP distributions would have allowed larger point cloud segments to be used to align point clouds using the vertical shift and registration methods, which would have improved the quality and accuracy of the vertical shifts and registrations.

The fourth and final mistake made during data acquisition was insufficient RTK observation times at GCPs. Shorter observation times resulted in high positional uncertainties at GCPs, causing point clouds to be 'pulled' in disagreeing directions due to slight errors in the GCP positions. The results of this were large point cloud errors and general inaccuracies in point cloud geometry, which were compounded during point cloud comparisons. The LoD and significant change estimates at the four high-fill sections emphasize the strong influence of the RTK measurements. Almost the entire embankment at the high-fill sections was not considered significant change. This essentially means that deformations at the high-fills sections can not be classified as actual deformations. RTK observation times were increased year-to-year but not enough to reduce GCP positional uncertainties to a level appropriate for the small-scale deformation measurements. Nevertheless,

despite the inconclusive significant change results, the author attempted to derive meaning from the deformation measurements.

The combination of the four mistakes made the alignment of point clouds difficult. The behaviour and magnitude of deformations were highly sensitive to the vertical shift magnitude and rotation registration process. Modifying point cloud data to address the data acquisition mistakes introduced sources of error that make the deformation results unreliable. The objective of the UAV monitoring was to validate UAV deformations at KM-82 with the SAA displacement data to give confidence in deformation measurements at the other high-fill sections. However, because of the issues discussed above, UAV deformations at KM-82 were not comparable to SAA data and could not be validated. There was no other method available to validate UAV deformations at the other high-fill sections. The author provided their best interpretation of the results while considering the various sources of error and high degree of uncertainty.

I intended to use the UAV deformations to investigate the geotechnical causes and factors contributing to deformation of embankments on permafrost. Unfortunately, issues that occurred on-site during data acquisition limited the accuracy of the results and prevented confident examination of embankment deformations. Given that the UAV and TLS deformation results were found to be inconsistent and inconclusive, much work needs to be done in improving the performance of this emerging technology.

5.3 Summary of Results and Discussion

High-fill sections along ITH showed deformations including toe subsidence and lateral spreading. Some of the high-fill sections showed positive change at the upper-slope and negative change at the lower-slope, while other sections showed the opposite behaviour. Deformations on the east and west slopes at each high-fill section were non-uniform and inconsistent. The inaccuracy of GCP positions measured by the RTK survey system limited the accuracy of reconstructed point clouds and

restricted small-scale deformations from being measured. Furthermore, the behaviours and magnitudes of UAV and TLS deformations were highly sensitive to the point cloud alignment methods. UAV and TLS measured deformations were not comparable to instrumentation displacement data at KM-82. No significant differences were detected between deformations of the geotextile reinforced and non-reinforced zones. Failing to validate the UAV deformations with the instrumentation data at KM-82 decreased the reliability of deformations detected at the other high-fill sections. The causes of detected deformations were conjectured, but inaccuracies of the point clouds and alignment methods limited the identification of deformation mechanisms.

If monitoring small-scale deformations by UAV photogrammetry or TLS, an RTK system is not the best method for measuring GCP positions. With RTK systems, measurement uncertainties of GCP positions are often too high, especially in the vertical direction, and cause inaccuracies when georeferencing point clouds. When deciding to use UAV photogrammetry or TLS for deformation monitoring, two critical factors must be considered: expected deformation magnitude and survey area size. Generally, UAV photogrammetry is better suited for monitoring deformations of embankments, unless small deformations are expected and the survey area is appropriately sized for TLS. Deformation results obtained by the albris were slightly more accurate but comparable to the Phantom results. The Phantom could have produced equivalent results if imagery was captured from shorter distances to counteract the lower-quality camera. Overall, the author's opinion is that the performance of the albris does not justify its high cost compared to the Phantom.

CHAPTER 6: CONCLUSION

This last chapter summarizes the research work that was completed; states conclusions, which were derived from the research objectives and based on the calibration tests and deformation monitoring; and provides recommendations for practitioners using UAV photogrammetry or TLS to monitor deformations. Lastly, a guideline that provides step-by-step instructions for using UAV photogrammetry to monitor deformations is included.

6.1 Summary

The Inuvik-Tuktoytaktuk Highway (ITH) in Northwest Territories, Canada was built during winter on ice-rich continuous permafrost with no cuts in the ground to preserve the permafrost foundation. Several high-fill sections were required along the highway to meet vertical geometry specifications. Embankments built on permafrost during winter are susceptible to deformations in the summer immediately following construction as ice within the embankment melts and in subsequent years as permafrost at the embankment toe thaws. One high-fill section at KM-82 on ITH was reinforced with wicking woven geotextiles to improve slope stability by providing a direct path to transport water out of the embankment fill and tensile resistance on the slopes. Instrumentation was installed in the reinforced test zone and a non-reinforced control zone to measure horizontal and vertical displacements and temperatures within the embankment.

Unmanned aerial vehicle (UAV) photogrammetry and terrestrial laser scanning (TLS) were used to survey the high-fill sections in three subsequent years and determine deformations. The senseFly albris and DJI Phantom 4 Pro UAVs were used to acquire aerial imagery and Pix4D processed the imagery to reconstruct point clouds. The FARO Focus^{3D} X 330 laser scanner and FARO SCENE software were used to acquire and process scan data to generate point clouds. The Leica GS14 antennas and CS20 controller were the RTK survey system used to measure ground control point (GCP) positions for georeferencing UAV and TLS point clouds. UAV photogrammetry and TLS are

both relatively new technologies being for monitoring the deformation of structures. Significant time was dedicated to learning about the technologies, developing best operating practices, calibrating the technologies to quantify their accuracies, and designing the on-site surveys.

The research section at KM-82 and three other high-fill sections along ITH were monitored. KM-48 and KM-49 were both 8 m high embankments. KM-117 was the thickest embankment section on ITH, standing 12 m high. TLS was only conducted at KM-82 and UAV monitoring was performed at all high-fill sections. Improvements to the data acquisition methods were implemented each year to reduce errors. Accuracies of the UAV and TLS point clouds were quantified based on GCP errors.

Some of the point clouds were not properly georeferenced and required alignment prior to deformation measurement. Point clouds were aligned in CloudCompare using two methods: vertical shifting and registration by the iterative closest point (ICP) algorithm. After alignment, point clouds from each year were compared using the multiscale model-to-model cloud comparison (M3C2) algorithm in CloudCompare to determine deformations. An analysis of embankment cross-sections extracted from the point clouds was also performed for each high-fill section.

Due to the novelty of research methods and technologies used, a few mistakes were made on-site during data acquisition, primarily when using the RTK survey system to measure GCP positions. Georeferencing point clouds with the inaccurate GCP positions caused errors in the UAV and TLS reconstructed point clouds. Although the results were not as conclusive as originally intended, several lessons were learned that will be valuable for future researchers and practitioners using UAV photogrammetry and TLS to monitor deformations. Through this research, techniques were developed to: calibrate UAV photogrammetry and TLS instruments to measure deformation; investigate factors that influence point cloud accuracy and design surveys based on the findings; estimate positional errors within UAV and TLS derived point clouds; align point clouds that are improperly georeferenced using two methods; critique measured deformations by considering the influence of reconstruction and alignment errors; and interpret deformations through the lens of

permafrost degradation dynamics. As far as the author is aware, this is the first time that UAV photogrammetry and TLS have been used together to measure deformations of an embankment in the Arctic. One critical finding of the research was the importance of accurate and well-distributed GCPs. Sophisticated sensors and advanced imaging technologies can produce extremely detailed reconstructions; however, as this research showed, the ability of the technologies to accurately measure deformations depends strongly on the accuracy of the GCP network and georeferencing process. Although GCPs may seem supplementary to the UAV or TLS data acquisition, the importance of accurate GCPs cannot be understated and appropriate time should be taken to set up a well-distributed GCP network and measure high-quality GCP positions with precise survey equipment.

6.2 Conclusions

The following conclusions are derived from the research objectives and based on the technology calibration tests and deformation monitoring results at the high-fill sections:

1. UAV photogrammetry and TLS are powerful imaging technologies that can reconstruct high-quality 3D point clouds for monitoring deformation of structures. However, the accuracy of GCPs used to georeference point clouds must be appropriately low to maintain the high accuracy of the UAV and TLS derived point clouds. In this research, the inaccuracy of GCP positions measured by the RTK survey system limited the accuracy of reconstructed point clouds and restricted the measurement of small-scale deformations.
2. High-fill sections along ITH showed deformations including toe subsidence and lateral spreading. However, these deformations could not be validated because of unreliable georeferencing accuracies and alignment methods.
3. The behaviours and magnitudes of UAV and TLS deformations were highly sensitive to the point cloud alignment methods. Some of the high-fill sections showed positive change at the upper-slope and negative change at the lower-slope, and other sections showed the

opposite behaviour. Deformations on the east and west slopes at each high-fill section were non-uniform. Furthermore, deformations of the albris and Phantom showed high variability.

4. UAV measured deformations underestimated the instrumentation displacement data at KM-82 by approximately 30 mm, while TLS measured deformations were reasonably close to the instrumentation data after point cloud alignment. No significant differences were detected between deformations of the geotextile reinforced and non-reinforced zones.
5. Deformation channels parallel to culverts were detected at KM-82 and KM-117 by both the albris and Phantom UAVs. The channels were approximately 100 mm deep and located at the upper-slope at KM-82 and down the entire sideslopes at KM-117. It is unclear what caused the deformation channels to form; yet, it is hypothesized that the culverts are a contributing factor. Heat flowing through the culvert in summer could influence the thermal conditions of the fill material surrounding the culvert and manifest as deformations at the embankment surface. Further research and more UAV monitoring is required to confirm the channel behaviour and determine the underlying deformation mechanism.
6. Mistakes made during the data acquisition of GCP positions using the RTK survey system prevented proper comparison of point clouds and caused the deformation results to be inconsistent and inconclusive. Given the strong influence of GCP measurements on point cloud accuracies, care must be taken to properly lay out the GCP network and set up the RTK system.
7. Causes and factors contributing to deformations of the high-fill sections were not determined. General deformation behaviours were conjectured, but inaccuracies of the point clouds and alignment methods limited the identification of deformation mechanisms.
8. Uncertainty of deformation measurements can be quantified using a spatially variable level of detection (LoD) based on point cloud registration errors and surface roughness. UAV and

TLS point cloud registration errors can be estimated by analyzing GCP errors in the point clouds.

9. Improvements to the data acquisition methods each year significantly improved the accuracy of reconstructed point clouds and decreased the LoD of deformation measurements. These improvements included: a) RTK survey system—installing permanent benchmarks at each section and increasing the observation time at GCPs; b) UAV—including oblique images (at optimal viewing angle of 45°), decreasing image GSD, and increasing the number of GCPs; and c) TLS—increasing the total number of targets and including targets along the road surface that are scanned for both sideslopes to generate a single point cloud.
10. UAV photogrammetry and TLS can both be used to monitor deformations of structures. Two critical factors that must be considered when deciding which technology to use for deformation monitoring are the expected deformation magnitude and the survey area size. In this research, TLS point clouds achieved mean scan point errors ≤ 5 mm; yet, target errors increased to approximately 15 mm when georeferenced with GCPs. Based on this observation and reported TLS accuracies in literature, TLS is better suited for monitoring smaller-scale sites and measuring small-scale deformations. UAV photogrammetry is better suited for monitoring larger areas with deformation magnitudes greater than TLS. UAV photogrammetry is especially useful for remote areas with poor access, where TLS would be challenging. TLS is also less affected by wind and adverse weather conditions. Generally, UAV photogrammetry is better suited for monitoring deformations of embankments, unless small deformations are expected and the survey area is appropriately sized for TLS.
11. The senseFly albris and DJI Phantom 4 Pro can both capture imagery to reconstruct high-accuracy point clouds for deformation monitoring. Results obtained by the albris were slightly more accurate but comparable to the Phantom results. The Phantom could produce

equivalent results if imagery is captured from shorter distances to counteract the lower-quality camera. The Phantom has advantages over the albris including it is easier to control, has longer battery life, and is substantially less expensive. In the author's opinion, the performance of the albris does not justify its high cost compared to the Phantom.

12. An RTK system is not the best method for measuring GCP positions if small-scale deformations (e.g. < 50 mm) are being monitored by UAV photogrammetry or TLS. Although RTK systems are simple to use and can acquire data relatively quickly, measurement uncertainties of GCP positions are often too high, especially in the vertical direction, and cause inaccuracies when georeferencing point clouds. RTK measurement uncertainties can be reduced by increasing the observation time at GCPs; however, major time increases are often infeasible when conducting UAV surveys due to uncertainty and time restrictions associated with unpredictable weather conditions.

6.3 Recommendations

Based on the results and conclusions of this research, the following are recommended for monitoring deformations using UAV photogrammetry or TLS:

1. The Government of Northwest Territories Department of Infrastructure (GNWT-DOI) should use UAV photogrammetry to monitor deformations of critical sections along ITH. UAV photogrammetry should be used over TLS for the following reasons: a) it can cover larger areas in less time; b) setting up surveys is faster and less labour intensive; c) good-quality results with sufficient accuracy can be obtained with a UAV that costs substantially less than a TLS system. Note that anyone flying a UAV in Canada requires a pilot license and must abide to Transport Canada regulations. It is known that GNWT-DOI is already using UAVs to monitor some of their infrastructure. This thesis may provide valuable information that could help them to improve their data acquisition and processing methods. The

deformations results showed that close-range and accurate imagery is required to detect small-scale deformations of the embankment in order to predict larger instabilities before they occur.

2. When monitoring deformations of embankments constructed during winter in permafrost regions, monitoring should begin immediately following construction. The largest embankment deformations occur in the summer after construction as ice in the fill material melts. It is important to obtain a baseline model of the embankment prior to thawing and deformation. It is also recommended to conduct multiple surveys during the first year to capture the progression of deformations. An example of this would be to survey once at the start of spring immediately after snowmelt, once or twice during summer, and once in the fall. This would provide good monitoring over the embankment's critical deformation period in the first year.
3. Deformation monitoring with UAV photogrammetry or TLS should be coupled with another means of measuring deformation, such as survey equipment or instrumentation, to validate results.
4. UAV or TLS data acquisition and processing methods should produce results with a deformation LoD appropriate for the expected magnitude of deformations on-site. Practice UAV flights or TLS scans of the planned on-site survey and data processing should be performed to estimate the deformation LoD prior to fieldwork. If the determined point cloud errors and LoD are too large, data acquisition methods should be adjusted until an appropriate LoD is reached. Adjusting data acquisition methods could include modifying the TLS scan or UAV flight parameters, increasing the GCP observation time if using an RTK system, or improving the survey setup by using more GCPs or targets. Although this approach may consume time at the beginning of the project, confidence in the data acquisition methods and expected errors will be invaluable later in the project. Accurate

LoD estimates appropriate for the expected deformations are essential for the practitioner's ability to draw meaningful conclusions from the measured deformations.

5. Survey benchmarks should be established on-site to reference all UAV or TLS surveys to a consistent coordinate system. If the project is on permafrost, steel rods hammered deep into the ground are a suitable benchmark. Benchmark coordinates can be determined with an RTK base station set up on the benchmark.
6. A total station should be used to measure GCP positions if small-scale deformations (e.g. < 50 mm) are being monitored with UAV photogrammetry or TLS. Total stations can measure points with sub-millimetre accuracy in significantly less time than it takes RTK systems to measure points with 5–10 mm accuracy. One limiting characteristic of total stations is that sightlines are required from the benchmark to GCPs.
7. For small-scale deformation monitoring applications, if an RTK system is to be used for measuring GCP positions, the observation time at each GCP should be 5–7 minutes (minimum 3 minutes) in order to reduce GCP positional errors to acceptable levels.
8. A few permanent GCPs should be installed at each site being monitored by UAV photogrammetry. An example of a permanent GCP would be a steel rod hammered into the ground with a tip designed for checkerboard GCPs to be attached for the duration of UAV surveys. Direct comparison of permanent GCP positions in the point clouds from each UAV survey would allow for the recognition and correction of any systematic errors that develop (e.g. vertical errors in point clouds).
9. The GCP network for UAV monitoring must encompass the entire section being monitored in order to reduce doming errors. Deformation measurements outside GCP coverage are unreliable.
10. A combination of cloud-to-cloud and target-based registration methods are recommended for processing TLS scan data. Cloud-to-cloud registration should be used to align scans and

generate the point cloud geometry. Target-based registrations should then be used to georeference the point cloud with the GCP targets. Combining the two registration methods will maintain the millimetre-level accuracy of the point cloud geometry and the georeferencing accuracy will be dependent on the quality of GCP positional data.

6.4 Guideline for using UAV Photogrammetry to Monitor Deformations

The calibration tests and embankment deformation monitoring in this research work allowed for the development of an operational guideline for using UAV photogrammetry to monitor deformations. A guideline was not created for TLS because less effort was dedicated to developing the TLS methods and work remains to improve them. The author is confident that the procedures and techniques developed for monitoring with UAV photogrammetry are refined and practical.

The guideline for using UAV photogrammetry to monitor deformations is Appendix B. It was developed for the application of monitoring deformation of embankments, but it can be applied to a variety of other structures or landforms. The guideline not only outlines recommended methods but also the missteps to avoid, which are often overlooked. There is some repetition in the guideline because it is meant to be a stand-alone document that does not require reference to sections in this thesis. The guideline is recommended for any practitioners using UAV photogrammetry to monitor deformations, including researchers, surveyors, construction contractors, and government agencies.

REFERENCES

Abellán, A., Vilaplana, J. M., Calvet, J., García-Sellés, D., & Asensio, E. (2011). Rockfall monitoring by Terrestrial Laser Scanning - Case study of the basaltic rock face at Castellfollit de la Roca (Catalonia, Spain). *Natural Hazards and Earth System Science*, *11*(3), 829–841. https://doi.org/10.5194/nhess-11-829-2011

Abellán, A., Oppikofer, T., Jaboyedoff, M., Rosser, N. J., Lim, M., & Lato, M. J. (2014). Terrestrial laser scanning of rock slope instabilities. *Earth Surface Processes and Landforms*, *39*(1), 80–97. https://doi.org/10.1002/esp.3493

Argue, G. H., Fullerton, J. A., Johnston, G. H., & Peckover, F. L. (1981). Roads, railways and airfields. In G. H. Johnston (Ed.), *Permafrost Engineering and Construction* (pp. 345–391). New York: Wiley.

Barnhart, T. B., & Crosby, B. T. (2013). Comparing two methods of surface change detection on an evolving thermokarst using high-temporal-frequency terrestrial laser scanning, Selawik River, Alaska. *Remote Sensing*, *5*(6), 2813–2837. https://doi.org/10.3390/rs5062813

Batenipour, H., Kurz, D., Alfaro, M., Graham, J., & Kalynuk, K. (2010). Results from an Instrumented Highway Embankment on Degraded Permafrost. *63rd Canadian Geotechnical Conference & 6th Canadian Permafrost Conference*, 512–519.

Brasington, J., Langham, J., & Rumsby, B. (2003). Methodological sensitivity of morphometric estimates of coarse fluvial sediment transport. *Geomorphology*, *53*(3–4), 299–316. https://doi.org/10.1016/S0169-555X(02)00320-3

Buffi, G., Manciola, P., Grassi, S., Barberini, M., & Gambi, A. (2017). Survey of the Ridracoli Dam: UAV–based photogrammetry and traditional topographic techniques in the inspection of vertical structures. *Geomatics, Natural Hazards and Risk*, *8*(2), 1562–1579. https://doi.org/10.1080/19475705.2017.1362039

Bush, E., & Lemmen, D. S. (2019). *Canada's Changing Climate Report*. Ottawa, ON.

Cigna, F., Banks, V., Donald, A., Donohue, S., Graham, C., Hughes, D., … Parker, K. (2017). Mapping Ground Instability in Areas of Geotechnical Infrastructure Using Satellite InSAR and Small UAV Surveying: A Case Study in Northern Ireland. *Geosciences*, *7*(3), 51. https://doi.org/10.3390/geosciences7030051

CloudCompare. (2019). CloudCompare (version 2.10) [GPL software]. Retrieved from http://www.cloudcompare.org/

Cook, K. L. (2017). An evaluation of the effectiveness of low-cost UAVs and structure from motion for geomorphic change detection. *Geomorphology*, *278*, 195–208. https://doi.org/10.1016/j.geomorph.2016.11.009

De Guzman, E. M. B., & Alfaro, M. C. (2018). Geotechnical properties of fibrous and amorphous peats for the construction of road embankments. *Journal of Materials in Civil Engineering*, *30*(7), 1–12. https://doi.org/10.1061/(ASCE)MT.1943-5533.0002325

De Guzman, E. M. B., Stafford, D., Alfaro, M. C., Doré, G., & Arenson, L. U. (2018). Large-scale direct shear testing of compacted frozen soil under freezing and thawing conditions. *Cold Regions Science and Technology*, *151*, 138–147. https://doi.org/10.1016/j.coldregions.2018.03.011

De Guzman, E. M., Alfaro, M., Arenson, L., & Dore, G. (2019, submitted). Thermal Regime of Highway Embankments in the Arctic: Field Observations and Numerical Simulations. *Journal of Geotechnical and Geoenvironmental Engineering*.

DJI. (2018). Phantom 4 Pro. Retrieved from https://www.dji.com/ca/phantom-4-pro

Donahue, B., Wentzel, & Berg, R. (2013). *Guidelines for RTK/RTN GNSS Surveying in Canada*. https://doi.org/http://dx.doi.org/10.1016/j.biologicals.2009.02.010

Durham Geo-Enterprises Inc. (2020). DGSI Slope Indicator: Piezometers. Retrieved from https://durhamgeo.com/piezometers/

Eltner, A., Baumgart, P., Maas, H. G., & Faust, D. (2015). Multi-temporal UAV data for automatic measurement of rill and interrill erosion on loess soil. *Earth Surface Processes and Landforms*, *40*(6), 741–755. https://doi.org/10.1002/esp.3673

Eltner, A., Kaiser, A., Castillo, C., Rock, G., Neugirg, F., & Abellán, A. (2016). Image-based surface reconstruction in geomorphometry-merits, limits and developments. *Earth Surface Dynamics*, *4*(2), 359–389. https://doi.org/10.5194/esurf-4-359-2016

Esch, D. C. (1983). Design and Performance of Road and Railway Embankments on Permafrost. In *4th International Conference on Permafrost*.

Fan, L., Smethurst, J., Powrie, W., & Sellaiya, A. (2014). Seasonal slope surface deformation measured with TLS. *IOP Conference Series: Earth and Environmental Science*, *17*(1). https://doi.org/10.1088/1755-1315/17/1/012264

FARO Technologies Inc. (2015). *FARO Laser Scanner Focus3D X 330 Manual*.

FARO Technologies Inc. (2019a). SCENE.

FARO Technologies Inc. (2019b). *Laser Scanner Best Practices*.

FARO Technologies Inc. (2016). *SCENE 6.0 User Manual*.

Fonstad, M. A., Dietrich, J. T., Courville, B. C., Jensen, J. L., & Carbonneau, P. E. (2013). Topographic structure from motion: A new development in photogrammetric measurement. *Earth Surface Processes and Landforms*, *38*(4), 421–430. https://doi.org/10.1002/esp.3366

Fortier, R., LeBlanc, A.-M., & Yu, W. (2011). Impacts of permafrost degradation on a road embankment at Umiujaq in Nunavik (Quebec), Canada. *Canadian Geotechnical Journal*, *48*, 720–740. https://doi.org/10.1139/T10-101

Furukawa, Y., Curless, B., Seitz, S. M., & Szeliski, R. (2010). Towards internet-scale multi-view stereo. *Proceedings of the IEEE Computer Society Conference on Computer Vision and Pattern Recognition*, 1434–1441. https://doi.org/10.1109/CVPR.2010.5539802

Furukawa, Y., & Ponce, J. (2007). Accurate , Dense , and Robust Multi-View Stereopsis, *1*(1), 1–14. https://doi.org/10.1109/CVPR.2007.383246

Girardeau-Montaut, D., Roux, M., Marc, R., & Thibault, G. (2005). Change detection on points cloud data acquired with a ground laser scanner. *International Archives of Photogrammetry, Remote Sensing and Spatial Information Sciences*, *36*(3), W19. https://doi.org/10.1.1.221.8313

Gómez-Gutiérrez, Á., de Sanjosé-Blasco, J. J., de Matías-Bejarano, J., & Berenguer-Sempere, F. (2014). Comparing two photo-reconstruction methods to produce high density point clouds and DEMs in the Corral del Veleta Rock Glacier (Sierra Nevada, Spain). *Remote Sensing*, *6*(6), 5407–5427. https://doi.org/10.3390/rs6065407

Government of Northwest Territories. (2013). *Inuvik To Tuktoyaktuk Highway Construction Drawings*.

Gruen, A., & Akca, D. (2005). Least squares 3D surface and curve matching. *ISPRS Journal of Photogrammetry and Remote Sensing*, *59*(3), 151–174. https://doi.org/10.1016/j.isprsjprs.2005.02.006

Harwin, S., & Lucieer, A. (2012). Assessing the accuracy of georeferenced point clouds produced via multi-view stereopsis from Unmanned Aerial Vehicle (UAV) imagery. *Remote Sensing*, *4*(6), 1573–1599. https://doi.org/10.3390/rs4061573

Heritage, G. L., & Large, A. R. G. (2009). Principles of 3D Laser Scanning. *Laser Scanning for the Environmental Sciences*, 21–34.

Hinzman, L. D., Bettez, N. D., Bolton, W. R., Chapin, F. S., Dyurgerov, M. B., Fastie, C. L., … Yoshikawa, K. (2005). Evidence and implications of recent climate change in Northern Alaska and other Arctic regions. *Climatic Change*, *72*(3), 251–298. https://doi.org/10.1007/s10584-005-5352-2

Hsieh, Y. C., Chan, Y. C., & Hu, J. C. (2016). Digital elevation model differencing and error estimation from multiple sources: A case study from the Meiyuan Shan landslide in Taiwan. *Remote Sensing*, *8*(3). https://doi.org/10.3390/rs8030199

Immerzeel, W. W., Kraaijenbrink, P. D. A., Shea, J. M., Shrestha, A. B., Pellicciotti, F., Bierkens, M. F. P., & De Jong, S. M. (2014). High-resolution monitoring of Himalayan glacier dynamics using unmanned aerial vehicles. *Remote Sensing of Environment*, *150*, 93–103. https://doi.org/10.1016/j.rse.2014.04.025

James, M. R., & Robson, S. (2012). Straightforward reconstruction of 3D surfaces and topography with a camera: Accuracy and geoscience application. *Journal of Geophysical Research: Earth Surface*, *117*(3), 1–17. https://doi.org/10.1029/2011JF002289

James, M. R., & Robson, S. (2014). Mitigating systematic error in topographic models derived from UAV and ground-based image networks. *Earth Surface Processes and Landforms*, *39*(10), 1413–1420. https://doi.org/10.1002/esp.3609

James, M. R., Robson, S., D'Oleire-Oltmanns, S., & Niethammer, U. (2017). Optimising UAV topographic surveys processed with structure-from-motion: Ground control quality, quantity and bundle adjustment. *Geomorphology*, *280*, 51–66. https://doi.org/10.1016/j.geomorph.2016.11.021

Jaud, M., Passot, S., Le Bivic, R., Delacourt, C., Grandjean, P., & Le Dantec, N. (2016). Assessing the Accuracy of High Resolution Digital Surface Models Computed by PhotoScan® and MicMac® in Sub-Optimal Survey Conditions. *Remote Sensing*, *8*. https://doi.org/10.3390/rs8060465

Javernick, L., Brasington, J., & Caruso, B. (2014). Modeling the topography of shallow braided rivers using Structure-from-Motion photogrammetry. *Geomorphology*, *213*, 166–182. https://doi.org/10.1016/j.geomorph.2014.01.006

Kovacevic, M. S., Gavin, K., Oslakovic, I. S., & Bacic, M. (2016). A New Methodology for Assessment of Railway Infrastructure Condition. *Transportation Research Procedia*, *14*, 1930–1939. https://doi.org/10.1016/j.trpro.2016.05.160

Lague, D., Brodu, N., & Leroux, J. (2013). Accurate 3D comparison of complex topography with terrestrial laser scanner: Application to the Rangitikei canyon (N-Z). *ISPRS Journal of*

Photogrammetry and Remote Sensing, *82*, 10–26. https://doi.org/10.1016/j.isprsjprs.2013.04.009

Lane, S. N., Westaway, R. M., & Hicks, D. M. (2003). Estimation of erosion and deposition volumes in a large, gravel-bed, braided river using synoptic remote sensing. *Earth Surface Processes and Landforms*, *28*(3), 249–271. https://doi.org/10.1002/esp.483

Lato, M. (2018). Personal communication (interview).

Lato, M. J., Hutchinson, D. J., Gauthier, D., Edwards, T., & Ondercin, M. (2015). Comparison of airborne laser scanning, terrestrial laser scanning, and terrestrial photogrammetry for mapping differential slope change in mountainous terrain, *52*, 129–140.

Lato, M., Mitchell, A., Porter, M., & Gaib, S. (2017). Monitoring landslide velocity at Ten Mile Slide with ground based LiDAR. In *GeoOttawa*.

Laussedat, A. (1899). *La Métrophotographie*. Paris: Gauthier-Villars.

Leica Geosystems. (2019a). Leica Infinity. Heerbrugg, Switzerland. https://doi.org/10.1007/SpringerReference_28001

Leica Geosystems. (2019b). *Leica Geosystems Total Station Comparison Chart*.

Leica Geosystems. (2016). *Leica Viva GS14 Data sheet*. Heerbrugg, Switzerland.

Lichti, D. D., & Jamtsho, S. (2006). Angular resolution of terrestrial laser scanners. *Photogrammetric Record*, *21*(114), 141–160. https://doi.org/10.1111/j.1477-9730.2006.00367.x

Lim, M., Mills, J., & Rosser, N. (2009). Laser scanning surveying of linear features: Considerations and applications. *Laser Scanning for the Environmental Sciences*, 245–261. https://doi.org/10.1002/9781444311952.ch15

Lowe, D. G. (2004). Distinctive Image Features from Scale-Invariant Keypoints David. *International Journal of Computer Vision*. https://doi.org/10.1023/B:VISI.0000029664.99615.94

Lowe, D. G. (1999). Object Recognition from Local Scale-Invariant Features. In *Proceedings of the International Conference on Computer Vision*. Corfu. https://doi.org/10.1130/2011.2482(04)

McGregor, R., Hayley, D., Wilkins, G., Hoeve, E., Grozic, E., Roujanski, V., … Doré, G. (2010). *Guidelines for Development and Management of Transportation Infrastructure in Permafrost Regions*. Transportation Association of Canada. Ottawa.

Measurand. (2019). Measurand's ShapeArray. Retrieved from https://measurand.com/

Meeks, C. T., Bonneau, D. A., Hutchinson, D. J., & Gauthier, D. (2017). The Use of Unmanned Aerial Vehicles (UAVs) for Slope Stability Assessment. In *GeoOttawa*.

Miller, P. E., Mills, J. P., Barr, S. L., Lim, M., Barber, D., Parkin, G., … Hall, J. (2008). Terrestrial Laser Scanning for Assessing the Risk of Slope Instability along Transport Corridors. *The International Archives of the Photogrammetry, Remote Sensing and Spatial Information Sciences*, 495–500.

Monserrat, O., & Crosetto, M. (2008). Deformation measurement using terrestrial laser scanning data and least squares 3D surface matching. *ISPRS Journal of Photogrammetry and Remote Sensing*, *63*(1), 142–154. https://doi.org/10.1016/j.isprsjprs.2007.07.008

Mukupa, W., Roberts, G. W., Hancock, C. M., & Al-Manasir, K. (2017). A review of the use of terrestrial laser scanning application for change detection and deformation monitoring of structures. *Survey Review*, *49*(353), 99–116. https://doi.org/10.1080/00396265.2015.1133039

Natural Resources Canada. (2019). Precise Point Positioning. Retrieved from https://webapp.geod.nrcan.gc.ca/geod/tools-outils/ppp.php

Pesci, A., Teza, G., & Bonali, E. (2011). Terrestrial laser scanner resolution: Numerical simulations and experiments on spatial sampling optimization. *Remote Sensing*, *3*(1), 167–184. https://doi.org/10.3390/rs3010167

Petrie, G., & Toth, C. K. (2009). Terrestrial Laser Scanners. In *GIM International*.

Pix4D. (2019). Pix4Dmapper. Lausanne, Switzerland.

Przybilla, H.-J., & Wester-Ebbinghaus, W. (1979). Bildflug mit ferngelenktem Kleinflugzeug. *Bildmessung Und Luftbildwessen*, *47*, 137–142.

Rampton, V. N. (1980). *Quarternary Geology of the Tuktoyaktuk Coastlands, Northwest Territories*. *Geological Survey of Canada*.

Ridolfi, E., Buffi, G., Venturi, S., & Manciola, P. (2017). Accuracy analysis of a dam model from drone surveys. *Sensors (Switzerland)*, *17*(8). https://doi.org/10.3390/s17081777

Rothmund, S., Vouillamoz, N., & Joswig, M. (2017). Mapping slow-moving alpine landslides by UAV — Opportunities and limitations. *The Leading Edge*, *36*(7), 571–579. https://doi.org/10.1190/tle36070571.1

Saghravani, S. R., Mustapha, S. bin, & Saghravani, S. F. (2009). Accuracy Comparison of RTK-GPS and Automatic Level for Height Determination in Land Surveying. *MASAUM Journal Of Reviews and Surveys*, *1*(1), 10–13.

senseFly. (2016). *albris Extended User Manual*. Cheseaux-Lausanne, Switzerland.

senseFly. (2019). eMotion 3. Lausanne, Switzerland.

Shao, Z., Yang, N., Xiao, X., Zhang, L., & Peng, Z. (2016). A multi-view dense point cloud generation algorithm based on low-altitude remote sensing images. *Remote Sensing*, *8*(5). https://doi.org/10.3390/rs8050381

Siebert, S., & Teizer, J. (2014). Mobile 3D mapping for surveying earthwork projects using an Unmanned Aerial Vehicle (UAV) system. *Automation in Construction*, *41*, 1–14. https://doi.org/10.1016/j.autcon.2014.01.004

Stewart, B. (2017, October 23). New Arctic coast highway opens up remote Tuktoyaktuk. *CBC News*. Retrieved from https://www.cbc.ca/news/canada/north/new-arctic-coast-highway-opens-up-remote-tuktoyaktuk-1.4363029

Stumpf, A., Malet, J. P., Allemand, P., Pierrot-Deseilligny, M., & Skupinski, G. (2015). Ground-based multi-view photogrammetry for the monitoring of landslide deformation and erosion. *Geomorphology*, *231*, 130–145. https://doi.org/10.1016/j.geomorph.2014.10.039

Tahar, K. N. (2013). An evaluation on different number of ground control points in unmanned aerial vehicle photogrammetric block. In *International Archives of the Photogrammetry, Remote Sensing and Spatial Information Sciences* (Vol. XL-2/W2). https://doi.org/10.5194/isprsarchives-XL-2-W2-93-2013

Tarnocai, C., Nixon, M. F., & Kutny, L. (2004). Circumpolar-Active-Layer-Monitoring (CALM) sites in the Mackenzie Valley, northwestern Canada. *Permafrost and Periglacial Processes*, *15*(2), 141–153. https://doi.org/10.1002/ppp.490

Tonkin, T. N., & Midgley, N. G. (2016). Ground-control networks for image based surface reconstruction: An investigation of optimum survey designs using UAV derived imagery and structure-from-motion photogrammetry. *Remote Sensing*, *8*. https://doi.org/10.3390/rs8090786

Trimble. (2019). Critical factors affecting RTK accuracy. Retrieved September 9, 2019, from https://www.trimble.com/OEM_ReceiverHelp/V4.44/en/PositionModes_CriticalFactorsRTK.html

van der Sluijs, J., Kokelj, S., Fraser, R., Tunnicliffe, J., & Lacelle, D. (2018). Permafrost Terrain Dynamics and Infrastructure Impacts Revealed by UAV Photogrammetry and Thermal Imaging. *Remote Sensing*, *10*(11), 1734. https://doi.org/10.3390/rs10111734

Vermeer, M., & Ayehu, G. T. (2018). *Digital Aerial Mapping - a Hands-On Course*.

Wade, M. (2015). Should You Buy a Fixed Wing or Rotary Drone? Retrieved January 13, 2019, from https://waypoint.sensefly.com/buy-fixed-wing-drone-or-rotary/

Warren, F. J., & Lemmen, D. S. (2014). *Canada in a Changing Climate: Sector Perspectives on Impacts and Adaptation*. Ottawa, ON.

Wester-Ebbinghaus, W. (1980). Aerial Photography By Radio Controlled Model Helicopter. *The Photogrammetric Record*, *10*(55), 85–92. https://doi.org/10.1111/j.1477-9730.1980.tb00006.x

Westoby, M. J., Brasington, J., Glasser, N. F., Hambrey, M. J., & Reynolds, J. M. (2012). "Structure-from-Motion" photogrammetry: A low-cost, effective tool for geoscience applications. *Geomorphology*, *179*, 300–314. https://doi.org/10.1016/j.geomorph.2012.08.021

Wheaton, J. M., Brasington, J., Darby, S. E., & Sear, D. A. (2010). Accounting for uncertainty in DEMs from repeat topographic surveys: Improved sediment budgets. *Earth Surface Processes and Landforms*, *35*(2), 136–156. https://doi.org/10.1002/esp.1886

Williams, P. J. (1986). *Pipelines and permafrost: science in a cold climate. The Carleton University Press*. https://doi.org/10.2307/1551707

Xu, H. (2012). Application of GPS-RTK technology in the land change survey. *Procedia Engineering*, *29*, 3454–3459. https://doi.org/10.1016/j.proeng.2012.01.511

Yi, S., Woo, M. K., & Arain, M. A. (2007). Impacts of peat and vegetation on permafrost degradation under climate warming. *Geophysical Research Letters*, *34*. https://doi.org/10.1029/2007GL030550

Appendix A

Ground Control Point (GCP) Uncertainty and Error Data

RTK Survey Uncertainty Data

2017 KM-117 RTK Uncertainty Measurements

Point	Easting	Northing	Elevation	Horz. Err. (mm)	Vert. Err. (mm)	3D Err. (mm)
2017	583052.15	7683668.48	21.376	25	50	56
2016	583044.95	7683591.1	19.8871	30	60	68
2012	582948.64	7683810.19	31.532	7	15	17
2011	583026.24	7683822.95	27.4353	6	15	16
2010	583070.45	7683773.02	16.7121	6	14	15
2009	583021.15	7683693.79	26.7519	6	17	18
2007	583002.56	7683743.36	27.9327	6	17	18
2006	582968.79	7683724.79	20.6732	6	20	21
2005	582978.78	7683660.32	22.2637	6	24	25
2003	582987.66	7683597.53	25.7263	7	24	25
Max				30	60	68
Min				6	14	15
Mean				10	26	28
Std. Dev.				9	16	18
RMS				13	30	33

2018 KM-48 RTK Uncertainty Measurements

Point	Easting	Northing	Elevation	Horz. Err. (mm)	Vert. Err. (mm)	3D Err. (mm)
601	558899.88	7633293.15	60.202	5	9	10
602	558889.54	7633278.67	56.253	7	13	15
603	558897.00	7633271.70	57.182	7	12	14
604	558894.71	7633264.44	56.491	7	13	15
605	558907.24	7633268.60	59.568	6	11	13
606	558952.38	7633280.78	57.806	6	10	12
607	558948.01	7633289.64	58.316	7	14	16
608	558947.32	7633295.03	57.580	8	15	17
609	558939.87	7633306.10	58.695	7	14	16
610	558931.64	7633330.17	60.517	7	13	14
611	558910.14	7633305.15	64.168	9	18	20
612	558932.47	7633275.75	63.867	6	12	13
Max				9	18	20
Min				5	9	10
Mean				7	13	14
Std. Dev.				1	2	3
RMS				7	13	15

2018 KM-49 RTK Uncertainty Measurements

Point	Easting	Northing	Elevation	Horz. Err. (mm)	Vert. Err. (mm)	3D Err. (mm)
700	558406.75	7634227.54	45.606	6	11	13
701	558384.68	7634141.39	46.826	5	9	11
702	558376.67	7634130.57	44.634	6	11	13
703	558382.04	7634124.65	45.444	9	17	19
704	558377.57	7634119.65	44.542	6	10	12
705	558390.05	7634108.24	47.157	6	10	11
706	558439.76	7634108.76	47.830	7	12	14
707	558429.77	7634132.41	46.930	7	13	14
708	558423.20	7634142.43	47.156	6	10	11
709	558418.81	7634152.51	46.742	6	11	13
710	558417.01	7634155.77	46.541	6	11	13
711	558396.34	7634153.25	50.452	6	10	12
712	558417.18	7634115.30	52.692	6	11	12
Max				9	17	19
Min				5	9	11
Mean				6	11	13
Std. Dev.				1	2	2
RMS				6	11	13

2018 KM-82 UAV RTK Uncertainty Measurements

Point	Easting	Northing	Elevation	Horz. Err. (mm)	Vert. Err. (mm)	3D Err. (mm)
1401	569229.42	7657368.42	17.042	6	11	12
1402	569206.22	7657365.39	14.959	6	12	14
1403	569183.47	7657350.48	14.817	7	13	14
1404	569168.92	7657341.49	14.592	5	10	11
1406	569174.71	7657284.71	12.741	6	12	14
1407	569182.97	7657294.70	13.728	6	11	12
1409	569214.92	7657309.98	13.820	6	11	13
1410	569224.32	7657327.22	15.430	6	12	14
1411	569240.83	7657362.27	20.357	6	11	13
1412	569163.44	7657306.86	18.413	6	11	12
Max				7	13	14
Min				5	10	11
Mean				6	11	13
Std. Dev.				0	1	1
RMS				6	11	13

2018 KM-82 TLS RTK Uncertainty Measurements

Point	Easting	Northing	Elevation	Horz. Err. (mm)	Vert. Err. (mm)	3D Err. (mm)
14016	569207.96	7657321.43	18.728	5	9	10
14015	569228.68	7657332.44	19.390	5	9	10
14014	569223.57	7657319.92	18.703	5	9	11
14013	569206.57	7657306.59	16.817	4	7	8
14012	569196.65	7657309.39	18.125	6	10	12
14011	569190.57	7657323.19	21.967	5	8	10
14010	569208.75	7657333.13	22.354	6	9	11
14009	569225.65	7657341.94	22.906	4	7	9
14008	569193.89	7657351.13	18.307	19	27	33
14007	569208.76	7657369.52	18.398	8	14	16
14006	569197.12	7657367.03	18.172	8	13	15
14005	569183.62	7657359.75	18.142	6	10	11
14004	569175.87	7657349.49	18.036	6	10	12
14003	569187.00	7657334.42	21.989	4	7	9
14002	569203.76	7657342.71	22.195	5	9	10
14001	569220.18	7657351.71	22.637	5	8	9
Max				19	27	33
Min				4	7	8
Mean				6	10	12
Std. Dev.				3	5	6
RMS				7	11	14

2018 KM-117 RTK Uncertainty Measurements

Point	Easting	Northing	Elevation	Horz. Err. (mm)	Vert. Err. (mm)	3D Err. (mm)
2001	582985.27	7683742.84	19.475	6	12	14
2002	583023.17	7683697.02	23.078	5	10	11
2003	583004.20	7683747.41	24.191	6	12	13
2004	582974.55	7683723.58	16.405	6	11	12
2005	582984.55	7683717.71	15.893	8	15	17
2006	582976.50	7683701.56	16.249	6	13	14
2007	582993.89	7683683.79	18.602	5	10	11
2008	583055.52	7683712.76	14.283	6	11	13
2009	583058.39	7683739.50	12.873	6	11	12
2010	583053.58	7683743.16	13.239	6	11	12
2011	583048.75	7683764.56	15.046	6	12	14
2012	583038.25	7683784.83	17.171	6	11	13
Max				8	15	17
Min				5	10	11
Mean				6	12	13
Std. Dev.				1	1	2
RMS				6	12	13

2019 KM-48 RTK Uncertainty Measurements

Point	Easting	Northing	Elevation	Horz. Err. (mm)	Vert. Err. (mm)	3D Err. (mm)
601	558931.26	7633278.54	63.704	4	9	9
602	558911.50	7633307.66	64.509	4	8	9
603	558891.29	7633326.82	62.131	4	9	10
604	558890.75	7633292.67	57.631	4	9	10
605	558891.68	7633267.03	55.861	4	9	10
606	558910.24	7633248.90	60.188	4	8	9
607	558933.46	7633224.15	62.928	4	8	9
608	558935.71	7633241.98	64.629	4	8	9
609	558964.32	7633235.55	62.927	4	7	8
610	558956.89	7633263.51	60.315	4	7	8
611	558954.28	7633296.55	57.247	3	7	7
612	558942.63	7633317.89	59.057	4	7	8
613	558928.61	7633346.25	61.534	3	7	7
Max				4	9	10
Min				3	7	7
Mean				4	8	9
Std. Dev.				0	1	1
RMS				4	8	9

2019 KM-49 RTK Uncertainty Measurements

Point	Easting	Northing	Elevation	Horz. Err. (mm)	Vert. Err. (mm)	3D Err. (mm)
701	558411.10	7634099.82	53.253	4	7	7
702	558397.61	7634148.65	50.442	4	7	7
703	558420.77	7634162.50	46.723	4	7	8
704	558433.12	7634137.67	46.939	4	7	8
705	558443.31	7634114.49	47.235	4	7	8
706	558454.68	7634077.29	50.425	4	6	7
707	558459.22	7634041.15	54.444	4	7	8
708	558437.40	7634051.45	57.287	4	6	7
709	558419.15	7634019.81	54.831	4	7	8
710	558402.48	7634053.97	50.114	4	6	7
711	558384.21	7634079.70	44.983	4	7	8
712	558378.20	7634120.35	44.403	4	7	9
713	558374.10	7634149.91	45.478	4	7	8
Max				4	7	9
Min				4	6	7
Mean				4	7	8
Std. Dev.				0	0	0
RMS				4	7	8

2019 KM-82 UAV RTK Uncertainty Measurements

Point	Easting	Northing	Elevation	Horz. Err. (mm)	Vert. Err. (mm)	3D Err. (mm)
1401	569243.67	7657338.88	17.646	3	6	7
1402	569223.34	7657320.84	14.744	3	6	6
1403	569192.93	7657322.33	18.268	3	5	6
1404	569204.01	7657297.81	12.769	3	6	6
1405	569175.16	7657284.80	12.449	3	5	6
1406	569147.67	7657276.85	15.439	3	5	6
1407	569146.22	7657296.83	18.501	3	6	6
1408	569133.55	7657312.58	16.145	4	7	8
1409	569155.40	7657333.16	13.901	4	6	7
1410	569181.83	7657348.38	14.368	3	6	7
1411	569207.35	7657362.19	14.471	4	7	8
1412	569232.94	7657369.47	17.299	4	7	8
1413	569227.89	7657353.96	19.231	3	6	7
Max	[redacted]			4	7	8
Min				3	5	6
Mean				3	6	7
Std. Dev.				0	1	1
RMS				3	6	7

2019 KM-82 TLS RTK Uncertainty Measurements

Point	Easting	Northing	Elevation	Horz. Err. (mm)	Vert. Err. (mm)	3D Err. (mm)
1401	569223.64	7657351.33	19.472	4	8	9
1402	569228.36	7657341.82	19.63	4	8	9
1403	569190.37	7657321.10	18.575	4	8	9
1404	569184.68	7657331.43	18.622	4	8	9
1405	569181.82	7657338.87	15.962	4	9	10
1406	569179.65	7657345.18	14.567	4	9	10
1407	569180.64	7657360.77	14.851	4	10	11
1408	569197.08	7657372.06	14.955	4	11	11
1409	569208.66	7657366.80	15.064	4	12	13
1410	569218.05	7657359.12	16.174	4	11	11
1411	569229.69	7657336.45	17.514	4	12	13
1412	569230.89	7657323.70	15.917	5	14	15
1413	569222.90	7657313.01	14.868	4	12	13
1414	569211.72	7657301.74	13.419	4	13	13
1415	569199.80	7657303.62	13.914	3	9	9
1416	569195.88	7657309.85	14.992	4	9	10
Max				5	14	15
Min				3	8	9
Mean				4	10	11
Std. Dev.				0	2	2
RMS				4	10	11

2019 KM-117 RTK Uncertainty Measurements

Point	Easting	Northing	Elevation	Horz. Err. (mm)	Vert. Err. (mm)	3D Err. (mm)
2001	582990.23	7683825.51	29.678	3	6	7
2002	583004.49	7683747.33	23.684	3	6	7
2003	583036.42	7683809.21	18.660	4	8	9
2004	583055.48	7683780.28	13.442	3	7	7
2005	583059.20	7683742.35	11.573	3	7	8
2006	583052.30	7683696.18	15.527	4	8	9
2007	583043.91	7683642.32	17.822	3	7	8
2008	583022.58	7683704.82	22.730	4	8	8
2009	583010.54	7683630.26	22.371	3	7	8
2010	582992.31	7683646.48	18.433	3	7	8
2011	582978.27	7683687.58	15.735	4	8	9
2012	582975.47	7683722.81	15.771	3	7	8
2013	582974.22	7683750.57	18.233	3	8	8
2014	582972.24	7683786.93	22.910	3	7	8
Max	[redacted]			4	8	9
Min				3	6	7
Mean				3	7	8
Std. Dev.				0	1	1
RMS				3	7	8

UAV Photogrammetry GCP (Checkpoint) Error Data

2017 KM-117 albris UAV GCP Checkpoint Errors

Check Point	X Err. (m)	Y Err. (m)	Z Err. (m)	Horz. Err. (m)	3D Err. (m)
2003	-0.0019	0.0096	0.1375	0.0098	0.1378
2005	0.0230	0.0121	0.0204	0.0260	0.0330
2006	0.0171	0.0108	-0.0702	0.0202	0.0731
2007	-0.0086	0.0033	-0.0004	0.0092	0.0092
2009	-0.0090	-0.0256	-0.0277	0.0271	0.0388
2010	-0.0236	-0.0004	-0.0386	0.0236	0.0452
2011	0.0053	-0.0036	0.0524	0.0064	0.0528
2012	-0.0039	0.0217	-0.0045	0.0220	0.0225
2016	0.0131	0.0112	-0.0324	0.0172	0.0367
2017	0.0063	0.0054	-0.0053	0.0083	0.0098
Mean	0.0018	0.0045	0.0031	0.0170	0.0459
Std. Dev.	0.0140	0.0127	0.0580	0.0079	0.0376
RMS	0.0134	0.0129	0.0551	0.0186	0.0581

2018 KM-48 albris UAV GCP Checkpoint Errors

Check Point	X Err. (m)	Y Err. (m)	Z Err. (m)	Horz. Err. (m)	3D Err. (m)
601	0.0006	0.0049	0.0235	0.0049	0.0240
602	0.0154	-0.0001	-0.0452	0.0154	0.0478
604	-0.0032	-0.0101	-0.0139	0.0106	0.0175
605	0.0050	-0.0048	0.0118	0.0069	0.0137
606	0.0138	0.0031	-0.0244	0.0141	0.0282
608	-0.0100	-0.0188	-0.0191	0.0213	0.0286
609	-0.0200	0.0281	-0.0150	0.0345	0.0376
610	0.0215	-0.0048	-0.0062	0.0220	0.0229
611	-0.0084	0.0040	0.0483	0.0093	0.0492
612	-0.0112	0.0005	0.0184	0.0112	0.0215
Mean	0.0004	0.0002	-0.0022	0.0150	0.0291
Std. Dev.	0.0134	0.0122	0.0274	0.0088	0.0121
RMS	0.0127	0.0116	0.0261	0.0172	0.0313

2018 KM-48 Phantom UAV GCP Checkpoint Errors

Check Point	X Err. (m)	Y Err. (m)	Z Err. (m)	Horz. Err. (m)	3D Err. (m)
601	-0.0154	-0.0204	0.0116	0.0256	0.0281
602	-0.0152	-0.0145	0.0013	0.0210	0.0210
604	-0.0218	0.0246	0.0148	0.0329	0.0360
605	-0.0052	0.0167	0.0000	0.0175	0.0175
606	0.0308	0.0262	0.0038	0.0404	0.0406
608	0.0092	-0.0142	0.0113	0.0169	0.0203
609	-0.0005	0.0143	0.0009	0.0143	0.0143
610	0.0362	-0.0493	-0.0075	0.0612	0.0616
611	-0.0136	-0.0250	-0.0167	0.0285	0.0330
612	0.0134	0.0180	-0.0299	0.0224	0.0374
Mean	0.0018	-0.0024	-0.0010	0.0281	0.0310
Std. Dev.	0.0201	0.0257	0.0138	0.0141	0.0141
RMS	0.0192	0.0245	0.0131	0.0311	0.0337

2018 KM-49 albris UAV GCP Checkpoint Errors

Check Point	X Err. (m)	Y Err. (m)	Z Err. (m)	Horz. Err. (m)	3D Err. (m)
701	0.0052	-0.0174	-0.0057	0.0182	0.0190
702	-0.0091	0.0119	-0.0012	0.0150	0.0150
704	0.0118	-0.0017	-0.0159	0.0119	0.0199
705	-0.0086	-0.0083	0.0003	0.0120	0.0120
706	-0.0115	0.0115	-0.0097	0.0163	0.0189
707	-0.0082	-0.0043	-0.0268	0.0093	0.0284
708	-0.0126	0.0012	0.0038	0.0127	0.0132
710	0.0304	0.0070	-0.0027	0.0312	0.0313
711	-0.0108	0.0066	0.0168	0.0127	0.0210
712	0.0102	0.0009	0.0235	0.0102	0.0256
Mean	-0.0003	0.0007	-0.0018	0.0149	0.0204
Std. Dev.	0.0142	0.0092	0.0146	0.0063	0.0064
RMS	0.0135	0.0087	0.0140	0.0161	0.0213

2018 KM-49 Phantom UAV GCP Checkpoint Errors

Check Point	X Err. (m)	Y Err. (m)	Z Err. (m)	Horz. Err. (m)	3D Err. (m)
701	-0.0081	-0.0329	-0.0092	0.0339	0.0351
702	-0.0184	0.0009	0.0064	0.0184	0.0195
704	0.0025	-0.0019	0.0127	0.0031	0.0131
705	-0.0366	0.0016	-0.0123	0.0366	0.0386
706	-0.0112	0.0521	-0.0085	0.0533	0.0540
707	0.0011	-0.0057	-0.0010	0.0058	0.0059
708	0.0105	0.0000	0.0258	0.0105	0.0279
710	0.0646	-0.0103	0.0108	0.0654	0.0663
711	-0.0121	-0.0041	-0.0070	0.0128	0.0146
712	0.0065	0.0222	-0.0130	0.0231	0.0265
Mean	-0.0001	0.0022	0.0005	0.0263	0.0301
Std. Dev.	0.0266	0.0221	0.0130	0.0208	0.0189
RMS	0.0252	0.0211	0.0123	0.0329	0.0351

2018 KM-82 albris UAV GCP Checkpoint Errors

Check Point	X Err. (m)	Y Err. (m)	Z Err. (m)	Horz. Err. (m)	3D Err. (m)
1401	-0.0021	0.0078	0.0053	0.0081	0.0097
1402	0.0017	-0.0183	0.0172	0.0184	0.0252
1403	0.0150	0.0100	-0.0063	0.0180	0.0191
1404	-0.0054	0.0039	-0.0167	0.0067	0.0180
1406	-0.0070	-0.0189	-0.0216	0.0202	0.0295
1407	0.0072	-0.0145	0.0024	0.0162	0.0164
1409	-0.0070	0.0012	-0.0148	0.0071	0.0164
1410	-0.0281	0.0043	0.0163	0.0284	0.0328
1411	0.0134	0.0126	-0.0069	0.0184	0.0196
1412	0.0128	0.0116	0.0149	0.0173	0.0228
Mean	0.0001	0.0000	-0.0010	0.0159	0.0209
Std. Dev.	0.0131	0.0124	0.0144	0.0068	0.0068
RMS	0.0124	0.0118	0.0137	0.0171	0.0219

2018 KM-82 Phantom UAV GCP Checkpoint Errors

Check Point	X Err. (m)	Y Err. (m)	Z Err. (m)	Horz. Err. (m)	3D Err. (m)
1401	-0.0224	0.0139	-0.0076	0.0264	0.0274
1402	-0.0213	0.0050	0.0070	0.0219	0.0230
1403	0.0150	0.0285	0.0173	0.0322	0.0366
1404	0.0002	0.0353	0.0117	0.0353	0.0372
1406	0.0065	-0.0119	-0.0206	0.0136	0.0247
1407	0.0111	-0.0268	0.0265	0.0290	0.0393
1409	-0.0003	-0.0202	-0.0157	0.0202	0.0256
1410	-0.0169	-0.0223	0.0188	0.0280	0.0337
1412	0.0269	0.0356	-0.0290	0.0446	0.0532
1413	0.0051	0.0047	-0.0201	0.0069	0.0213
Mean	0.0004	0.0042	-0.0012	0.0258	0.0322
Std. Dev.	0.0163	0.0239	0.0197	0.0108	0.0098
RMS	0.0154	0.0231	0.0187	0.0278	0.0335

2018 KM-117 albris UAV GCP Checkpoint Errors

Check Point	X Err. (m)	Y Err. (m)	Z Err. (m)	Horz. Err. (m)	3D Err. (m)
2001	0.0065	0.0017	0.0102	0.0067	0.0122
2002	-0.0024	0.0071	0.0126	0.0075	0.0147
2003	0.0041	0.0044	0.0127	0.0060	0.0141
2004	0.0123	-0.0004	-0.0374	0.0123	0.0394
2006	0.0085	0.0023	-0.0296	0.0088	0.0309
2007	-0.0100	-0.0177	0.0212	0.0203	0.0294
2008	-0.0083	-0.0151	-0.0155	0.0172	0.0232
2009	-0.0169	0.0029	-0.0126	0.0171	0.0213
2011	0.0021	0.0054	-0.0086	0.0058	0.0104
2012	-0.0030	0.0132	0.0346	0.0135	0.0372
Mean	-0.0007	0.0004	-0.0012	0.0115	0.0233
Std. Dev.	0.0091	0.0096	0.0231	0.0053	0.0105
RMS	0.0087	0.0091	0.0220	0.0126	0.0253

2019 KM-48 albris UAV GCP Checkpoint Errors

Check Point	X Err. (m)	Y Err. (m)	Z Err. (m)	Horz. Err. (m)	3D Err. (m)
601	-0.0044	0.0048	0.0063	0.0065	0.0091
602	0.0021	-0.0044	0.0160	0.0049	0.0167
603	0.0027	0.0077	0.0080	0.0082	0.0114
604	0.0014	0.0090	-0.0033	0.0091	0.0097
605	0.0041	-0.0053	-0.0139	0.0067	0.0154
606	0.0023	-0.0044	-0.0166	0.0050	0.0173
607	0.0014	0.0005	-0.0079	0.0015	0.0080
608	-0.0016	0.0020	0.0149	0.0026	0.0151
609	0.0052	-0.0095	-0.0061	0.0108	0.0124
610	0.0005	0.0050	0.0104	0.0050	0.0116
611	-0.0015	-0.0019	-0.0167	0.0024	0.0169
612	-0.0018	-0.0040	0.0012	0.0044	0.0045
613	-0.0058	-0.0022	-0.0151	0.0062	0.0163
Mean	0.0004	-0.0002	-0.0018	0.0056	0.0127
Std. Dev.	0.0032	0.0056	0.0120	0.0027	0.0040
RMS	0.0031	0.0054	0.0117	0.0062	0.0132

2019 KM-48 Phantom UAV GCP Checkpoint Errors

Check Point	X Err. (m)	Y Err. (m)	Z Err. (m)	Horz. Err. (m)	3D Err. (m)
601	0.0152	0.0115	-0.0168	0.0191	0.0254
602	-0.0172	-0.0064	-0.0073	0.0184	0.0198
603	-0.0311	-0.0311	0.0138	0.0440	0.0461
604	-0.0151	-0.0185	0.0100	0.0239	0.0259
605	-0.0019	0.0045	0.0285	0.0049	0.0289
606	-0.0133	-0.0014	-0.0102	0.0134	0.0168
607	-0.0134	0.0029	-0.0031	0.0137	0.0141
608	-0.0177	0.0011	-0.0114	0.0177	0.0211
609	0.0111	0.0281	-0.0235	0.0302	0.0383
610	0.0235	0.0088	0.0096	0.0251	0.0269
611	0.0417	-0.0005	0.0066	0.0417	0.0422
612	0.0366	0.0041	0.0085	0.0368	0.0378
613	0.0126	-0.0150	-0.0588	0.0196	0.0620
Mean	0.0024	-0.0009	-0.0042	0.0237	0.0312
Std. Dev.	0.0228	0.0148	0.0217	0.0116	0.0136
RMS	0.0220	0.0142	0.0213	0.0262	0.0338

2019 KM-49 albris UAV GCP Checkpoint Errors

Check Point	X Err. (m)	Y Err. (m)	Z Err. (m)	Horz. Err. (m)	3D Err. (m)
701	-0.0017	0.0047	0.0106	0.0050	0.0117
702	-0.0037	-0.0046	0.0123	0.0059	0.0136
703	0.0025	0.0047	-0.0050	0.0053	0.0073
704	-0.0071	0.0005	-0.0013	0.0071	0.0072
705	-0.0023	-0.0012	0.0041	0.0026	0.0049
706	-0.0048	-0.0032	-0.0178	0.0058	0.0187
707	-0.0039	-0.0044	-0.0181	0.0059	0.0190
708	0.0047	0.0037	0.0128	0.0060	0.0141
709	0.0004	-0.0125	0.0180	0.0125	0.0219
710	0.0018	-0.0004	-0.0081	0.0018	0.0083
711	0.0091	0.0040	-0.0028	0.0099	0.0103
712	0.0044	0.0000	-0.0076	0.0044	0.0088
713	0.0049	0.0029	-0.0107	0.0057	0.0121
Mean	0.0003	-0.0004	-0.0010	0.0060	0.0122
Std. Dev.	0.0047	0.0049	0.0118	0.0028	0.0052
RMS	0.0045	0.0047	0.0114	0.0066	0.0131

2019 KM-49 Phantom UAV GCP Checkpoint Errors

Check Point	X Err. (m)	Y Err. (m)	Z Err. (m)	Horz. Err. (m)	3D Err. (m)
701	-0.0089	0.0057	-0.0148	0.0106	0.0182
702	-0.0037	-0.0082	-0.0120	0.0090	0.0150
703	0.0473	-0.0196	-0.0223	0.0512	0.0558
704	0.0173	-0.0014	0.0067	0.0174	0.0186
705	0.0170	0.0041	0.0256	0.0175	0.0310
706	0.0161	-0.0019	0.0042	0.0162	0.0167
707	0.0211	0.0315	-0.0043	0.0379	0.0382
708	0.0101	0.0122	-0.0175	0.0158	0.0236
709	-0.0282	-0.0042	-0.0282	0.0285	0.0401
710	-0.0317	0.0037	0.0080	0.0319	0.0329
711	-0.0154	0.0018	0.0165	0.0155	0.0226
712	-0.0214	-0.0157	0.0109	0.0265	0.0287
713	-0.0165	-0.0121	-0.0044	0.0205	0.0209
Mean	0.0002	-0.0003	-0.0024	0.0230	0.0279
Std. Dev.	0.0233	0.0131	0.0161	0.0119	0.0117
RMS	0.0223	0.0126	0.0156	0.0257	0.0301

2019 KM-82 albris UAV GCP Checkpoint Errors

Check Point	X Err. (m)	Y Err. (m)	Z Err. (m)	Horz. Err. (m)	3D Err. (m)
1401	0.0065	0.0065	0.0038	0.0092	0.0099
1402	-0.0030	-0.0018	-0.0106	0.0035	0.0112
1403	-0.0019	-0.0011	0.0119	0.0022	0.0121
1404	0.0005	0.0073	-0.0054	0.0073	0.0091
1405	-0.0048	0.0052	-0.0097	0.0071	0.0120
1406	-0.0043	0.0006	0.0126	0.0043	0.0133
1407	-0.0019	0.0047	0.0232	0.0051	0.0237
1408	-0.0025	-0.0094	-0.0247	0.0097	0.0265
1409	0.0008	-0.0094	-0.0169	0.0094	0.0194
1410	0.0083	0.0005	0.0123	0.0083	0.0148
1411	0.0029	-0.0048	0.0111	0.0056	0.0124
1412	-0.0021	-0.0021	-0.0100	0.0030	0.0104
1413	0.0002	-0.0015	-0.0016	0.0015	0.0022
Mean	-0.0001	-0.0004	-0.0003	0.0059	0.0136
Std. Dev.	0.0040	0.0054	0.0140	0.0029	0.0064
RMS	0.0038	0.0052	0.0135	0.0065	0.0150

2019 KM-82 Phantom UAV GCP Checkpoint Errors

Check Point	X Err. (m)	Y Err. (m)	Z Err. (m)	Horz. Err. (m)	3D Err. (m)
1401	0.0227	0.0085	-0.0040	0.0242	0.0246
1402	0.0086	-0.0033	-0.0277	0.0092	0.0292
1403	-0.0100	0.0015	-0.0153	0.0101	0.0183
1404	0.0219	0.0109	0.0111	0.0245	0.0269
1405	0.0093	0.0044	0.0167	0.0103	0.0196
1406	-0.0087	0.0120	-0.0103	0.0148	0.0180
1407	-0.0206	0.0259	0.0102	0.0331	0.0346
1408	0.0008	0.0004	-0.0048	0.0009	0.0049
1409	-0.0030	-0.0263	0.0045	0.0265	0.0269
1410	-0.0071	-0.0185	0.0243	0.0198	0.0314
1411	-0.0024	-0.0143	0.0075	0.0145	0.0163
1412	0.0041	0.0004	-0.0008	0.0041	0.0042
1413	-0.0019	0.0061	-0.0067	0.0064	0.0093
Mean	0.0011	0.0006	0.0004	0.0153	0.0203
Std. Dev.	0.0123	0.0139	0.0140	0.0097	0.0098
RMS	0.0119	0.0133	0.0135	0.0179	0.0224

2019 KM-117 albris UAV GCP Checkpoint Errors

Check Point	X Err. (m)	Y Err. (m)	Z Err. (m)	Horz. Err. (m)	3D Err. (m)
2001	-0.0061	0.0161	0.0575	0.0172	0.0600
2002	0.0082	-0.0011	0.0161	0.0083	0.0181
2003	-0.0076	-0.0002	-0.0098	0.0076	0.0124
2004	-0.0053	-0.0071	-0.0329	0.0089	0.0341
2005	-0.0183	0.0002	-0.0004	0.0183	0.0183
2006	-0.0109	0.0011	-0.0042	0.0110	0.0117
2007	-0.0055	-0.0062	0.0201	0.0083	0.0217
2008	-0.0064	0.0048	0.0300	0.0080	0.0310
2009	-0.0047	-0.0045	0.0187	0.0065	0.0198
2010	0.0045	-0.0159	-0.0624	0.0165	0.0646
2011	0.0173	-0.0008	-0.0229	0.0173	0.0287
2012	0.0062	0.0062	-0.0065	0.0088	0.0109
2013	0.0049	-0.0010	-0.0147	0.0050	0.0155
2014	0.0102	0.0026	-0.0145	0.0105	0.0179
Mean	-0.0010	-0.0004	-0.0019	0.0109	0.0261
Std. Dev.	0.0096	0.0073	0.0294	0.0045	0.0169
RMS	0.0093	0.0070	0.0284	0.0117	0.0307

TLS GCP Target Error Data

2018 and 2019 KM-82 TLS GCP Target Errors

Survey	2018-west	2018-east	2019
	26.98	29.73	31.59
	26.56	21.46	31.24
	17.13	19.91	27.88
	16.38	17.47	25.19
	15.29	15.07	19.15
	14.86	12.62	18.38
	13.60	12.12	17.54
	10.28	11.43	17.49
	9.57	11.31	17.22
	9.20	11.10	17.18
	7.30	10.21	16.89
	6.23		16.82
3D Errors	3.93		16.64
			16.01
			15.37
			14.77
			13.87
			12.74
			11.88
			11.79
			11.61
			9.63
			8.73
			8.43
			7.56
Max	27.0	29.7	31.6
Min	3.9	10.2	7.6
Mean	13.6	15.7	16.6
Std. Dev.	7.1	6.0	6.5
RMS	15.3	16.7	17.8

Appendix B

Guideline for using UAV Photogrammetry to Monitor Deformations

Guideline for using UAV Photogrammetry to Monitor Deformations

This guideline outlines the methods and techniques that should be applied when using an unmanned aerial vehicle (UAV) with structure-from-motion (SfM) photogrammetric processing to monitor deformations of structures or landforms. The guideline covers all aspects of UAV monitoring, from the pre-site planning stage to the fieldwork, post-processing of data. The guideline not only outlines recommended methods but also the missteps to avoid, which are often overlooked. The guideline is recommended for any practitioners using UAV photogrammetry to monitor deformations, including researchers, surveyors, construction contractors, and government agencies.

1. BACKGROUND

UAV-SfM is a powerful technology that can generate accurate reconstructions while being easy to use and relatively inexpensive. Deformation monitoring with a UAV can be done for projects over a wide range of scales and environments, for both man-made structures and natural landforms. UAV monitoring is especially useful in remote areas with limited site access.

1.1 UAV Models

There are two main classifications of UAVs: fixed-wing and rotary. Fixed-wing UAVs cruise at higher speeds and can therefore cover larger areas. They also have longer flight times due to their aerodynamic design, making them suitable for large mapping, agricultural, and environmental projects. Rotary UAVs cruise at lower speeds, have shorter flight times, and have lower capacities to resist wind forces. For these reasons, they are more suited for monitoring smaller areas and obtaining more accurate measurements for surveying and construction monitoring. Many modern UAVs are capable of flying autonomously on user-designed missions. Autonomous flights allow for more efficient and consistent flights that provide more reliable results in the form of higher-quality reconstructions. It is more challenging to obtain comparable results with UAVs that can only be flown

manually. However, manual flight UAVs can still produce sufficiently accurate reconstructions and detect deformations if imagery is intelligently acquired.

1.2 SfM Processing

SfM is a series of feature-matching and positioning algorithms that process imagery to generate point clouds of the scene viewed in the imagery. The simple and automated workflow of SfM has made UAV photogrammetry more attractive for nontechnical users and has promoted its widespread use. SfM processing requires a set overlapping images to accurately reconstruct a scene. SfM-reconstructed point clouds are not generated in a real-world coordinate system and require control points to georeference point clouds to a certain coordinate system. Point clouds can be georeferenced using positional geotag data of the images obtained by the UAV; however, the accuracy of this method is not fully understood yet. Currently, the most common and proven method for georeferencing point clouds is to use ground control points (GCPs). A GCP is an easily identifiable point with known coordinates that can be marked in images. Artificial GCPs such as checkerboard targets are commonly used in UAV photogrammetry.

1.3 Deformation Measurement

Deformation is determined by comparing two 3D point clouds. The difference between the point clouds is the deformation that occurred. Compared to the sensing instruments available for reconstructing 3D point clouds, solutions for comparing point clouds are scarce. The most common methods for determining deformation between point clouds are presented in *Section 4*. An important concept in deformation monitoring is the minimum level of detection (LoD), also called the confidence interval. The LoD defines the minimum statistically significant change that can be detected and is typically calculated for a 95% confidence interval. Put simply, LoD is a numerical method of separating deformations large enough to be considered as actual change from deformations that could merely be due to point cloud errors. Standard error assessments of GCPs, such as RMS error, can be used to estimate the LoD.

2. PRE-SITE PLANNING

2.1 UAV Certifications

- All UAV operators must obtain the proper certifications
- UAV rules and regulations vary widely between countries and it is crucial to be abide diligently.
- Certifications may include: pilot license, registration of UAV, radio communication certificate, approval/permission to operate in an area, and others.

2.1.1 UAV Operations in Canada

- UAV pilots must follow the rules in the Canadian Aviation Regulations (CARs) Part IX—Remotely Piloted Aircraft Systems (RPAS).
- UAV operations are categorized into Basic or Advanced operations. Basic operations are those that: 1) fly in uncontrolled airspace; 2) fly more than 30 m horizontally from bystanders; and 3) never fly over bystanders. If any of these criteria are not satisfied, it is considered an Advanced operation.
- A person must pass either the Basic or Advanced online pilot test provided by Transport Canada. Pilot tests cover a wide range of topics including safety, rules and regulations, flight planning in Canadian airspace with NAV CANADA, meteorology, insurance and liability, and UAV mission planning.
- All UAVs must be registered with Transport Canada.

2.2 UAV-SfM Survey Design

2.2.1 UAV Flight and Image Acquisition

- A good UAV survey design will consider all the parameters below and strike a balance between them.

- Designing UAV flights is more suited for autonomous flying UAVs, where the flight parameters can be defined. Flight parameters can only be estimated during flight of manual controlled UAVs.
- Further considerations when designing UAV surveys:
    - UAV battery life, time available in the field, required accuracy of the point clouds, and required LoD for deformations.

Image Quality

- UAVs with better cameras (i.e. higher resolution) capture more detailed images that improve feature identification and matching during SfM processing.
- When purchasing a UAV, consider the camera resolution.

Image Network

- Flying a UAV in a horizontal grid pattern capturing nadir (straight down) images at uniform spacing is recommended. This image network is an efficient use of UAV battery and provides uniform coverage.
- Drawback: A systematic vertical doming error can develop due to the self-calibration of camera parameters during SfM processing. The doming error causes the centre of the reconstruction to be stretched upwards and the edges to be pulled downwards.
- Two techniques to reduce doming errors: 1) a good well-distributed GCP network (discussed in detail below); 2) include additional oblique imagery.
- A small number of additional oblique images can significantly reduce doming errors. 10–20 oblique images that together view the full scene is recommended. The optimal viewing angle for oblique images 45° to the ground surface.

Image Overlap

- Higher image overlap improves the accuracy and density of the reconstructed point cloud.

- Image overlap should be consistent across the study area to ensure uniform coverage. Minimum image overlap: 75% in both directions (parallel and perpendicular to the UAV flight direction).

Ground Sampling Distance (GSD)

- GSD is the distance between pixel centres measured on the ground.
- GSD represents the combined effect of the camera quality (most-likely set at this point based on the UAV model) and camera-to-surface distance. Higher UAV flight altitude results in a lower GSD, and vice-versa.
- A lower GSD increases the level of detail in imagery and improves reconstruction accuracy and density.
- Lowering GSD, however, increases the required number of images and therefore increases the time and number of flights.
- When designing UAV surveys, GSD is often the design parameter and camera-to-surface distance is a function of the GSD.

Number of Images

- Generally, a higher number of images increases the density and accuracy of the reconstructed point cloud.
- Increasing the number of images also increases computation time, so the number of images needs to be chosen appropriately for the project.
- Typically, the survey area, image overlap, and GSD are defined first and the number of images is determined accordingly.

Surface Characteristics

- Surface characteristics plays a key role in identifying features during SfM processing.

- Surveying snow and water will produce poor results because these surfaces have few distinct features and can absorb and scatter light.
- Vegetation causes poor reconstructions because vegetation can move (from the wind) during flights and can appear different depending on the camera's perspective.

Lighting Conditions

- Bright, sunny days are not ideal because strong shadows and glares can occur.
- Overcast but bright days are optimal.
- UAV surveys should not last longer than 30 minutes to avoid distinct changes in light conditions.

2.2.2 GCP Network

- It is important to perform site reconnaissance, understand the site conditions, and plan the GCP network in advance.

GCP Principles

- A minimum of three GCPs is required to georeference a point cloud.
- GCPs should be equally spaced throughout survey area.
- GCPs should encompass the entire survey area, being located around the perimeter and scattered throughout.
- GCPs should be placed at varying elevations throughout the survey area, with more in areas of high relief.

Number of GCPs

- Increasing the number of GCPs provides a more robust solution that is less sensitive to error at any one point.
- The number of GCPs will depend on the quality of GCP measurements, survey area size, and required LoD for the deformation measurements.

- It is better to have too many GCPs than not enough. If additional GCPs are not providing accuracy improvements, extra GCPs can be used as checkpoints to provide error estimates of the reconstructed point cloud.
- The optimal distance between GCPs is 1/5 to 1/10 the distance of the object of interest.
- As a general guideline, a minimum of 8–12 GCPs is recommended.

2.2.3 Trial UAV Surveys

- Trial UAV surveys with the GCP network at site-scale should be performed prior to fieldwork to estimate the expected LoD.
- Data acquisition and processing methods should produce results with a LoD appropriate for the expected deformations on-site.
- If the determined LoD is too large, data acquisition methods should be adjusted until an appropriate LoD is reached.
- Possible adjustments: modifying the UAV flight parameters, increasing the number of GCPs, or increasing the GCP observation time if using an RTK system.
- Accurate LoD estimates appropriate for the expected deformations are essential for the practitioner's ability to draw meaningful conclusions from the measured deformations.

2.3 Preparing for Fieldwork

- Prepare and pack an operation travel kit that includes:
    - Equipment for the UAV system – batteries, propellers, controllers, etc.
    - Safety equipment – radios, flashlights, fire extinguisher, etc.
    - Personal protective equipment – safety vests, sunglasses, hard hats, sunscreen, etc.
- Assess weather forecasts to determine if UAV flights will be possible. Weather forecasting should begin a week in advance and continue until the operation day.
- Ensure all batteries for the UAV and other equipment are charged and packed.

3. FIELDWORK

3.1 Establish Survey Benchmark

- A survey benchmark should be established on-site at the start of fieldwork.
- Benchmarks must be stable features that can be marked, measured, and accessible. If a suitable feature does not exist, install one by hammering a rod deep into the ground.
- If absolute coordinates are required (i.e. georeferencing to a real-world coordinate system), use an RTK survey system to measure the benchmark's position. The RTK base station should be set up above the benchmark and allowed to locate for a minimum of 6 hours.
    - Connect the RTK base station to an external battery because batteries in the base station may not last the full 6 hours.
- If absolute coordinates are not required, the benchmark coordinates are not necessary. As long as each survey is referenced to the same benchmark, relative deformations can be determined.
    - For simplicity, the benchmark coordinates can be defined as (0, 0, 0) or (100, 100, 100), or any (X, Y, Z) coordinates that suit the site conditions.

3.2 Prepare Site for UAV Flights

- If in an area near people or vehicles, set up safety signs notifying others of the UAV flights being conducted.
- In crowded areas, this could include setting up a boundary that others cannot enter.

3.3 Set Up and Measure GCP Network

- Lay out the GCP network as planned.
    - Keep in mind the GCP Principles: equally spaced, surrounding and scattered throughout the survey area, and varying elevations.

- Measure the GCP positions using accurate survey equipment. The best equipment for measuring GCP positions are an RTK survey system and a total station.
    - RTK systems are simple to set up, measure data points, and are effective on sites that cover a large area or have poor sightlines. However, point measurement uncertainties with RTK systems can be large, especially in the vertical direction, and cause inaccuracies when georeferencing point clouds. The measurement uncertainties are not an issue for large-scale deformation monitoring, but issues can arise when small-scale deformations (e.g. < 50 mm) are being monitored. RTK measurement uncertainties can be reduced by increasing the observation time at GCPs; however, major time increases are often infeasible when conducting UAV surveys due to uncertainty and time restrictions associated with unpredictable weather conditions.
        - If an RTK system is to be used for small-scale deformation monitoring, the observation time at each GCP should be 5–7 minutes in order to reduce GCP positional errors to acceptable levels.
    - Total stations are more suitable for measuring GCP positions on smaller sites where small-scale deformations (e.g. < 50 mm) are being monitored. Total stations can measure points with sub-millimetre accuracy in significantly less time than it takes RTK systems to measure points with 5–10 mm accuracy. One limiting characteristic of total stations is that sightlines are required from the benchmark to GCPs.

3.4 Perform Pre-Flight Checklist

- Confirm weather conditions are suitable for the UAV.
    - Most UAVs cannot operate below 0°C or in rain.
    - UAVs are sensitive to strong winds. As a general guideline, wind speed at ground level should be less than 10 m/s.

- Ensure all UAV system components are not damaged and working properly.
    - This includes but is not limited to: the camera, positioning sensors, propellers, batteries, GPS/GNSS system.
- Confirm the data link between the UAV and ground control station (e.g. controller) is established and strong.
- Ensure two-way radios or other communication devices are working properly between the pilot and any personnel involved in the operation (e.g. visual observers).
- Ensure the survey area is clear of all persons and the landing/takeoff area is clear of any objects.

3.5 Conduct UAV Flights

- It is highly recommended to have a visual observer for operations to assist with monitoring the UAV. The visual observer should be located away from the pilot (opposite side of survey area) and maintain communication through radios or cellphones.
- The UAV must remain within visual line-of-sight (VLOS) during an operation.
- Maintain awareness of the survey area. If people or vehicles enter the survey area, the UAV will need to avoid them, and the operation may need to be paused until the survey area is clear.
- Closely monitor the UAV battery during flights. It is recommended to bring the UAV to the landing point to change batteries at a minimum of 30% battery.
- Closely monitor the weather conditions during flights. Wind speeds are often faster at higher altitudes. If the UAV windspeed tolerance is exceeded, land the UAV and wait until wind speeds are reduced to complete the operation.

3.6 Perform Post-Flight Checklist

- General broadcast to the UAV team that the operation is complete.

- Inspect the UAV for any visual damage to the body, propellers, camera, etc.
- Collect the GCPs and take down any site safety signs or notices.

3.7 Acquire Control Measurements for Validating UAV Deformations

- Deformation monitoring with UAV should be coupled with another means of measuring deformation, such as instrumentation or survey equipment, to validate results.
- Any instrumentation that measures ground or structural movements are appropriate. Instrumentation examples: ShapeArrays, settlement systems, slope inclinometers.
- Using survey equipment to measure positions and displacement of features allows for validation by comparing the feature positions in reconstructed point clouds. Survey equipment examples: total station, RTK system.
    - Features must be easily identifiable and stable to be located and compared in point clouds. If these types of features don't exist on the site, consider installing checkpoints that can be used for this purpose.

4. POST-PROCESSING

4.1 SfM Processing – Point Cloud Reconstruction

4.1.1 SfM Software

- Many software programs are available for SfM processing of images. The primary function of all software is to generate point clouds by processing images.
- Two broad classification: commercial (cost money) or open-source (free).
    - Commercial software will be more user-friendly and often include additional features such as generating meshes, surface models, and point cloud analysis.
        - Examples: Pix4D, Agisoft Photoscan, Autodesk ReCap.
    - Open-source SfM software will get the job done but with limited features.

- Examples: ARC3D, Bundler & PMVS2, CMP SfM, VisualSFM

4.1.2 SfM Processing Recommendations

- Include GCPs in the bundle adjustment (i.e. 1-stage georeferencing) to minimize systematic positional errors in the reconstructed point cloud.
    - Only including GCPs to georeference after the point cloud has been generated (i.e. 2-stage georeferencing) causes larger errors.
- Identify GCP locations on the images themselves rather than in the reconstructed point cloud to reduce errors and improve overall accuracy.
- Do not down-sample images (reduced in size) for processing. Down-sampling images results in fewer features identified.
- If the software is having difficulty matching images and generating an accurate point cloud, manually identify and mark common features between images. Manually marking features can improve the bundle adjustment and point cloud reconstruction.
- Every SfM software will have different parameters and options for processing. Experiment with the parameters to determine the optimal settings that will produce the most accurate and dense point clouds.

4.1.3 Point Cloud Accuracy Assessment

- Visually inspect point clouds to identify any glaring errors in structure. A common error to look out for is single surfaces that are reconstructed as multiple surfaces. This error identifies that not all images are registered correctly.
- Error in a reconstructed point cloud can be assessed with respect to accuracy and precision.
    - Accuracy is the closeness of a measurement to a reference.
    - Precision is the repeatability of a measurement.

- The accuracy of a point cloud can be estimated by comparing a control point's computed coordinates in the reconstruction to its reference coordinates. Checkpoints should be used for this because checkpoints are not included in the SfM processing and provide an unbiased estimate of point cloud errors.
    - If a UAV survey does not have enough GCPs measured to assign checkpoints, assign one GCP as a checkpoint and reprocess the point cloud to determine error estimates at the checkpoint. Work through the set of GCPs, marking GCPs as checkpoints and determining its errors one-by-one. The checkpoint error dataset can then be analyzed to estimate the overall errors in the entire point cloud.
- The precision in a point cloud can be measured by measuring the roughness of points along a planar surface (e.g. concrete surface). The variance or deviation of points normal to the planar surface can be analyzed to estimate the precision of points within the point cloud.
- Root mean squared (RMS) is the best measurement of error because it accounts for the mean error and variance.
    - Mean error: estimate of accuracy.
        - Issue: positive and negative deviations can compensate for each other.
    - Standard deviation of errors: estimate of precision.
        - Issue: only provides confidence intervals around the mean error.
- Error measurements should be augmented by visualisation of the spatial error distribution to protect against systematic errors.

4.2 Point Cloud Alignment

- Point cloud alignment is the process of registering point clouds together. It is not necessary if georeferencing is accurate.

- Point cloud alignment is required if issues occurred while measure GCPs and georeferencing was not accurately performed.
- Alignment can be performed in point cloud processing software. One of the best software for point cloud alignment (and many other cloud comparison techniques) is CloudCompare.
    - CloudCompare is an open-source, free software developed for processing and analyzing 3D point clouds and meshes. The software is commonly used by researchers in the change detection and deformation monitoring fields of science and engineering.

4.2.1 Point Cloud Alignment Techniques

Manual Alignment

- Manual translation and/or rotation of one point cloud to align with another.
- Good technique to start with for a rough point cloud alignment.
- Challenging to accurately align, particularly when rotation of a point cloud is involved.

Common Point Alignment

- Common points are selected in both point clouds and the point clouds are aligned based on the point positions. A minimum of three points is required for alignment.
- The method is more accurate with a higher number of common points and when common points are spread across the full point clouds. If possible, select static points that have not been displaced between the two point clouds.
- Method can be time-consuming finding distinct features in both point clouds and accurately marking them.
- Because only a small number of points are selected, the alignment accuracy is strongly influenced by the accuracy of those points.
- Generally, this method is used for rough alignments.

Iterative Closest Point (ICP) Algorithm

- ICP is a least squares matching algorithm that transforms (translation and rotation) one point cloud (called the source or aligned point cloud) to a reference point cloud. The combined distance between the two point clouds is minimized in each iteration until an optimal alignment is achieved.
- ICP allows for fine registration of point clouds. Point clouds must be roughly aligned before executing ICP.
- ICP can be performed in CloudCompare.
- If the point clouds being aligned have stable areas where no deformation occurred, align using ICP based on those areas. This is often the case in rockfall monitoring applications.
    - One method to accomplish this is to copy the point clouds and delete all parts except the stable areas. Align the stables areas using ICP, then apply the ICP transformation matrix to the full point clouds.
- If there are no areas in the point clouds that are certainly stable, the ICP algorithm can be executed on the full point clouds. Performing ICP on larger areas generally reduces influence of smaller areas that have deformed and provides a relatively accurate alignment.
    - However, aligning point clouds based on unstable areas that have deformed is inherently flawed. Effort should be made to remove areas that have certainly deformed in order to maximize alignment of stable areas and improve the overall alignment accuracy.

4.3 Deformation Measurement

- Deformation is determined by comparing two point clouds and measuring distances between them.
- Many programs are designed for comparing point clouds to determine deformations.

    - CloudCompare is free, powerful, and has many functions and tools for point cloud comparisons. Additionally, much of the research and development in cloud comparison methods is performed in CloudCompare.

- There are several methods and techniques that can be used to measure deformation between point clouds. The four most common are discussed here, and other techniques are mentioned below.

4.3.1 Deformation Measurement Methods

DoD – Digital Surface Model (DSM) of Difference

- A DSM is a raster surface dataset produced by gridding a point cloud. A DSM includes 3D data in a 2.5D format – the Z (vertical) coordinate is a value attributed to the XY location in the grid. The Z value is determined by interpolation of the local data points.
- A DoD is the comparison of two DSMs by differentiating elevations on a pixel-by-pixel basis.
- DoD is useful for detecting 1D deformation of planar geometries, such as consolidation settlement of infrastructure.
- Interpolating point cloud data to produce a DSM reduces surface details and limits the ability of DoD to detect small-scale deformations.
- DoD comparisons are not suitable for many projects because deformation is often not limited to one direction.

C2C – Cloud-to-Cloud

- C2C comparisons are performed directly on the point clouds and do not require interpolating or gridding. It is the simplest and fastest method for point cloud comparisons.
- Its most basic version measures the distance between a point in the compared cloud to the closest point in the reference cloud. Improvements in C2C distance accuracy can be made by performing a least squares fit of the closest point neighbours in the reference cloud.

- C2C is highly sensitive to point cloud roughness, outliers, and differing point densities, which can cause deformations to be inaccurate.

C2M – Cloud-to-Mesh

- C2M comparisons involve creating a detailed 3D meshed surface of the reference point cloud and calculating the cloud-to-mesh distance along the mesh surface normal.
- This method generally provides accurate distance measurements, but issues arise in areas where the two point clouds do not overlap or where the point cloud contains very few points.
- Mesh interpolation issues:
    - Mesh construction smooths out small-scale details.
    - Interpolation introduces an additional source of error to the comparison.
    - Interpolation artifacts may bias deformation measurements.
- C2M is best suited for situations where an accurate baseline 3D model exists (e.g. from a laser scanner) and UAV point clouds can be compared to the baseline mesh surface.

M3C2 – Multiscale Model-to-Model Cloud Comparison

- M3C2 is a newer and more sophisticated method for measuring deformations between point clouds that has proved to be effective and accurate.
- M3C2 operates directly on point clouds without meshing or gridding, computes deformation along the local normal surface direction, and estimates an LoD for each distance measurement.
- M3C2 provides significant change estimates, that is categorizes deformations greater than LoD as significant. This feature allows the user to focus on the significant deformations.
- Drawback: M3C2 has more parameters to define than other methods. It can take time to determine appropriate parameter values.

Other Deformation Measurement Methods

- Calculating volume changes.
- Tracking displacement of discrete features.
- Comparing cross-sections.

4.3.2 Deformation Measurement Recommendations

- For all deformation measurement methods, a parametric analysis should be performed to investigate the effect that the method's parameters have on the results.
    - DoD: Investigate the effects of the grid size on the accuracy of results and processing time to determine optimal grid size.
    - M3C2: Lague et al. (2013) provides guidance on selecting parameters.
- Validate the deformation results of one method by using a different method.
    - Example: If using M3C2 to measure deformations, perform C2C or C2M comparisons to confirm the M3C2 results are reasonable.
- UAV deformations should be compared to on-site instrumentation or survey data to validate the results.

5. CONCLUSION

UAV photogrammetry with SfM processing is a powerful technology that can rapidly produce accurate point clouds for deformation monitoring. The methods and techniques presented in this guideline were developed over a three-year period of using UAVs to monitor small-scale deformations of embankments in the Canadian Arctic. The author hopes this guideline helps practitioners to successfully conduct UAV flights and accurately measure deformations of structures and landforms.